

University of Warwick institutional repository: <http://go.warwick.ac.uk/wrap>

**A Thesis Submitted for the Degree of PhD at the University of Warwick**

<http://go.warwick.ac.uk/wrap/57941>

This thesis is made available online and is protected by original copyright.

Please scroll down to view the document itself.

Please refer to the repository record for this item for information to help you to cite it. Our policy information is available from the repository home page.

Cyclic Behaviour of Hollow and  
Concrete-Filled Circular Hollow Section  
Braces

by

Therese Sheehan

A thesis submitted in partial fulfilment of the requirements for the

degree of

Doctor of Philosophy in Engineering

University of Warwick, School of Engineering

July 2013

## Contents

List of Figures .....	vii
List of Tables.....	xx
Notations .....	xxvii
Acknowledgements .....	xxxviii
Declaration .....	xxxix
Abstract .....	xl
Chapter 1 Introduction.....	1
1.1 Seismic design.....	1
1.2 Tubular structures in earthquake design.....	2
1.3 Hot-finished and cold formed steel .....	3
1.4 Outline of thesis.....	4
Chapter 2 Literature Review .....	6
2.1 Introduction .....	6
2.2 Seismic design.....	6
2.2.1 Structural framing configurations .....	6
2.2.2 Design approaches.....	7
2.2.3 Strength, stiffness and ductility .....	10
2.3 Steel material behaviour.....	13
2.3.1 Tubular sections .....	13
2.3.2 Steel section type.....	15

## Contents

2.3.3 Cyclic response of steel .....	16
2.4 Concrete-filled tubes .....	19
2.4.1 Background .....	19
2.4.2 Concrete-filled tubes in seismic applications .....	22
2.4.3 Steel-concrete interface .....	23
2.5 Numerical modelling .....	24
2.5.1 Background .....	24
2.5.2 Steel constitutive model in ABAQUS .....	25
2.5.3 Concrete constitutive model in ABAQUS .....	25
2.5.4 Geometric imperfections .....	29
2.6 Concluding remarks .....	29
Chapter 3 Laboratory Experiments .....	30
3.1 Introduction .....	30
3.2 Material tests .....	30
3.2.1 Tensile coupon tests .....	30
3.2.2 Concrete material tests .....	33
3.3 Stub column tests.....	35
3.3.1 Test preparation .....	35
3.3.2 Results .....	38
3.4 Bracing tests .....	41
3.4.1 Specimen preparation .....	41

## Contents

3.4.2 Test procedure .....	45
3.4.3 Deformation and failure .....	48
3.4.4 Displacement ductility.....	51
3.4.5 First cycle buckling loads.....	53
3.4.6 Post-buckling compressive strength.....	55
3.4.7 Tensile load and load degradation.....	60
3.4.8 Energy dissipation .....	62
3.4.9 Lateral displacements .....	73
3.5 Concluding remarks .....	92
Chapter 4 Numerical Simulations of Hollow Steel Braces .....	94
4.1 Introduction .....	94
4.2 Modelling of hollow steel braces .....	94
4.2.1 Element type and mesh size .....	94
4.2.2 Boundary conditions and loading .....	99
4.2.3 Steel constitutive model .....	100
4.2.4 Failure prediction .....	104
4.2.5 Imperfection amplitudes.....	107
4.2.6 Verification of FE model.....	117
4.2.7 Parametric studies.....	124
4.3 Concluding remarks .....	134

## Contents

Chapter 5 Numerical Simulations of Concrete-Filled Tubular Braces .....	136
5.1 Introduction .....	136
5.2 Modelling of concrete-filled steel braces .....	136
5.2.1 Boundary conditions and loading .....	136
5.2.2 Element type and mesh.....	136
5.2.3 Contact modelling .....	137
5.2.4 Concrete constitutive model .....	138
5.2.5 Verification of FE model.....	146
5.3 Concluding remarks .....	154
Chapter 6 Design Recommendations .....	155
6.1 Introduction .....	155
6.2 First cycle buckling load .....	155
6.3 Post-buckling resistance .....	159
6.4 Tensile resistance .....	163
6.5 Ductility.....	164
6.6 Concluding remarks .....	169
Chapter 7 Conclusions and Recommendations for Further Work .....	171
7.1 Summary .....	171
7.2 Conclusions .....	174
7.3 Suggestions for future research .....	177
References .....	179

## Contents

APPENDIX A	Supplementary data for modelling of hollow steel braces .....	187
A.1	Local imperfection amplitude determination. No. of cycles to fracture for CF-H-1500 .....	188
A.2	Verification of finite element models .....	205
A.3	Load-displacement hysteresis curves for parametric studies .....	214

## List of Figures

Figure 1.1	The University Hall of Berkeley, California.....	1
Figure 1.2	Crystal Cathedral, California.....	2
Figure 1.3	Taipei 101, Taiwan.....	3
Figure 2.1	Framing configurations for earthquake-resistant buildings: (a) moment-resisting frame; (b) concentrically braced frame; (c) eccentrically braced frame.....	6
Figure 2.2	Two-surface cyclic plasticity model in terms of (a) stresses in 3D space; (b) uniaxial stress-strain relationship.....	17
Figure 2.3	Lateral pressure in concrete-filled tube.....	20
Figure 2.4	Stress-strain relationship for concrete in tension.....	27
Figure 2.5	Stress-strain relationship for concrete under compression.....	28
Figure 3.1	Tensile coupon specimen (a) locations on tubular cross-section; (b) dimensions.....	31
Figure 3.2	Tensile testing set-up.....	32
Figure 3.3	Stress-strain curves for hot-finished and cold formed steel coupons.....	32
Figure 3.4	Test set-up for measuring stub-column local imperfections.....	36
Figure 3.5	Strain-gauge locations for stub column tests.....	37



## List of Figures

Figure 3.6	Load-displacement relationships for hot-finished and cold formed stub columns.....	38
Figure 3.7	Stub column (a) at beginning of test; (b) during test after occurrence of local buckling; (c) at end of test.....	39
Figure 3.8	Concrete trial compactions.....	42
Figure 3.9	Cyclic test specimen end connection details.....	44
Figure 3.10	Set-up for measuring global imperfections of bracing test-specimens.....	45
Figure 3.11	Cyclic loading protocol (ECCS, 1986).....	46
Figure 3.12	Test-rig and instrumentation.....	47
Figure 3.13	Local buckling and failure at (a) mid-height of HF-H-1500; (b) mid-height and base of HF-F1-1500.....	48
Figure 3.14	Global deformed shape for (a) hollow specimen; (b) concrete-filled specimen.....	50
Figure 3.15	Direction of global deflection of cold formed braces.....	51
Figure 3.16	First cycle buckling loads from experiments.....	54
Figure 3.17	Post-buckling resistance in 1 <sup>st</sup> cycle at each displacement amplitude for 1500 mm specimens.....	56
Figure 3.18	Post-buckling resistance in 1 <sup>st</sup> cycle at each displacement amplitude for 3000 mm specimens.....	56

## List of Figures

Figure 3.19	Post-buckling resistance versus non-dimensional slenderness for $\mu_{\Delta} = 2$ .....	59
Figure 3.20	Post-buckling resistance versus non-dimensional slenderness for $\mu_{\Delta} = 3$ .....	59
Figure 3.21	Post-buckling resistance versus non-dimensional slenderness for $\mu_{\Delta} = 5$ .....	60
Figure 3.22	Assumed biaxial stress state for steel tube.....	61
Figure 3.23	Maximum tensile force for 1 <sup>st</sup> cycle at each displacement amplitude.....	62
Figure 3.24	Load-displacement response for HF-H-1500.....	63
Figure 3.25	Load-displacement response for CF-H-1500.....	63
Figure 3.26	Load-displacement response for HF-F1-1500.....	64
Figure 3.27	Load-displacement response for HF-F2-1500.....	64
Figure 3.28	Load-displacement response for CF-F1-1500.....	65
Figure 3.29	Load-displacement response for CF-F2-1500.....	65
Figure 3.30	Load-displacement response for HF-H-3000.....	66
Figure 3.31	Load-displacement response for CF-H-3000.....	66
Figure 3.32	Load-displacement response for HF-F1-3000.....	67
Figure 3.33	Load-displacement response for HF-F2-3000.....	67

## List of Figures

Figure 3.34	Load-displacement response for CF-F1-3000.....	68
Figure 3.35	Load-displacement response for CF-F2-3000.....	68
Figure 3.36	Load-displacement hysteresis loop for cold formed members in 13 <sup>th</sup> cycle.....	70
Figure 3.37	Accumulated energy dissipation for 1500 mm specimens.....	72
Figure 3.38	Accumulated energy dissipation for 3000 mm specimens.....	73
Figure 3.39	Relationship between axial load and lateral displacement at the mid-height for specimen (a) HF-H-1500; (b) CF-H-1500; (c) HF-F1-1500; (d) HF-F2-1500; (e) CF-F1-1500; (f) CF-F2-1500.....	74
Figure 3.40	Relationship between axial load and lateral displacement at the mid-height for specimen (a) HF-H-3000; (b) CF-H-3000; (c) HF-F1-3000; (d) HF-F2-3000; (e) CF-F1-3000; (f) CF-F2-3000.....	75
Figure 3.41	Lateral displacement at brace mid-height for low axial displacements: (a) geometry of deformed member; (b) assumed sinusoidal function.....	76
Figure 3.42	Assumed geometry for plastic mechanism of brace.....	77
Figure 3.43	Lateral deflections for 1500 mm hot-finished braces in 3 <sup>rd</sup> cycle of each amplitude.....	79
Figure 3.44	Lateral deflections for hot-finished 1500 mm specimens in the 3 <sup>rd</sup> cycle at each displacement amplitude with proposed second order polynomial, Equation (3.19).....	80

## List of Figures

Figure 3.45	Relationship between predicted and actual mid-height lateral deflections for 1500 mm hot-finished specimens using Equation (3.18).....	81
Figure 3.46	Relationship between predicted and actual mid-height lateral deflections for 1500 mm hot-finished specimens using Equation (3.19).....	82
Figure 3.47	Lateral mid-height deflections for hot-finished 3000 mm specimens in the 3 <sup>rd</sup> cycle at each displacement amplitude with linear predictive expression (3.20).....	83
Figure 3.48	Lateral mid-height deflections for hot-finished 3000 mm specimens in the 3 <sup>rd</sup> cycle at each displacement amplitude with second order predictive expression (3.21).....	83
Figure 3.49	Relationship between predicted and actual mid-height lateral deflections for 3000 mm hot-finished specimens using Equation (3.20).....	84
Figure 3.50	Relationship between predicted and actual mid-height lateral deflections for 3000 mm hot-finished specimens using Equation (3.21).....	85
Figure 3.51	Lateral mid-height deflections for hot-finished specimens of all lengths in the 3 <sup>rd</sup> cycle of each displacement amplitude.....	86
Figure 3.52	Relationship between predicted and actual mid-height lateral deflections for hot-finished specimens using Equation (3.22).....	87

## List of Figures

Figure 3.53	Lateral mid-height deflections for cold formed 1500 mm specimens in the 3 <sup>rd</sup> cycle of each displacement amplitude.....	88
Figure 3.54	Lateral mid-height deflections for cold formed 3000 mm specimens in the 3 <sup>rd</sup> cycle of each displacement amplitude.....	88
Figure 3.55	Lateral mid-height deflections for cold formed specimens of all lengths in the 3 <sup>rd</sup> cycle of each displacement amplitude.....	89
Figure 3.56	Relationship between predicted and actual mid-height lateral deflections for 1500 mm cold formed specimens using Equation (3.23).....	90
Figure 3.57	Relationship between predicted and actual mid-height lateral deflections for 3000 mm cold formed specimens using Equation (3.24).....	91
Figure 3.58	Relationship between predicted and actual mid-height lateral deflections for cold formed specimens of all lengths using Equation (3.25).....	91
Figure 4.1	Finite element model of specimen CF-H-1500 .....	95
Figure 4.2	Relative mesh size and monitoring area for (a) Mesh 1; (b) Mesh 2; (c) Mesh 3; (d) Mesh 4; (e) Mesh 5.....	96
Figure 4.3	Variation in (a) minimum in-plane strain with mesh size for selected region at quarter-length; (b) maximum strain with mesh size for selected region at quarter-length.....	97

## List of Figures

Figure 4.4	Variation in (a) minimum strain with mesh size for a selected region at specimen end; (b) maximum strain with mesh size for a selected region at specimen end.....	98
Figure 4.5	Variation in (a) minimum strain with mesh size for a selected region at mid-length; (b) maximum strain with mesh size for a selected region at mid-length.....	99
Figure 4.6	Development of yield surface for ABAQUS® nonlinear isotropic/kinematic hardening model: (a) isotropic component; (b) kinematic component.....	100
Figure 4.7	Determination of isotropic hardening component for steel material model.....	103
Figure 4.8	Determination of kinematic hardening component for steel material model.....	103
Figure 4.9	Illustration of rainflow analysis technique.....	106
Figure 4.10	Strain variation along brace length for model of CF-H-1500.....	110
Figure 4.11	Strain variation around circumference for model of CF-H-1500....	111
Figure 4.12	Deformed shape at mid-length showing: (a) peak strain at edge of compression face; (b) Region A; (c) Region B; (d) Region C.....	112
Figure 4.13	Deformed shape at mid-length showing: (a) peak strain at centre of compression face; (b) Region D; (c) Region E; (d) Region F.....	113

## List of Figures

Figure 4.14	Rows of elements used for predicting the number of cycles to fracture.....	114
Figure 4.15	Load displacement hysteresis curves for specimen CF-H-1500.....	119
Figure 4.16	Load displacement hysteresis curves for specimen HF-H-1500.....	120
Figure 4.17	Load displacement hysteresis curves for specimen CF-H-3000.....	120
Figure 4.18	Load displacement hysteresis curves for specimen HF-H-3000.....	121
Figure 4.19	Load displacement hysteresis curves for specimen S7C (Elchalakani <i>et al.</i> , 2003).....	121
Figure 4.20	Load displacement hysteresis curves for specimen CHS-C (Packer <i>et al.</i> , 2010).....	122
Figure 4.21	Load displacement hysteresis curves for specimen 721 (Takeuchi and Matsui, 2011).....	122
Figure 4.22	Load displacement hysteresis curves for specimen 728 (Takeuchi and Matsui, 2011).....	123
Figure 4.23	Load displacement hysteresis curves for specimen 732 (Takeuchi and Matsui, 2011).....	123
Figure 4.24	Buckled shape at mid-length for specimens CF13, HF9 and HF13.....	126
Figure 4.25	Relationship between number of cycles to failure and global slenderness for cross-section classifications of (a) Class 1; (b) Class 2; (c) Class 3; (d) Class 4 in accordance with BS EN 1993-1-1 (2005).....	127

## List of Figures

Figure 4.26	Relationship between number of cycles to failure and cross-sectional slenderness for global slenderness values of (a) $\bar{\lambda} = 0.5$ ; (b) $\bar{\lambda} = 1.0$ ; (c) $\bar{\lambda} = 1.5$ ; (d) $\bar{\lambda} = 2.0$ in accordance with BS EN 1993-1-1 (2005).....	128
Figure 4.27	Comparison between predicted and actual values of displacement ductility, $\mu_{\Delta}$ .....	130
Figure 4.28	Relationship between normalised energy dissipation during 8 <sup>th</sup> cycle and (a) global slenderness, $\bar{\lambda}$ ; (b) local slenderness, $D/t\epsilon^2$ .....	131
Figure 4.29	Comparison between predicted and actual energy dissipation during 8 <sup>th</sup> cycle for cold formed and hot-finished specimens.....	132
Figure 4.30	Relationship between total normalised energy dissipation prior to specimen failure and (a) global slenderness, $\bar{\lambda}$ ; (b) local slenderness, $D/t\epsilon^2$ .....	133
Figure 4.31	Comparison between predicted and actual total energy dissipation prior to specimen failure.....	134
Figure 5.1	Variation in strain over monitoring area with increasing mesh density.....	137
Figure 5.2	Effect of $K_c$ on yield surface in deviatoric space.....	140
Figure 5.3	Concrete constitutive behaviour in compression from Hu <i>et al.</i> (2003).....	143



## List of Figures

Figure 5.4	Relationship between tensile stress and crack width for concrete...144
Figure 5.5	Illustration of stiffness recovery factors for concrete in tension and compression.....145
Figure 5.6	Deformed shape of FE specimen CF-F-1500: (a) cross-section view at mid-length; (b) side view of specimen.....147
Figure 5.7	Load displacement hysteresis curves for specimen CF-F1-1500....149
Figure 5.8	Load displacement hysteresis curves for specimen CF-F2-1500....150
Figure 5.9	Load displacement hysteresis curves for specimen HF-F1-1500....150
Figure 5.10	Load displacement hysteresis curves for specimen HF-F2-1500....151
Figure 5.11	Load displacement hysteresis curves for specimen CF-F1-3000....151
Figure 5.12	Load displacement hysteresis curves for specimen CF-F2-3000....152
Figure 5.13	Load displacement hysteresis curves for specimen HF-F1-3000....152
Figure 5.14	Load displacement hysteresis curves for specimen HF-F2-3000....153
Figure 6.1	Post-buckling resistance of FE and laboratory test specimens at $\mu_{\Delta} = 2$ .....160
Figure 6.2	Post-buckling resistance of FE and laboratory test specimens at $\mu_{\Delta} = 3$ .....161
Figure 6.3	Post-buckling resistance of FE and laboratory test specimens at $\mu_{\Delta} = 5$ .....162

## List of Figures

Figure 6.4	Relationship between predicted displacement ductility and global slenderness for hot-finished hollow steel sections.....	166
Figure 6.5	Relationship between predicted displacement ductility and global slenderness for cold formed hollow steel sections.....	167
Figure 6.6	Relationship between predicted displacement ductility and local slenderness for hot-finished hollow steel sections.....	168
Figure 6.7	Relationship between predicted displacement ductility and local slenderness for cold formed hollow steel sections.....	169
Figure A.1.1	Regions at edge of compression face for monitoring strain progressions.....	188
Figure A.1.2	Buckled shape of cold formed CHS at mid-length, showing (a) Element undergoing maximum strains ('peak' element) at compression face edge; (b) Region A for monitoring strains; (c) Region B; (d) Region C.....	189
Figure A.1.3	Regions at centre of compression face for monitoring strain progressions.....	197
Figure A.1.4	Buckled shape of cold formed CHS at mid-length, showing (a) Elements undergoing maximum strains ('peak' elements) at centre of compression face; (b) Region D for monitoring strains; (c) Region E; (d) Region F.....	198

## List of Figures

Figure A.3.1	Load-displacement relationship for CF1.....	214
Figure A.3.2	Load-displacement relationship for CF2.....	215
Figure A.3.3	Load-displacement relationship for CF3.....	215
Figure A.3.4	Load-displacement relationship for CF4.....	216
Figure A.3.5	Load-displacement relationship for CF5.....	216
Figure A.3.6	Load-displacement relationship for CF6.....	217
Figure A.3.7	Load-displacement relationship for CF7.....	217
Figure A.3.8	Load-displacement relationship for CF8.....	218
Figure A.3.9	Load-displacement relationship for CF9.....	218
Figure A.3.10	Load-displacement relationship for CF10.....	219
Figure A.3.11	Load-displacement relationship for CF11.....	219
Figure A.3.12	Load-displacement relationship for CF12.....	220
Figure A.3.13	Load-displacement relationship for CF13.....	220
Figure A.3.14	Load-displacement relationship for CF14.....	221
Figure A.3.15	Load-displacement relationship for CF15.....	221
Figure A.3.16	Load-displacement relationship for CF16.....	222
Figure A.3.17	Load-displacement relationship for HF1.....	222
Figure A.3.18	Load-displacement relationship for HF2.....	223

## List of Figures

Figure A.3.19 Load-displacement relationship for HF3.....	223
Figure A.3.20 Load-displacement relationship for HF4.....	224
Figure A.3.21 Load-displacement relationship for HF5.....	224
Figure A.3.22 Load-displacement relationship for HF6.....	225
Figure A.3.23 Load-displacement relationship for HF7.....	225
Figure A.3.24 Load-displacement relationship for HF8.....	226
Figure A.3.25 Load-displacement relationship for HF9.....	226
Figure A.3.26 Load-displacement relationship for HF10.....	227
Figure A.3.27 Load-displacement relationship for HF11.....	227
Figure A.3.28 Load-displacement relationship for HF12.....	228
Figure A.3.29 Load-displacement relationship for HF13.....	228
Figure A.3.30 Load-displacement relationship for HF14.....	229
Figure A.3.31 Load-displacement relationship for HF15.....	229
Figure A.3.32 Load-displacement relationship for HF16.....	230

## List of Tables

Table 2.1	Behaviour factor, $q$ , limits for various structural types in BS EN 1998-1 (2004).....	9
Table 2.2	Cross-sectional classification requirements for each structural ductility class in BS EN 1998-1 (2004).....	10
Table 2.3	Cross-section classification limits for steel tubes in BS EN 1993-1-1 (2005).....	14
Table 2.4	Cross-sectional limit recommendations for concrete-filled tubes (Bergmann <i>et al.</i> , 1995).....	21
Table 3.1	Nominal steel tube dimensions and material properties.....	31
Table 3.2	Results of tensile coupon tests.....	33
Table 3.3	Concrete properties from material tests.....	34
Table 3.4	Stub column details.....	37
Table 3.5	Maximum loads from stub column tests.....	40
Table 3.6	Summary of bracing specimens.....	43
Table 3.7	Maximum numbers of cycles and loads.....	52
Table 3.8	First cycle buckling loads from experiments.....	54
Table 3.9	Maximum tensile forces.....	61
Table 3.10	Energy dissipated at various stages of testing.....	71

## List of Tables

Table 3.11	Summary of predictive expressions for lateral deflections at the mid-height and corresponding coefficients of variation.....	92
Table 4.1	Mesh densities used for sensitivity study.....	96
Table 4.2	Buckling load for CF-H-1500 with various global imperfection amplitudes.....	108
Table 4.3	Buckling load for CF-H-3000 with various global imperfection amplitudes.....	108
Table 4.4	No. of cycles to fracture for local imperfection = $t/100$ , taking centre of compression face; scaled fracture parameters from Nip <i>et al.</i> (2010b).....	115
Table 4.5	No. of cycles to fracture for local imperfection = $t/100$ , taking edge of compression face; scaled fracture parameters from Nip <i>et al.</i> (2010b).....	115
Table 4.6	Specimens used for validation of FE model.....	117
Table 4.7	Material parameters for FE models.....	118
Table 4.8	Comparison between FE and experimental results.....	118
Table 4.9	Specimen details for cold formed steel parametric studies.....	124
Table 4.10	Specimen details for hot finished steel parametric studies.....	125
Table 5.1	Proposed mesh densities for concrete-filled tubes.....	137

## List of Tables

Table 5.2	Comparison between laboratory test specimens and finite element model results for concrete-filled tubular braces.....	146
Table 6.1	Comparison between maximum first cycle buckling loads in tests/FE and predictions from BS EN 1993-1-1 (2005)/BS EN 1994-1-1 (2004) for cold formed members.....	157
Table 6.2	Comparison between maximum first cycle buckling loads in tests/FE and predictions from BS EN 1993-1-1 (2005)/BS EN 1994-1-1 (2004) for hot-finished members.....	158
Table 6.3	Outline of ductility classes in BS EN 1998-1 (2004).....	165
Table A.1.1	No. of cycles to fracture for local imperfection = $t/25$ , taking edge of compression face; original fracture parameters $\varepsilon'_f$ and $c$ from Nip <i>et al.</i> (2010b).....	191
Table A.1.2	No. of cycles to fracture for local imperfection = $t/50$ , taking edge of compression face; original fracture parameters $\varepsilon'_f$ and $c$ from Nip <i>et al.</i> (2010b).....	192
Table A.1.3	No. of cycles to fracture for local imperfection = $t/100$ , taking edge of compression face; original fracture parameters $\varepsilon'_f$ and $c$ from Nip <i>et al.</i> (2010b).....	192
Table A.1.4	No. of cycles to fracture for local imperfection = $t/200$ , taking edge of compression face; original fracture parameters $\varepsilon'_f$ and $c$ from Nip <i>et al.</i> (2010b).....	193

## List of Tables

Table A.1.5	No. of cycles to fracture for local imperfection = $t/500$ , taking edge of compression face; original fracture parameters $\varepsilon'_f$ and $c$ from Nip <i>et al.</i> (2010b).....	193
Table A.1.6	No. of cycles to fracture for local imperfection = $t/25$ , taking edge of compression face; scaled fracture parameters $\varepsilon'_f$ and $c$ from Nip <i>et al.</i> (2010b).....	194
Table A.1.7	No. of cycles to fracture for local imperfection = $t/50$ , taking edge of compression face; scaled fracture parameters $\varepsilon'_f$ and $c$ from Nip <i>et al.</i> (2010b).....	194
Table A.1.8	No. of cycles to fracture for local imperfection = $t/100$ , taking edge of compression face; scaled fracture parameters $\varepsilon'_f$ and $c$ from Nip <i>et al.</i> (2010b).....	195
Table A.1.9	No. of cycles to fracture for local imperfection = $t/200$ , taking edge of compression face; scaled fracture parameters $\varepsilon'_f$ and $c$ from Nip <i>et al.</i> (2010b).....	195
Table A.1.10	No. of cycles to fracture for local imperfection = $t/500$ , taking edge of compression face; scaled fracture parameters $\varepsilon'_f$ and $c$ from Nip <i>et al.</i> (2010b).....	196
Table A.1.11	No. of cycles to fracture for local imperfection = $t/25$ , taking centre of compression face; original fracture parameters $\varepsilon'_f$ and $c$ from Nip <i>et al.</i> (2010b).....	199



## List of Tables

Table A.1.12	No. of cycles to fracture for local imperfection = $t/50$ , taking centre of compression face; original fracture parameters $\varepsilon'_f$ and $c$ from Nip <i>et al.</i> (2010b).....	200
Table A.1.13	No. of cycles to fracture for local imperfection = $t/100$ , taking centre of compression face; original fracture parameters $\varepsilon'_f$ and $c$ from Nip <i>et al.</i> (2010b) .....	200
Table A.1.14	No. of cycles to fracture for local imperfection = $t/200$ , taking centre of compression face; original fracture parameters $\varepsilon'_f$ and $c$ from Nip <i>et al.</i> (2010b) .....	201
Table A.1.15	No. of cycles to fracture for local imperfection = $t/500$ , taking centre of compression face; original fracture parameters $\varepsilon'_f$ and $c$ from Nip <i>et al.</i> (2010b) .....	201
Table A.1.16	No. of cycles to fracture for local imperfection = $t/25$ , taking centre of compression face; scaled fracture parameters $\varepsilon'_f$ and $c$ from Nip <i>et al.</i> (2010b).....	202
Table A.1.17	No. of cycles to fracture for local imperfection = $t/50$ , taking centre of compression face; scaled fracture parameters $\varepsilon'_f$ and $c$ from Nip <i>et al.</i> (2010b) .....	202
Table A.1.18	No. of cycles to fracture for local imperfection = $t/100$ , taking centre of compression face; scaled fracture parameters $\varepsilon'_f$ and $c$ from Nip <i>et al.</i> (2010b).....	203

## List of Tables

Table A.1.19	No. of cycles to fracture for local imperfection = $t/200$ , taking centre of compression face; scaled fracture parameters $\varepsilon'_f$ and $c$ from Nip <i>et al.</i> (2010b).....	203
Table A.1.20	No. of cycles to fracture for local imperfection = $t/500$ , taking centre of compression face; scaled fracture parameters $\varepsilon'_f$ and $c$ from Nip <i>et al.</i> (2010b) .....	204
Table A.2.1	No. of cycles to fracture for CF-H-1500 using original fracture parameters $\varepsilon'_f$ and $c$ from Nip (2010b).....	206
Table A.2.2	No. of cycles to fracture for CF-H-1500 using scaled fracture parameters $\varepsilon'_f$ and $c$ from Nip (2010b).....	207
Table A.2.3	No. of cycles to fracture for HF-H-1500 using original fracture parameters $\varepsilon'_f$ and $c$ from Nip (2010b).....	208
Table A.2.4	No. of cycles to fracture for HF-H-1500 using scaled fracture parameters $\varepsilon'_f$ and $c$ from Nip (2010b).....	209
Table A.2.5	No. of cycles to fracture for CF-H-3000 using original fracture parameters $\varepsilon'_f$ and $c$ from Nip (2010b).....	210
Table A.2.6	No. of cycles to fracture for CF-H-3000 using scaled fracture parameters $\varepsilon'_f$ and $c$ from Nip (2010b).....	211
Table A.2.7	No. of cycles to fracture for HF-H-3000 using original fracture parameters $\varepsilon'_f$ and $c$ from Nip (2010b).....	212
Table A.2.8	No. of cycles to fracture for HF-H-3000 using scaled fracture parameters $\varepsilon'_f$ and $c$ from Nip (2010b).....	213

## List of Tables

Table A.3.1	Estimated number of cycles to fracture for parametric studies.....	231
-------------	--	-----

## Notations

$a$	empirical constant (Tremblay, 2002)
$A_a$	cross-sectional area of steel tube
$A_c$	cross-sectional area of concrete
$b$	rate of change of yield surface size with increasing plastic strain
$b$	empirical constant (Tremblay, 2002)
$c$	empirical constant (Tremblay, 2002)
$c$	fatigue ductility exponent
$C_k$	initial kinematic hardening modulus
$C_u$	maximum compressive resistance (CAN/CSA-S16, 1994)
$C'_u$	post-buckling resistance
$d_c$	compressive damage parameter for concrete
$d_t$	tensile damage parameter for concrete
$D$	damage index for Miner's Rule (Miner, 1945)
$D$	cross-section outer diameter
$e$	eccentricity parameter for flow rule in concrete damaged plasticity model
$E$	modulus of elasticity

## Notations

$E_c$	static elastic modulus of concrete
$E_E$	strain energy at yield
$E_a$	modulus of elasticity of steel
$E_s$	modulus of elasticity of steel
$E_{t,H}$	total hysteretic energy dissipated before failure
$E_0$	elastic modulus of concrete (as assumed in damaged plasticity model)
$f_c$	concrete stress
$f_{cd}$	concrete design resistance (BS EN 1994-1-1, 2004)
$f_1$	lateral pressure on confined concrete
$f_u$	ultimate stress (tensile coupons)
$f_y$	steel yield stress (hot-finished)/0.2% proof stress (cold formed)
$f_{yd}$	steel design yield strength (BS EN 1994-1-1, 2004)
$f_{y,max}$	maximum measured yield stress of material
$f_1$	longitudinal stress in steel tube
$f_2$	transverse stress in steel tube
$f'_c$	compressive strength of unconfined concrete
$f'_{cc}$	compressive strength of confined concrete
$F$	yield function for concrete plasticity model (Lubliner, 1989)

## Notations

$F_y$	steel yield strength (CAN/CSA-S16, 1994)
$F_y$	the force required to cause yielding of the steel cross-section
$G$	function for non-associated flow rule of concrete
$G_f$	fracture energy of concrete (Hillerborg, 1976)
$h$	RHS section depth (outer dimension)
$i$	stage in stress-strain model for kinematic hardening
$I$	second moment of area of cross-section
$I_a$	second moment of area of steel cross-section
$I_c$	second moment of area of concrete cross-section
$k$	backstress number in kinematic hardening model
$k_{ci}$	variable for relating compression damage parameter, $d_c$ to strain (Goto, 2010)
$k_1$	variable for determining strength of confined concrete, $f'_{cc}$
$k_2$	variable for determining the strain, $\epsilon'_{cc}$ , corresponding to the maximum stress of confined concrete
$k_3$	factor for determining ultimate stress of confined concrete (Hu <i>et al.</i> , 2003)
$K_c$	ratio of the second stress invariant on the tensile meridian to that on the compressive meridian at initial yield

## Notations

$K_e$	correction factor for calculating effective stiffness of composite cross-section (BS EN 1994-1-1 (2004))
$L$	specimen length
$L_H$	distance between plastic hinges in brace
$n$	exponent for compression damage relationship (Goto, 2010)
$n$	parameter for determining column compressive strength, $C_u$ (CAN/CSA-S16, 1994)
$n_i$	number of cycles at a particular strain amplitude
$N_{b,Rd}$	member buckling resistance (BS EN 1993-1-1, 2005; BS EN 1994-1-1, 2004)
$N_c$	maximum brace compressive resistance per cycle (experiments)
$N_{cr}$	elastic critical buckling force
$N_{c,max}$	maximum brace compressive resistance (experiments)
$N_{c,\mu\Delta=2}$	brace compressive resistance at displacement ductility = 2
$N_{c,\mu\Delta=3}$	brace compressive resistance at displacement ductility = 3
$N_{c,\mu\Delta=5}$	brace compressive resistance at displacement ductility = 5
$N_f$	number of cycles to fracture
$N_{fi}$	number of cycles to fracture at a particular strain amplitude
$N_{pl,Rd}$	cross-section compressive resistance
$N_{pl,test}$	maximum stub-column load

## Notations

$N_t$	maximum brace tensile resistance per cycle (experiments)
$N_{t,max}$	maximum tensile resistance (experiments)
$N_{t,y}$	predicted yield force from tensile tests
$p$	pressure invariant for concrete
$P_n$	compressive resistance of member (AISC, 2002)
$q$	behaviour factor (BS EN 1998-1, 2004)
$q_{(CM)}$	second stress invariant on the compressive meridian
$q_{(TM)}$	second stress invariant on the tensile meridian
$\bar{q}$	second stress invariant for concrete
$Q_\infty$	maximum change in size of yield surface
$r$	steel strain-hardening parameter (Nakashima <i>et al.</i> , 1992)
$R$	parameter for computing the stress-strain constitutive relationship of confined concrete (Saenz, 1964)
$R_E$	parameter for computing the stress-strain constitutive relationship of confined concrete (Saenz, 1964)
$R_\varepsilon$	parameter for computing the stress-strain constitutive relationship of confined concrete (Saenz, 1964)
$R_\sigma$	parameter for computing the stress-strain constitutive relationship of confined concrete (Saenz, 1964)
$S_1$	first material deviatoric stress



## Notations

$S_2$	second material deviatoric stress
$S_3$	third material deviatoric stress
$t$	steel tube thickness
$u_{cr}$	crack-width of concrete
$w_c$	compression stiffness recovery factor (ABAQUS® concrete damaged plasticity model)
$w_t$	tension stiffness recovery factor (ABAQUS® concrete damaged plasticity model)
$W_T$	total energy dissipated prior to failure (normalised with respect to $W_y$ )
$W_y$	yield energy ( $= f_{yd} A_a \delta_y$ )
$W_8$	energy dissipated in 8 <sup>th</sup> loading cycle (normalised with respect to $W_y$ )
$x$	position on longitudinal member axis
$y$	lateral deflection of member
$\alpha$	function for Lubliner yield function (Lubliner, 1989)
$\alpha$	parameter for calculating post-buckling resistance (Nakashima <i>et al.</i> , 1992)
$\alpha$	overall backstress given by summation of $\alpha_k$ values (steel kinematic hardening model)

## Notations

$\alpha_i$	$i$ th backstress (steel kinematic hardening model)
$\alpha_k$	$k^{\text{th}}$ backstress (steel kinematic hardening model)
$\alpha_u$	value by which the horizontal seismic design action is multiplied in order to form plastic hinges in a number of sections sufficient for the development of overall structural instability, while all other design actions remain constant
$\alpha_1$	value by which the horizontal seismic design action is multiplied in order to first reach the plastic resistance of any member in the structure, while all other design actions remain constant
$\beta$	parameter for calculating post-buckling resistance (Nakashima <i>et al.</i> , 1992)
$\beta$	function for Lubliner yield function (Lubliner, 1989)
$\gamma$	function for Lubliner yield function (Lubliner, 1989)
$\gamma_k$	rate of decrease of $C_k$ with increasing plastic deformation
$\gamma_{\text{ov}}$	overstrength of material
$\delta$	axial displacement
$\delta_c$	axial compressive displacement
$\delta_{\text{max}}$	maximum axial displacement
$\delta_y$	yield displacement of member ( $= f_y/E \times L$ )
$\Delta$	lateral displacement of brace at the mid-length
$\Delta\epsilon_p$	cyclic strain amplitude for fatigue life prediction (Coffin, 1954; Manson, 1954)

## Notations

$\Delta\varepsilon^{\text{pl}}$	difference between maximum compressive and tensile strain values in a particular cycle
$\varepsilon$	$\sqrt[3]{(235/f_y)}$ (parameter for cross-section classification in BS EN 1993-1-1 (2005))
$\varepsilon$	material strain
$\varepsilon_c$	compressive strain
$\varepsilon_c$	concrete strain
$\varepsilon_{cp}$	plastic strain for compression damage relationship (Goto, 2010)
$\varepsilon_i$	$i$ th strain (steel kinematic hardening model)
$\varepsilon_t$	tensile strain
$\varepsilon_0$	strain at yield for compression damage relationship (Goto, 2010)
$\varepsilon_c^{\text{el}}$	inelastic compressive strain
$\varepsilon_t^{\text{el}}$	inelastic tensile strain
$\varepsilon^{\text{pl}}$	plastic strain
$\varepsilon_c^{\text{pl}}$	maximum compressive strain per cycle
$\varepsilon_t^{\text{pl}}$	maximum tensile strain per cycle
$\varepsilon'_c$	strain of unconfined concrete at maximum stress, $f'_c$
$\varepsilon'_{cc}$	strain of confined concrete at maximum stress, $f'_{cc}$

## Notations

$\varepsilon_f'$	fatigue ductility coefficient (steel material parameter)
$\bar{\varepsilon}^{pl}$	equivalent plastic strain (steel hardening model)
$\bar{\varepsilon}_i^{pl}$	$i^{th}$ equivalent plastic strain
$\tilde{\varepsilon}^{pl}$	equivalent plastic strain (concrete damaged plasticity model)
$\tilde{\varepsilon}_c^{pl}$	compressive equivalent plastic strain
$\tilde{\varepsilon}_t^{pl}$	tensile equivalent plastic strain
$\eta_a$	reduction parameter for steel resistance (BS EN 1994-1-1, 2004)
$\eta_c$	parameter to account for confinement effect in concrete (BS EN 1994-1-1, 2004)
$\lambda$	non-dimensional global slenderness (CAN/CSA-S16, 1994)
$\bar{\lambda}$	non-dimensional global slenderness (BS EN 1993-1-1, 2005; BS EN 1994-1-1, 2004)
$\dot{\lambda}$	plastic loading factor (concrete damaged plasticity model)
$\mu$	ductility ( $= \delta/\delta_y$ )
$\mu$	viscosity parameter for concrete damaged plasticity model
$\mu_c$	compressive displacement ductility
$\mu_f$	fracture ductility
$\mu_t$	tensile displacement ductility

## Notations

$\mu_{\Delta}$	displacement ductility
$\mu_{\varepsilon}$	material ductility
$\mu_{\theta}$	rotation ductility
$\mu_{\chi}$	curvature (section) ductility
$\sigma$	material stress
$\sigma_{b0}$	initial equibiaxial compressive yield stress
$\sigma_c$	compressive stress
$\sigma_{cu}$	ultimate compressive stress
$\sigma_{c0}$	initial uniaxial compressive yield stress
$\sigma_i$	$i$ th stress (steel kinematic hardening model)
$\sigma_n$	the maximum stress in a stabilised cycle (kinematic hardening model)
$\sigma_t$	tensile stress
$\sigma_{t0}$	tensile stress of concrete at cracking
$\sigma_1$	the stress at the initiation of yield in a stabilised cycle (kinematic hardening model)
$\sigma^s$	the stabilised size of the yield surface
$\sigma^0$	size of yield surface (steel material model in ABAQUS®)
$\sigma_n^c$	maximum compressive stress per cycle
$\sigma_n^t$	maximum tensile stress per cycle

## Notations

$\sigma|_0$  yield stress at zero plastic strain

$\bar{\sigma}_c$  effective compressive cohesion stress (concrete damaged plasticity model)

$\bar{\sigma}_t$  effective tensile cohesion stress (concrete damaged plasticity model)

$\hat{\bar{\sigma}}_{\max}$  maximum principal effective stress

$\Phi$  confinement index (Cai, 1987)

$\psi$  angle of dilation of concrete

## **Acknowledgements**

I would like to express my sincere gratitude to my supervisor, Dr. Tak-Ming Chan, Associate Professor in Structural Engineering at the University of Warwick. Over the past three years he has shown tremendous encouragement and patience in guiding me through this research project. I would also like to thank Emeritus Professor Roger Johnson and Professor Toby Mottram for providing valuable advice and expertise, particularly when preparing for the laboratory experiments.

I wish to acknowledge the financial support from Tata Steel, particularly Mr. Trevor Mustard, without which the laboratory experiments would not have been possible.

I am highly grateful to the technical staff in the strong floor and workshops of the School of Engineering in the University of Warwick, particularly Mr. Colin Banks, Mr. Ryan Griffith, Mr. Robert Bromley, Mr. Juan Munoz-Leal, Mr. Graham Canham, Mr. Christopher Fountain, Mr. Peter Meesum, Mr. Charles Joyce, Mr. Dave Robinson and Mr. Paul Hedley, who contributed greatly to the laboratory experiments, both in the preparation and execution.

I would like to thank the administrative staff in the School of Engineering for their assistance during my time spent as a research student, particularly Ms. Kerrie Hatton. I am also thankful to all of my colleagues, past and present, in Room D030 for creating a pleasant and productive working environment.

Finally, I wish to express my appreciation to my parents, Margaret and Dan, and my siblings, Tim, Christine and Louise, who have shown me continuous love and support over the last three years and throughout my education.

## Declaration

This thesis is submitted to the University of Warwick in support of my application for the degree of Doctor of Philosophy. It has been composed by myself and has not been submitted in any previous application for any degree.

Parts of this thesis have been published by the author

Sheehan, T. and Chan, T. M. (2012). Concrete-filled circular hollow sections under cyclic axial loading. *Tubular Structures XIV: The 14<sup>th</sup> International Symposium on Tubular Structures (ISTS14)*, London, 12<sup>th</sup>-14<sup>th</sup> Sept 2012, CRC Press, London: 43-50.

Sheehan, T. and Chan, T. M. (2013). Cyclic response of hollow and concrete-filled CHS braces. *Proceedings of the ICE – Structures and Buildings* (in press).

available online Feb 2013

doi: 10.1680/stbn.12.00033



## **Abstract**

Presented in this thesis is an investigation on the response of hot-finished and cold formed, hollow and concrete-filled circular hollow section braces in earthquake-resisting concentrically braced frames. The role of these braces is to act as structural ‘fuses’ in the frame, dissipating the seismic energy by undergoing plastic deformations. Circular hollow sections offer aesthetic and structural advantages over conventional rectangular hollow sections owing to the uniformity of the section geometry. Distinct behaviour is observed between cold formed and hot-finished tubes, since the cold formed sections retain a higher degree of residual stresses from manufacturing. Braces subjected to cyclic loading fail after the occurrences of global and local buckling, but the performance can be enhanced by employing concrete infill. The concrete-filled steel tube is an optimum combination of the two materials, resulting in an efficient, economic and practical structural member.

Experiments were performed in which cyclic axial loading was applied to hollow and composite braces of each section type. Hot-finished specimens exhibited superior ductility to cold formed members. Concrete infill enhanced the tensile resistance for members of all lengths, the compressive resistance of shorter members and the number of cycles to failure. Finite element models were subsequently developed with ABAQUS® software, using the inbuilt nonlinear isotropic/kinematic hardening model and the damaged plasticity model to define the steel and concrete characteristics. Reliable simulations were achieved for the hollow braces but further work is required for the composite braces.

Both local and global slenderness values influenced the specimen response. Expressions were proposed to predict the displacement ductility and energy dissipation capability of hollow braces in terms of these parameters. The findings suggest that distinct guidelines could be developed for introduction into Eurocode 8 for each steel section type, and that the benefits of concrete infill could be taken into account in dissipative design.

# Chapter 1

## Introduction

### 1.1 Seismic design

This thesis addresses the effectiveness of hollow and concrete-filled circular hollow section braces in concentrically braced earthquake-resisting buildings. In this type of structure, the braces resist the lateral forces and provide a means to absorb the damage of the earthquake while the surrounding structural components remain intact. One example of this popular system is the University Hall of Berkeley in California, as shown in Figure 1.1.



Figure 1.1 The University Hall of Berkeley, California (image from [www.bizjournals.com](http://www.bizjournals.com))

With several of the world's most populous cities affected by earthquakes, safe design for these extreme loading conditions is crucial. Furthermore there is increasing pressure to improve the sustainability and appearance of urban developments, and

thus engineers must endeavour to provide innovative solutions that meet these challenges. Hence variations on systems such as the concentrically braced frame are being continually developed to optimise their performance.

### 1.2 Tubular structures in earthquake design

Tubular members are highly suited to earthquake-resistant buildings owing to their torsional resistance. Their aesthetic qualities render them favourable for architects, and they are a popular choice in seismically active regions of the world. Figure 1.2 presents the Crystal Cathedral in California, which is supported by an intricate system of white steel tubes.

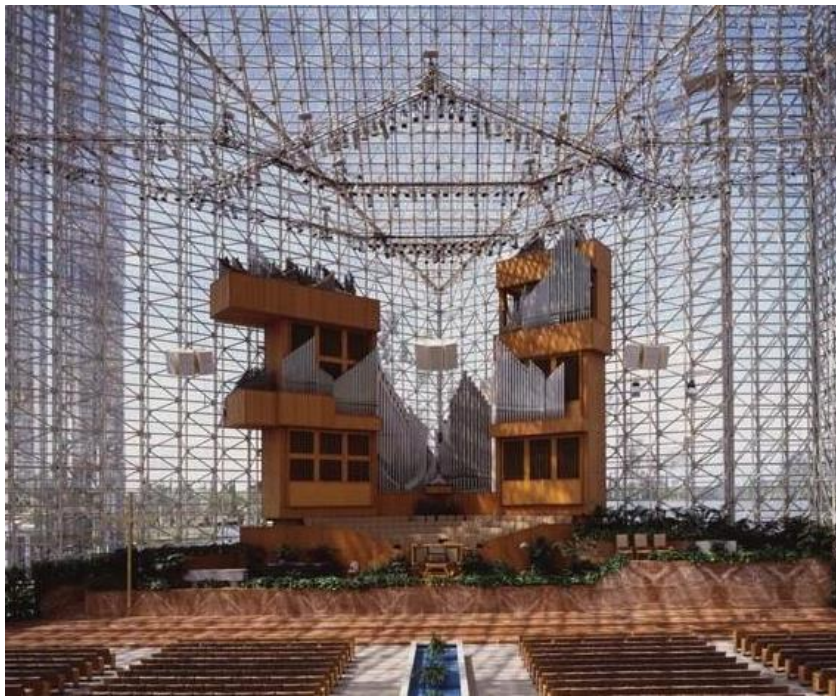


Figure 1.2 Crystal Cathedral, California (image from <http://cal-catholic.com>)

The strength and stiffness of steel tubes has been exploited further by filling the internal void with concrete. Concrete-filled tubes were used to provide the necessary stiffness in the ‘super columns’ of Taipei 101, shown in Figure 1.3, which was formerly the world’s tallest building.



Figure 1.3 Taipei 101, Taiwan (image from [www.systemair.com](http://www.systemair.com))

Although concrete-infill has predominantly been utilised to enhance the performance of tubular columns, it has also been shown to improve the strength and ductility of other member types. This PhD work explores the enhancement provided to tubular braces by the presence of concrete infill, in which there is an increasing level of interest, both in research and in industry.

### **1.3 Hot-finished and cold formed steel**

Sections formed from two different manufacturing processes are compared in this thesis: hot-finished and cold formed tubes. Cold formed steel has been employed for load bearing structures in the UK since the 1940s and usage has become more widespread with the development of suitable design guidelines. Some advantages to this product are the increase in yield stress from the forming process and the production of sections with closer geometric tolerances than those of hot-finished

sections. Sections are formed by passing the flat steel plates between a series of rollers, which form it into the tubular shape, squeezing together the edges and applying electric resistance welding (ERW). Hot-finished tubes undergo a similar manufacturing process but are passed through a furnace in the later stages, alleviating a considerable amount of the residual stresses which remain in cold formed sections. The research had as an aim to compare the suitability of each section type for seismic applications and the potential enhancement provided by concrete infill to each section.

### **1.4 Outline of thesis**

There are six chapters in the thesis subsequent to this brief introduction.

Chapter 2 provides a review of the relevant literature, covering research on hollow and concrete-filled tubular members and finite element modelling. It also describes the approaches adopted in seismic engineering design with a particular focus on the European design guidelines outlined in BS EN 1998-1 (2004).

Chapter 3 presents the laboratory work which was carried out on the strong floor of the University of Warwick. This chapter covers compressive stub column tests and cyclic bracing tests using both hot-finished and cold formed hollow and concrete-filled tubes. Preparation for the tests including the material testing, specimen manufacture and test-rig arrangement are discussed in addition to the experimental results.

Chapters 4 and 5 cover the numerical simulations of hollow and concrete-filled tubular braces respectively. Each chapter outlines the background to modelling the materials, the boundary conditions and the simplifications/assumptions which were used. The models are verified using the results of the experiments. In cases where a

## Chapter 1 Introduction

satisfactory correlation is obtained between the models and the laboratory test results, parametric studies are carried out over a wider range of specimen sizes.

Chapter 6 discusses the results of Chapters 3-5 further and compares the findings with those expected from design recommendations, highlighting the implications of this research on the design guidelines.

Chapter 7 provides a final review of the preceding chapters, a summary of the main conclusions derived from this thesis and suggestions for future work in this field.

## Chapter 2

### Literature Review

#### 2.1 Introduction

This chapter provides a general review of the background theory and previous research relating to this thesis. Various design approaches for earthquake-resisting buildings are presented in addition to the types of steel section explored in this work and the use of concrete-filled tubes. The development of finite element models is also discussed. Further details of the work are provided in subsequent chapters.

#### 2.2 Seismic design

##### 2.2.1 Structural framing configurations

A number of framing systems are used in seismic-resistant buildings in order to provide lateral stability and to dissipate the energy of the earthquake through plastic deformations of individual components. Some examples of commonly adopted systems are moment-resisting frames (MRFs), concentrically braced frames (CBFs) and eccentrically braced frames (EBFs), as shown in Figure 2.1.

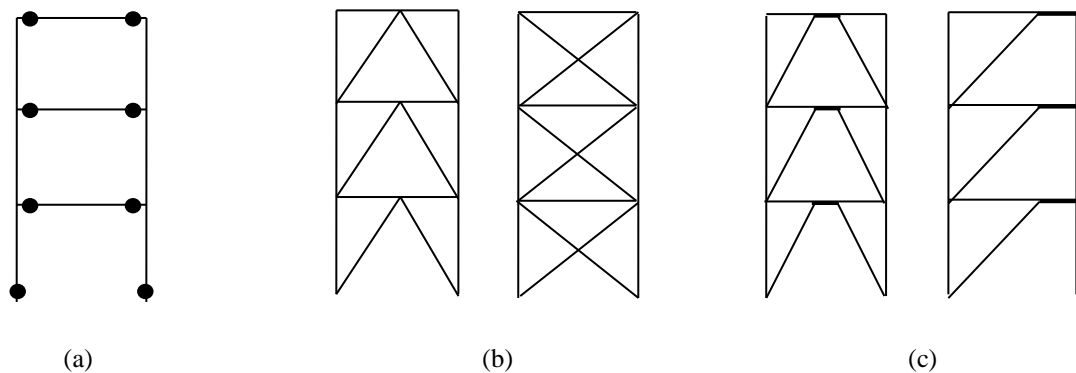


Figure 2.1 Framing configurations for earthquake-resistant buildings: (a) moment-resisting frame; (b) concentrically braced frame; (c) eccentrically braced frame

Each system employs a different mechanism to absorb the seismic loading. Energy dissipation in moment resisting frames is achieved through the formation of plastic hinges, usually in the beams. In eccentrically braced frames, energy is mainly absorbed in zones known as ‘shear links’, between points of intersection of the braces with the beam. This thesis examines the response of concentrically braced frames in which the braces are the dissipative members. Concentrically braced frames often give an unsatisfactory response, as buckling of the compression braces reduces the strength and stiffness of the system leading to asymmetric behaviour of the system between compressive and tensile elements. Furthermore, excessive deformation of these members can potentially damage surrounding structural and non-structural components. Several measures have been proposed to mitigate premature buckling, including encasing the steel core in mortar (buckling restrained braces (BRBs)). This research project considers concrete-filled tubular braces which combine structural efficiency with superior constructability, cost-efficiency and visual appeal to encased members.

### **2.2.2 Design approaches**

Two different design approaches can be adopted for earthquake-resistant structures: direct design and capacity design. Direct design involves identifying individual actions on a local level and designing for these based on either strength or ductility, without considering the system as a whole. On the other hand, a failure mechanism is assumed for capacity design. The members involved are designed to provide enough ductility for the mechanism, while the remaining sections in the structure are selected to have adequate strength to ensure that their behaviour remains elastic. This type of design is based on both strength and ductility.



Several factors can influence the failure mode, interfering with the hierarchy of beams-connections-columns failure in MRFs or braces-beams-connections-columns in CBFs. One such factor is the presence of non-structural elements. Brittle/sudden failures are another issue, for example the fracture of weld or the parent material, bolt shear or tension failures and member buckling, shear or tension failures. These occurrences are generally accounted for in design by the concept of overstrength, which is the ratio of the actual strength of a component or system to the design strength. There are several sources of overstrength in earthquake-resisting buildings such as:

1. The use of load factors and multiple load cases in design
2. Differences between the design material strength and actual material strength, including the effects of strain-hardening
3. The contribution of non-structural elements in resisting the seismic loading
4. Structural redundancy
5. The confinement effect in concrete.

Overstrength can have both positive and negative consequences. For example, flexural overstrength in beams of MRFs can lead to column failure and storey collapse mechanisms. BS EN 1998-1 (2004) takes overstrength into account in a number of different ways. Firstly, it defines a material overstrength factor,  $\gamma_{ov}$ , such that the maximum measured yield stress,  $f_{y,max}$ , should not exceed  $1.1\gamma_{ov}f_y$ , where  $f_y$  is the yield stress of the steel. The recommended value of  $\gamma_{ov}$  is 1.25. BS EN 1998-1 (2004) also defines an overstrength factor for a system,  $\alpha_u/\alpha_1$ , where  $\alpha_u$  is the value by which the horizontal seismic design action is multiplied in order to form plastic hinges in a number of sections sufficient for the development of overall structural instability, while all other design actions remain constant and  $\alpha_1$  is the value by

which the horizontal seismic design action is multiplied in order to first reach the plastic resistance in any member in the structure, while all other design actions remain constant. This factor can be determined by using a pushover analysis.

In BS EN 1998-1 (2004) structural elements are classified as dissipative or non-dissipative according to their function and designed accordingly. Non-dissipative elements are designed to maintain their response in the elastic range whereas dissipative elements are designed to undergo plastic deformations. Structures are classified according to their energy-dissipation capabilities as ductility capacity low (DCL), ductility capacity medium (DCM) or ductility capacity high (DCH). Since structural systems are capable of undergoing nonlinear behaviour and deformations beyond the elastic limit, BS EN 1998-1 (2004) introduces a behaviour factor ' $q$ ' which allows for the reduction in design forces obtained from the elastic response spectrum for dissipative behaviour and governs the degree of overstrength in the system design. Different ' $q$ ' limits are assigned to structures of each energy dissipation classification, which are presented in Table 2.1 for steel-framed buildings.

Table 2.1 Behaviour factor,  $q$ , limits for various structural types in BS EN 1998-1 (2004)

Type of structure	Ductility Class	
	DCM	DCH
Moment resisting frames	4	$5\alpha_w / \alpha_1$
Concentrically braced frames: diagonal braces	4	4
Concentrically braced frames: v-braces	2	2.5
Eccentrically braced frames	4	$5\alpha_w / \alpha_1$
Inverted pendulum	2	$2\alpha_w / \alpha_1$
Structures with concrete cores/walls	4	$4\alpha_w / \alpha_1$
Moment resisting frames with unconnected infills, in contact with frame	2	2
Moment resisting frames with unconnected infills, isolated from frame	4	$5\alpha_w / \alpha_1$

For structures with a high ductility classification,  $q$  is usually represented in terms of the overstrength factor,  $\alpha_u / \alpha_1$ . The cross-sectional requirements for each ductility classification are given in Table 2.2. Class 1 sections are generally required for structures which are classified as DCH.

Table 2.2 Cross-sectional classification requirements for each structural ductility class in BS EN 1998-1 (2004)

Ductility Class	Reference value of $q$	Required cross-section class
DCL	$q \leq 1.5 - 2.0$	-
DCM	$1.5 \leq q < 2.0$	Class 1, 2 or 3
	$2.0 \leq q < 4.0$	Class 1 or 2
DCH	$q > 4.0$	Class 1

As stated previously, the steel braces in concentrically braced frames are designed to dissipate the energy. For composite frames, energy dissipation is assumed to be achieved by steel elements only, without the contribution of concrete components. However, previous tests conducted by Broderick *et al.* (2005) on hollow and concrete-filled RHS braces demonstrated that concrete-filled specimens can endure a greater number of cycles than hollow braces and thus may dissipate a greater amount of energy overall than hollow specimens prior to failure. Hence account could be taken of the concrete contribution under certain circumstances. This thesis investigates the enhancement provided by concrete infill to circular hollow section braces and examines whether or not the recommendations of Table 2.2 are suitable for concrete-filled sections.

### 2.2.3 Strength, stiffness and ductility

In general, seismic design is based on the strength, stiffness and ductility of individual members or systems of members. However, these parameters are not

always the same. For example, in a single degree of freedom (SDOF) structure, the strength and stiffness are in proportion, but this relationship becomes more complicated for multiple degree of freedom (MDOF) structures. The meanings of the terms stiffness, strength and ductility can vary significantly, depending on the context. For example, 'stiffness' usually refers to the tangent stiffness (for a load-displacement curve) but often the secant stiffness is employed, in order to avoid negative values which would occur on the descending slope.

As outlined in Section 2.2.1 compressive strength degradation can have a detrimental effect on the performance of concentrically braced framing systems. If a bracing member initially undergoes a number of low loading cycles, then the effect of strain hardening may increase the buckling load, but under repeated cycles at larger amplitudes, the compressive resistance is reduced. AISC (2002) and CSA (1994) guidelines provide expressions to predict the compressive strength of a member under large axial displacement amplitudes (post-buckling resistance). Expressions have also been proposed by Nakashima *et al.* (1992) and Tremblay (2002) following experiments on seismic steel braces. These are discussed further in Chapter 3.

Ductility is defined as the ability of a material, component connection or structure to undergo inelastic deformations with acceptable degrees of stiffness and strength reduction. Brittle structures fail suddenly and at a much lower inelastic deformation than ductile structures. Energy dissipation, which is the ability of a structure to absorb and dissipate energy through plastic deformations, is used to evaluate the ductile response. For low levels of energy dissipation, structures should be designed to withstand lateral forces in the region of their own weight in order to remain in the elastic range, which is uneconomical in most cases. The four main types of ductility identified in seismic engineering are material ductility ( $\mu_e$ ), section (curvature)

ductility ( $\mu_\chi$ ), rotation ductility ( $\mu_\theta$ ) and displacement ductility ( $\mu_\Delta$ ). Displacement and rotation ductility are frequently used as these refer to the global (member) deformation. The degree of energy dissipation depends on the ductility of a component and a higher ultimate stress/yield stress ratio for the materials enables further spreading of inelasticity and hence higher levels of energy dissipation. High global ductility depends on high local ductility, and thus the curvature ductility factor needs to considerably exceed the displacement ductility factor.

Different measures have been employed by previous researchers to define ductility for braces in CBFs. Elchalakani *et al.* (2003) used a ductility index (D.I.) which corresponded to the axial displacement of the brace at which the load was reduced by 20% from the maximum value. Nip *et al.* (2010a), Tremblay (2002) and Sheehan and Chan (2013) defined displacement ductility,  $\mu_\Delta$ , in terms of the maximum axial displacement amplitude achieved by the brace. Goggins *et al.* (2006) considered the axial displacement at which failure occurred. Ductility can also be based on the hysteretic energy, given by:  $\mu = E_{t,H}/E_E$ .  $E_E$  is the strain energy at yield:  $E_E = 0.5F_y\delta_y$  with  $F_y$  the force required to cause yielding of the steel cross-section, and  $\delta_y$  the yield displacement parameter defined by the material yield stress and member length.  $E_{t,H}$  is the hysteretic energy dissipated before failure. In this thesis, failure is defined as the occurrence of fracture across the face of the steel tube.

The main measure of ductility to be considered for axially loaded braces is the displacement ductility, which is significantly influenced by global slenderness. BS EN 1998-1 (2004) stipulates that braces should have a non-dimensional global slenderness value,  $\bar{\lambda}$ , between 1.3 and 2.0 for x-bracing configurations and less than 2.0 for all other types of concentrically braced frame.  $\bar{\lambda}$  is equal to  $\sqrt{(Af_y/N_{cr})}$  where

$A$  is the cross-sectional area and  $N_{cr}$  is the elastic critical force for the relevant buckling mode based on the gross cross-sectional properties. An increase in  $\bar{\lambda}$  decreases the flexural buckling load of the member but has been shown to increase the number of cycles endured before failure, as demonstrated by Nip *et al.* (2010a). This parameter has also been shown to affect the shape of the hysteresis curve and energy dissipation characteristics. Hence in this thesis, members of different bracing lengths will be compared in order to verify the influence of  $\bar{\lambda}$  on various aspects of the performance.

### 2.3 Steel material behaviour

#### 2.3.1 Tubular sections

Steel tubular sections are becoming increasingly popular owing to both their appearance and structural efficiency. Rectangular tubular sections are often selected for their constructability and geometry and a significant amount of research has been carried out on these for cyclic bracing applications, e.g. Nip *et al.* (2010a), Shaback and Brown (2003). Curved sections have become more widespread in recent times however, since these have a superior appearance to rectangular sections. Elchalakani *et al.* (2003) conducted a series of cyclic axial tests on cold formed circular hollow section braces and Sheehan and Chan (2013) tested hollow and concrete-filled circular hollow section braces. One advantage of the circular hollow section is the lower susceptibility to local buckling under pure compression in comparison with the rectangular hollow section for the same volume of steel. BS EN 1993-1-1 (2005) defines four cross-sectional classification types for structural steel sections based on their resistance to local buckling. Cross-sections which are thick relative to their width are categorised as Class 1 since these have the rotational capacity to form a

plastic hinge during plastic analysis of the structure. Class 2 cross-sections can obtain the section plastic moment resistance but have limited rotational capacity owing to local buckling. Sections which are unable to achieve the full plastic moment resistance but which can reach the yield strength in the extreme compressive fibre are classified as Class 3 cross-sections. Class 4 sections are those in which the occurrence of local buckling prevents the attainment of yield stress in the section. Classes 1 – 3 are fully effective in compression, whereas a reduced cross-sectional area is used for calculating the compressive resistance of Class 4 sections. The cross-sectional slenderness limits for tubular hollow sections in BS EN 1993-1-1 (2005) are given in Table 2.3. The cross-sectional slenderness is defined in this table as the ratio between cross-section width ( $D$  for circular sections and  $h$  for rectangular sections) and tube wall thickness ( $t$ ). Circular sections offer a greater degree of continuity around the perimeter than rectangular sections and in the case of concrete-filled tubes they provide a more uniform confining pressure to the concrete core. Hence circular hollow sections have been selected for this research. Since Class 1 sections are recommended in BS EN 1998-1 (2004) for structures with a high ductility class (Table 2.2), these were chosen for the initial investigations.

Table 2.3 Cross-section classification limits for steel tubes in BS EN 1993-1-1 (2005)

Limit	Rectangular hollow section ( $h/t$ )	Circular hollow section ( $D/t$ )
Class 1	$33\varepsilon$	$50\varepsilon^2$
Class 2	$38\varepsilon$	$70\varepsilon^2$
Class 3	$42\varepsilon$	$90\varepsilon^2$

where  $\varepsilon = \sqrt{235/f_y}$  and  $f_y$  is the material yield stress

### 2.3.2 Steel section type

A number of methods are used to manufacture steel tubes. This thesis compares hot-finished and cold formed carbon steel sections. Similar processes are used in the early stages of manufacturing but the methods deviate in the final phase. In both cases, the material is initially uncoiled and levelled to form flat plates. The edges are then trimmed and the material is cut into strips of a suitable size for the intended cross-section. These are then passed through a series of rollers to produce the tubular shape and welded with a high frequency induction welder. Once the weld has been trimmed, non-destructive tests are conducted before the final inspection is carried out and the members are dispatched. The manufacture of cold formed tubes is performed entirely at ambient temperature whereas hot-finished sections are passed through a furnace in the final stage, reaching a temperature of approximately 900°C. Consequently these sections retain significantly lower residual stresses than the equivalent cold formed sections. Most of the research on cyclic tubular braces to date has focussed on cold formed carbon steel members. However, Nip *et al.* (2010a) compared the response of hot-finished and cold formed carbon steel RHS braces with stainless steel members. The hot-rolled carbon steel exhibited superior behaviour to the cold formed sections and the stainless steel generally endured a greater number of cycles than the carbon steels. Each of the materials exhibits distinct stress-strain behaviour. Hot-finished steel is linear up to yielding and then undergoes a yield plateau followed by strain hardening, whereas cold formed carbon and stainless steels have nonlinear stress-strain relationships throughout and do not possess a yield plateau. The differences in bracing performance observed by Nip *et al.* (2010a) can be partially accounted for by these material characteristics but are also influenced by the geometry and manufacturing of the sections. In the case of



cold formed RHS sections, the material in the corner regions underwent significant strain-hardening that altered the material properties in comparison with the flat faces of the tubes. This phenomenon was not a significant issue for the hot-finished RHS tubes due to the heat treatment in the final phase of manufacturing.

Two steel section types are compared in this thesis: hot-finished carbon steel and cold formed carbon steel circular hollow sections. Although the circular section shape does not vary around the perimeter to the same extent as the rectangular hollow section, residual stresses from the cold forming process may still affect the section performance in comparison with the hot-finished specimens.

### **2.3.3 Cyclic response of steel**

Under repeated loading cycles the constitutive behaviour of steel is altered and experiences phenomena such as an expanding yield surface, variation in the plastic modulus and the Bauschinger effect. The term ‘Bauschinger effect’ refers to the reduction in material strength that occurs during loading reversals, which can be attributed to the movement of dislocations in the microscopic structure of the material. Several models have been developed over the years to capture the response of steel under cyclic loading. The models discussed in this thesis are rate-independent and consist of the following four basic components

1. A yield function, beyond which the response becomes plastic
2. A flow rule, defining the increase in plastic strain with respect to stress
3. A hardening rule, governing the development of the yield surface
4. A loading criterion, in order to differentiate elastic unloading from plastic loading.

Mroz (1967) and Iwan (1967) developed multi-surface plasticity models, consisting of several surfaces in space between the yield stress and ultimate stress, each of which was governed by a different plastic hardening modulus and hardening rule. These models proved to be difficult to implement in numerical models owing to the level of detail, leading to the development of a two-surface model by Dafalias and Popov (1976). This consisted of a yielding/loading surface in stress space and a bounding surface. The two surfaces are shown with respect to the 3D deviatoric stress-space in Figure 2.2(a) and a typical cycle of the stress-strain relationship is given in Figure 2.2(b).

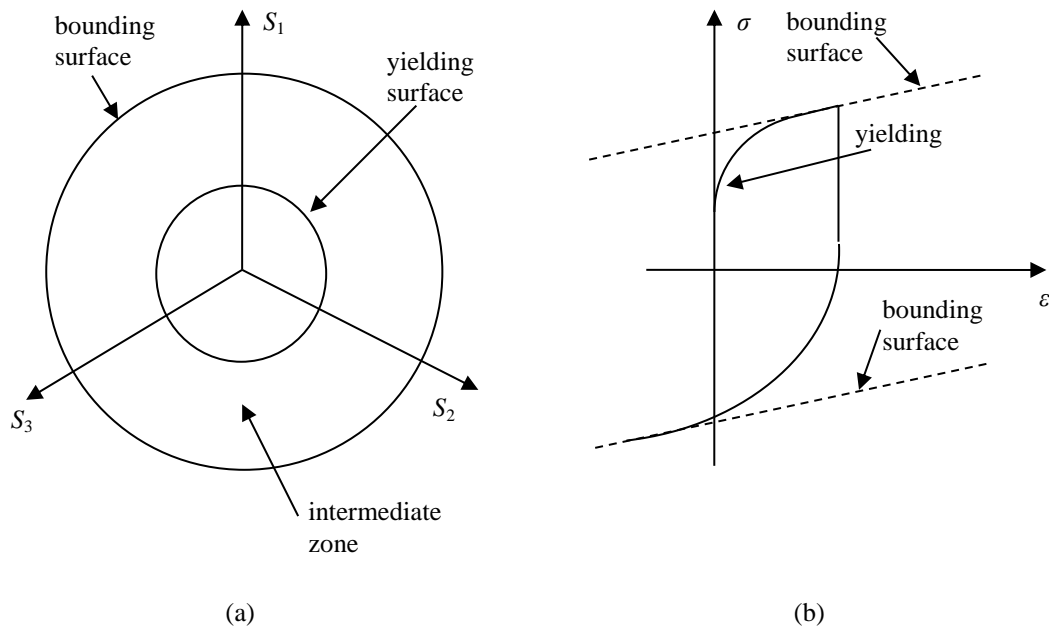


Figure 2.2 Two-surface cyclic plasticity model in terms of (a) stresses in 3D space; (b) uniaxial stress-strain relationship

While the stress field lies within the yielding surface, the behaviour is elastic and once the stress goes beyond this region and into the intermediate zone between the two surfaces, the response becomes plastic. Both surfaces may expand or contract (isotropic hardening) or translate in space (kinematic hardening). The two-surface model has been being adopted and modified by several researchers such as Chaboche

(1986) and Shen (1995). Despite its popularity, there are some short-comings in that the two surfaces do not adequately capture the yield plateau and full implementation of the model in numerical simulations requires a large number of internal variables.

Alternatives to the two-surface model were considered for this research. To counteract some of the issues, Goto *et al.* (2010) developed a three-surface cyclic plasticity model, which includes a discontinuous surface that lies between the yielding and bounding surfaces, at which the plastic hardening modulus is recalculated. The yield plateau of the steel can be accounted for by utilising this discontinuity in the stiffness. The model was implemented by Goto *et al.* (2010) in ABAQUS® with a user subroutine. There are some advantages to using a subroutine in this manner, since it grants the user control over the material parameters and the evolution of these during loading cycles, unlike the inbuilt-material models. Despite the advantages of this model, the determination of the input parameters and its implementation in the finite element analysis are complex.

In addition to the stress-strain response, this thesis also addresses the fatigue life of steel under strain reversals. Fatigue can be classified as high cycle fatigue, in which specimens typically endure more than  $10^4$  loading cycles before failure, or low cycle fatigue, in which a lower number of cycles create fatigue fracturing. Both stress-based and strain-based approaches have been considered by previous researchers for predicting the fatigue life. Strain-based approaches are favourable for low cycle fatigue applications as the strains tend to be in the plastic range. Coffin (1954) and Manson (1954) developed an expression to predict the number of cycles to failure for steel, which can be expressed as:

$$\frac{\Delta \varepsilon_p}{2} = \varepsilon'_f (2N_f)^c \quad (2.1)$$

where  $\Delta\epsilon_p/2$  is the plastic strain amplitude,  $2N_f$  is the number of reversals to failure,  $\epsilon'_f$  is the fatigue ductility coefficient and  $c$  is the fatigue ductility exponent. Since the strain magnitudes in cyclically loaded braces vary between each cycle, an equation known as Miner's Rule (Miner, 1945) can be employed to calculate the accumulated damage with each cycle amplitude. This is given as.

$$D = \sum_{i=1}^n \frac{n_i}{N_{fi}} \quad (2.2)$$

where  $N_{fi}$  is the number of cycles to failure for a particular strain amplitude and  $n$  is the number of cycles undergone by the test specimen at that strain. According to this damage model, failure occurs when the value of  $D$  reaches 1. The cyclic plasticity model for steel and fatigue life estimation are discussed in more detail in Chapter 4.

## 2.4 Concrete-filled tubes

### 2.4.1 Background

In recent years, concrete-filled tubes have been used instead of hollow steel members, owing to their superior strength and ductility. For structural steel, the value of Poisson's ratio is typically close to 0.3. Under low strains, the conventional value for concrete is usually lower than this, say at 0.2. As the strain increases, so does Poisson's ratio until it exceeds the value for steel. Hence as the member is compressed axially, the lateral expansion of the concrete quickly surpasses that of the steel, but failure is prevented as it is confined by the tube. Furthermore, the presence of the concrete core stiffens the tube and prevents inward buckling. The lateral pressure exerted between the two materials is shown in Fig. 2.3.

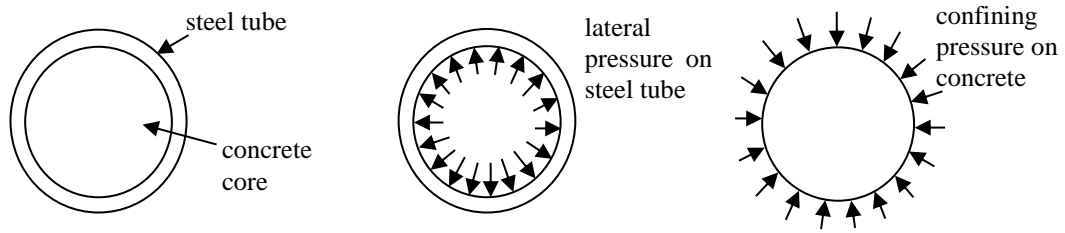


Figure 2.3 Lateral pressure in concrete-filled tube

The confinement provided to the concrete core in this situation is classified as ‘passive’ confinement, i.e. there is no initial lateral pressure and it initiates from the expansion of the concrete core. The efficiency of concrete-filled stub columns under compression has been demonstrated by numerous experiments on circular, rectangular and elliptical concrete-filled tubes such as by Cai (1987), Johnsson and Gylltoft (2002), Yang *et al.* (2008) and Young and Ellobody (2006). Research has also been conducted on the performance of concrete-filled tubes in tension by Han *et al.* (2011) and under combined compression and bending by Sheehan *et al.* (2012), establishing the benefits of using concrete infill for a variety of loading scenarios. Some researchers have paid particular attention to the increase in concrete compressive strength provided by lateral confinement. Mander *et al.* (1988) derived a relationship using data from experiments in which concrete was confined by steel hoops. Cai (1987) conducted a series of tests involving 57 concrete-filled CHS stub columns, covering a range of  $D/t$  ratios from which an expression was derived to predict the squash load, accounting for the enhancement of the confining effect. BS EN 1994-1-1 (2004) also provides formulae to account for the increase in compressive strength. According to BS EN 1994-1-1 (2004), the plastic resistance of a concrete-filled tube,  $N_{pl,Rd}$ , is calculated using Equations (2.3) – (2.5).

$$N_{pl,Rd} = \eta_a A_a f_{yd} + A_c f_{cd} \left( 1 + \eta_c \frac{t}{D} \frac{f_{yd}}{f_{cd}} \right) \quad (2.3)$$

where  $\eta_a$  and  $\eta_c$  depend on the eccentricity of applied loading. When the compressive load is concentric the load eccentricity is zero and:

$$\eta_a = 0.25(3 + 2\bar{\lambda}) \quad (2.4)$$

$$\eta_c = 4.9 - 18.5\bar{\lambda} + 17\bar{\lambda}^2 \quad (2.5)$$

All other symbol definitions from the above equations are given in the notations list. The overall response is influenced by numerous parameters. The lateral expansion of the concrete varies with concrete grade, with a higher rate of expansion generally observed for higher strength concrete. Hence, under the same axial strain, a higher strength concrete will resist a greater axial load while also exerting a larger lateral pressure on the steel tube. Therefore the steel tube wall must be thick enough to withstand this additional force. Hence using a higher strength concrete may increase the ultimate load but does not necessarily enhance all aspects of economy or structural performance. Thalayan *et al.* (2009) conducted a series of static and variable loading tests on concrete-filled tubular columns, employing normal strength and high strength concretes, to find that wider tensile cracks occurred in the high-strength concrete than in the normal strength material.

In Bergmann *et al.* (1995) the following cross-sectional limits are given for concrete-filled tubular columns to prevent local buckling.

Table 2.4 Cross-sectional limit recommendations for concrete-filled tubes (Bergmann *et al.*, 1995)

Steel Grade	235	275	355	460
<b>Circular tubes: <math>D/t</math></b>	90	77	60	46
<b>Rectangular tubes: <math>h/t</math></b>	52	48	42	37

The limits in Table 2.4 are given for individual steel grades (instead of expressing them in terms of  $\varepsilon$  as in Table 2.3) and correspond to  $90\varepsilon^2$  (Classes 1 to 3) for circular tubes and  $52\varepsilon$  (Classes 1 to 3) for rectangular sections. Comparing these limits with those for hollow sections presented in Table 2.3, the concrete significantly enhances the allowable dimensions for rectangular sections but does not contribute as much to the circular section. However, the efficiency of the circular shape with the uniformity of confining pressure and research findings to date suggest that greater account of the concrete contribution could be taken in these design provisions.

### **2.4.2 Concrete-filled tubes in seismic applications**

The superior strength and ductility render concrete-filled tubes highly suitable for seismic structures. These provide an effective alternative to traditional steel or encased components, either as bracing in CBFs or as columns in MRFs. The presence of the concrete core delays the buckling of the steel tube and results in a more easily constructed, cost-efficient and visually appealing option than an encased member.

Several researchers have explored the use of concrete-filled tubes as columns, subjected to an axial compressive load and cyclic lateral load. Ge and Usami (1996), Mao and Xiao (2006) and Varma *et al.* (2002) conducted experiments on square or rectangular concrete-filled columns, while Elremaily and Azizinamini (2002) and Fam *et al.* (2004) tested concrete-filled circular columns. Some researchers have also investigated the behaviour of concrete-filled rectangular braces under cyclic axial loading, such as Broderick *et al.* (2005), Lee *et al.* (2000) and Liu and Goel (1988). Liu and Goel (1988) found that for large  $h/t$  ratios (i.e. cross-sections susceptible to local buckling), the region of plasticity was enhanced for a concrete-

filled tube when compared with a hollow steel tube and hence there was a greater amount of energy dissipation. It was assumed that the same effect would not be observed for cross-sections with smaller  $h/t$  ratios. However, concrete-filled tubes tended to endure greater numbers of loading cycles than the equivalent hollow sections, even in the case of sections with low  $h/t$  values, and hence the overall energy dissipation could be enhanced by the prolonged brace life. The benefits of concrete infill are apparent in the case of rectangular hollow section braces but less research has been carried out on circular hollow section braces. Furthermore, there are few direct comparisons between the performance of hot-finished and cold formed circular sections, despite previous demonstration of the difference in performance for hot and cold-finished rectangular hollow section braces by Nip *et al.* (2010a). The main question posed by this thesis is: to what extent does concrete infill influence the cyclic behaviour of CHS braces, and how is this affected by the section manufacturing method?

### **2.4.3 Steel-concrete interface**

As discussed previously, energy absorption is a vital function of braces in concentrically braced frames and this parameter has been shown to be affected not only by the loading capacity and fatigue life of members but also by the bond between steel and concrete. Fam *et al.* (2004) compared the results of compositely loaded columns with members in which load was applied to the concrete core only, with or without the presence of cohesion between the two materials. The plastic hinge length was shorter for the specimens which were loaded on concrete only and bonded to steel than for compositely loaded or unbonded specimens. In addition to this, the initial axial stiffness was found to be lower for unbonded specimens than for



bonded columns. Therefore to ensure the maximum benefit of the concrete in this study, bonded conditions were assumed and braces were loaded compositely.

### 2.5 Numerical modelling

#### 2.5.1 Background

In recent years, increasing attention has been paid to numerical simulations of seismic bracing tests. The speed and economy offered by this approach has been exploited to provide a wider range of data than would be feasible through laboratory testing alone. Reliable simulations of cyclic members have been achieved using macro-models consisting of beam elements along the length, such as the elasto-plastic analysis of hollow tubes conducted by Mamaghani *et al.* (1996), or the modelling of concrete-filled tubes by Hajjar and Gourley (1997) and Hajjar *et al.* (1997). Since local buckling behaviour has proven to be instrumental in the failure of laboratory test specimens, full 3D finite element models are also popular, as they afford a more detailed examination of local deformations. Kuşyılmaz and Topkaya (2011) created full 3D models of CHS braces using ANSYS® software and examined the variation in local plastic stains in addition to the cycle of local buckling initiation. For this thesis, full 3D models were created for analysis using ABAQUS®. This software has previously been utilised for hollow and concrete-filled tubes under monotonic loading (Chan and Gardner, 2008; Hu *et al.*, 2003; Dai and Lam, 2010), and proved capable of capturing the response of steel and concrete components under these conditions. ABAQUS® has also been used to simulate hollow steel members under cyclic loading, such as by Nip *et al.* (2010a) for rectangular hollow section braces and Takeuchi and Matsui (2011), and Sheehan *et*

*al.* (2013) for circular hollow section braces and for concrete-filled tubular columns by Goto *et al.* (2010).

### 2.5.2 Steel constitutive model in ABAQUS

ABAQUS® provides two inbuilt material models for the cyclic hardening of steel, the linear kinematic hardening model and the nonlinear isotropic/kinematic hardening model, but also accommodates the use of separate user-defined material models. Nip *et al.* (2010a) used the inbuilt nonlinear isotropic/kinematic hardening model with input parameters for the material model definition obtained from cyclic coupon tests, and obtained satisfactory results. Takeuchi and Matsui (2011) calibrated the isotropic/kinematic hardening model using the results of tensile coupon tests. Goto *et al.* (2010) implemented a user defined three-surface plasticity model in which the material parameters were calibrated from tensile coupon tests and cyclic member tests. This model was better able to capture the yield plateau effect and hardening effect than the inbuilt models but required a greater number of input parameters. Following the successful implementation of ABAQUS® models for hollow tubular braces (Sheehan *et al.*, 2013), the finite element analysis for this research utilised a similar approach to Takeuchi and Matsui (2011) and Nip *et al.* (2010a) by using the inbuilt steel material model. Further details of the nonlinear isotropic/kinematic hardening model and input parameters are covered in Chapter 4.

### 2.5.3 Concrete constitutive model in ABAQUS

The prediction of the concrete material constitutive response is a complex issue. This is because it undergoes both hardening and softening under compressive stress and exhibits phenomena such as cracking and tension stiffening. Darwin and Pecknold (1976) focussed on rate-dependent orthotropic models, but this approach has had limited success in capturing the multiaxial response of concrete under cyclic

loading. Plasticity models have also been explored, such as by Buyukozturk (1977) since they are suitable for a wider range of applications. However, these do not always capture the stiffness degradation and cracking behaviour of the concrete.

A number of options are available in ABAQUS® for modelling concrete under cyclic loading conditions. The smeared cracking model is one popular choice for defining the material constitutive behaviour. This model is intended for simulating reinforced concrete under monotonic loading and low confining pressure but can also be used for plain concrete. The model employs an isotropically hardening yield surface under compressive stresses and also implements a smeared cracking model for small compressive stresses and tensile stresses. A crack detection surface is used to monitor the occurrence of cracks and once this arises, a damaged elasticity model is utilised to describe the reversible part of the damage. The effect of the cracks is taken into account by altering the strength and stiffness but individual cracks are not accounted for. The energy required to open a unit area of crack is defined by Hillerborg (1976). There are some disadvantages to using the smeared cracking model. The response under compression is over-simplified, assuming isotropic hardening and an associated flow rule, which does not comply with experimental evidence. In addition to this the model frequently encounters numerical difficulties when applied to cyclic loading, as discussed by Goto *et al.* (2010).

Another option for simulating concrete material behaviour is the damaged plasticity model. Conversely to the smeared cracking model, the damaged plasticity model is suited to cyclic loading conditions. This is a plasticity model using non-associated flow to describe the material hardening and allows for the stiffness recovery effects between cycle reversals to be taken into account. Two variables,  $\tilde{\epsilon}_t^{pl}$  and  $\tilde{\epsilon}_c^{pl}$ , are

used to control the yield surface, and are referred to as the tensile and compressive equivalent plastic strains. The yield function is taken from Lubliner (1989), and includes the modifications of Lee and Fenves (1998) to account for the different development of strength under tension and compression. Further details of the yield function are provided in Chapter 5.

As shown in Figure 2.4 the damaged plasticity model, under uniaxial tension, has a linear stress-strain relationship with a constant stiffness of  $E_0$  up to the onset of cracking at a stress value of  $\sigma_{t0}$ . After this the stress decreases with increasing plastic strain,  $\varepsilon_t$ . When unloaded, the material exhibits a new reduced stiffness denoted by  $(1-d_t)E_0$ , where  $d_t$  is the tensile damage. The equivalent plastic tensile strain,  $\tilde{\varepsilon}_t^{pl}$ , is equal to the total strain minus the elastic strain corresponding to the damaged material,  $\varepsilon_t^{el}$ . This is illustrated in Figure 2.4.

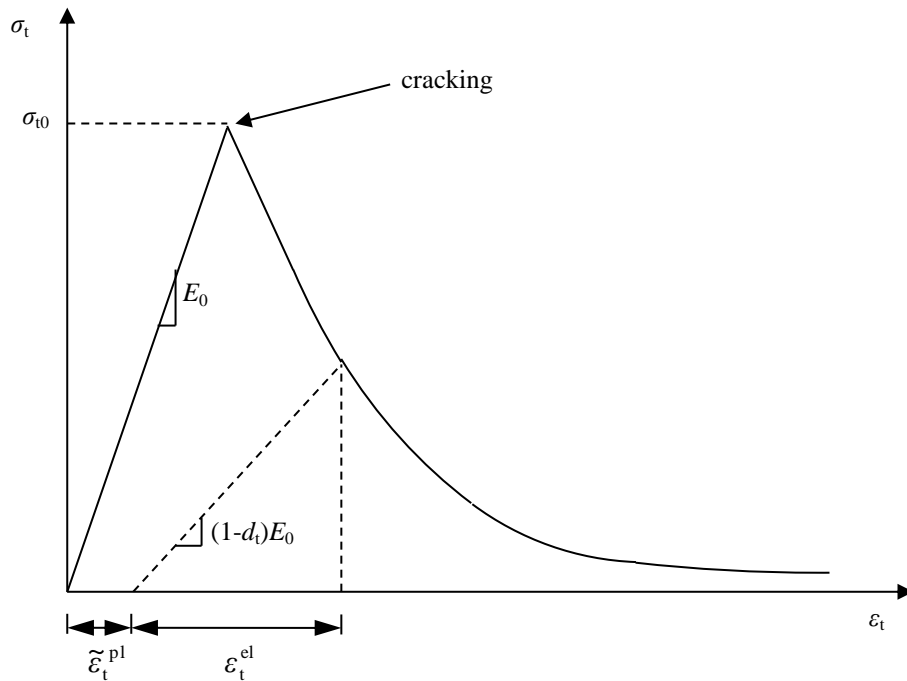


Figure 2.4 Stress-strain relationship for concrete in tension

Under uniaxial compression the material response is linear up to the initial yield stress,  $\sigma_{c0}$ . This is followed by strain hardening until the ultimate stress,  $\sigma_{cu}$ , is reached, and strain softening subsequent to this. The stress-strain response under compression, with  $\varepsilon_c$  positive, is illustrated in Figure 2.5. The stiffness of the concrete during unloading is given as  $(1-d_c)E_0$  where  $d_c$  is the compressive damage, and similarly to the previously discussed tensile behaviour, the equivalent compressive plastic strain,  $\tilde{\varepsilon}_c^{pl}$ , is computed in terms of the elastic strain for the damaged concrete,  $\varepsilon_c^{el}$ . Values of the damage parameters,  $d_t$  and  $d_c$ , range from zero (no loss of strength) to 1.0 (total loss of strength) and they are functions of the equivalent plastic strains. Under tensile loading, the fracture energy criterion from Hillerborg (1976) is used. Since it is more suited to cyclic loading conditions, the damaged plasticity model was selected for this research project. Further details of the implementation of this concrete material model are provided in Chapter 5.

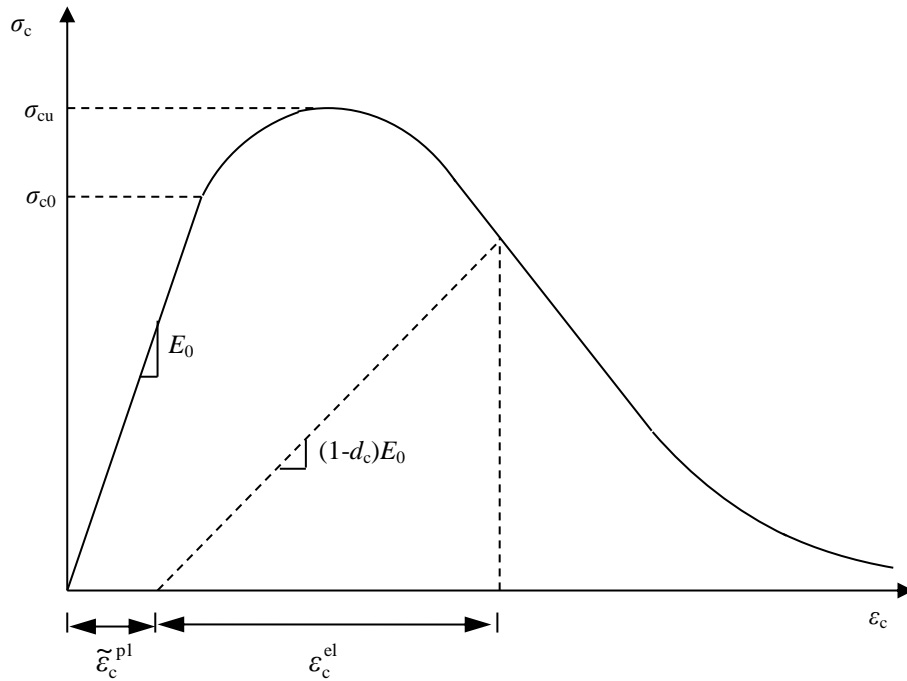


Figure 2.5 Stress-strain relationship for concrete under compression

### **2.5.4 Geometric imperfections**

Both local buckling and global buckling were instrumental in the deformation and failure of the laboratory test specimens. Incorporation of the real test conditions is crucial to induce these instabilities and to obtain a reasonable simulation of the brace response. ABAQUS® provides a number of options for including imperfections in the models. One popular approach is to perform an Eigenbuckling analysis from which a suitably scaled buckled mode shape is employed to alter the original geometry. The disadvantage of this method is the time and computational demand of conducting a separate analysis in addition to the difficulties in obtaining a suitable buckling mode. The finite element work for this thesis used a more straightforward approach. The nodal coordinates were altered directly to include the local imperfections. The local imperfection amplitudes along the brace's length were defined by a sine wave. The global imperfections in this study were implemented by applying an equivalent lateral load at the mid-length. Suitable amplitudes for local and global imperfections are discussed in more detail in Chapter 4.

### **2.6 Concluding remarks**

A review has been provided of the background research which provides the foundation for this project. Seismic design approaches and structural configurations have been discussed and the suitability of the proposed test specimens to these has been highlighted. The response of steel and concrete to earthquake loading has been considered in anticipation of the laboratory tests. The aim of the project is to execute the test program, to subsequently extend the test results using finite element analysis in ABAQUS® and to assess the implications of the results for existing seismic design guidelines.

## **Chapter 3**

### **Laboratory Experiments**

#### **3.1 Introduction**

A series of laboratory tests were devised to assess the behaviour of hollow and concrete-filled, cold formed and hot-finished CHS braces under cyclic axial loading. The objective of this endeavour was to explore the suitability of these members for use as braces in concentrically braced earthquake-resistant frames, considering parameters such as the maximum tensile and compressive resistances, load-carrying capacity, ductility, energy dissipation capability, and deformed shape. Two brace-lengths were used: 1500 mm and 3000 mm, to give non-dimensional global slenderness values close to 1.0 and 2.0. Prior to the bracing member experiments, some preliminary tests were also carried out to examine the material and cross-sectional behaviour. These involved tensile coupon tests, concrete material tests and compressive stub column tests. All work was conducted in the Structures Laboratory at the University of Warwick.

#### **3.2 Material tests**

##### **3.2.1 Tensile coupon tests**

The types of circular hollow steel section were a Celsius 355 hot-finished tube and a Hybox 355 cold formed section. Nominal dimensions, yield stress/0.2% proof stress,  $f_y$ , and ultimate stress,  $f_u$ , for the two CHS sections are summarized in Table 3.1. Sections with low diameter-thickness ( $D/t$ ) ratios (Class 1 in accordance with BS EN 1993-1-1 (2005)) were selected to provide a high rotational capacity under seismic actions.

## Chapter 3 Laboratory Experiments

Table 3.1 Nominal steel tube dimensions and material properties

Steel	$D$ mm	$t$ mm	$f_y$ N/mm <sup>2</sup>	$f_u$ N/mm <sup>2</sup>
Hot-finished	48.3	3.2	355	510
Cold formed	48.3	3.0	355	470 - 630

Four longitudinal coupons were cut from each tube. One of these was located at the seam weld and the others were distributed at equal distances around the section circumference, as shown in Figure 3.1(a). Tensile coupon tests were carried out in accordance with BS EN ISO 6892-1 (2009). The dimensions of the specimens are shown in Figure 3.1(b). The coupon ends were flattened prior to testing in order to match the flat grips of the testing machine. The coupons were dimensioned in order to mitigate the influence of work-hardening from this process on the central region. Two post-yield strain gauges (TML strain gauges, series ‘YFLA’) were used for each coupon (one on each face) in order to measure longitudinal strain. The test set-up is shown in Figure 3.2.

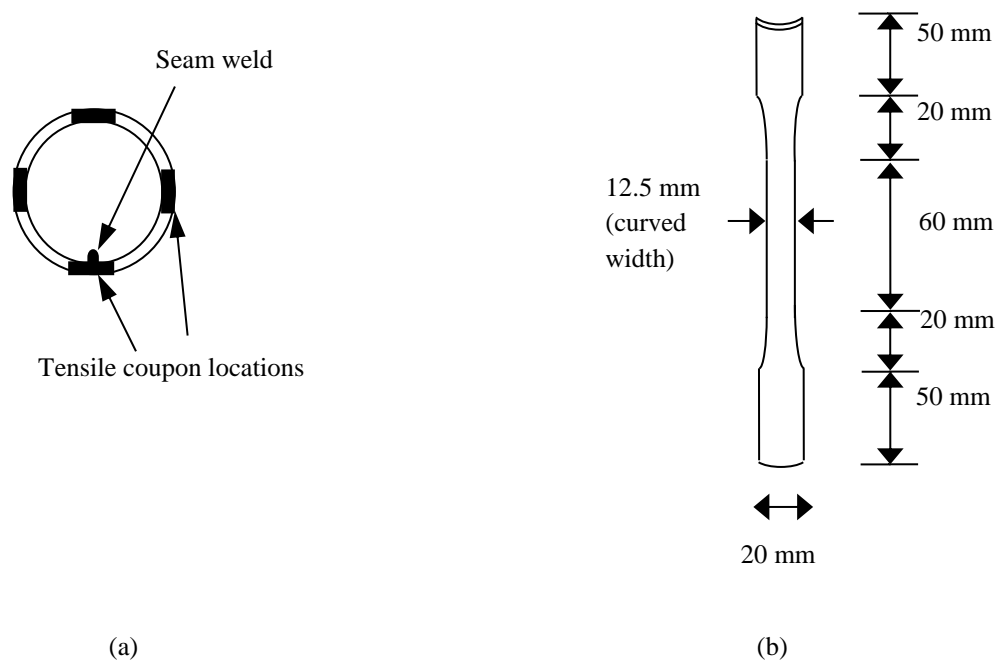


Figure 3.1 Tensile coupon specimen (a) locations on tubular cross-section; (b) dimensions



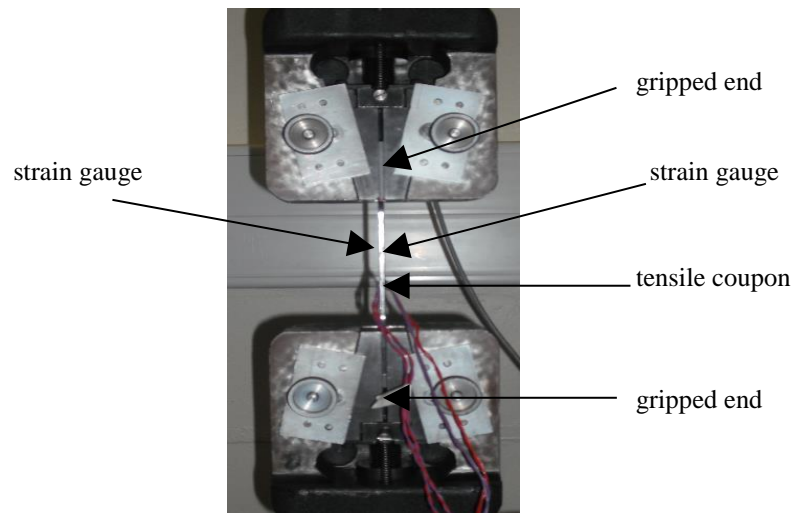


Figure 3.2 Tensile testing set-up

Resulting stress-strain relationships correlated closely to those expected, with the hot-rolled steel exhibiting linear behaviour up to yield, followed by a plateau before advancing into the strain hardening region. In contrast, the cold formed material was non-linear in the initial stages of the test and did not display a plateau during yield. A sample curve for each material type is presented in Figure 3.3.

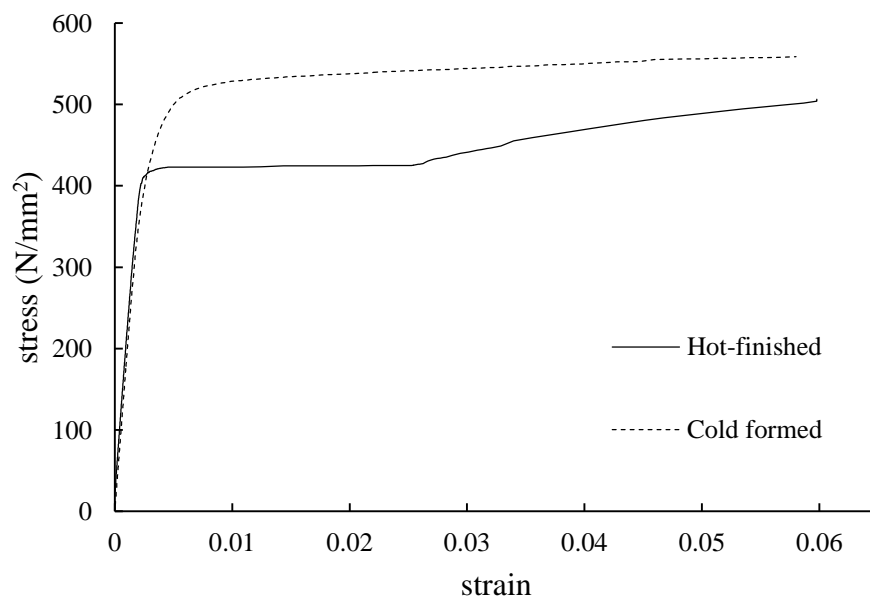


Figure 3.3 Stress-strain curves for hot-finished and cold formed steel coupons

## Chapter 3 Laboratory Experiments

From each batch of coupons, the seam weld coupon results were omitted. From the remaining three coupons, the average yield stress (hot-finished)/0.2% proof stress (cold formed)  $f_y$ , ultimate stress  $f_u$ , modulus of elasticity  $E$  and percentage elongation after fracture are presented in Table 3.2.

Table 3.2 Results of tensile coupon tests

Section type	Coupon	Nominal $f_y$ N/mm <sup>2</sup>	Measured $f_y$ N/mm <sup>2</sup>	$f_u$ N/mm <sup>2</sup>	$E$ N/mm <sup>2</sup>	% elongation after fracture	$1.1\gamma_{ov}f_y$
Hot-finished	Coupon 1	355	392	541	218000	46	488
	Coupon 2		423	552	198000	33	
	Coupon 3		430	545	203000	33	
	<b>Average</b>		<b>415</b>	<b>546</b>	<b>206000</b>	<b>37</b>	
Cold formed	Coupon 1	355	502	579	181000	23	488
	Coupon 2		492	567	186000	39	
	Coupon 3		504	575	185000	27	
	<b>Average</b>		<b>499</b>	<b>573</b>	<b>184000</b>	<b>30</b>	

As mentioned in Chapter 2, BS EN 1998-1 (2004) states that the measured material yield strength should not exceed  $1.1\gamma_{ov}f_y$ , where a value of 1.25 is proposed for the overstrength factor,  $\gamma_{ov}$ , and  $f_y$  refers to the design strength. It is worth noting that the 0.2% proof stress of the cold formed specimens, given in Table 3.2, exceeds the recommended value. This would need to be taken into account in design, since it may induce a larger load than anticipated on connected structural elements, e.g. columns.

### 3.2.2 Concrete material tests

The concrete mix was designed to meet two objectives. The first was to have a compressive cylinder strength in the range of 25 – 30 MPa (C20/25 – C25/30 in

accordance with BS EN 1992-1-1 (2004)), since BS EN 1998-1 (2004) recommends a minimum concrete class of C20/25 for dissipative composite structures. Also, it has been found that concrete strengths greater than 28 MPa do not significantly enhance the behaviour, as shown by Liu and Goel (1988). As indicated in sections 3.1 and 3.2.1, the test specimens were relatively long (1500/3000 mm) with a small outer diameter (48.3 mm) and hence the second objective was to achieve a mix that could be compacted in the long, slender tubes without undergoing segregation.

Five trial mixes were explored in order to meet the two objectives. The design mix proportion for each of the mixes is presented in Table 3.3, in addition to details of the final mixes used for the stub columns, 1500 mm braces and 3000 mm braces. A maximum coarse aggregate size of 6.35 mm was used for all mixes. The compressive cylinder strength at 7 days and 28 days was measured for each specimen in accordance with BS EN 12390-3 (2003) and the compressive strength and static modulus of elasticity were also recorded for the final test specimens on the day of testing. The mean values of these are included in Table 3.3.

Table 3.3 Concrete properties from material tests

Concrete mix	Mix proportions				Cylinder strength (N/mm <sup>2</sup> )			Static elastic modulus (N/mm <sup>2</sup> )
	water	cement	aggregate		7 days	28 days	test date	
			coarse	fine				
Trial Mix 1	0.50	1.00	2.00	1.32	36.9	42.8	-	-
Trial Mix 2	0.54	1.00	2.50	2.20	25.3	32.8	-	-
Trial Mix 3	0.55	1.00	2.04	1.78	25.0	36.4	-	-
Trial Mix 4	0.65	1.00	2.10	2.84	18.3	20.7	-	-
Trial Mix 5	0.77	1.00	4.18	1.27	14.1	18.3	-	-
Stub columns	0.72	1.00	2.86	2.30	16.0	21.0	25.5	19900
1500 mm braces	0.72	1.00	2.86	2.30	17.1	25.0	29.4	20100
3000 mm braces	0.72	1.00	2.86	2.30	15.1	21.9	30.7	23400

The first mix used a water-cement ratio of 0.50 and had a fine-to-coarse aggregate ratio of 0.66 but this produced a compressive strength of 42.8 MPa and was difficult to compact. In subsequent mixes, a superior degree of compaction and more desirable compressive strengths were obtained by employing higher water-cement and fine-to-coarse aggregate ratios. The final concrete mix used a water-cement ratio of 0.72 and a fine-to-coarse aggregate ratio of 0.80. Details of the compaction procedure will be discussed in section 3.4.1.

### 3.3 Stub column tests

#### 3.3.1 Test preparation

Compressive stub column tests were conducted to establish the degree of concrete confinement provided by each of the steel types, and to characterize the cross-section which would later be utilized for the intermediate-length ( $\bar{\lambda} = 0.78 - 0.92$ ) and long ( $\bar{\lambda} = 1.72 - 2.02$ ) specimens. Eight stub columns of length 100 mm were tested. Prior to testing, local geometric imperfections were measured at 10 mm intervals along each of the four sides of the tube using the test set-up shown in Figure 3.4. In addition to this, the thickness ( $t$ ) and diameter ( $D$ ) of the tube were measured using a ball micrometer screw. Three values of  $D$  and  $t$  were recorded for each tube and the average values of these are presented in Table 3.4 along with the maximum outward and inward local imperfections that were measured using the set-up in Figure 3.4.

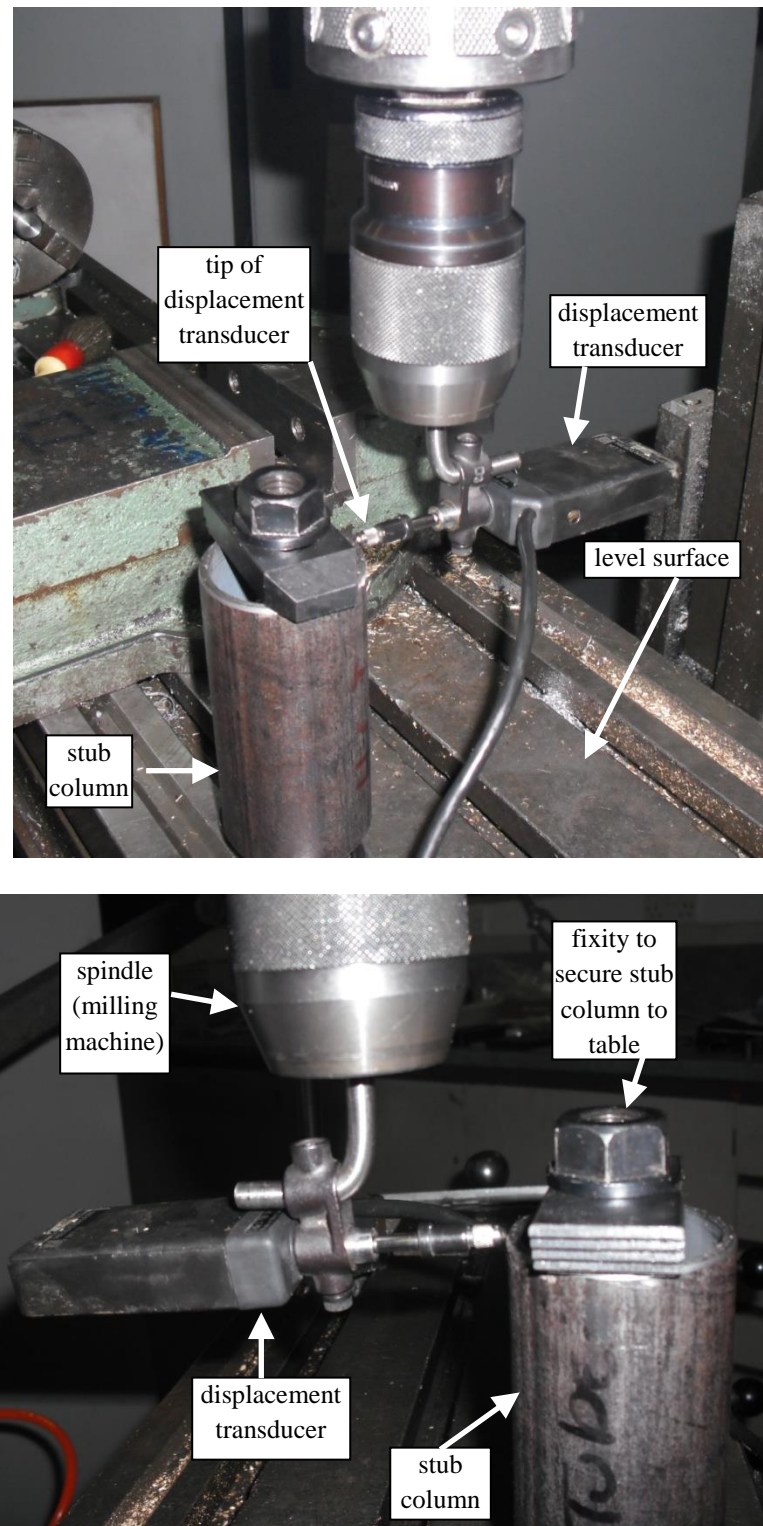


Figure 3.4 Test set-up for measuring stub-column local imperfections

Table 3.4 Stub column details

Specimen ID	Steel	Infill	Measured thickness	Measured diameter	Maximum imperfection	
			$t$ mm	$D$ mm	inwards $\mu\text{m}$	outwards $\mu\text{m}$
HF-H1-SC	Hot-finished	Hollow	3.17	48.64	22.84	45.02
HF-H2-SC	Hot-finished	Hollow	3.19	48.58	28.71	57.77
CF-H1-SC	Cold formed	Hollow	2.82	48.66	25.28	37.29
CF-H2-SC	Cold formed	Hollow	2.85	48.65	23.07	27.65
HF-F1-SC	Hot-finished	Concrete	3.24	48.61	9.81	27.82
HF-F2-SC	Hot-finished	Concrete	3.23	48.60	32.15	35.50
CF-F1-SC	Cold formed	Concrete	2.83	48.56	14.01	16.60
CF-F2-SC	Cold formed	Concrete	2.85	48.61	15.38	22.22

The nomenclature adopted for naming the specimens consisted of three parts. The first part of the specimen ID referred to the section type, i.e. ‘HF’ denoted hot-finished steel and ‘CF’ referred to cold formed steel. The second part distinguished between hollow (‘H’) and filled (‘F’) specimens and the final part referred to the specimen type (‘SC’ = stub column in this case). Four longitudinal, post-yield strain gauges (TML strain gauges, series ‘YFLA’) were positioned at the mid-height at 90° separations, as shown in Figure 3.5, allowing measurement of strains up to 15-20% elongation.

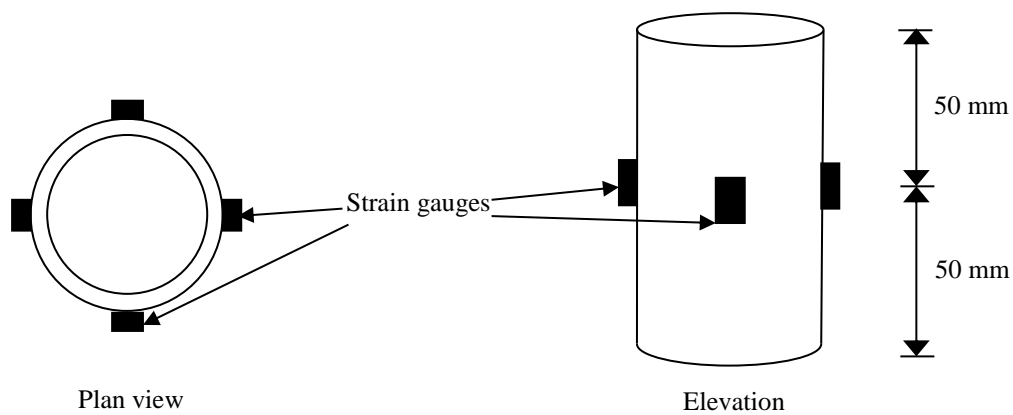


Figure 3.5 Strain-gauge locations for stub column tests

Specimens were loaded initially under load control at a rate of 0.1 kN/s, switching to displacement control at yield.

### 3.3.2 Results

Most stub columns failed in a similar manner, with local buckling of the steel occurring at either the top or bottom of the specimen. Load-axial displacement relationships were derived for each of the test-specimens, and examples of these are presented in Figure 3.6.

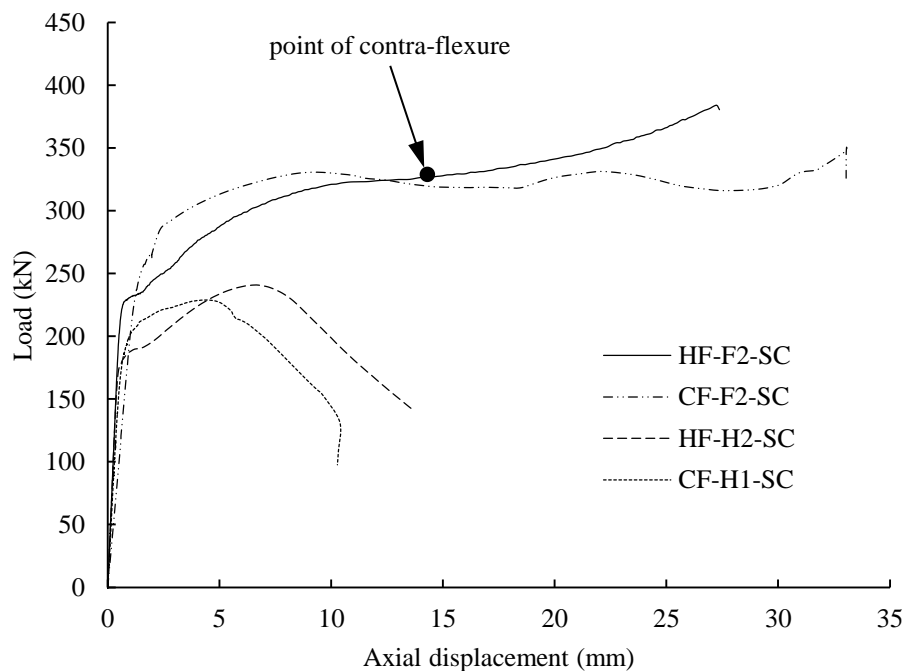


Figure 3.6 Load-displacement relationships for hot-finished and cold formed stub columns

The hot-finished tubes exhibited a distinct yield plateau which was not observed for the cold formed tubes. For the hollow stubs, the load decreased rapidly after reaching the ultimate value. However, the cold formed filled specimen sustained a high load well beyond the failure of its hollow counterpart. Furthermore, the load-displacement curve for the hot-finished filled specimen continued to increase after specimen failure. This can be explained by the significant changes that propagated

in the stub-column geometry as the test progressed. As the axial displacement increased, the stub column buckled in a ring-shaped mode at two or more locations along the length, and these rings were eventually compressed together, becoming very stiff. The test-specimen at the beginning, middle and end of the test is shown in Figures 3.7(a) to 3.7(c).

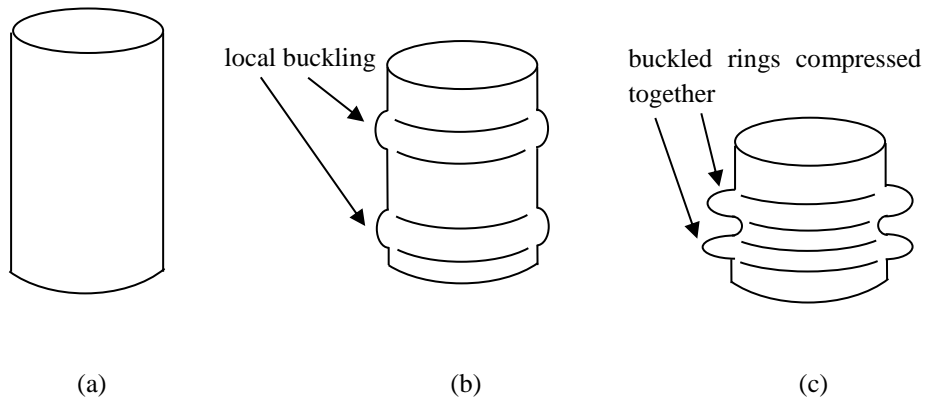


Figure 3.7 Stub column (a) at beginning of test; (b) during test after occurrence of local buckling; (c) at end of test

The load-displacement relationship for the hot-finished concrete-filled tubes was consistent with observations from Cai (1987) for thicker walled steel tubes, after testing 57 concrete-filled circular stub columns. Following the approach of Cai (1987), the ultimate load in the case of the filled hot-finished stubs was defined as the load at the point of contra-flexure in the curve, as shown in Figure 3.6 for specimen HF-F2-SC. This point signifies the transition in response resulting from the altered geometry. BS EN 1994-1-1 (2004) predicts the ultimate compressive resistance of short concrete-filled circular tube-columns using Equations (2.3) – (2.5). Several other relationships have been proposed by researchers for the ultimate squash load of concrete-filled tubes. Following experiments involving specimens with a range of  $D/t$  ratios, Cai (1987) proposed

$$N_{pl,Rd} = A_c f_{cd} (1 + \sqrt{\Phi} + 1.1 \Phi) \quad (3.1)$$



### Chapter 3 Laboratory Experiments

where  $\Phi = A_a f_{yd} / A_c f_{cd}$ .

The maximum test compressive loads ( $N_{pl,test}$ ) are summarised in Table 3.5.

Table 3.5 Maximum loads from stub column tests

<b>Specimen ID</b>	<b><math>N_{pl,test}</math> (kN)</b>	<b><math>N_{pl,Rd}</math> (kN) (BS EN 1993-1-1, 2005; BS EN 1994- 1-1, 2004)</b>	<b><math>N_{pl,Rd}</math> (kN) (Cai, 1987)</b>	<b><math>N_{pl,test}</math> (filled) <math>/N_{pl,test}</math> (hollow)</b>	<b><math>N_{pl,test}/N_{pl,Rd}</math> (BS EN 1993-1-1, 2005; BS EN 1994-1-1, 2004)</b>	<b><math>N_{pl,test}/</math> <math>N_{pl,Rd}</math> (Cai, 1987)</b>
HF-H1-SC	234	188	-	-	1.24	-
HF-H2-SC	241	188	-	-	1.28	-
CF-H1-SC	237	213	-	-	1.11	-
CF-H2-SC	229	213	-	-	1.07	-
HF-F1-SC	325	311	322	1.37	1.05	1.01
HF-F2-SC	324	311	322	1.36	1.04	1.01
CF-F1-SC	331	343	356	1.42	0.96	0.93
CF-F2-SC	360	343	356	1.55	1.05	1.01

The third column presents the maximum load predicted by BS EN 1993-1-1 (2005) and BS EN 1994-1-1 (2004). The resistance of the hollow sections was taken as the product of the cross-sectional area and steel yield stress and the resistance of the composite sections was calculated using Equations (2.3) – (2.5). The fourth column presents the maximum load predicted by Cai (1987) using Equation (3.1). All values in the third and fourth columns were calculated using the nominal cross-section dimensions and the measured material properties. The fifth column of Table 3.5 compares the resistance of each concrete-filled stub column with the equivalent hollow section while the sixth and seventh columns present the ratios between the maximum test loads and the predictions of the Eurocodes and Cai (1987) respectively. The hot-finished hollow tubes significantly exceeded the predicted ultimate load for hollow tubes given in BS EN 1993-1-1 (2005). The concrete infill enhanced the strength in all cases, with greater increases for cold formed tubes than

for hot-finished tubes, and this is also apparent in Figure 3.6. This was to be expected since the concrete occupied a greater percentage of the cross-sectional in the cold formed tubes (78%) than in the hot-finished tubes (75%). The maximum compressive strength showed very good agreement with predictions from BS EN 1994-1-1 (2004) and Cai (1987).

### **3.4 Bracing tests**

Following the stub column tests, cyclic axial tests were performed on twelve tubular braces.

#### **3.4.1 Specimen preparation**

A primary concern during manufacture of the test specimens was compacting the concrete in the steel tubes. Various methods of vibration for the wet concrete were investigated and an effective procedure was developed using a beam-vibrator and a rubber mallet. Specimens were cast vertically, with the vibrator clamped onto a loosely bolted steel frame which was in direct contact with the test specimen. This arrangement was found to provide ample pulsation without leading to segregation of the concrete mix and the method was aided by gently tapping the sides of the tube with the mallet. The tubes were filled in layers, with continuous vibration of the frame during casting and application of the mallet after each layer. After casting, the tops of the tubes were sealed with plastic to prevent the escape of moisture during curing.

Trial compactions were carried out using plastic tubes of the same dimensions as the test specimens and trial mixes 1 – 5 given in Table 3.3. The consistency of the mix was assessed afterwards by cutting open the pipe once the concrete had hardened and visually inspecting the content. The concrete core was broken into a number of

pieces along the length and the volume and weight of each piece was measured to calculate the density. Figure 3.8 illustrates the concrete core in each of these mixes beginning with Trial Mix 1 (top) and progressing through to Trial Mix 5 (bottom). The degree of consistency improved in the later mixes. Following these trial compactions, the final mix was designed using a high water-cement ratio (0.72) and a high fine to coarse aggregate (0.80) ratio.

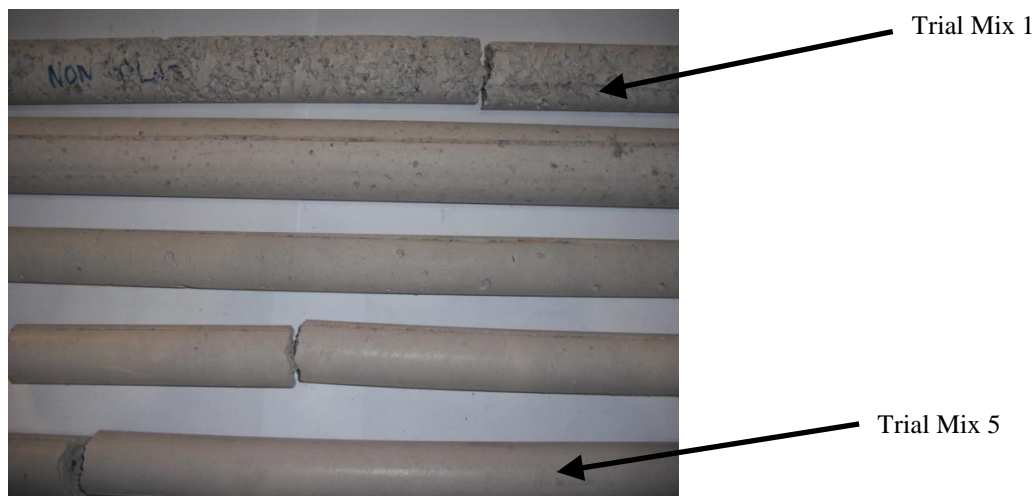


Figure 3.8 Concrete trial compactions

Two specimen lengths were manufactured: an ‘intermediate’ specimen which was 1500 mm long ( $\bar{\lambda} = 0.78 - 0.92$ ) and a ‘long’ specimen, which was 3000 mm long ( $\bar{\lambda} = 1.72 - 2.02$ ). Both hollow and filled braces were tested and a summary of these is provided in Table 3.6, in addition to non-dimensional slenderness values,  $\bar{\lambda}$ , calculated in accordance with BS EN 1993-1-1 (2005)/BS EN 1994-1-1 (2004). All members had fixed-ended conditions, and hence an effective length of  $0.7L$  was adopted, where  $L$  was the original member length. This value was used to allow for imperfections in the boundary conditions of the test set-up, such as small rotations at the ‘fixed’ ends or misalignment between the ends. The identification convention is similar to that of Table 3.4, with the final part referring to the bracing length.

Guidance regarding brace slenderness in concentrically braced frames is provided by BS EN 1998-1 (1994) as

$$1.3 < \bar{\lambda} \leq 2.0 \quad \text{for x-bracing} \quad (3.2)$$

$$\bar{\lambda} \leq 2.0 \quad \text{for other configurations} \quad (3.3)$$

Table 3.6 Summary of bracing specimens

Specimen	Steel	Core	$\bar{\lambda}$	$t$ mm	Maximum global imperfection	
					(unstiffened direction) mm	(stiffened direction) mm
HF-H-1500	Hot-finished	Hollow	0.78	3.18	0.58	0.49
CF-H-1500	Cold formed	Hollow	0.90	2.83	0.62	0.73
HF-F1-1500	Hot-finished	Concrete-filled	0.81	3.21	0.26	0.37
HF-F2-1500	Hot-finished	Concrete-filled	0.81	3.20	0.22	0.38
CF-F1-1500	Cold formed	Concrete-filled	0.92	2.85	0.67	0.73
CF-F2-1500	Cold formed	Concrete-filled	0.92	2.82	0.67	0.61
HF-H-3000	Hot-finished	Hollow	1.72	3.19	1.88	1.84
CF-H-3000	Cold formed	Hollow	1.98	2.81	2.95	3.86
HF-F1-3000	Hot-finished	Concrete-filled	1.78	3.19	1.50	1.52
HF-F2-3000	Hot-finished	Concrete-filled	1.78	3.22	1.30	1.34
CF-F1-3000	Cold formed	Concrete-filled	2.02	2.82	3.27	2.27
CF-F2-3000	Cold formed	Concrete-filled	2.02	2.84	3.46	2.76

All concrete-filled specimens were cast with the same concrete mix and compacted in the same manner. Both hollow and concrete-filled tubes were then welded onto 25 mm thick steel end plates. To ensure structural integrity of the welded end connections, two stiffening plates with dimensions of 125 mm × 50 mm × 8 mm were also welded onto the outside of each tube at these locations. These are illustrated in Figure 3.9.

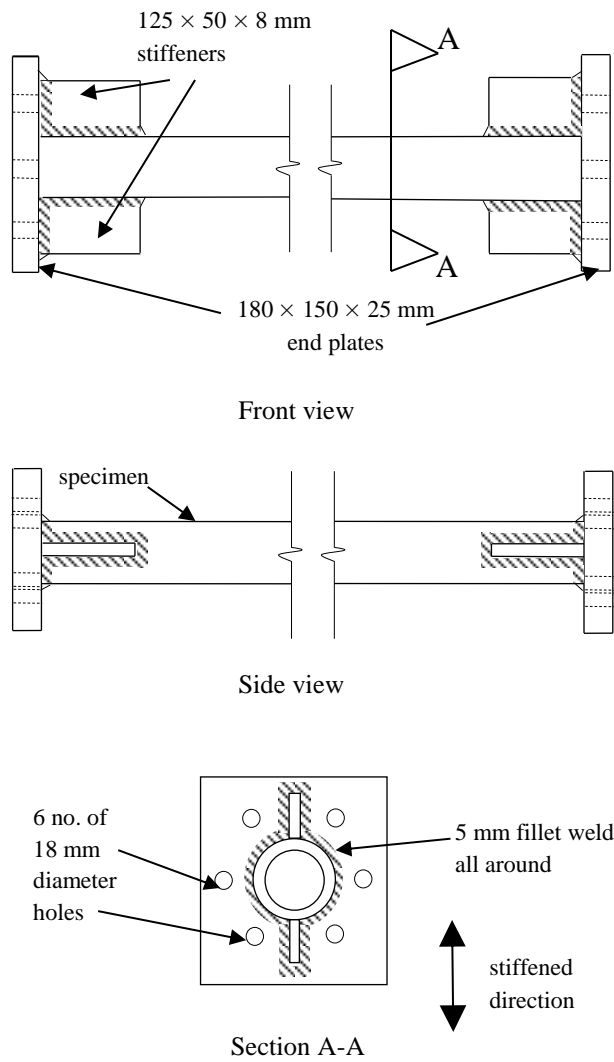


Figure 3.9 Cyclic test specimen end connection details

The surface profile was measured along four faces of the tube at 90° separations. Measurements were taken on a level table using a displacement transducer which was attached to a low-friction glider and rail system, as shown in Figure 3.10. The maximum global imperfections in directions parallel to and perpendicular to the plane of the end stiffeners are included in Table 3.6, in addition to the average measured tube wall thickness.

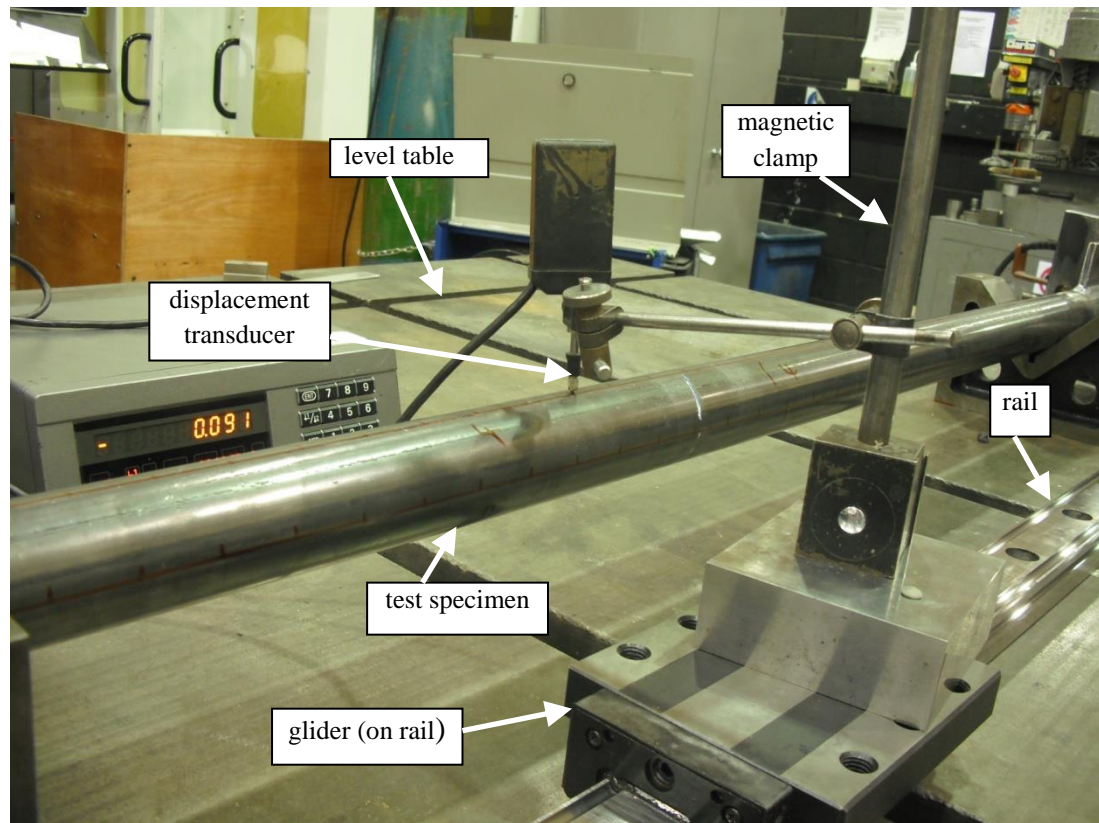


Figure 3.10 Set-up for measuring global imperfections of bracing test-specimens

### 3.4.2 Test procedure

Specimens were subjected to the cyclic loading protocol outlined in ECCS (1986). This protocol facilitated a direct comparison with test results from Nip *et al.* (2010a) and Broderick *et al.* (2005). Although this loading sequence does not represent a real earthquake it was developed as a standardised procedure to establish the response of individual elements, substructures or entire structures under cyclic loading. As introduced in Chapter 2, it is well-known that the behaviour of steel can deviate from the idealised elasto-plastic response after repeated loading cycles. In this research testing was executed on an individual brace member and the loading was applied directly, to represent part of the seismic action that would be experienced by this component within a complete structure. The loading procedure was symmetric in compression and tension, consisting of one displacement cycle at

### Chapter 3 Laboratory Experiments

amplitudes of  $0.25\delta_y$ ,  $0.5\delta_y$ ,  $0.75\delta_y$  and  $1.0\delta_y$  followed by three displacement cycles at each of  $2\delta_y$ ,  $4\delta_y$ ,  $6\delta_y$ ,  $8\delta_y$ , etc. up to failure, where  $\delta_y$  was the yield displacement of the specimen. This parameter was determined by using the values of yield stress/0.2% proof stress and the modulus of elasticity which were obtained from the tensile coupon tests (Table 3.2) to establish a quantity of yield strain, which was then multiplied by the member length to convert to displacement. In each cycle, specimens were first loaded in compression and then in tension.

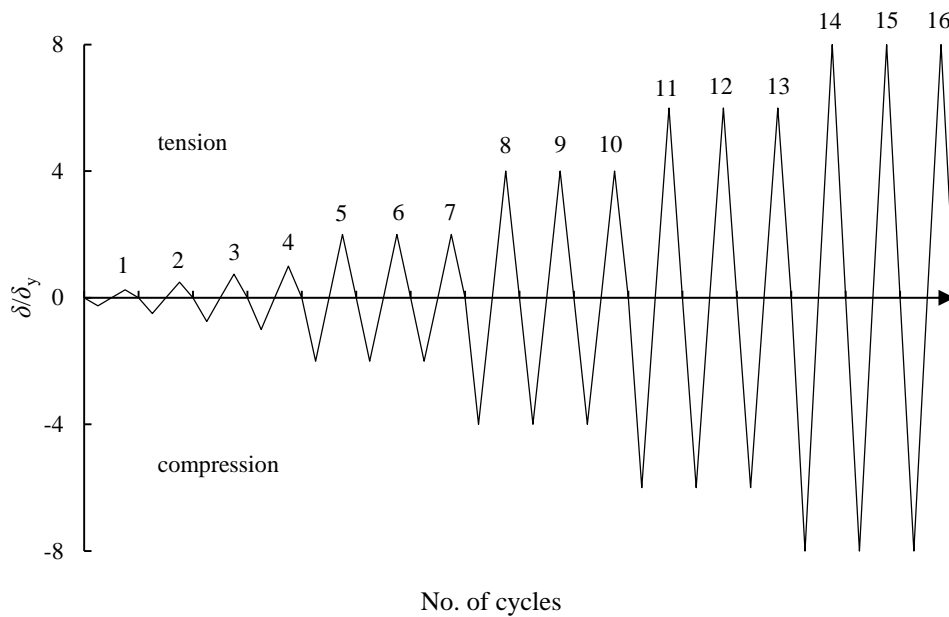


Figure 3.11 Cyclic loading protocol (ECCS, 1986)

A vertical, purpose-built test-rig was constructed for the tests, as shown in Figure 3.12. Specimens were connected to the test-rig using six Grade 8.8 M16 bolts at each end and cyclic displacements were applied with a 50-tonne hydraulic actuator. Load was measured using an inbuilt load cell and axial displacement was monitored with a linear variable displacement transducer (LVDT). Lateral displacements at the mid-height were measured using string potentiometers, in the plane of the frame and in the orthogonal direction, corresponding to the stiffened and unstiffened axes of the specimen ends. Longitudinal, post-yield strain gauges (TML strain gauges, series

‘YEFLA’) were utilized at the anticipated locations of plastic hinges: at the mid-length and close to the end-fixtures. Some measures were taken to improve test rig performance and to account for deviations from the idealised boundary conditions. High strength friction grip (HSFG) bolts were used at the corners of the test-rig to prevent slippage during cyclic loading. Displacement of the top beam was measured throughout the tests to account for the flexibility of the test-rig. Although fully restrained boundary conditions were assumed at the specimen ends, two inclinometers were employed to record any rotations which occurred, one in the plane of the frame and the second in the orthogonal direction.

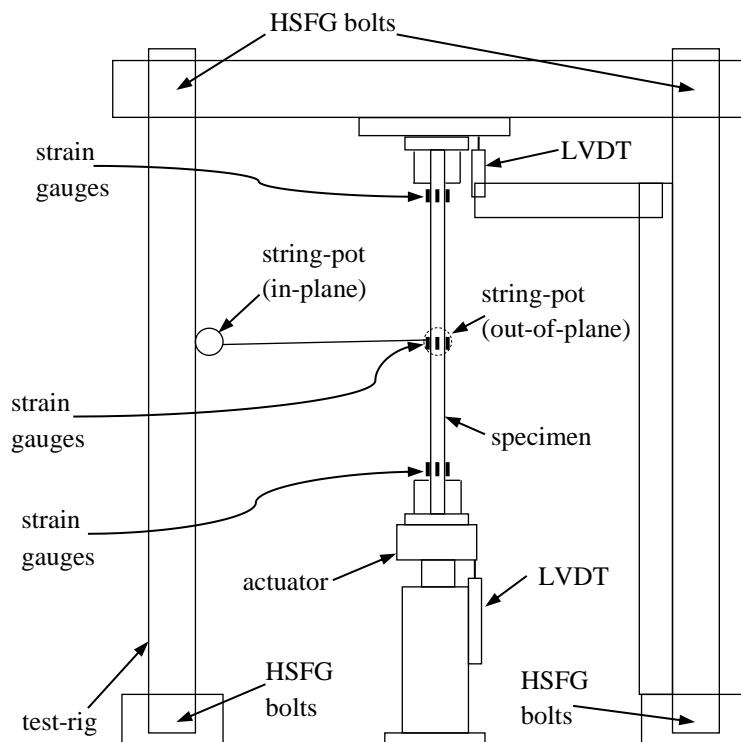
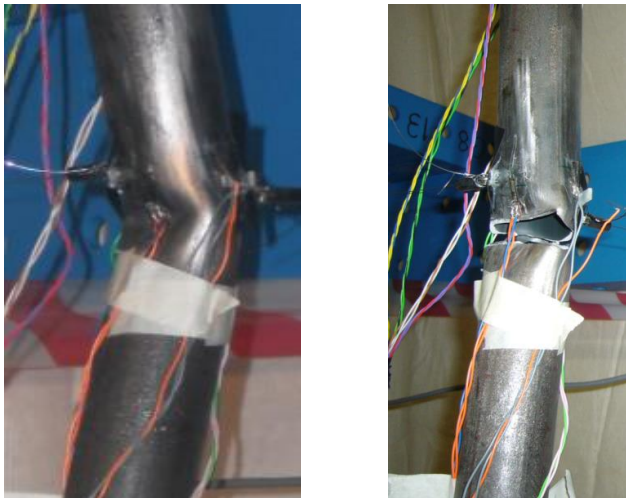


Figure 3.12 Test-rig and instrumentation

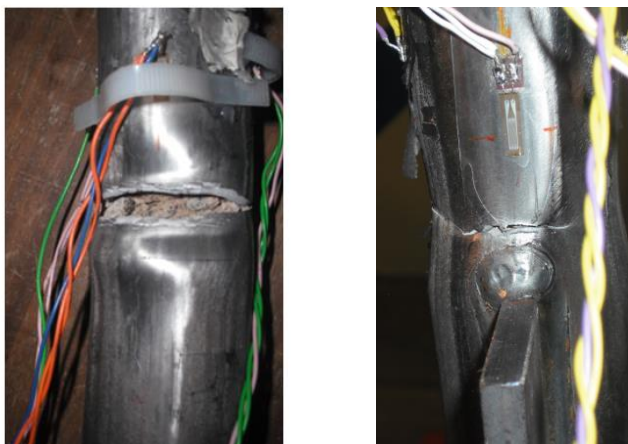


### 3.4.3 Deformation and failure

Each of the test specimens buckled globally about the unstiffened axis. As the axial displacement increased, so did the mid-height lateral displacement in the compression-half of each cycle, until local buckling propagated in one or more of the anticipated plastic hinge regions. Specimens eventually failed by rupture of the steel tube at the location of local buckling in the tensile half of the cycle. Hot-finished and cold formed hollow specimens underwent inward local buckling at the mid-height, as shown in Figure 3.13(a). Relatively little local deformation occurred in the hollow tubes other than at the mid-height.



(a)



(b)

Figure 3.13 Local buckling and failure at (a) mid-height of HF-H-1500; (b) mid-height and base of HF-F1-1500

Specimen HF-F1-1500 showed necking and outward local buckling at the base and mid-height, and eventually ruptured at these locations, as shown in Figure 3.13 (b). HF-F2-1500, CF-F1-1500 and CF-F2-1500 exhibited similar responses to HF-F1-1500. HF-F2-1500 eventually ruptured close to the top, and CF-F1-1500 and CF-F2-1500 failed adjacent to the base.

The global deformed shapes of a hollow and concrete-filled brace are presented in Figures 3.14(a) and 3.14(b) for comparison. The 1500 mm concrete-filled specimens took on a more curved profile along the length than the hollow specimens, which were effectively divided into two straight segments by the mid-height portion. This delayed the onset of local buckling for the concrete-filled braces. In addition to the deformations at the mid-height, local buckling occurred close to the ends of the concrete-filled specimens, but the buckling propagated outwards, increasing the section bending capacity. This, in addition to the improved distribution of plasticity along the length, enabled the concrete-filled specimens to endure a larger number of cycles than the hollow tubes.

The 3000 mm hollow specimens underwent similar behaviour to the 1500 mm hollow specimens but some differences were observed in the filled specimens. For the hot-finished filled tests, the maximum actuator stroke was reached before specimen failure had occurred. After three cycles at a displacement amplitude of  $14\delta_y$ , there were no obvious signs of local buckling and hence it is difficult to predict when ultimate failure would have occurred. For the cold formed filled tests, some signs of local buckling and necking were observed at the mid-height and close to the ends prior to fracture, but this was not as severe as in the case of the shorter tubes.

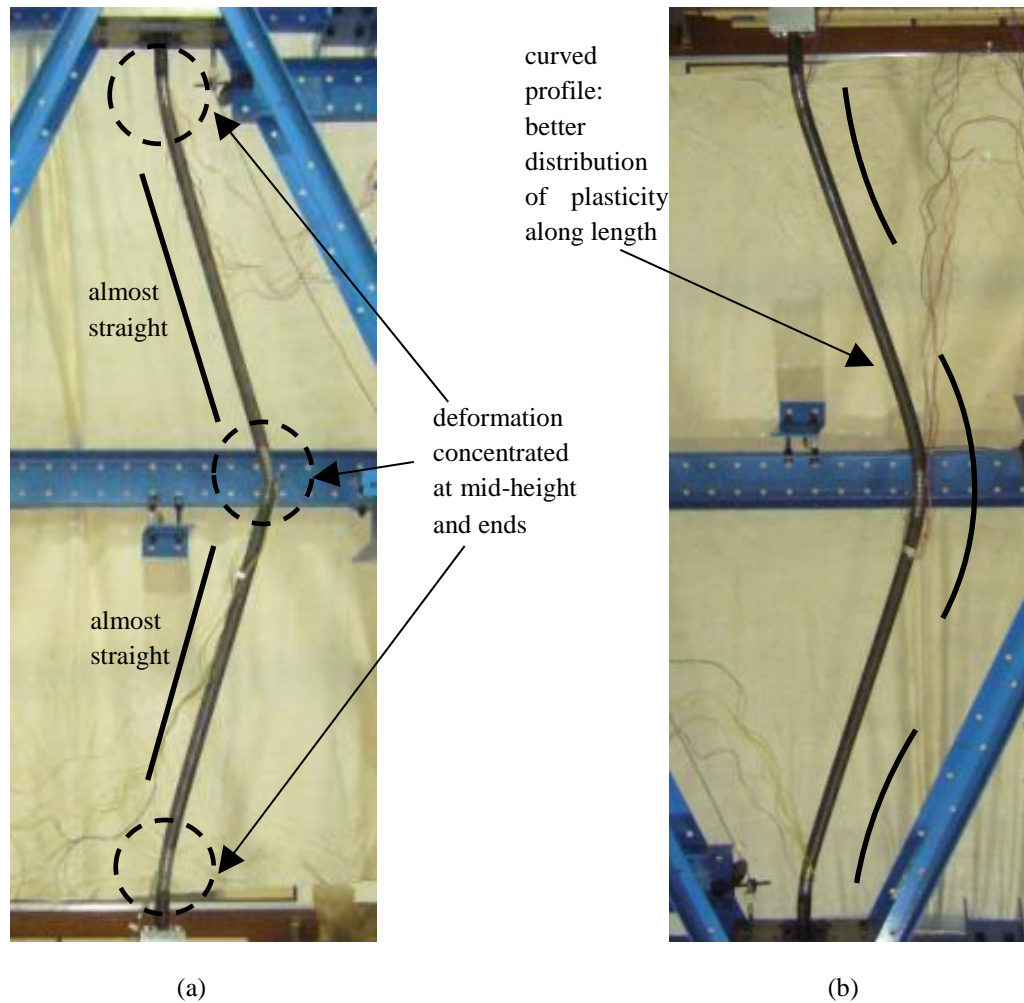


Figure 3.14 Global deformed shape for (a) hollow specimen; (b) concrete-filled specimen

For the hot-finished sections, lateral deflection occurred predominantly about the unstiffened axis but the cold formed sections showed significant lateral displacements in both directions, as shown in Figure 3.15. Possible causes of this are the residual stresses in the cross-section from the cold forming process, increased sensitivity to the global imperfection in the stiffened plane owing to the position of the seam weld, or out-of-roundness of the initial CHS cross-sectional shape. The cause of the lateral deformation observed cannot be confirmed without further experiments.

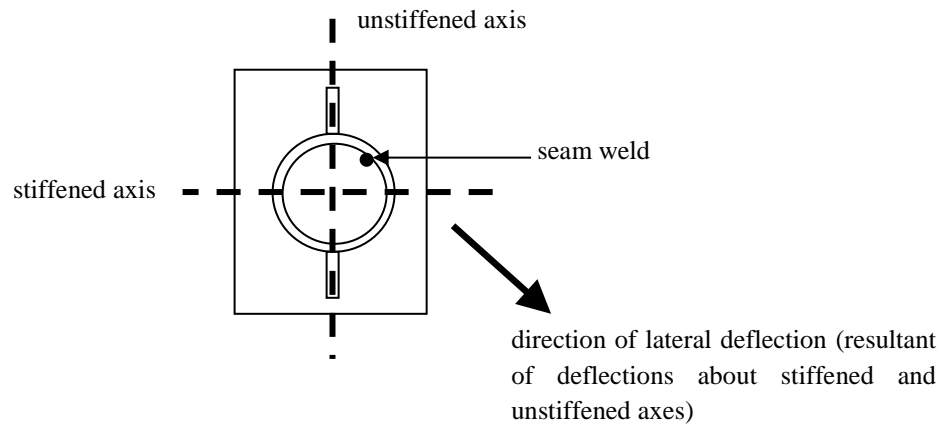


Figure 3.15 Direction of global deflection of cold formed braces

### 3.4.4 Displacement ductility

Displacement ductility,  $\mu_{\Delta}$ , is defined in this study as the ratio of maximum axial displacement to yield displacement, similar to the definition in Nip *et al.* (2010a) and Tremblay (2002). Table 3.7 summarises the total number of cycles to fracture and displacement ductility for each of the specimens. For both brace lengths, the hot-finished tubes endured a greater number of cycles than the cold formed tubes and the concrete-filled tubes gave a superior performance to the hollow specimens. In most cases however, the filled specimens failed at the same displacement amplitude as the hollow specimens, but in a later cycle, and hence the benefits of concrete infill are not apparent in the values of  $\mu_{\Delta}$ . As discussed in Section 3.4.3, it is expected that HF-F1-3000 and HF-F2-3000 would have surpassed the displacement ductility of their hollow counterpart. Therefore the concrete infill appears to contribute more to  $\mu_{\Delta}$  for hot-finished specimens than for cold formed specimens.

### Chapter 3 Laboratory Experiments

Table 3.7 Maximum numbers of cycles and loads

Specimen ID	$\bar{\lambda}$	No of cycles to fracture	$\mu_{\Delta}$	$\mu$	$\mu_f$
HF-H-1500	0.78	17	10	2.98	4.98
CF-H-1500	0.90	14	8	2.95	3.80
HF-F1-1500	0.81	28	16	2.45	8.44
HF-F2-1500	0.81	19	10	2.08	7.31
CF-F1-1500	0.92	15	8	2.41	5.38
CF-F2-1500	0.92	16	8	2.60	5.67
HF-H-3000	1.72	24	14	1.29	13.35
CF-H-3000	1.98	17	10	1.41	6.35
HF-F1-3000	1.78	25*	14	1.49	n/a
HF-F2-3000	1.78	25*	14	1.36	n/a
CF-F1-3000	2.02	17	10	1.26	9.56
CF-F2-3000	2.02	18	10	1.21	6.25

\*Note: Test terminated at actuator stroke limit

The ductility index for seismic bracing members has been treated differently by previous researchers. In Broderick *et al.* (2005) the ductility was calculated similarly to this study but using the axial displacement at the time of fracture. This is presented in the final column of Table 3.7 as  $\mu_f$ . This parameter followed similar trends to  $\mu_{\Delta}$ , with larger values observed for the longer specimens than the shorter ones. There was a significant increase in  $\mu_f$  between hollow and filled specimens, indicating that the concrete-filled specimens tended to fracture at a later stage in the loading protocol in Figure 3.11 than the hollow specimens.

Elchalakani (2003) defined ductility as

$$\mu = \frac{\delta_{\max}}{\delta_y} \quad (3.4)$$

where  $\delta_{\max}$  is defined as the axial displacement of the member at 80% of the peak compressive load, on the envelope curve for the cyclically loaded specimens. This measure is used in New Zealand design practice in accordance with NZS 4203

(1992).  $\mu$  is reported in Table 3.7. For the 1500 mm members, both cold formed and hot-finished hollow braces achieved higher ductility indices than the equivalent concrete-filled specimens. For 3000 mm specimens, a slightly higher  $\mu$  was achieved for hollow cold formed braces than for filled members but the trend was reversed for the hot-finished tubes. Overall, the shorter specimens achieved larger ductility indices than the longer members, showing slower load degradation with increasing axial displacement in the compressive resistance envelope. The values of  $\mu$  shown in Table 3.7 do not indicate any benefit to using concrete infill in axially loaded braces.

#### 3.4.5 First cycle buckling loads

The first cycle buckling loads ( $N_{c,max}$ ) are presented in Table 3.8 and Figure 3.16. Non-dimensional slenderness ( $\bar{\lambda}$ ) values and flexural buckling loads,  $N_{b,Rd}$  were calculated for hot-finished and cold formed hollow tubes using buckling curves ‘a’ and ‘c’ respectively from BS EN 1993-1-1 (2005). These curves were also used for predicting the buckling load of the concrete-filled tubes, but in this case  $\bar{\lambda}$  was determined following the approaches of Bergmann *et al.* (1995) and BS EN 1994-1-1 (2004). Here,  $\bar{\lambda}$  was taken as  $\sqrt{N_{pl,Rd}/N_{cr}}$  where  $N_{pl,Rd}$  was the plastic resistance of the cross-section and  $N_{cr}$  was the elastic critical buckling load.  $N_{cr}$  was calculated using an effective stiffness,  $(EI)_{eff} = E_a I_a + K_e E_c I_c$ , for the composite cross-sections in accordance with Clause 6.7.3.3 of BS EN 1994-1-1 (2004). The correction factor,  $K_e$  was taken as 0.8 as recommended for concrete-filled tubes by Bergmann *et al.* (1995). An effective length of  $0.7L$  was used in the calculations for both hollow and concrete-filled braces to account for imperfections in the specimen boundary conditions.

## Chapter 3 Laboratory Experiments

Table 3.8 First cycle buckling loads from experiments

Specimen ID	$\bar{\lambda}$	Cycle of global buckling	$N_{c,max}$ (kN)	$N_{b,Rd}$ (kN)	$N_{c,max}/N_{b,Rd}$
HF-H-1500	0.78	5	155	133	1.17
CF-H-1500	0.90	5	151	105	1.43
HF-F1-1500	0.81	5	174	152	1.14
HF-F2-1500	0.81	5	175	152	1.15
CF-F1-1500	0.92	5	174	147	1.18
CF-F2-1500	0.92	5	164	147	1.11
HF-H-3000	1.72	4	81	55	1.47
CF-H-3000	1.98	3	71	42	1.66
HF-F1-3000	1.78	3	83	61	1.36
HF-F2-3000	1.78	3	88	61	1.44
CF-F1-3000	2.02	3	72	54	1.33
CF-F2-3000	2.02	3	71	54	1.32

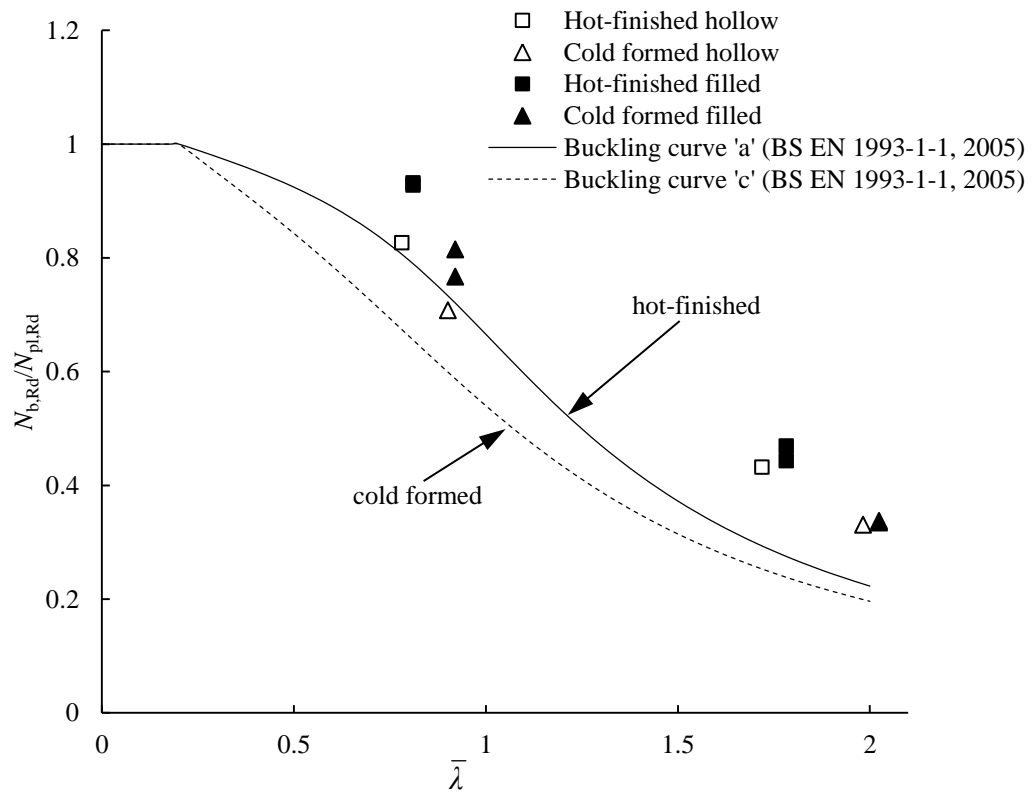


Figure 3.16 First cycle buckling loads from experiments

In all cases,  $N_{c,max}$  exceeded the values of  $N_{b,Rd}$ , particularly for the longer members. For the 1500 mm length situation, overall flexural buckling occurred during the 5<sup>th</sup> cycle, whereas for the 3000 mm length, failure was during the 3<sup>rd</sup> cycle, with the exception of HF-H-3000, which was in the 4<sup>th</sup> loading cycle. The overall trend shows some similarities to Nip *et al.* (2010a), in which global buckling occurred between the 3<sup>rd</sup> and 5<sup>th</sup> cycles, with specimens of a higher  $\bar{\lambda}$  ( $> 1.0$ ) generally buckling earlier. It is evident in Figure 3.16 that the first cycle peak buckling load is enhanced by the presence of concrete infill for the ‘intermediate’ length specimens.

### 3.4.6 Post-buckling compressive strength

The next parameter to be considered was the post-buckling behaviour. During each compressive half-cycle, the specimen attained the maximum compressive strength at an early stage of the cycle before buckling, and the resistance decreased as the axial compressive displacement of the member increased. This is significant in chevron-braced frames, as the degradation of compressive strength may occur prior to yielding in the tensile brace, inducing a net vertical force pulling downwards on the connecting beam. This may lead to the formation of a plastic hinge in the beam and hence would need to be taken into account in the design, as discussed by Tremblay (2002). Degradations of compressive resistance,  $N_c$ , are presented in Figures 3.17 and 3.18 in relation to axial displacement for both 1500 mm and 3000 mm specimens in their 1<sup>st</sup> cycle at each displacement amplitude. The presence of concrete infill increased the initial compressive strength for 1500 mm specimens. The compressive strength degradation at low displacement amplitudes ( $\delta/\delta_y < 5$ ) was greater for the concrete-filled specimens than for the hollow specimens but this trend was reversed at higher displacement amplitudes ( $\delta/\delta_y \geq 5$ ) for both hot-finished and



cold formed tubes. The concrete core had less impact on the post-buckling resistance of 3000 mm specimens however, as illustrated in Figure 3.18. Similar behaviour was observed for the 2<sup>nd</sup> and 3<sup>rd</sup> cycles at each displacement amplitude.

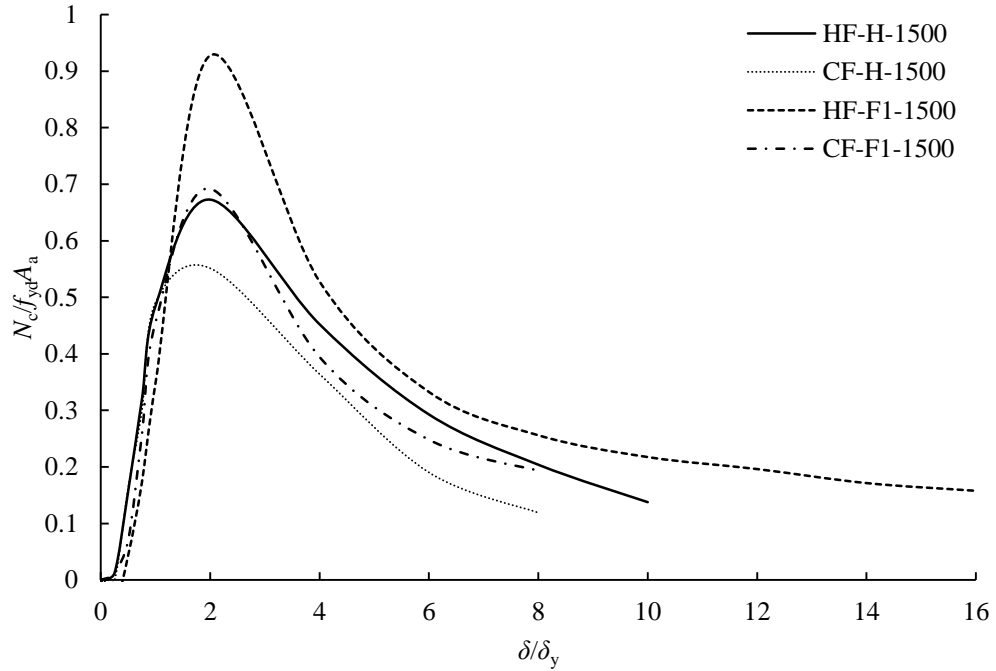


Figure 3.17 Post-buckling resistance in 1<sup>st</sup> cycle at each displacement amplitude for 1500 mm specimens

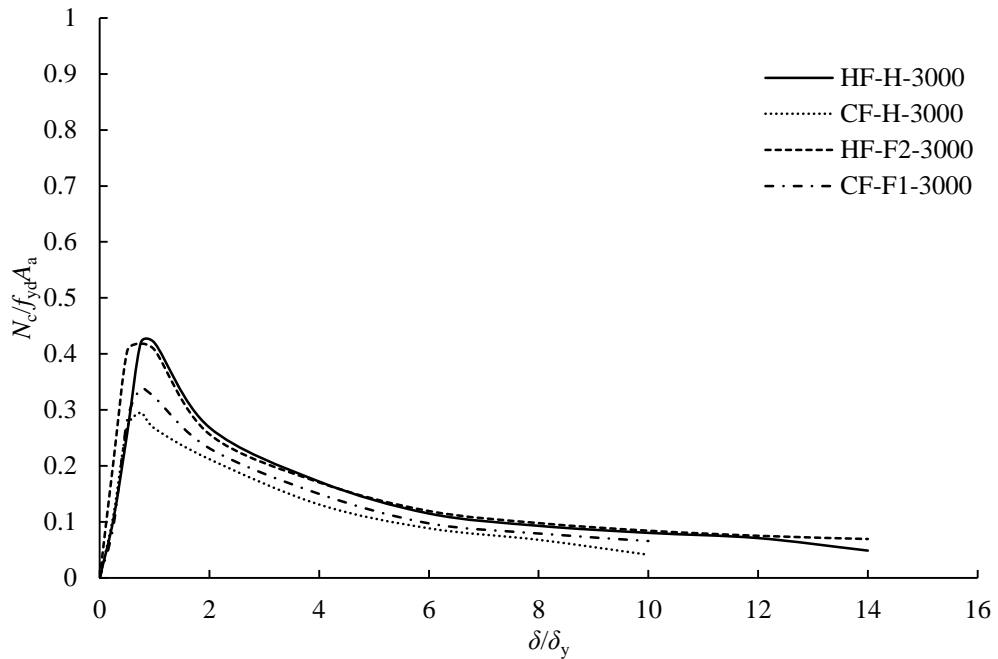


Figure 3.18 Post-buckling resistance in 1<sup>st</sup> cycle at each displacement amplitude for 3000 mm specimens

A number of predictions have been made regarding the post-buckling compressive strength of seismic steel braces. AISC (2002) guidelines assume a value of  $0.26P_n$  where  $P_n$  is the estimated maximum axial compressive strength. CSA (1994) guidelines provide a prediction of buckling resistance in terms of the global slenderness as follows:

$$C'_u = \frac{C_u}{1 + 0.35\lambda} \quad (3.5)$$

where  $C_u$  is the maximum compressive resistance from

$$C_u = \frac{A_a F_y}{(1 + \lambda^{2n})^{1/n}} \quad \text{where } n = 1.34 \quad (3.6)$$

Tremblay (2002) developed an expression for post-buckling resistance from the results of tests on 76 specimens, including a variety of cross-section shapes. The sections used were Class 1, since these were the most suitable for providing the required ductility under seismic loading. The expression for post-buckling resistance was presented as:

$$C'_u = A_a F_y (a + b\lambda^{-c}) \leq C_u \quad (3.7)$$

where values for  $a$ ,  $b$ , and  $c$  were obtained from test data. Other expressions have been proposed, such as by Nakishima *et al.* (1992), given by

$$C'_u = A_a F_y \left( \frac{1 - \alpha\beta}{1 - \beta} \right)^{4/3} \leq C_u \quad (3.8)$$

where

$$\alpha = \frac{8r^{3/4}}{5\lambda^{3/2}} \quad (3.9)$$

$$\beta = \alpha^{1/3} - \sqrt{\alpha^{2/3} + \frac{5}{3}\lambda^2 \frac{\delta_c}{\delta_y}} \quad (3.10)$$

Figures 3.19 - 3.21 compare the author's test results with predictions from AISC and Equations (3.5), (3.7) and (3.8) for displacement ductilities,  $\mu_{\Delta}$ , of 2, 3, and 5. Values of  $\mu_{\Delta}$  were selected following from Tremblay (2002), in order to cover the range of expected axial deformations for braces in symmetrical tension-compression configurations. It was observed by Tremblay (2002) that the post-buckling resistance remains almost constant for  $\mu_{\Delta} > 5$  and hence higher  $\mu_{\Delta}$  values were not examined. The test results given by the open (hollow) and solid (concrete-filled square (hot-finished) and triangular (cold formed) symbols showed satisfactory agreement with the CSA (1994) predictions under low displacement ductilities but these deviated towards predictions of Tremblay (2002) and Nakashima *et al.* (1992) as the displacement ductility increased. The AISC (2002) prediction was over-conservative in all cases. The concrete-filled tubes had significantly better post-buckling resistance when  $\bar{\lambda} < 1.0$  but this difference became negligible as  $\bar{\lambda}$  increased. Shorter members underwent more severe post-buckling resistance degradation than the longer braces as axial displacement increased and this is evident in Figures 3.19 - 3.21.

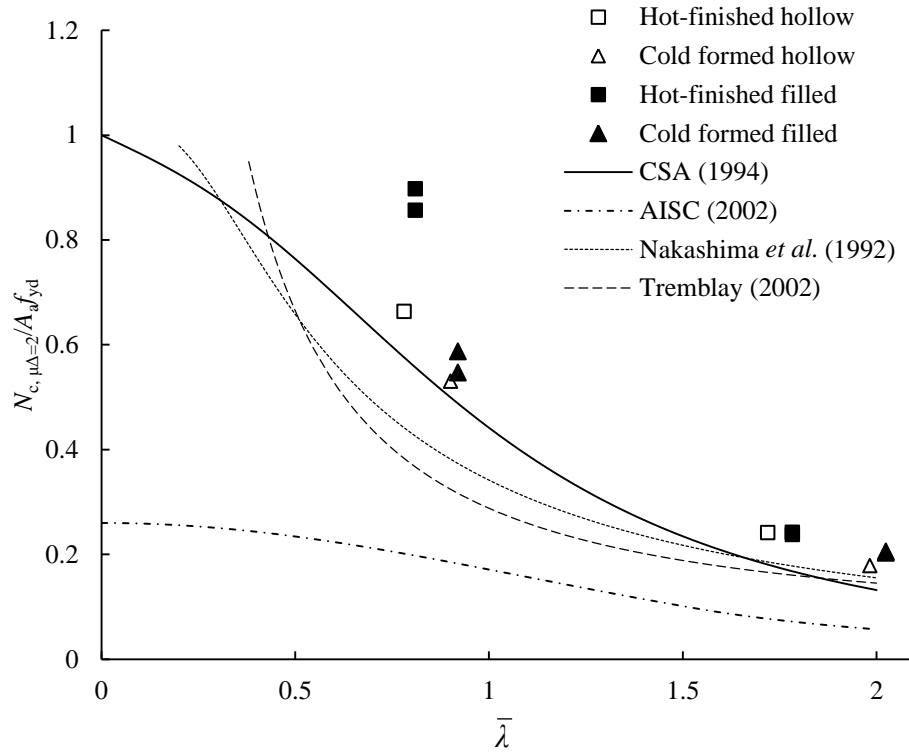


Figure 3.19 Post-buckling resistance versus non-dimensional slenderness for  $\mu_{\Delta} = 2$

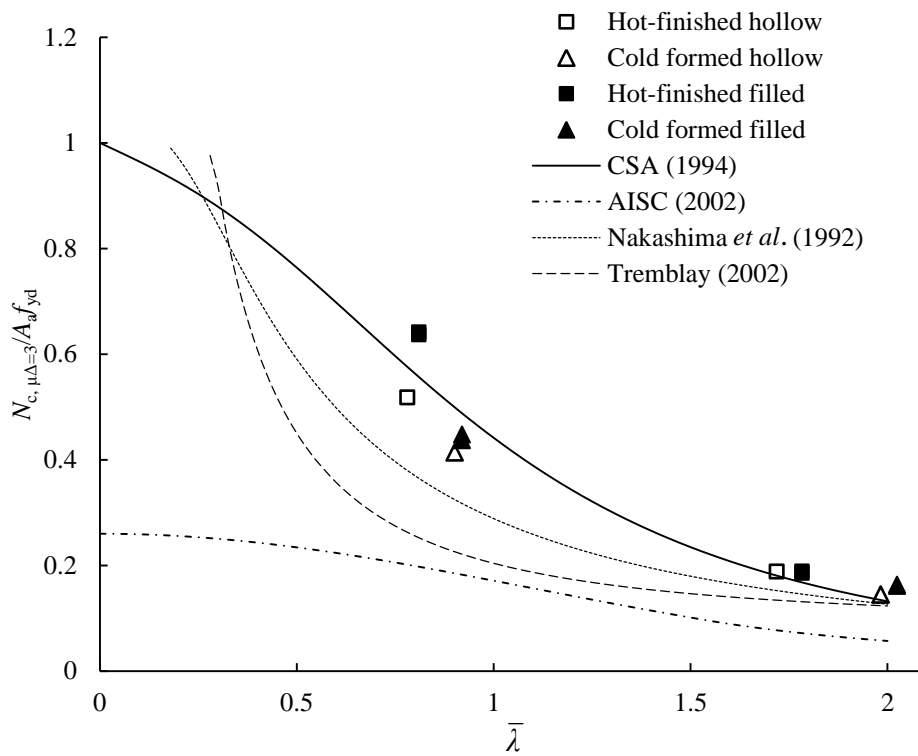
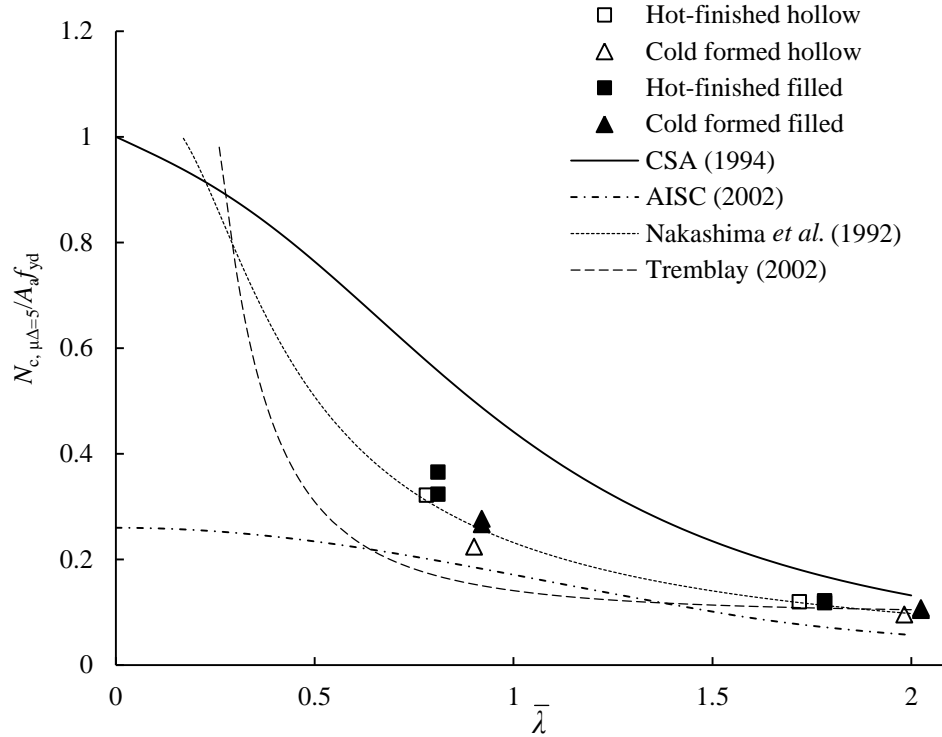


Figure 3.20 Post-buckling resistance versus non-dimensional slenderness for  $\mu_{\Delta} = 3$

Figure 3.21 Post-buckling resistance versus non-dimensional slenderness for  $\mu_{\Delta} = 5$ 

### 3.4.7 Tensile load and load degradation

The maximum tensile resistance for each specimen,  $N_{t,max}$ , is presented in Table 3.9 and compared with the yield strength of the steel cross-section ( $N_{t,y} = A_g f_{yd}$ ). The concrete-filled specimens had superior tensile resistance to the hollow members, for both steel section types. An increase in tensile resistance with concrete infill was observed by Han *et al.* (2011) from testing of short concrete-filled CHS columns subjected to axial tension. The concrete core provided some degree of tensile strength prior to cracking but under the prescribed loading conditions cracking of the core would have occurred at a reasonably early stage in the test. Prevention by the concrete of inward deformation of the steel tube wall can partially account for the increase in tensile resistance. However it can be largely attributed to the stress state of the steel induced by the lateral pressure from the concrete core. The consequential hoop stress combined with the applied axial load resulted in a state of

biaxial tension for the steel tube and assuming a von Mises yield criterion (Figure 3.22), the axial tensile resistance  $f_1$ , was increased from  $f_y$  by the presence of  $f_2$ .

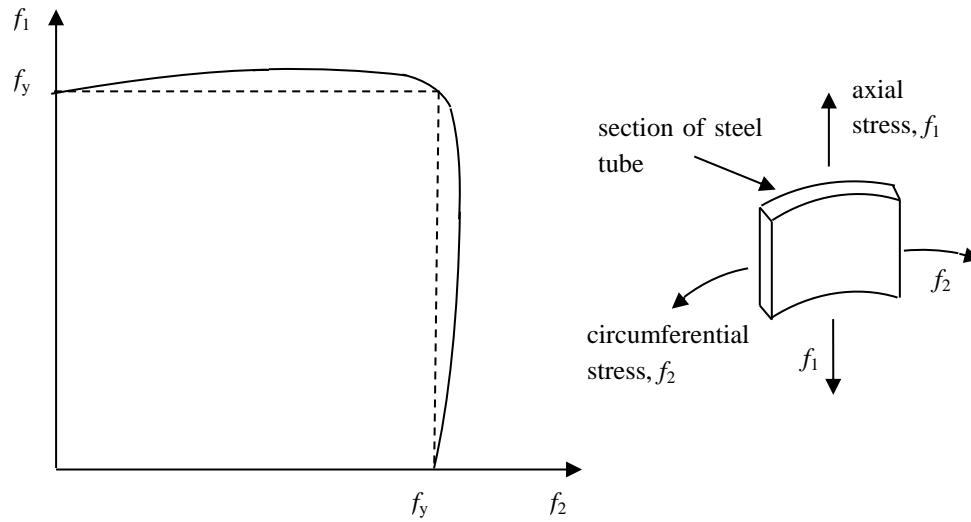


Figure 3.22 Assumed biaxial stress state for steel tube

Table 3.9 Maximum tensile forces

Specimen ID	$N_{t,max}$ kN	$N_{t,max}/N_{t,y}$	Enhancement in $N_{t,max}$ from concrete %
HF-H-1500	180	0.96	-
CF-H-1500	209	0.98	-
HF-F1-1500	198	1.05	10
HF-F2-1500	198	1.05	10
CF-F1-1500	220	1.03	5.3
CF-F2-1500	216	1.01	3.3
HF-H-3000	187	1.00	-
CF-H-3000	209	0.98	-
HF-F1-3000	203	1.08	8.6
HF-F2-3000	198	1.05	5.9
CF-F1-3000	223	1.05	6.7
CF-F2-3000	227	1.05	8.6

Filled and hollow specimen results were compared to evaluate the contribution to  $N_{t,max}$  of the concrete. Intermediate-length hot-finished tubes exhibited the greatest improvement, showing a 10 % difference, whereas intermediate cold formed

specimens experienced a lower enhancement, with an average of 4 %. Tensile load degradations are presented for the 3000 mm test specimens in the 1<sup>st</sup> displacement cycle at each amplitude in Figure 3.23. Not only did the concrete increase the maximum tensile strength in the early stages of the test, but it maintained this enhancement as the loading protocol progressed. Similar trends were seen for the 2<sup>nd</sup> and 3<sup>rd</sup> cycles at each axial displacement amplitude and for the bracing with  $\bar{\lambda} < 1.0$ .

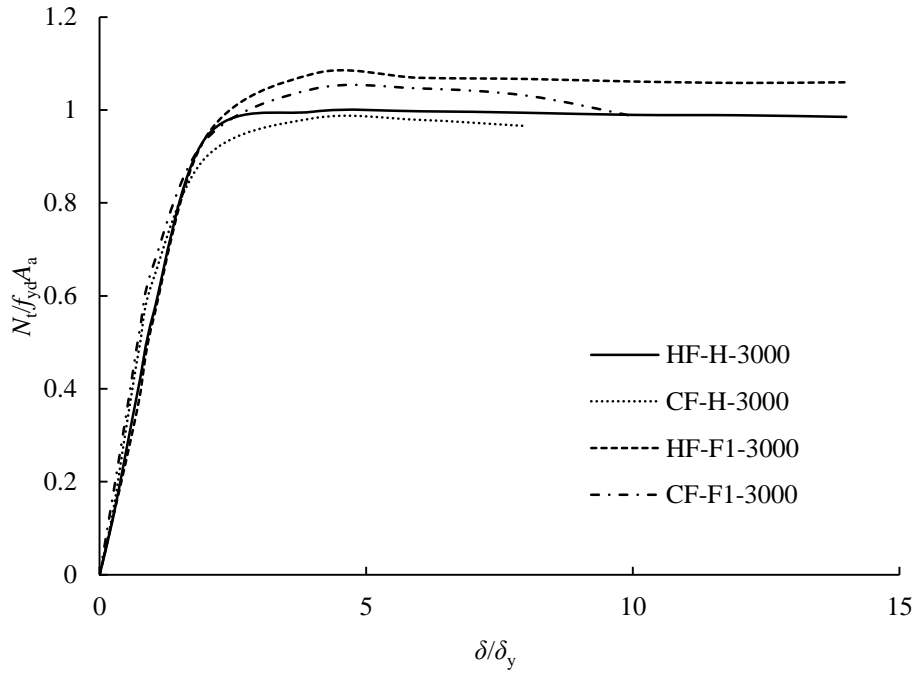


Figure 3.23 Maximum tensile force for 1<sup>st</sup> cycle at each displacement amplitude

### 3.4.8 Energy dissipation

The energy dissipation is defined in this thesis as the external work done and is equal to the area enclosed by the load-displacement hysteresis loops. These hysteresis curves are presented for each specimen in Figures 3.24 – 3.35.

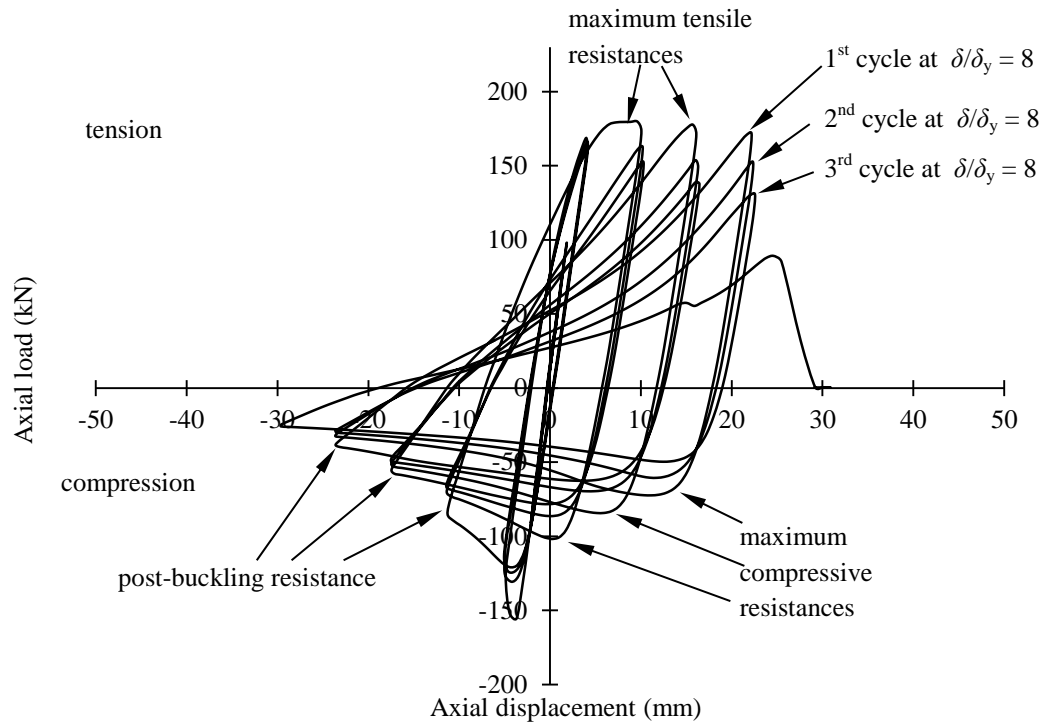


Figure 3.24 Load-displacement response for HF-H-1500

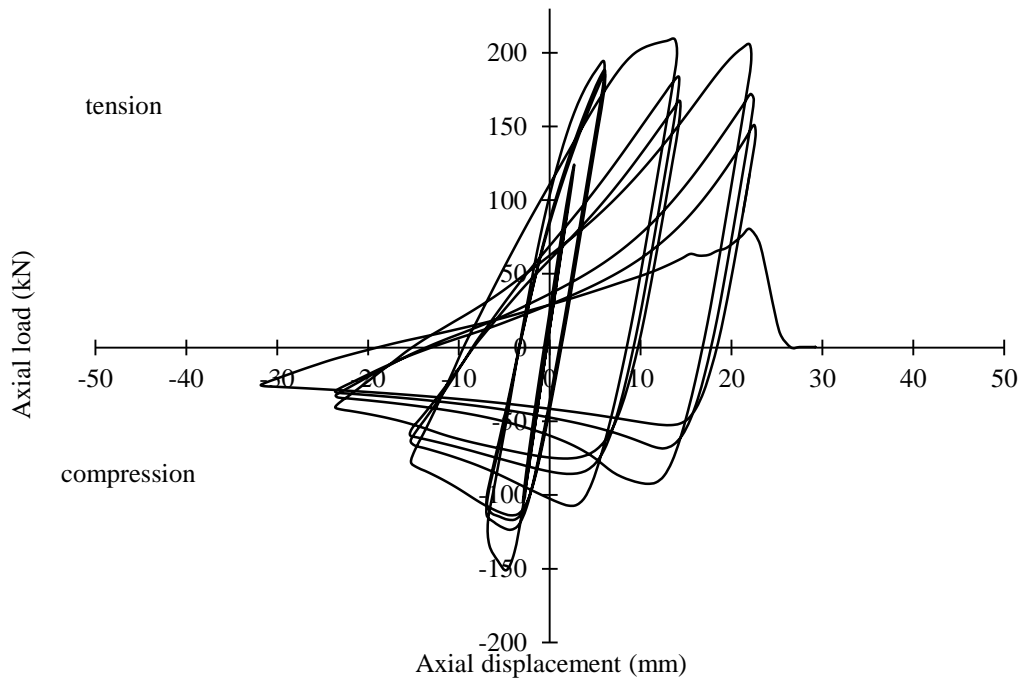


Figure 3.25 Load-displacement response for CF-H-1500



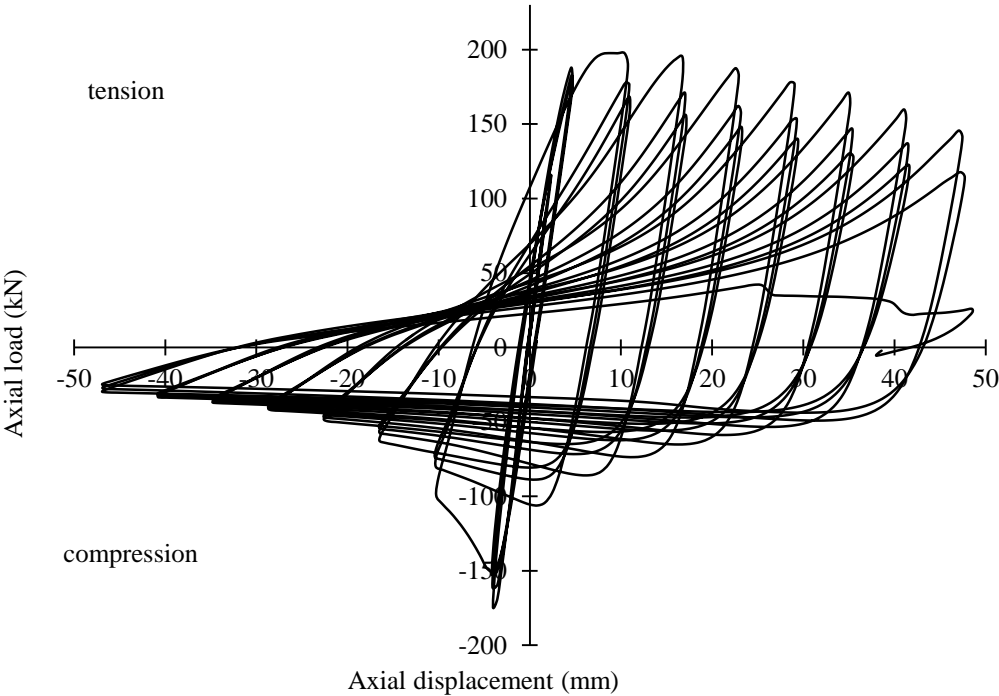


Figure 3.26 Load-displacement response for HF-F1-1500

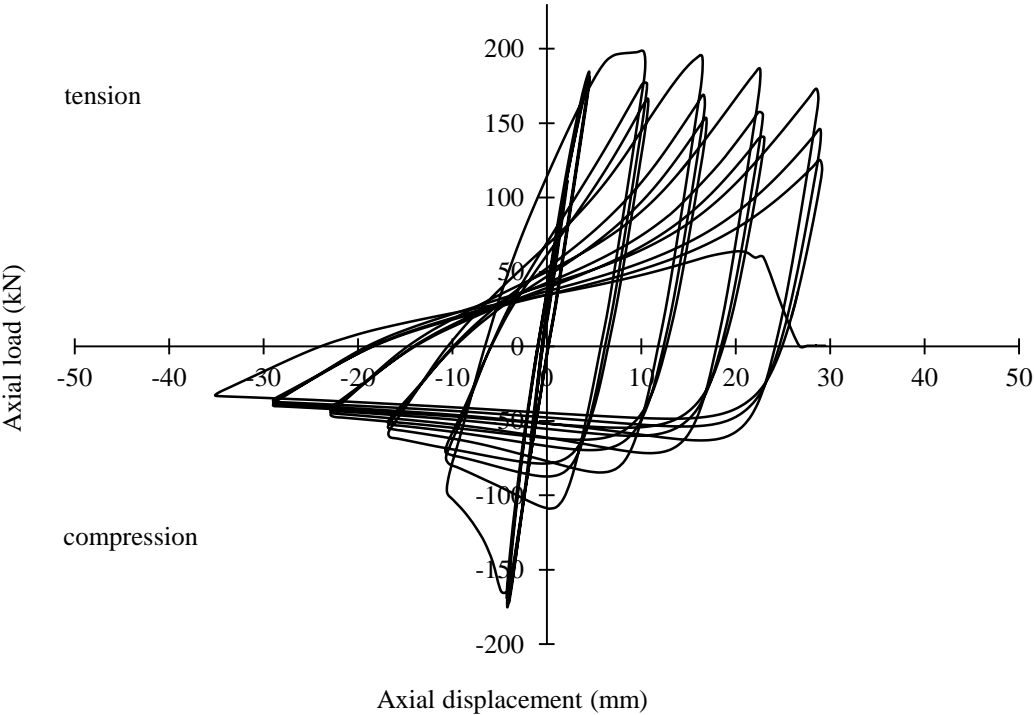


Figure 3.27 Load-displacement response for HF-F2-1500

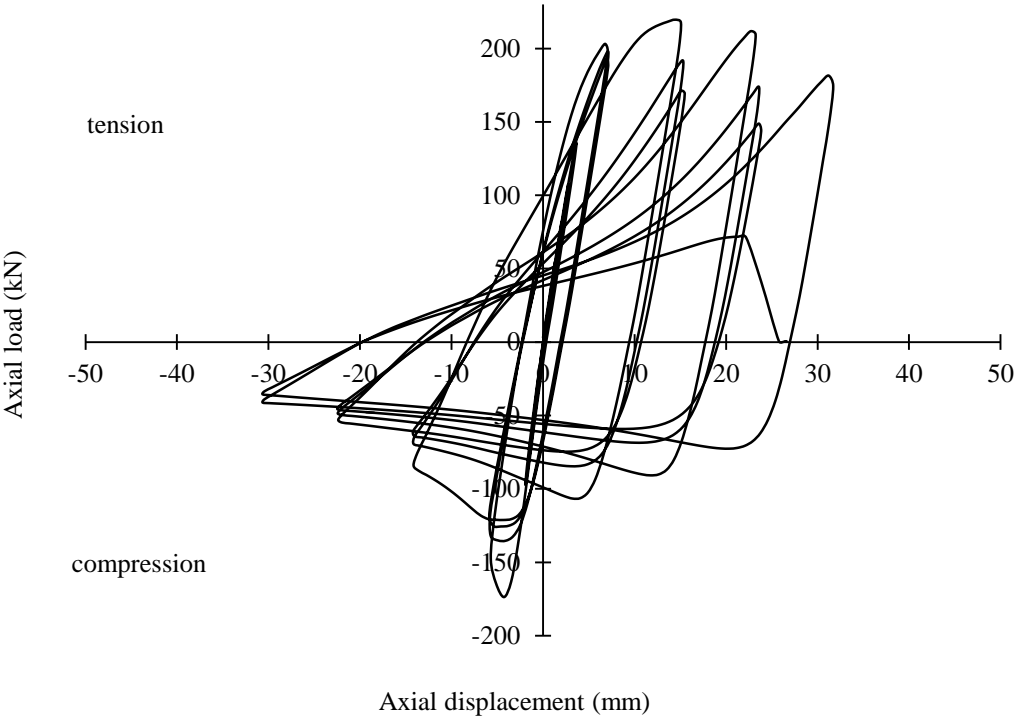


Figure 3.28 Load-displacement response for CF-F1-1500

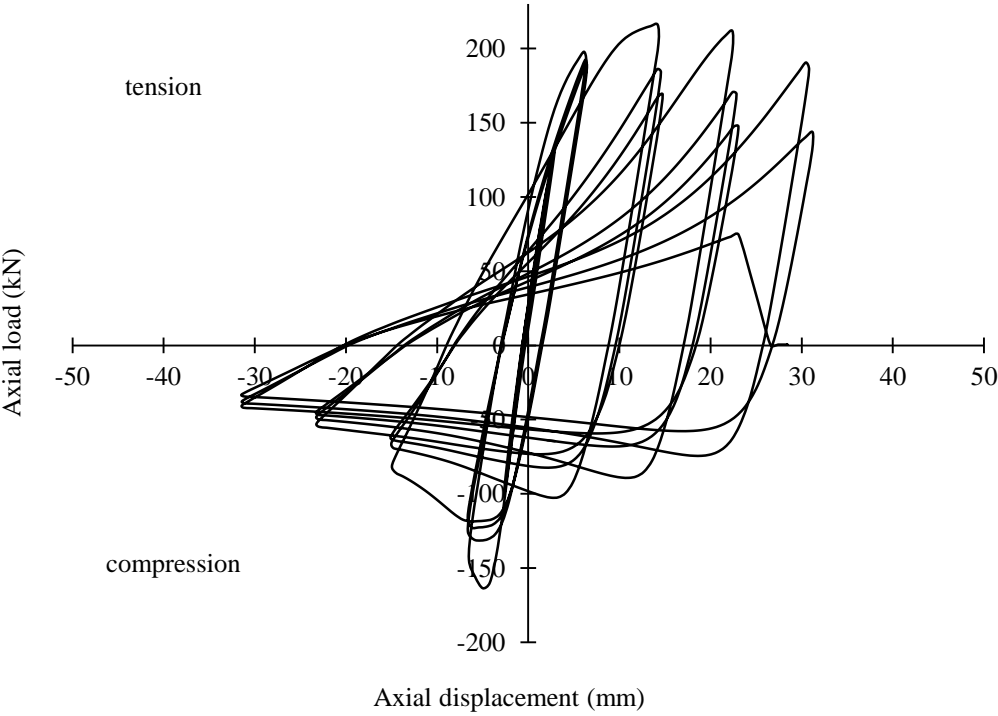


Figure 3.29 Load-displacement response for CF-F2-1500

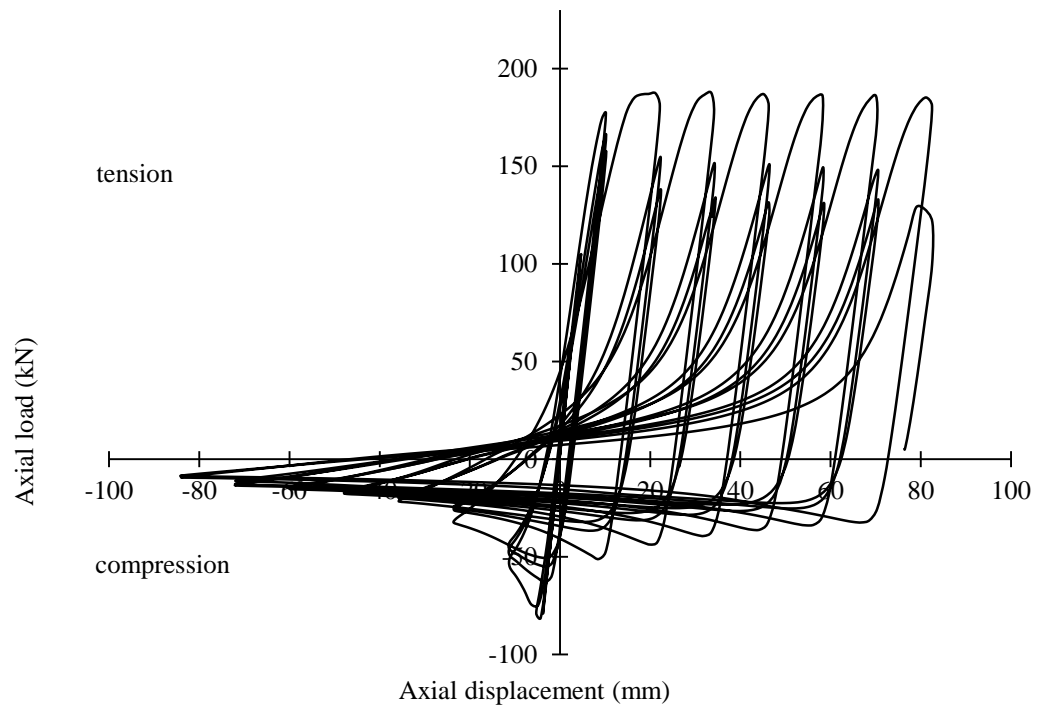


Figure 3.30 Load-displacement response for HF-H-3000

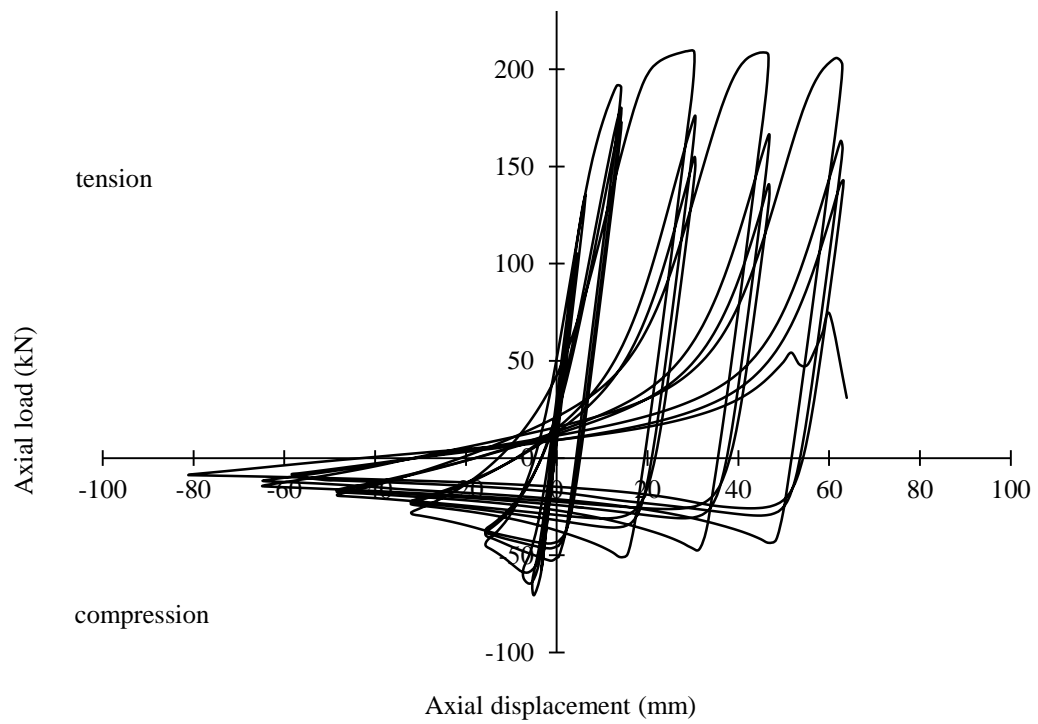


Figure 3.31 Load-displacement response for CF-H-3000

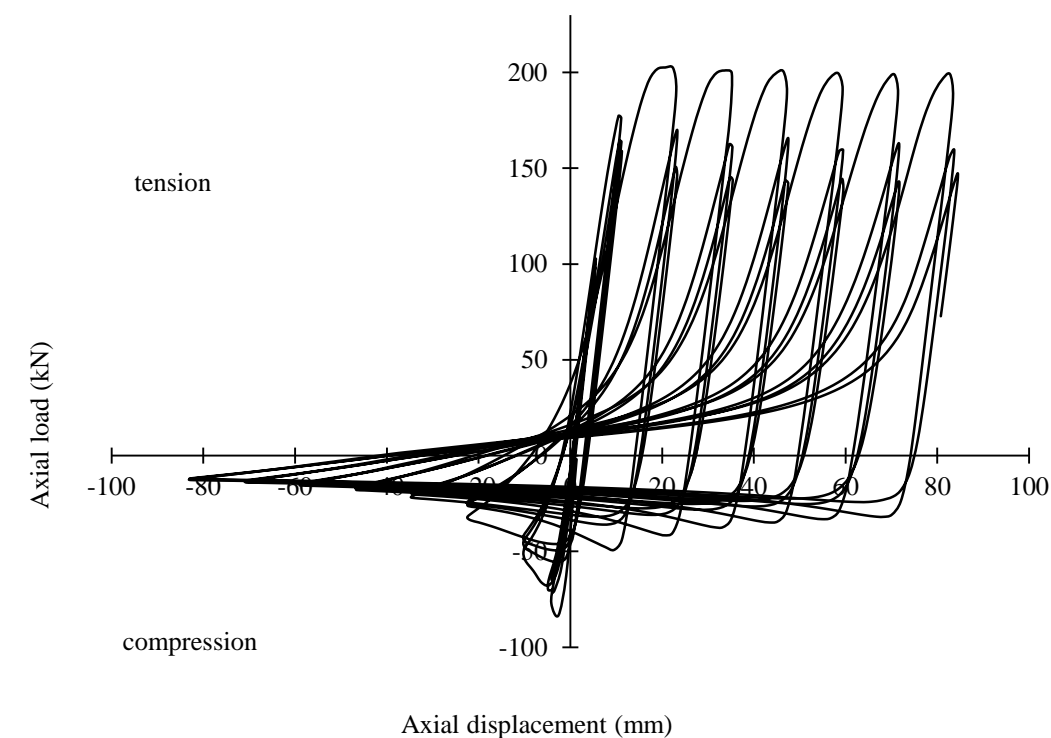


Figure 3.32 Load-displacement response for HF-F1-3000

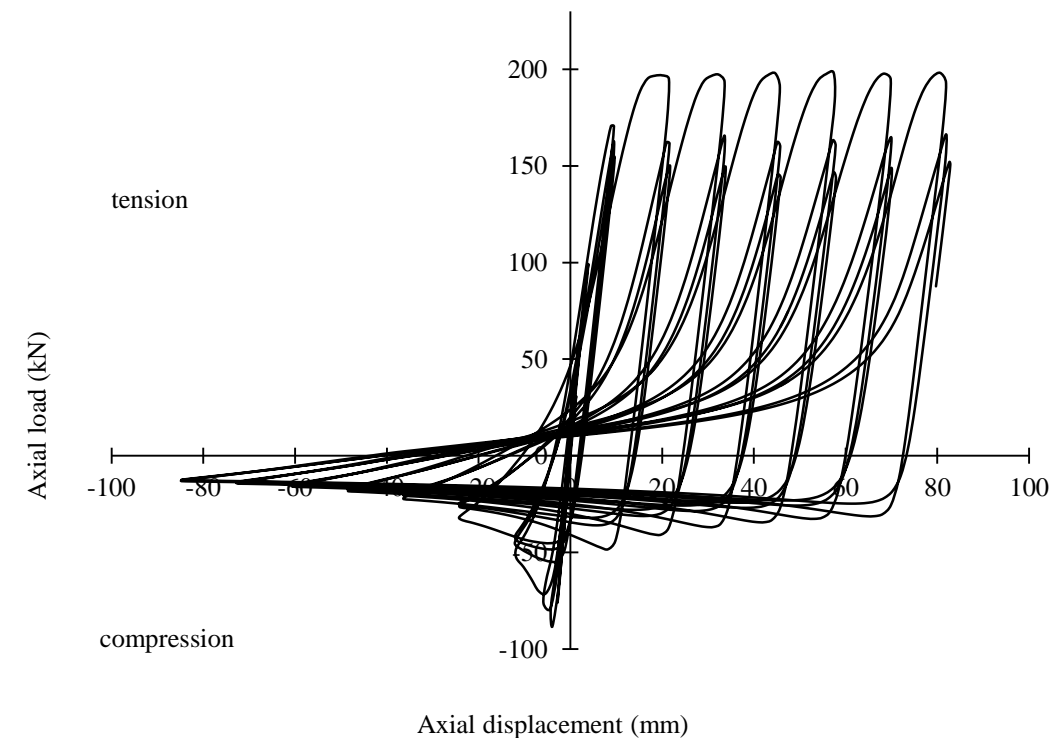


Figure 3.33 Load-displacement response for HF-F2-3000

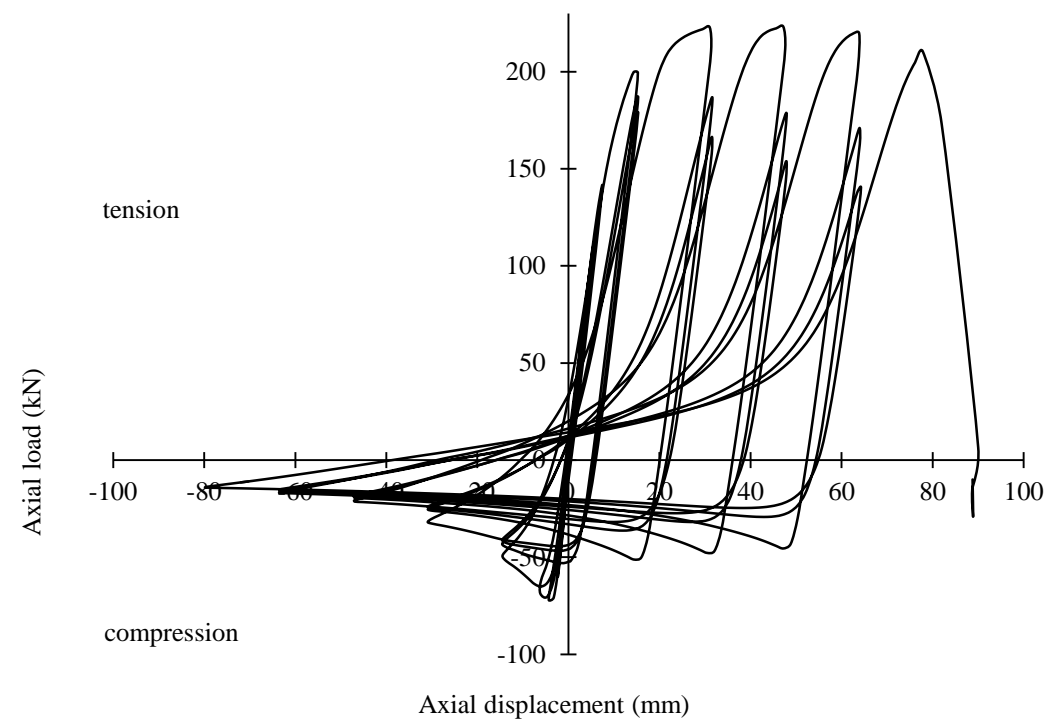


Figure 3.34 Load-displacement response for CF-F1-3000

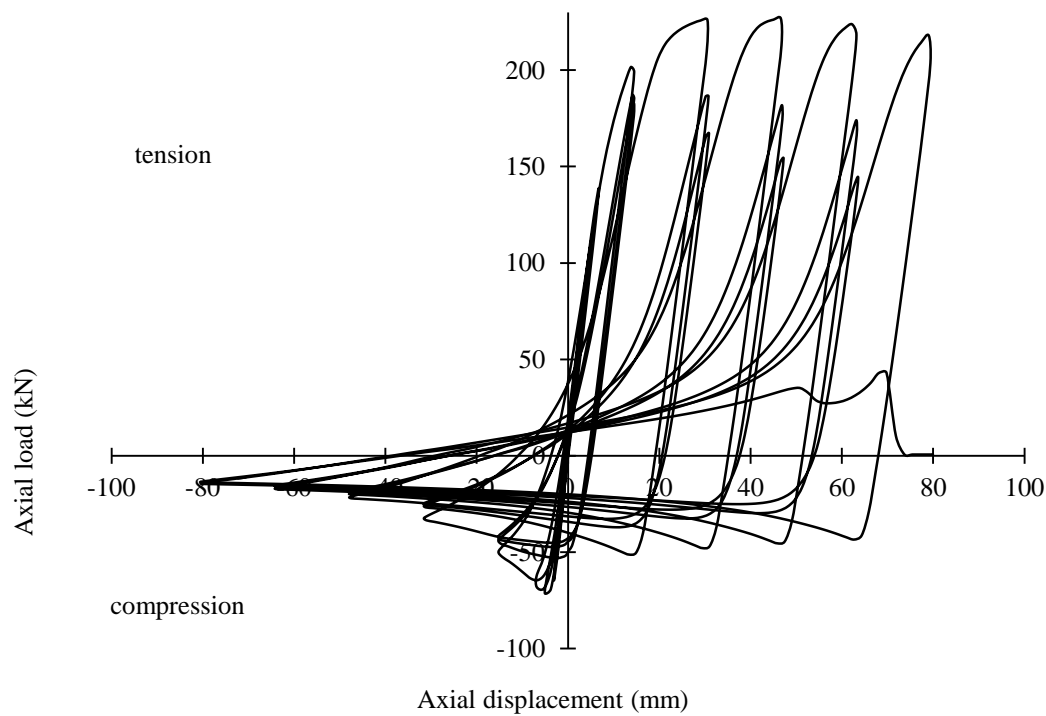


Figure 3.35 Load-displacement response for CF-F2-3000

Similar hysteresis behaviour was observed for each test specimen. Specimens exhibited high stiffness under compressive loading, followed by gradual degradation after flexural buckling. As the loading was reversed into tension, specimens initially showed low stiffness owing to straightening of the member, which had elongated in previous cycles. Points of interest in the load-displacement curves are highlighted in Figure 3.24 for specimen HF-H-1500. The locations of the maximum tensile and compressive forces and the post-buckling resistance are indicated in this figure. The maximum tensile and compressive resistances occurred during the first cycle at each amplitude, and these decreased during the second and third cycles. This is illustrated for the cycles at  $\delta/\delta_y = 8$  in Figure 3.24. The increase in length and residual out-of-straightness accounted for the apparent tensile resistance reduction in the second and third cycles at each axial displacement amplitude. The lengthening of the member in the first cycle of a particular displacement amplitude also reduced the buckling resistance in the compressive halves of the second and third cycles.

The shorter test specimens enclosed larger areas per hysteresis loop relative to  $\delta_y$  than the more slender braces. Figure 3.36 presents the load-displacement relationship during the 13<sup>th</sup> cycle for both hollow and filled cold formed tubes of each length.

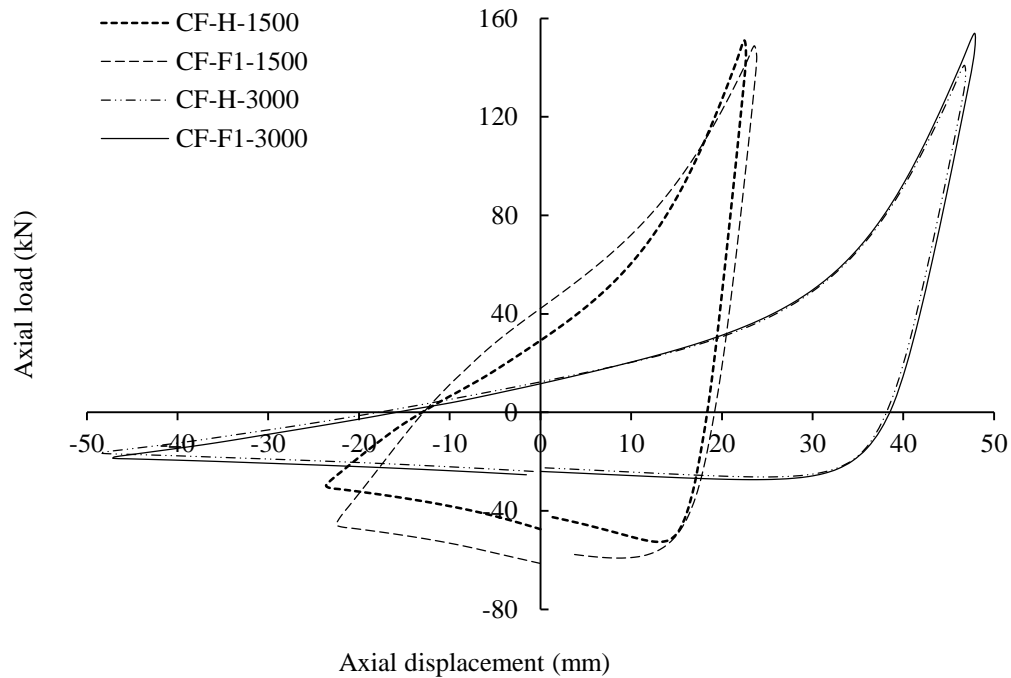


Figure 3.36 Load-displacement hysteresis loop for cold formed members in 13<sup>th</sup> cycle

Some differences were observed between the concrete-filled and hollow 1500 mm specimens, with the filled specimen hysteresis loop enclosing a greater area than the hollow one, depicting more energy dissipated per cycle. However, this was not as noticeable for the 3000 mm specimens. Furthermore, the concrete had a lesser influence on the shape of a hysteresis loop for hot-finished tubes of either length. Overall, the results indicated that the concrete infill did not greatly enhance the energy per cycle, but did increase the total energy dissipation owing to the number of additional cycles endured. Although the life of the brace was generally only prolonged by one or two cycles, the maximum energy dissipation occurred within the later cycles of each test, and thereby the concrete contribution noticeably enhanced the total accumulated energy dissipation. Table 3.10 presents the normalised energy dissipation in a number of individual test cycles in addition to the total accumulated energy dissipation.

### Chapter 3 Laboratory Experiments

Table 3.10 Energy dissipated at various stages of testing

Specimen ID	Normalised energy dissipation in			Total normalised energy dissipated
	8 <sup>th</sup> cycle	11 <sup>th</sup> cycle	14 <sup>th</sup> cycle	
HF-H-1500	5.3	6.9	8.0	59.1
CF-H-1500	5.0	6.1	2.8	33.1
HF-F1-1500	5.7	7.2	8.4	170.1
HF-F2-1500	4.2	5.8	7.1	84.4
CF-F1-1500	5.2	6.3	7.0	43.1
CF-F2-1500	5.0	6.2	7.0	48.2
HF-H-3000	3.3	3.8	4.3	61.1
CF-H-3000	3.1	3.5	3.8	26.7
HF-F1-3000	3.3	3.9	4.5	68.2
HF-F2-3000	3.3	3.9	4.6	69.9
CF-F1-3000	3.1	3.6	4.0	30.5
CF-F2-3000	3.1	3.7	4.1	32.5

Values in Table 3.10 are normalised with respect to  $W_y = f_{yd}A_a\delta_y$ , the product of the steel yield stress, cross-sectional area and yield displacement for the specimen. The energy dissipated in the 8<sup>th</sup> loading cycle (1<sup>st</sup> cycle at  $\delta/\delta_y = 4$ ) was examined by Nip *et al.* (2010a) and Goggins *et al.* (2006), since this was the cycle with the greatest degree of energy dissipation for the majority of specimens. Since the circular sections generally endured greater numbers of cycles than the rectangular sections used by Nip *et al.* (2010a) and Goggins *et al.* (2006), results are also presented in Table 3.10 for the 11<sup>th</sup> (1<sup>st</sup> cycle at  $\delta/\delta_y = 6$ ) and 14<sup>th</sup> (1<sup>st</sup> cycle at  $\delta/\delta_y = 8$ ) cycles, in addition to the total accumulated energy. Energy dissipation for each specimen decreased in the cycle prior to failure, which was the case for specimen CF-H-1500 (second row of Table 3.10) in the 14<sup>th</sup> cycle. The differences in accumulated energy dissipation between hot-finished and cold formed, filled and hollow specimens, are shown in Figures 3.37 and 3.38 for 1500 mm and 3000 mm long braces respectively.



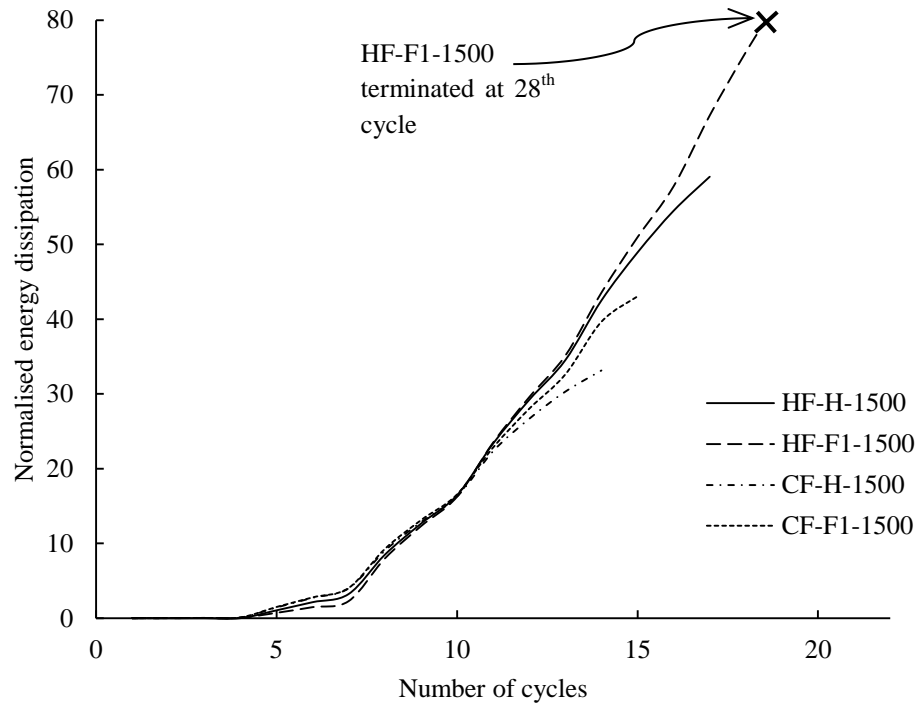


Figure 3.37 Accumulated energy dissipation for 1500 mm specimens

Up to the 10<sup>th</sup> cycle, little difference was apparent but results diverged during the later cycles. For both specimen lengths, the hot-finished tubes dissipated a greater amount of energy than the cold formed tubes. HF-F1-1500 and CF-F1-1500 showed superior energy dissipation to HF-H-1500 and CF-H-1500 respectively in the later stages of the test. Differences between hollow and filled specimens were almost negligible at 3000 mm, which is reflected in Figure 3.38.

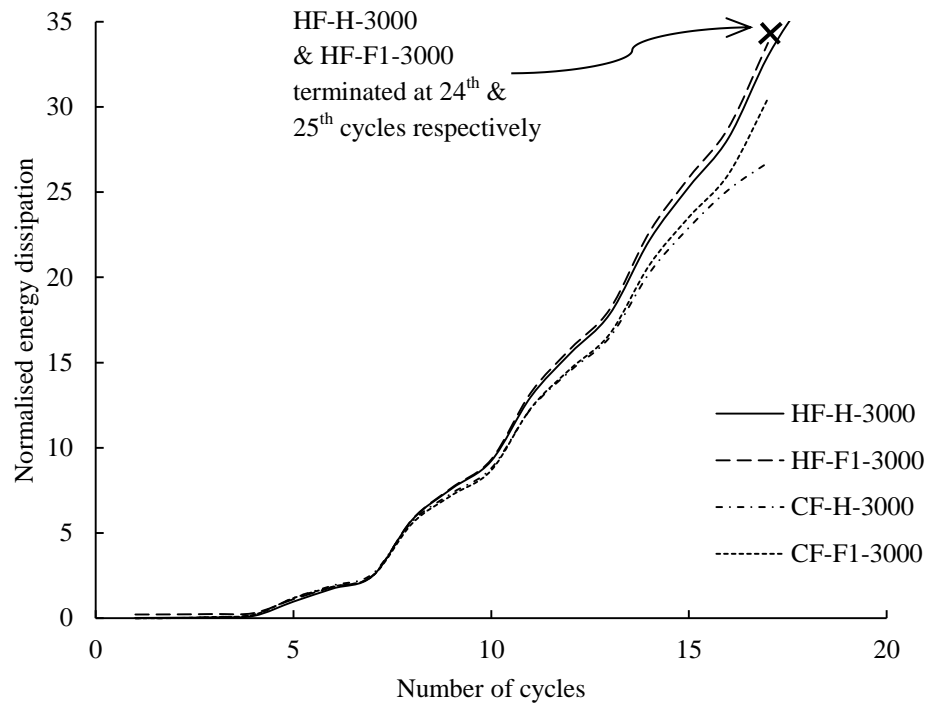


Figure 3.38 Accumulated energy dissipation for 3000 mm specimens

### 3.4.9 Lateral displacements

Another significant parameter is the lateral displacement of the brace at the mid-height, since excessive deformations can cause damage to surrounding structural and non-structural components. The relationship between axial load and lateral displacement at the mid-height is presented in Figures 3.39 and 3.40. Under cycles of increasing axial displacement the member elongated and so in every cycle there was a residual lateral displacement at the original ‘zero displacement’ position as the load changed from compression to tension.

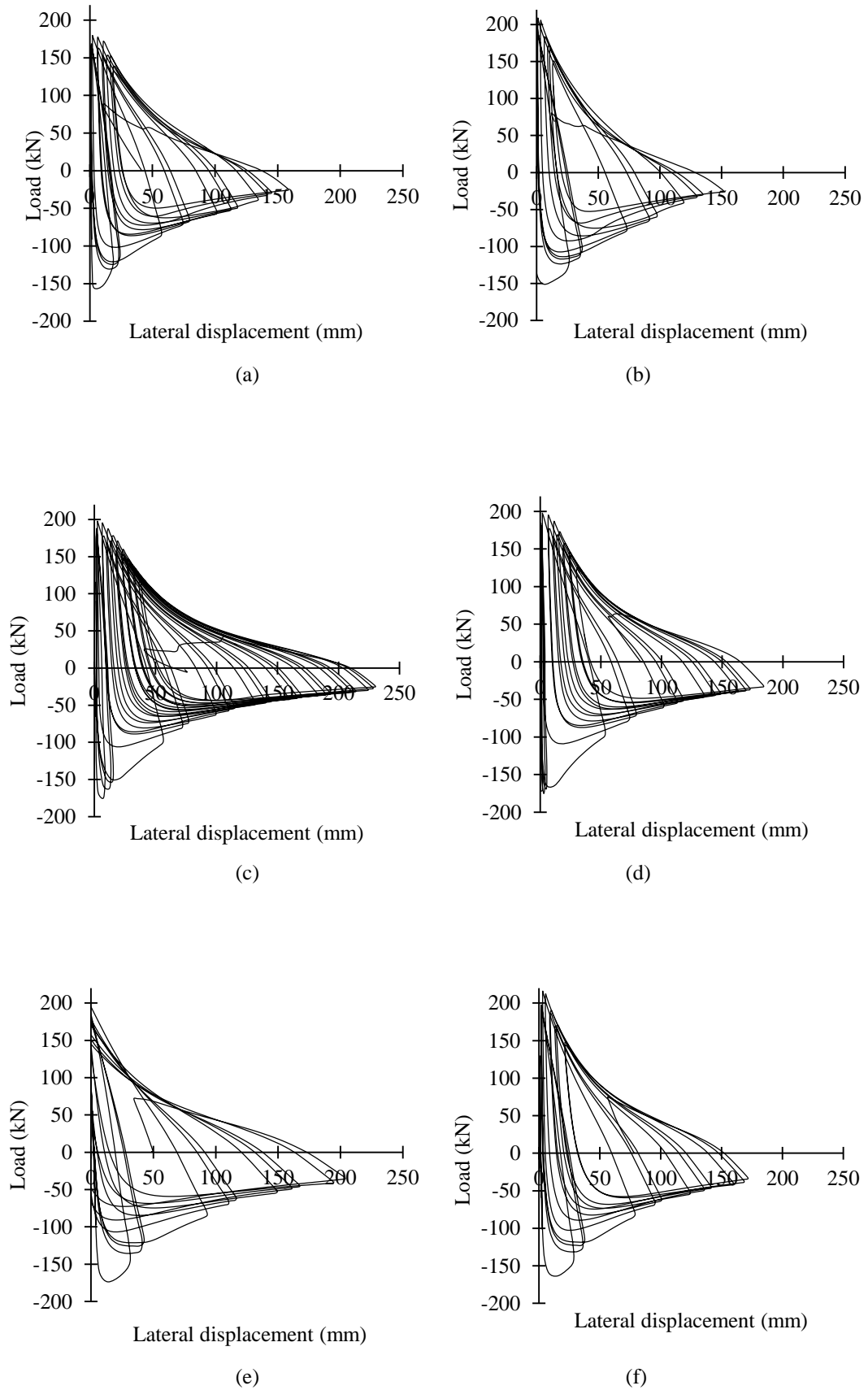


Figure 3.39 Relationship between axial load and lateral displacement at the mid-height for specimen (a) HF-H-1500; (b) CF-H-1500; (c) HF-F1-1500; (d) HF-F2-1500; (e) CF-F1-1500; (f) CF-F2-1500

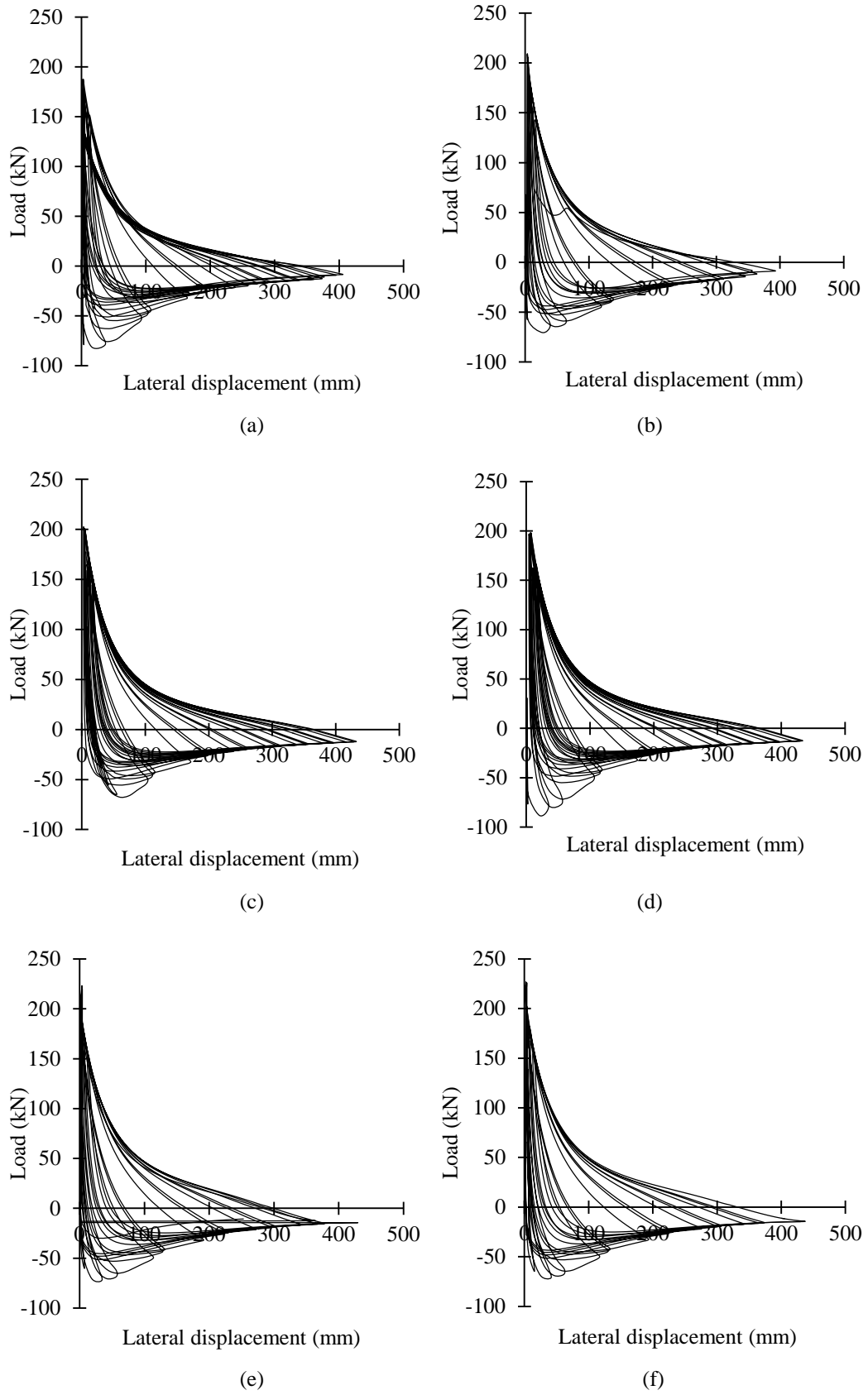


Figure 3.40 Relationship between axial load and lateral displacement at the mid-height for specimen (a) HF-H-3000; (b) CF-H-3000; (c) HF-F1-3000; (d) HF-F2-3000; (e) CF-F1-3000; (f) CF-F2-3000

Tremblay (2002) derived formulae for predicting the lateral displacement for both low and high displacement ductilities. Under low axial displacement, the response of the brace was assumed to be elastic and the deformed shape was described by a sinusoidal wave function, in the form of

$$y = \frac{\Delta}{2} \left( 1 - \cos \frac{2\pi x}{L} \right) \quad (3.11)$$

where  $L$  is the original length of the brace, the wave amplitude is  $\Delta/2$  and the period is equal to  $2\pi$ . The geometry of the brace is shown in Figure 3.41(a) and the constituents of the wave function are presented in Figure 3.41(b).

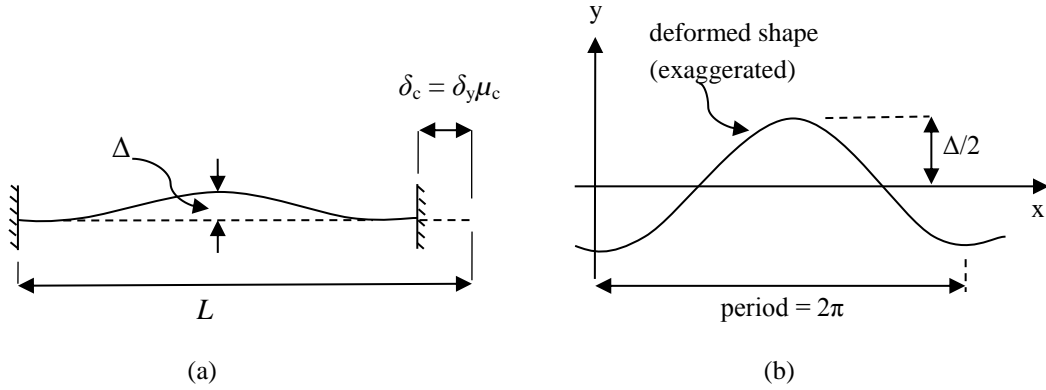


Figure 3.41 Lateral displacement at brace mid-height for low axial displacements: (a) geometry of deformed member; (b) assumed sinusoidal function

Assuming that the brace is incompressible the axial compressive displacement undergone in a particular cycle,  $\delta_c$ , can be related to the deformed shape and lateral displacement by:

$$\delta_c = \int_0^L \frac{1}{2} \left( \frac{dy}{dx} \right)^2 dx \quad (3.12)$$

Inserting for  $dy/dx$  using Equation (3.11) and integrating the Equation (3.12) provides Equation (3.13) to predict the lateral displacement at the mid-height,  $\Delta$ . This is related to the axial compressive displacement,  $\delta_c$ , and the brace length,  $L$ .

$$\Delta = \frac{2}{\pi} \sqrt{\delta_c L} \quad (3.13)$$

This expression does not take into account the permanent axial deformation resulting from the previous cycles however and thus Tremblay (2002) proposed a modified version of Equation (3.13) to take this into account, given as

$$\Delta = \frac{2}{\pi} \sqrt{(\mu_c - \mu_t - 1) \delta_y L} \quad (3.14)$$

where  $\mu_c$  and  $\mu_t$  refer to the compressive displacement ductility of the cycle in question and the tensile displacement ductility of the previous half-cycle respectively.

For higher axial displacements the deformed shape approaches that of a plastic mechanism as shown in Figure 3.42.

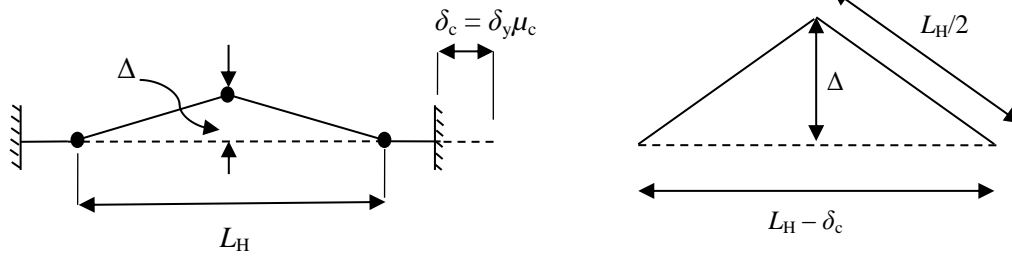


Figure 3.42 Assumed geometry for plastic mechanism of brace

In this case, the length,  $L_H$  refers to the distance between the plastic hinges near the brace ends. These were assumed to occur at a distance equal to the cross-section diameter from the end of the brace, following from the observations of Tremblay (2002). Applying Pythagoras' Theorem and omitting the  $\delta_c^2$  term (small axial displacements) the lateral displacement at the mid-length was related to  $L_H$  and  $\delta_c$  by

$$\Delta = \frac{1}{\sqrt{2}} \sqrt{\delta_c L_H} . \quad (3.15)$$

Similarly to the elastic response case, the lateral displacement prediction for the plastic hinge response needs to take into account the permanent elongations from previous cycles and hence can be modified to:

$$\Delta = \frac{1}{\sqrt{2}} \sqrt{(\mu_c - \mu_t - 1) \delta_y L_H} \quad (3.16)$$

Equations (3.14) and (3.16) were proposed to be lower and upper bounds to the lateral displacement at the mid-length, since as the applied loading protocol progresses, the brace undergoes global buckling at a relatively early stage but does not fully achieve the idealised geometry of the plastic mechanism prior to fracture. An alternative approach to that of Tremblay (2002) is to directly derive an equation for the lateral displacement using experimental data, which could capture the ‘intermediate’ behaviour between the two idealised situations envisaged by Tremblay (2002). Shaback and Brown (2003) proposed an empirically generated expression to cover the full range of displacement ductilities and this is given by (3.17).

$$\frac{\Delta}{L} (\%) = -\frac{1}{9} (\mu)^{1.9} + 2\mu \quad (3.17)$$

Following the approach of Shaback and Brown (2003), expressions were developed in this thesis using the laboratory test results, to provide reliable predictions for the lateral displacement of hollow and concrete-filled CHS braces. The first group of specimens to be considered were the 1500 mm hot-finished braces. Figure 3.43 depicts the maximum lateral displacement which occurred in the third cycle at each displacement amplitude.

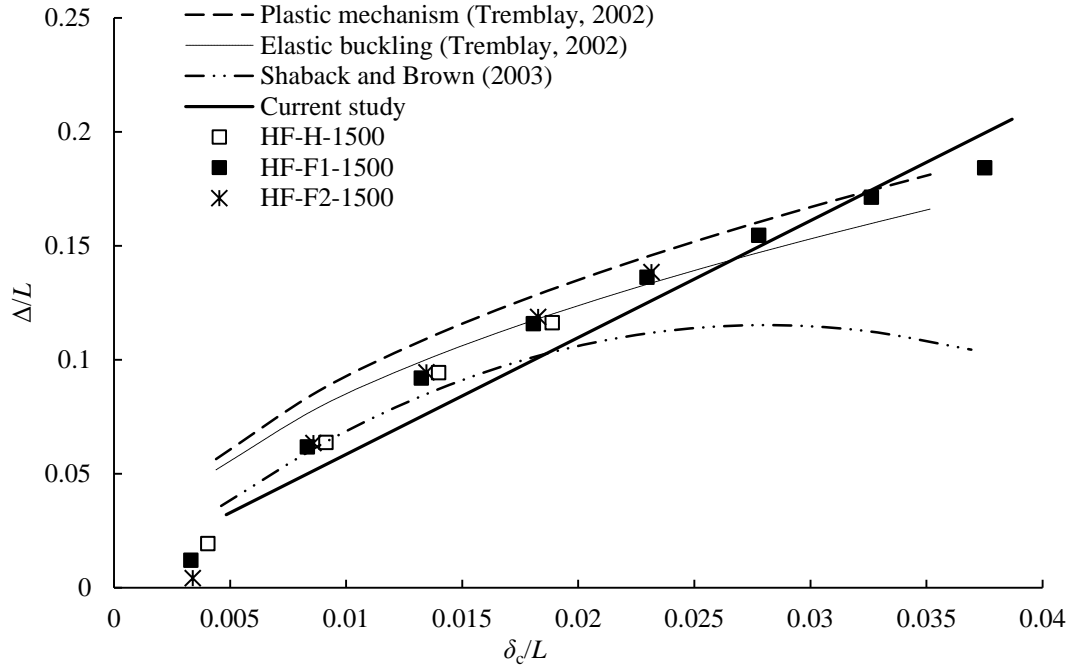


Figure 3.43 Lateral deflections for 1500 mm hot-finished braces in 3<sup>rd</sup> cycle of each amplitude

The predictions resulting from Equations (3.14) and (3.16) (Tremblay, 2002) and from Equation (3.17) (Shaback and Brown, 2003) are plotted in Figure 3.43. The vertical axis represents the lateral displacement at the mid-height,  $\Delta$ , normalised with respect to the brace length,  $L$ . The horizontal axis represents the corresponding axial compressive displacement,  $\delta_c$ , normalised with respect to  $L$ . A best-fit line was plotted through the data points for HF-H-1500, HF-F1-1500 and HF-F2-1500. Under low axial displacements, the predictions of Tremblay (2002) and Shaback and Brown (2003) overestimated the lateral displacement. As  $\delta_c$  increased,  $\Delta$  surpassed the prediction of Shaback and Brown (2003) for rectangular sections and approached the proposed upper bound of Tremblay (2002) (Equation 3.16). The application of this upper bound seemed feasible based on the results in Figure 3.43. However, the suggested ‘lower bound’ proved to be less effective since the predictions exceeded the observed lateral displacements for all axial displacements less than  $10\delta_y$  (axial displacement/length = 0.023). None of the previously proposed expressions given in



Figure 3.43 can capture the lateral displacement of the CHS braces over the full range of axial displacements. The observed discrepancies provided the motivation to develop an expression for the mid-height lateral deflection of circular hollow section braces, using the available test data. The best-fit line presented in Figure 3.43 has a coefficient of variation equal to 0.013 and is expressed as

$$\frac{\Delta}{L}(\%) = 1.24\mu_{\Delta} + 0.72 \quad (3.18)$$

From a visual inspection it appeared that an improved correlation could be achieved using a higher order polynomial in terms of  $\mu_{\Delta}$  and hence the following was proposed for comparison.

$$\frac{\Delta}{L}(\%) = -0.07\mu_{\Delta}^2 + 2.36\mu_{\Delta} + 2.75 \quad (3.19)$$

Equation (3.19) is plotted in Figure 3.44, along with the test results and the predictions of Tremblay (2002) and of Shaback and Brown (2003).

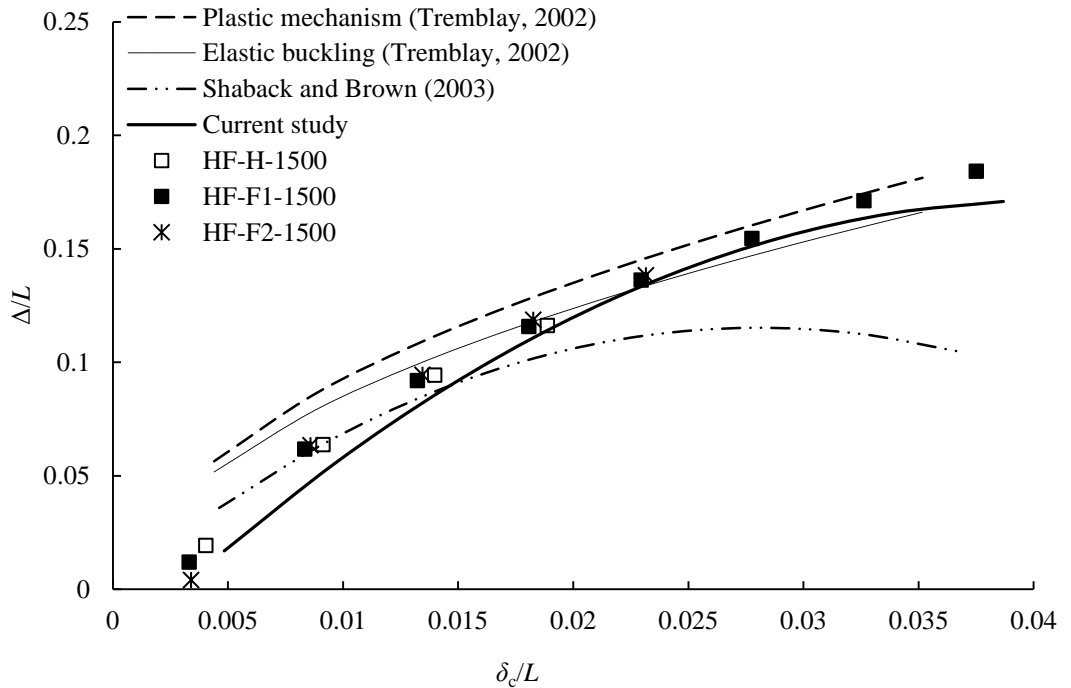


Figure 3.44 Lateral deflections for hot-finished 1500 mm specimens in the 3<sup>rd</sup> cycle at each displacement amplitude with proposed second order polynomial, Equation (3.19)

From Figure 3.44 it is evident that the second order polynomial proposed in this study shows a better overall correlation to the test data than both the linear expression and the previous predictions. The relationship between the predicted lateral displacements and actual lateral displacements for both the linear expression and second order equation are presented in Figures 3.45 and 3.46. Visual inspection of these confirms the superiority of Equation (3.19), with coefficient of variation equal to 0.0061 (compared with to 0.013 for Equation (3.18), as stated previously).

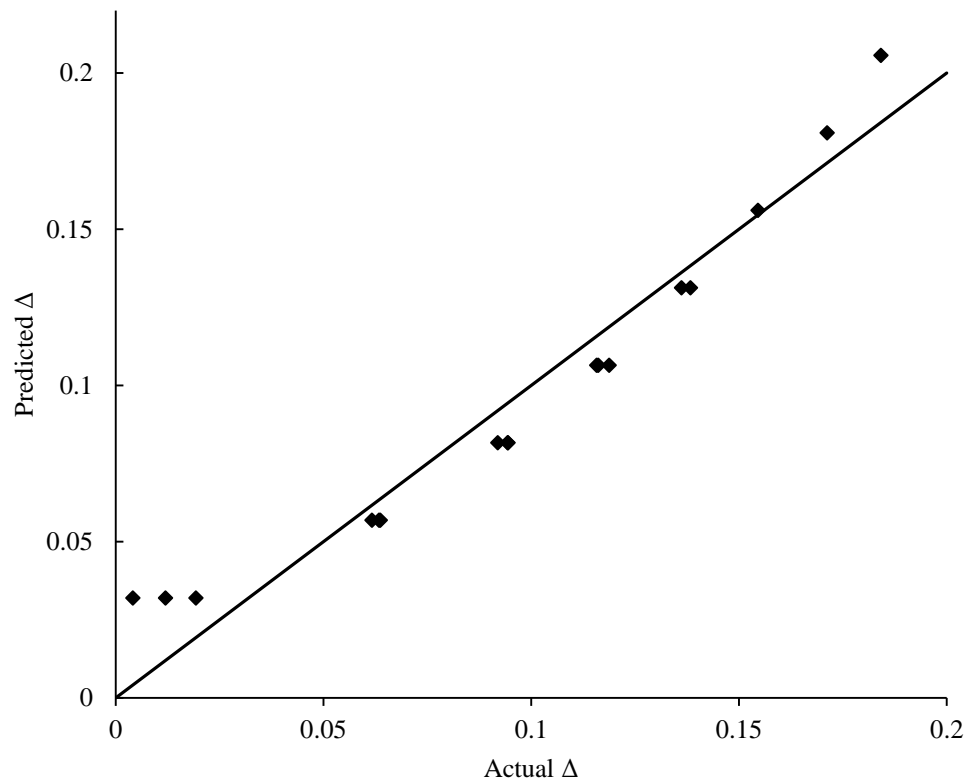


Figure 3.45 Relationship between predicted and actual mid-height lateral deflections for 1500 mm hot-finished specimens using Equation (3.18)

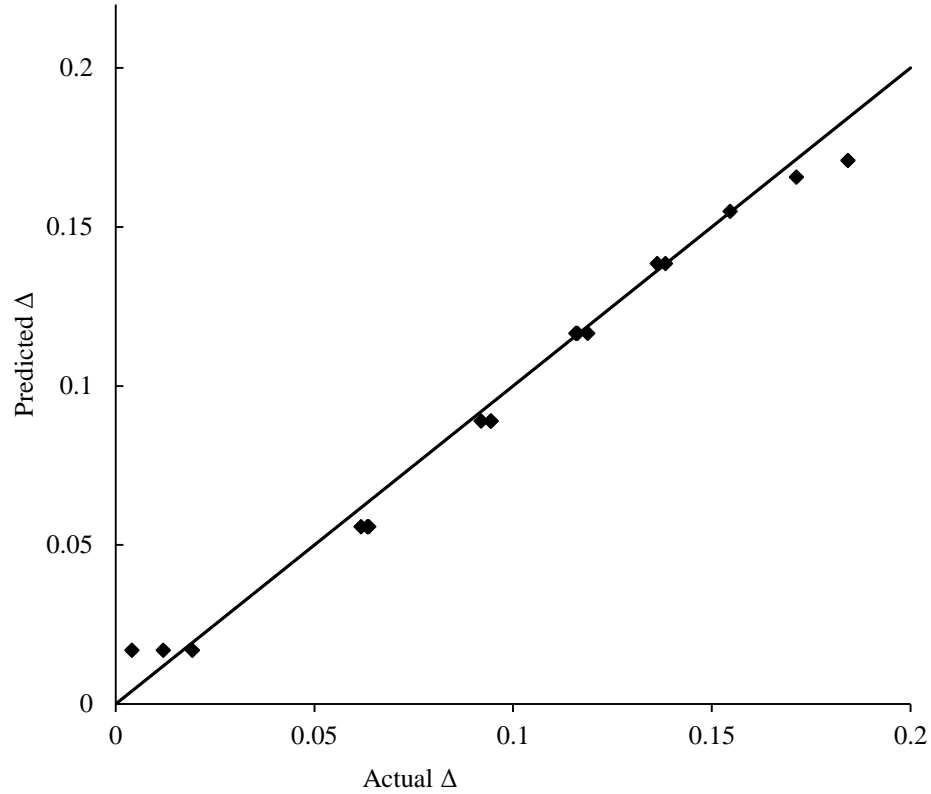


Figure 3.46 Relationship between predicted and actual mid-height lateral deflections for 1500 mm hot-finished specimens using Equation (3.19)

A similar approach was then taken for predicting the lateral displacements of the 3000 mm hot-finished braces, given by the following two expressions:

$$\frac{\Delta}{L}(\%) = 0.93\mu_{\Delta} + 3.3 \quad (3.20)$$

$$\frac{\Delta}{L}(\%) = -0.04\mu_{\Delta}^2 + 1.53\mu_{\Delta} + 1.53 \quad (3.21)$$

Again, a linear expression (Equation 3.20) and second order expression (Equation 3.21) were compared in order to find a suitable prediction. These equations are plotted in Figures 3.47 and 3.48 along with the test data.

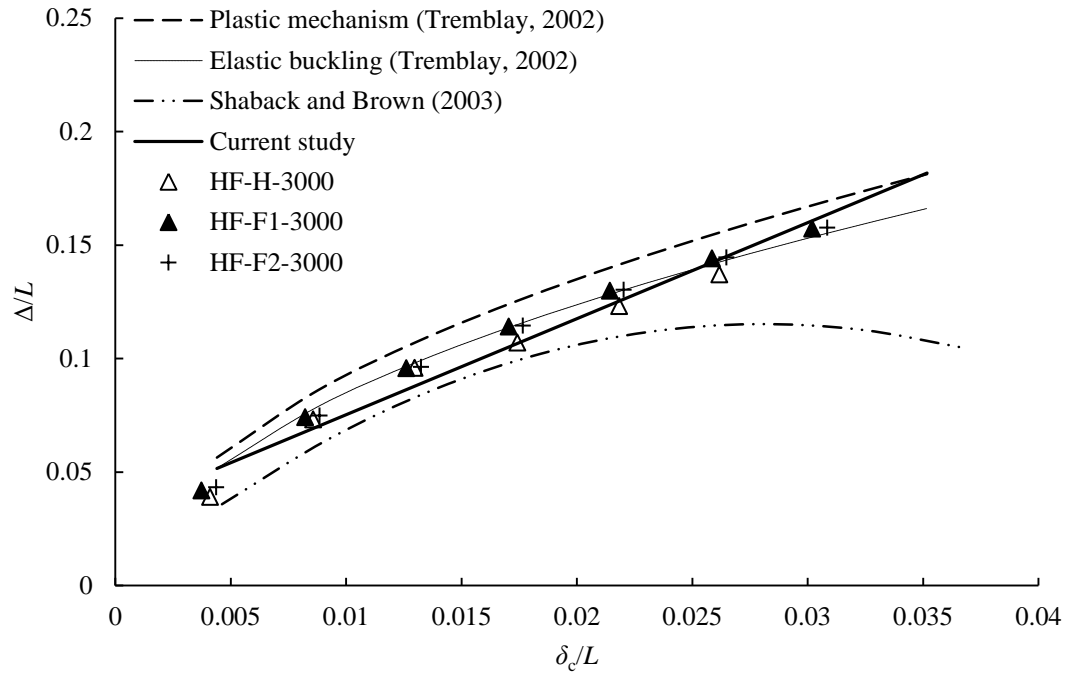


Figure 3.47 Lateral mid-height deflections for hot-finished 3000 mm specimens in the 3<sup>rd</sup> cycle at each displacement amplitude with linear predictive expression (3.20)

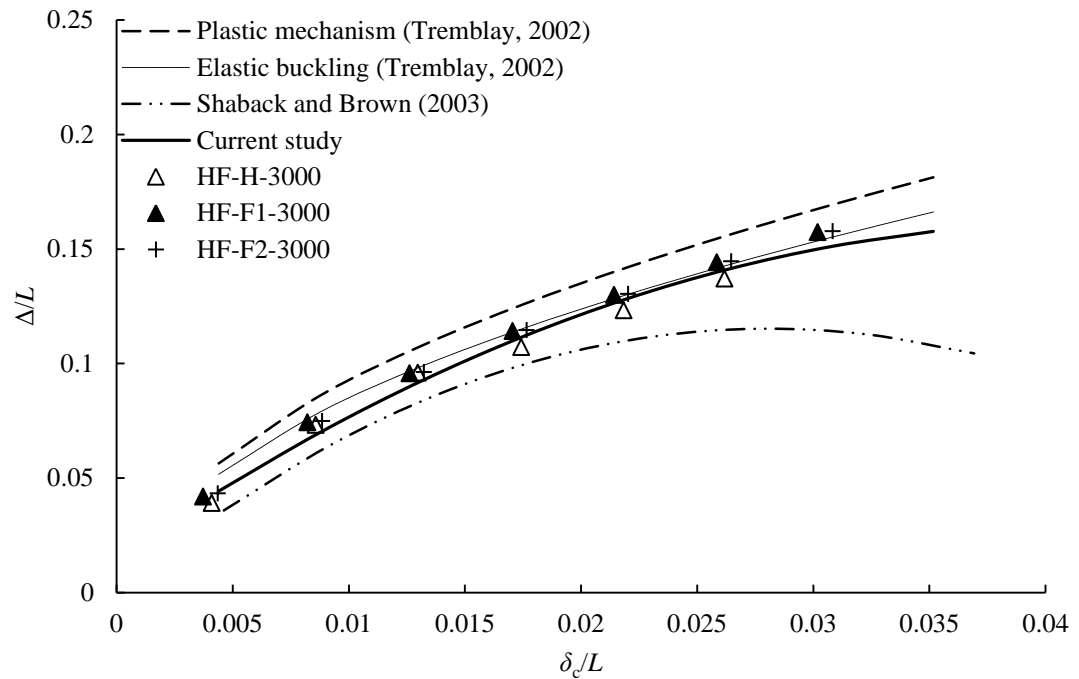


Figure 3.48 Lateral mid-height deflections for hot-finished 3000 mm specimens in the 3<sup>rd</sup> cycle at each displacement amplitude with second order predictive expression (3.21)

Similarly to the shorter hot-finished specimens, Equation (3.21) is capable of following the curved trend of the test-data. Equation (3.20) oversimplifies the relationship however, as demonstrated in Figure 3.47. Equation (3.21), plotted in Figure 3.48, lies between the predictions of Tremblay (2002) and Shaback and Brown (2003) for all values of axial displacement. The relationship between predicted and actual lateral displacements using Equations (3.20) and (3.21) are presented in Figures 3.49 and 3.50. The reliability of the second order polynomial is demonstrated here. The coefficients of variation for Equations (3.20) and (3.21) are 0.0063 and 0.0039.

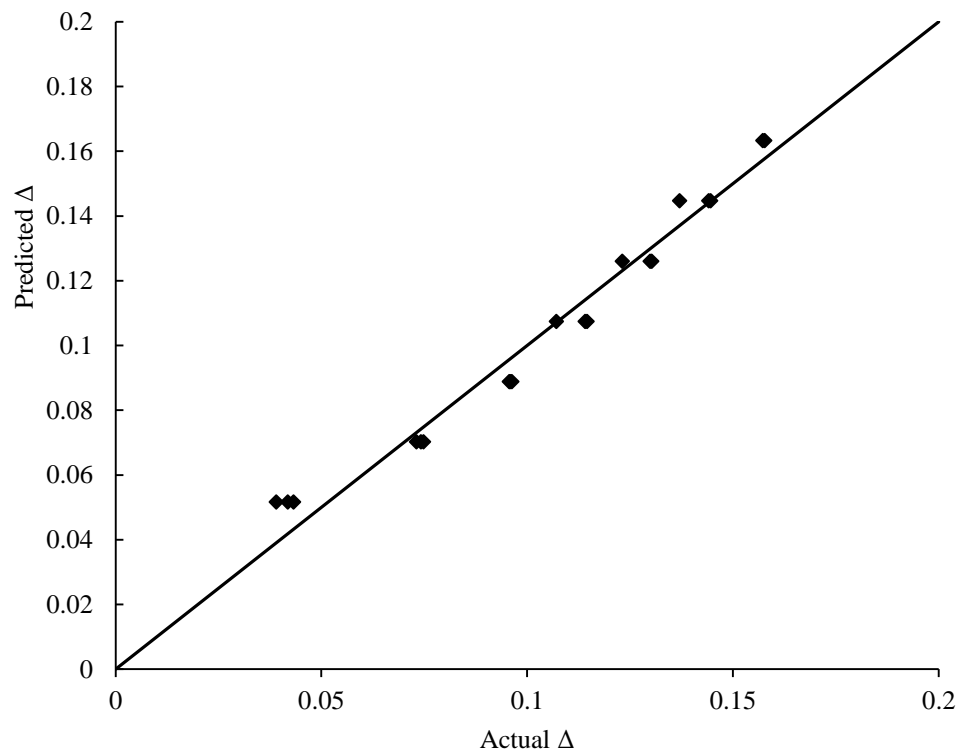


Figure 3.49 Relationship between predicted and actual mid-height lateral deflections for 3000 mm hot-finished specimens using Equation (3.20)

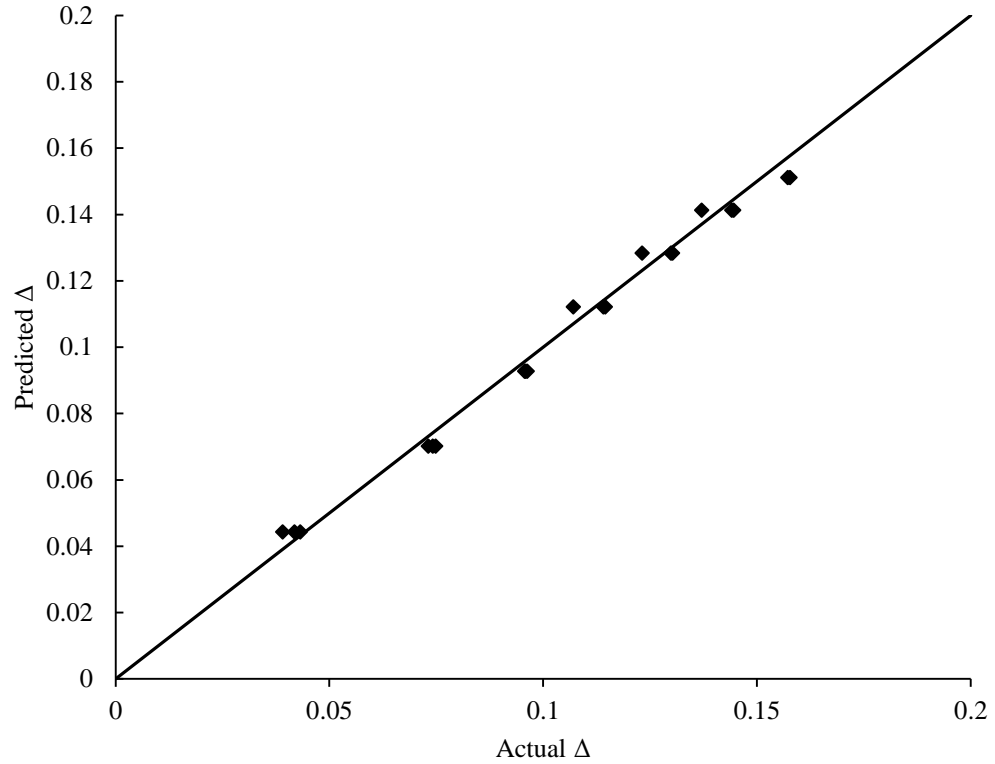


Figure 3.50 Relationship between predicted and actual mid-height lateral deflections for 3000 mm hot-finished specimens using Equation (3.21)

Since only two bracing lengths were used in the experiments and any length could be used in reality, it was decided to derive a single expression combining both lengths, which could be extended to any particular member slenderness. Combining all of the data led to the following equation:

$$\frac{\Delta}{L}(\%) = -0.05\mu_{\Delta}^2 + 1.88\mu_{\Delta} - 0.41 \quad (3.22)$$

This combined proposal is compared in Figure 3.51 with the test data and the predictions of Tremblay (2002) and Shaback and Brown (2003).

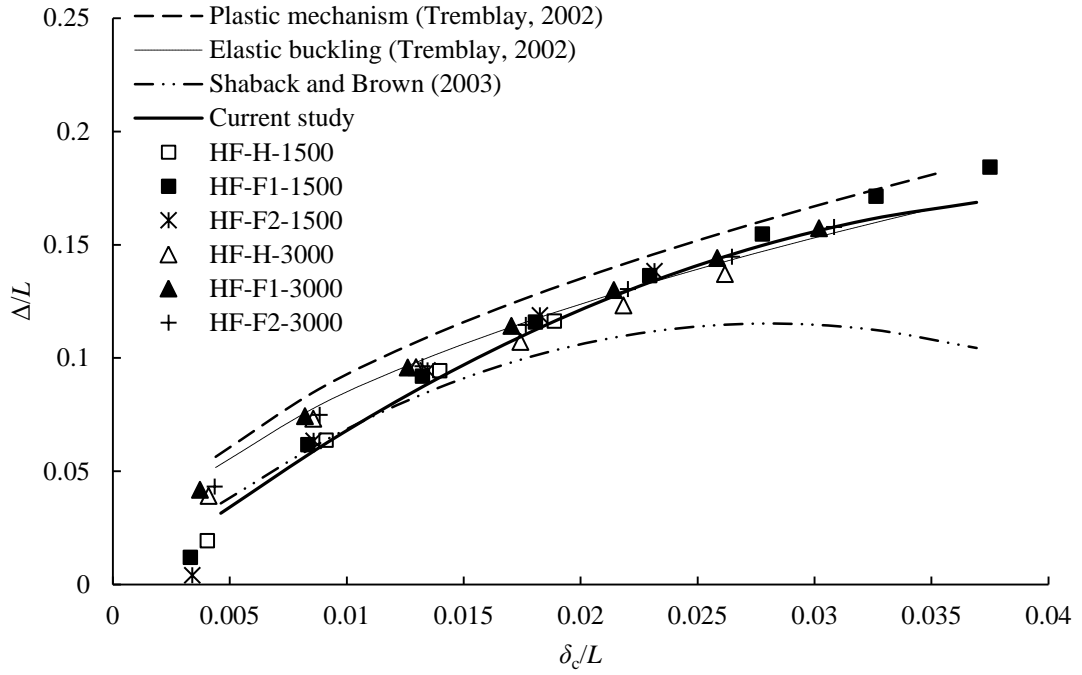


Figure 3.51 Lateral mid-height deflections for hot-finished specimens of all lengths in the 3<sup>rd</sup> cycle of each displacement amplitude

The lateral displacements observed in the experiments for 1500 mm and 3000 mm members varied significantly under low axial displacements. Under these conditions the predictions of this study provide a reasonable average between the test data of the 1500 mm and 3000 mm long test specimens. The lateral displacement predictions computed from Tremblay (2002) and Shaback and Brown (2003) greatly exceeded those which occurred in the 1500 mm brace experiments. The normalised lateral deflections from the test data, for each brace length, tended to converge for higher axial displacements. In this axial displacement range Equation (3.22) continued to show good agreement and hence it gave a better estimation overall than the predictions from previous researchers. The relationship between predicted displacement and actual lateral displacement for this combined expression is presented in Figure 3.52. Although the correlation is not as close as that of the individual expressions, Equation (3.22) still provides a reliable estimation of the lateral deflection at the mid-height, with a coefficient of variation equal to 0.0089.

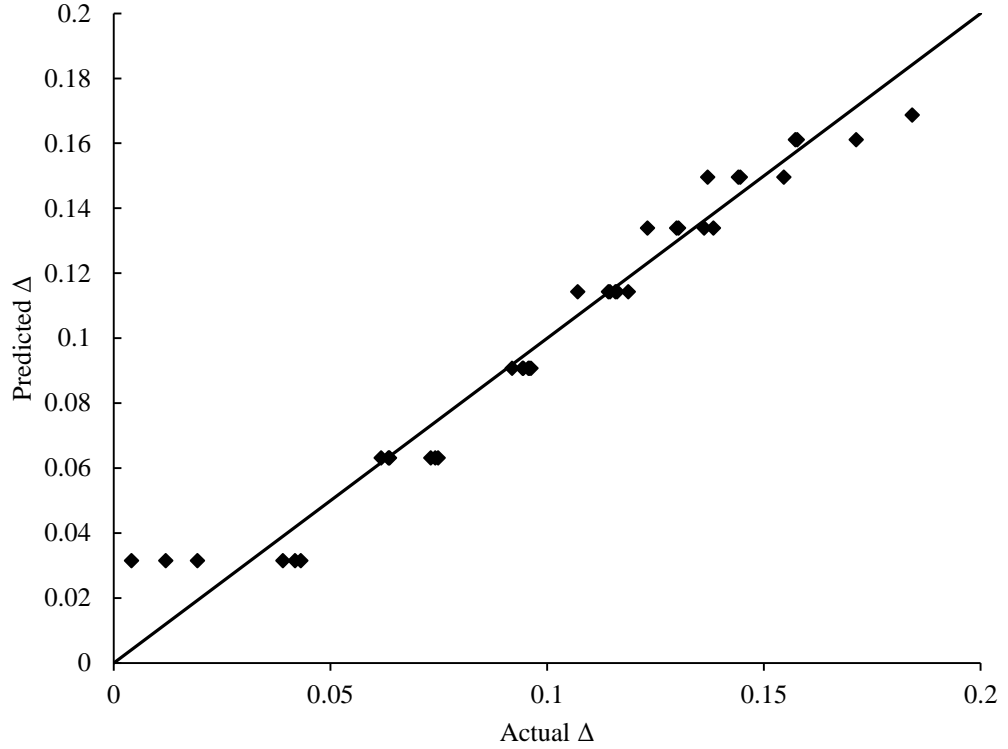


Figure 3.52 Relationship between predicted and actual mid-height lateral deflections for hot-finished specimens using Equation (3.22)

Separate equations were developed to predict the lateral displacement of cold formed braces. As mentioned previously, the longer cold formed braces exhibited significant deflections in the direction of the stiffened plane (relating to the welded end-stiffeners) in addition to the unstiffened direction. Hence for this study, the resultant displacement from these two components was taken as the lateral displacement. Expressions (3.23) and (3.24) were proposed separately to predict the lateral displacement of the 1500 mm and 3000 mm braces respectively. These figures are plotted with the test data in Figures 3.53 and 3.54.

$$\frac{\Delta}{L}(\%) = -0.21\mu_{\Delta}^2 + 3.87\mu_{\Delta} - 3.76 \quad (3.23)$$

$$\frac{\Delta}{L}(\%) = -0.08\mu_{\Delta}^2 + 2.25\mu_{\Delta} - 0.72 \quad (3.24)$$



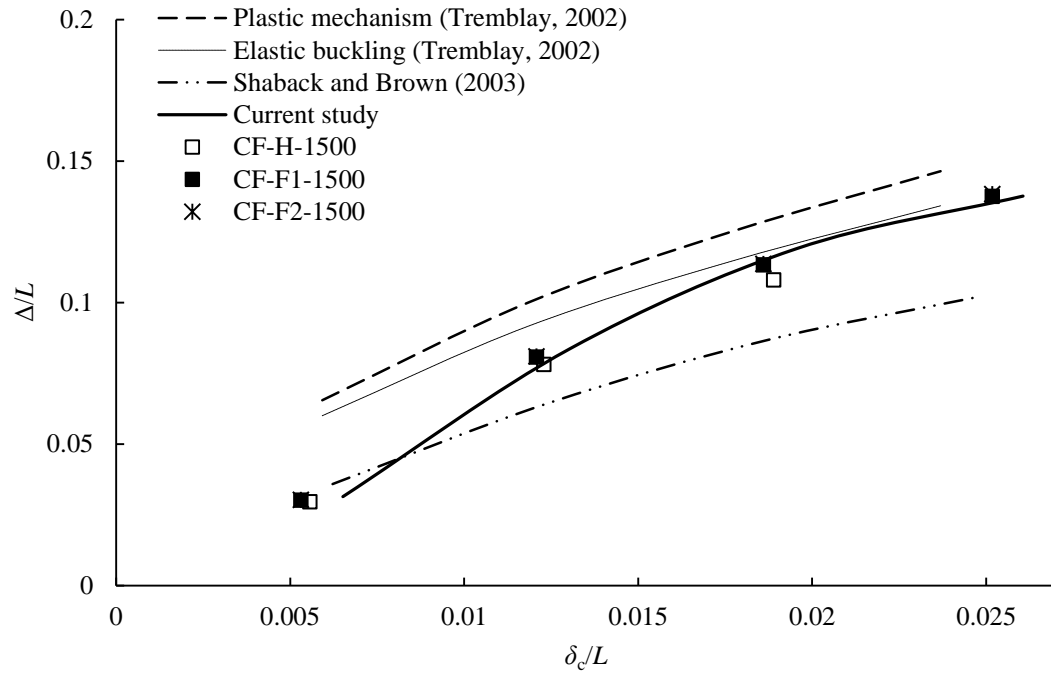


Figure 3.53 Lateral mid-height deflections for cold formed 1500 mm specimens in the 3<sup>rd</sup> cycle of each displacement amplitude

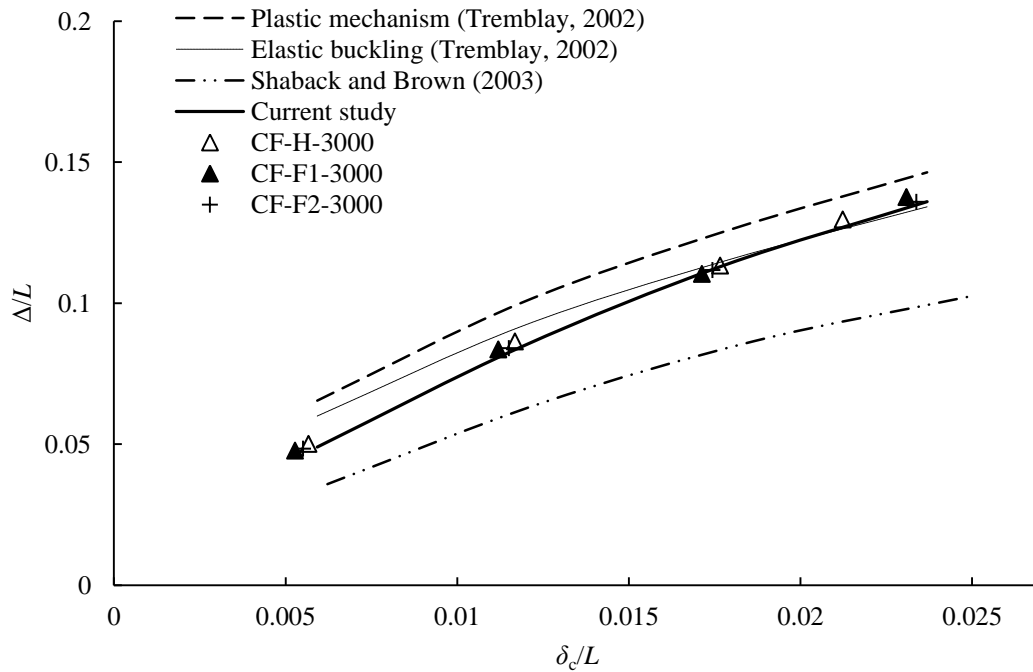


Figure 3.54 Lateral mid-height deflections for cold formed 3000 mm specimens in the 3<sup>rd</sup> cycle of each displacement amplitude

For each member length, the proposed expression provided a good fit to the test data, and was more reliable overall than the other predictions. The combined expression was proposed to account for cold formed members of all global slenderness values.

$$\frac{\Delta}{L}(\%) = -0.15\mu_{\Delta}^2 + 3.1\mu_{\Delta} - 0.157 \quad (3.25)$$

Equation (3.25) is plotted in Figure 3.55 with the test data and the predictions of Tremblay (2002) and Shaback and Brown (2003).

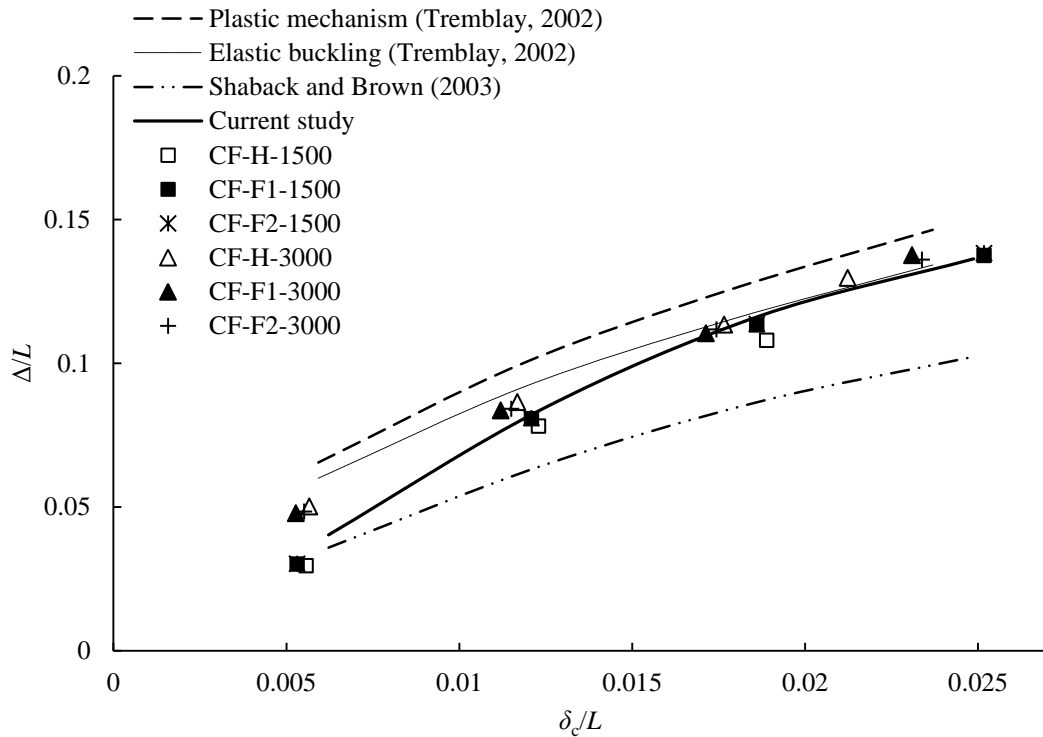


Figure 3.55 Lateral mid-height deflections for cold formed specimens of all lengths in the 3<sup>rd</sup> cycle of each displacement amplitude

Similarly to the case of the hot-finished braces, there was a sizeable variation across the data for low values of axial displacement, which diminished under greater displacement amplitudes. Consequently it would not be possible to cover members of all global slenderness ranges with one governing equation but the proposed expression in Equation (3.25) should provide a good estimation nonetheless. The

largest discrepancies occurred for the lower axial displacement values which would not be as critical from the designer's perspective. The differences in behaviour between members of various lengths suggest that with further experimental work, a relationship could be developed relating  $\Delta$  to both  $\mu_{\Delta}$  and  $\bar{\lambda}$ . Further work is also required to verify the precise direction of the net mid-height lateral deflection for slender cold formed members.

The relationship between the predicted displacements and actual displacements from Equations (3.23) to (3.25) are shown in Figures 3.56 to 3.58 for the cold formed members. There is a good agreement between the predictions and the test data in all cases. The final proposed equations for hot finished and cold formed sections and the corresponding coefficients of variation are summarised in Table 3.11.

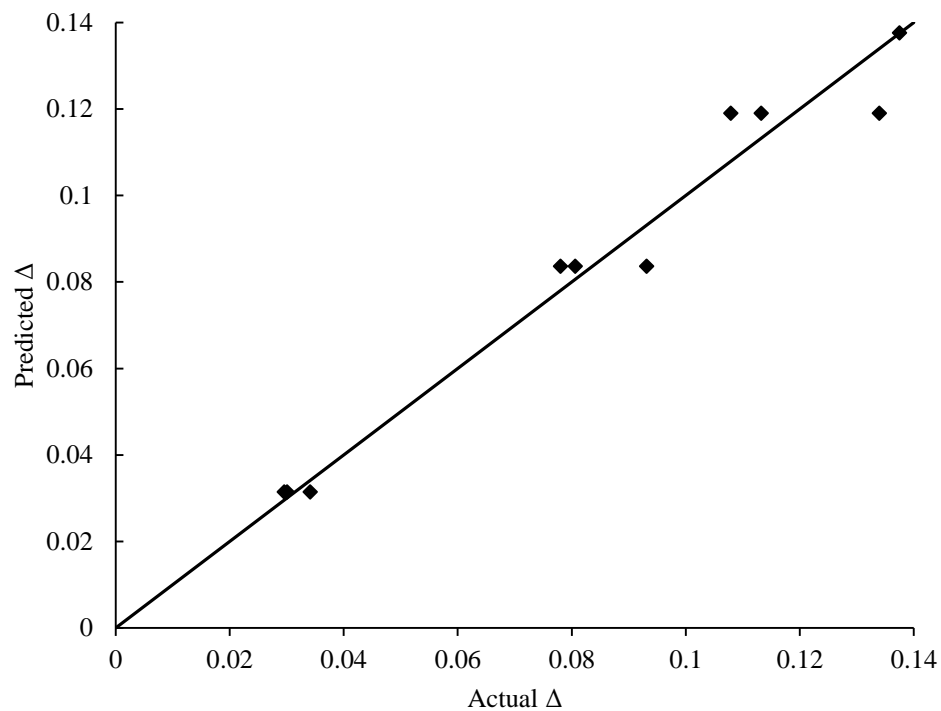


Figure 3.56 Relationship between predicted and actual mid-height lateral deflections for 1500 mm cold formed specimens using Equation (3.23)

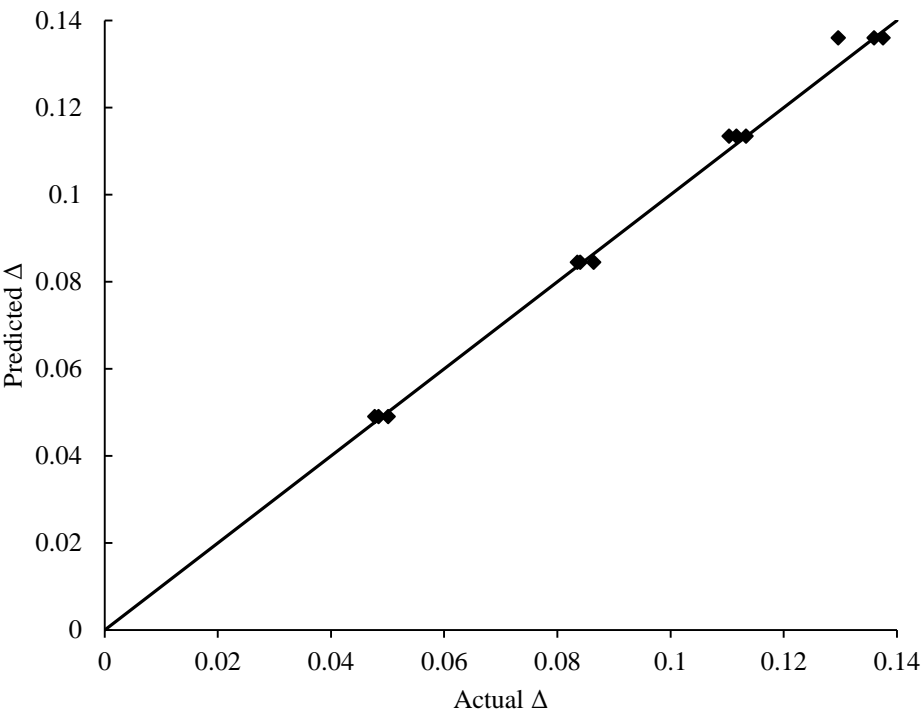


Figure 3.57 Relationship between predicted and actual mid-height lateral deflections for 3000 mm cold formed specimens using Equation (3.24)

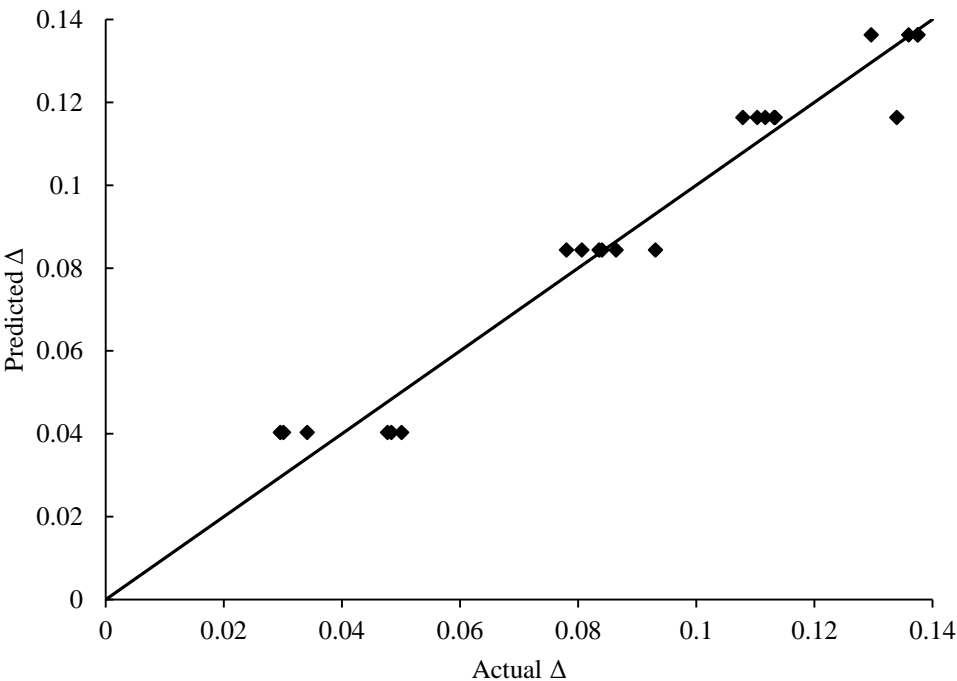


Figure 3.58 Relationship between predicted and actual mid-height lateral deflections for cold formed specimens of all lengths using Equation (3.25)

Table 3.11 Summary of predictive expressions for lateral deflections at the mid-height and corresponding coefficients of variation

Steel section type	Length (mm)	Expression for lateral displacement at mid-height	C.O.V.
Hot-finished	1500	$\frac{\Delta}{L}(\%) = -0.07\mu_{\Delta}^2 + 2.36\mu_{\Delta} + 2.75$	0.0061
Hot-finished	3000	$\frac{\Delta}{L}(\%) = -0.04\mu_{\Delta}^2 + 1.53\mu_{\Delta} + 1.53$	0.0039
Hot-finished	All lengths	$\frac{\Delta}{L}(\%) = -0.05\mu_{\Delta}^2 + 1.88\mu_{\Delta} - 0.41$	0.0089
Cold formed	1500	$\frac{\Delta}{L}(\%) = -0.21\mu_{\Delta}^2 + 3.87\mu_{\Delta} - 3.76$	0.0072
Cold formed	3000	$\frac{\Delta}{L}(\%) = -0.08\mu_{\Delta}^2 + 2.25\mu_{\Delta} - 0.72$	0.0023
Cold formed	All lengths	$\frac{\Delta}{L}(\%) = -0.15\mu_{\Delta}^2 + 3.1\mu_{\Delta} - 0.157$	0.0071

### 3.5 Concluding remarks

This chapter presents the experimental investigation of hollow and concrete-filled CHS braces at both cross-sectional and member levels. Compressive stub column tests demonstrated the benefits of concrete infill and the influence of tube wall thickness on the load-displacement relationship. The reliability of plastic resistance predictions in accordance with BS EN 1994-1-1 (2004) is also confirmed.

Braces of two lengths were tested and comparisons were drawn between compressive and tensile resistances, displacement ductility, failure mode, deformed shape and energy dissipation for each cross-section type. Concrete-filled specimens with non-dimensional slenderness values of less than 1.0 exhibited superior buckling and post-buckling resistances to hollow tubes but the concrete made a lesser contribution to these parameters in specimens with  $\bar{\lambda}$  close to 2.0. The concrete core increased the maximum tensile resistance for both 1500 mm and 3000 mm long specimens, by between 3.3 % and 10 %, showing the greatest contribution for 1500

mm hot-finished braces. The presence of concrete also increased the number of cycles to failure in all cases, which in turn enhanced the total energy dissipation. Distinctions were observed between the local deformations of the two specimen lengths, with global buckling behaviour dominating the 3000 mm specimen response, and a greater occurrence of local buckling for 1500 mm members. This difference is reflected in the buckling and post-buckling results but not in the tensile resistances, which are more consistent between shorter and longer braces.

The predicted buckling resistance using BS EN 1993-1-1 (2005)/BS EN 1994-1-1 (2004) showed good agreement with the test results for the shorter members but became more conservative at the longer length. For post-buckling resistance, models proposed by Tremblay (2002) and Nakashima *et al.* (1992) displayed good agreement with the results, while AISC (2002) and CSA (1994) guidelines tended to underestimate or overestimate the resistance.

Formulations by Tremblay (2002) and Shaback and Brown (2003) for the lateral deflection at the mid-height displayed significant discrepancies with the experimental results. New equations were proposed using a best fit approach to the experimental data, and separate relationships were suggested for hot-finished and cold formed braces. After examining the trends for each brace length, expressions were developed to cover all member lengths for ease of implementation in design, and a good agreement was found between these predictions and the laboratory test results.

The results provide motivation to conduct further research involving a wider range of  $\bar{\lambda}$  values and larger  $D/t$  ratios. Subsequent studies were conducted using finite element analysis, and these will be discussed in Chapters 4 and 5.

## **Chapter 4**

### **Numerical Simulations of Hollow Steel Braces**

#### **4.1 Introduction**

Following the experiments, numerical simulations of hollow and concrete-filled braces were executed using the finite element software package ABAQUS®. This chapter focuses on simulations of the hollow specimens and analysis of the concrete-filled braces will be presented and discussed in Chapter 5. Full three-dimensional models, including geometric imperfections, were created in order to capture both the overall load-displacement hysteresis response and the local behaviour. Results were compared with experimental data in order to verify the suitability of the chosen mesh size, boundary conditions, imperfection amplitudes and material constitutive models. Once satisfactory agreement was achieved between the models and experimental results, further parametric studies could be conducted at a later stage, to explore a wider range of cross-section and member sizes.

#### **4.2 Modelling of hollow steel braces**

##### **4.2.1 Element type and mesh size**

S4R general purpose shell elements were used for the steel tube. These are double-curved elements consisting of 4 nodes with 6 degrees of freedom per node. The optimum mesh size was determined by carrying out a sensitivity study in ABAQUS® using the 1500 mm long cold formed brace, CF-H-1500 from Chapter 3. Half of the tubular specimen was constructed as shown in Figure 4.1, and this was constrained to the plate at the end to simulate the boundary conditions of the experiment. The end plate was modelled using an analytical rigid element. Three

distinct regions are highlighted in Figure 4.1 where mesh size requirements were expected to vary: the specimen mid-length, quarter-length and end. A more refined mesh was employed at the end and mid-length over a distance equal to 3.0 times the section radius from the beginning of the study, since large local deformations were expected in these locations.

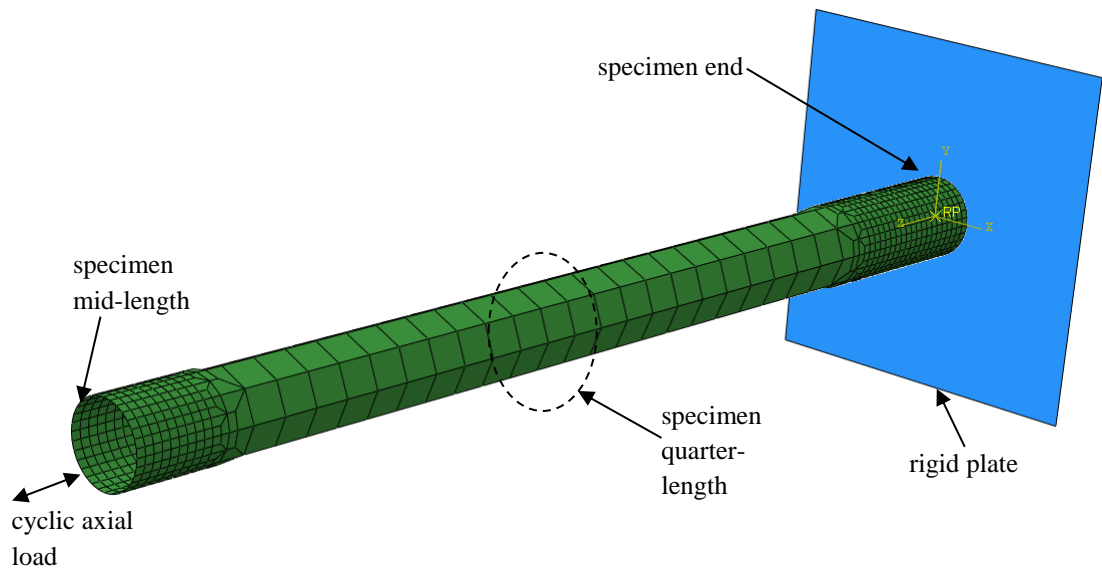


Figure 4.1 Finite element model of specimen CF-H-1500

Initially, a relatively coarse mesh was used consisting of eight elements around the circumference in areas of lower mesh density and thirty-two elements in the more refined zones. The specimen was subjected to the axial cyclic loading protocol outlined in the ECCS Guidelines (1986) (Figure 3.11), using displacement control. A global imperfection was incorporated into the model by applying an equivalent lateral load at the mid-length but no local imperfection was included at this stage. Following this, more refined meshes were employed. Five mesh sizes in total were examined, details of which are provided in Table 4.1.



Table 4.1 Mesh densities used for sensitivity study

Mesh	No. of elements around circumference (specimen quarter-length)	No. of elements around circumference (specimen end and mid-length)
Mesh 1	8	32
Mesh 2	16	64
Mesh 3	24	96
Mesh 4	32	128
Mesh 5	64	256

Sensitivity to mesh size was explored by comparing the maximum and minimum in-plane strains occurring over a specific area at the specimen mid-length, quarter-length and end. For the finer meshes, strains were determined by calculating the average strain across a number of elements equivalent in area to each of the elements selected for Mesh 1. The numbers of elements used for Meshes 1 – 5 are shown in Figures 4.2(a) – 4.2(e).

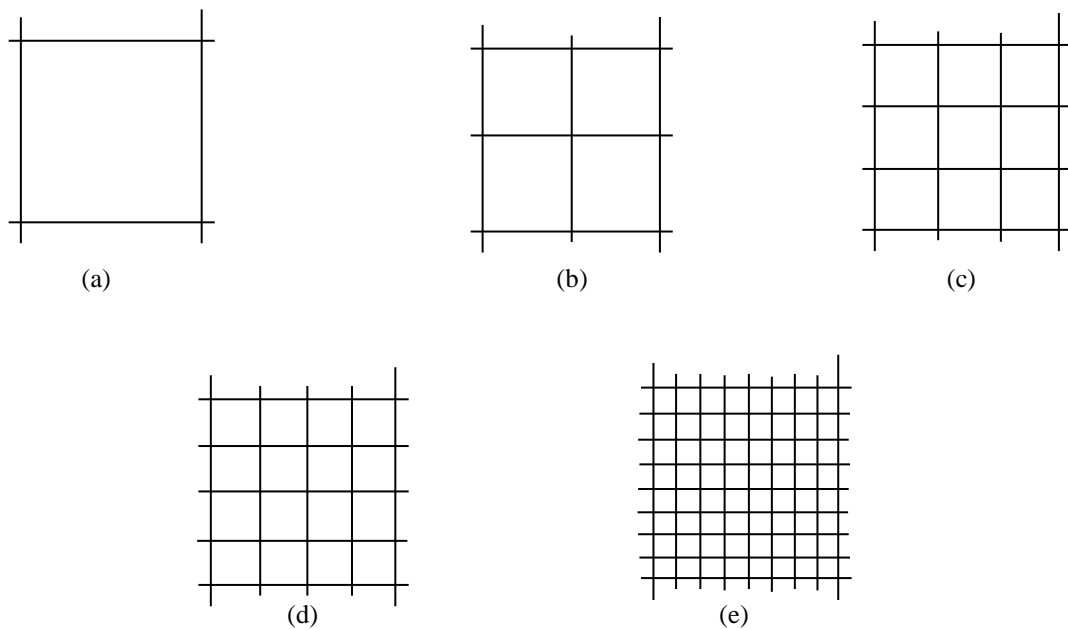
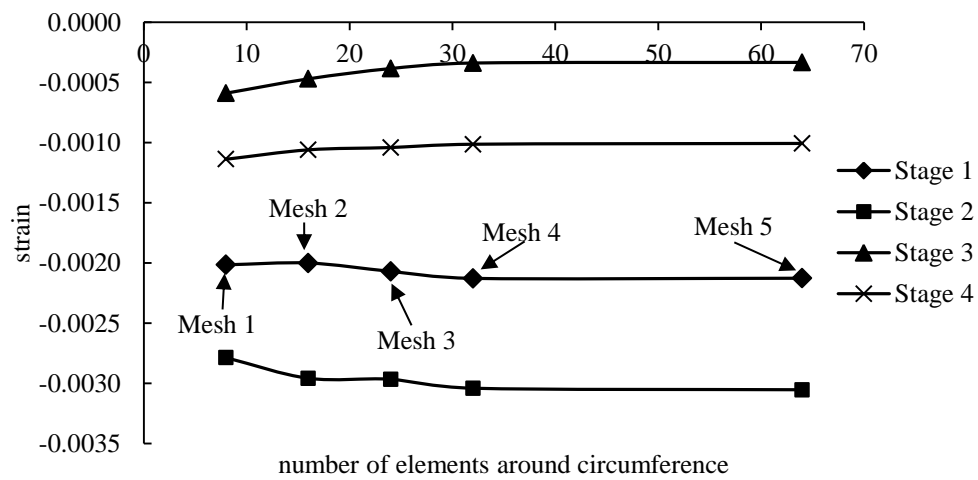
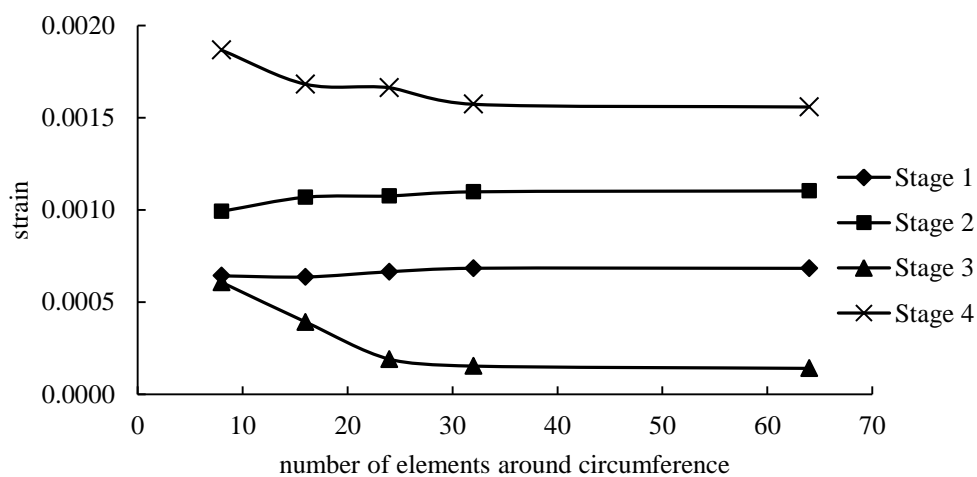


Figure 4.2 Relative mesh size and monitoring area for (a) Mesh 1; (b) Mesh 2; (c) Mesh 3; (d) Mesh 4; (e) Mesh 5

Figures 4.3(a) and 4.3(b) depict the variation in minimum and maximum in-plane strains respectively with increasing mesh refinement for the area of tube corresponding to a single element of Mesh 1, at different stages (Stages 1-4) of the loading procedure. These points were taken at the stage of the maximum compressive displacement in successive cycles. The change in strain is negligible for refinement beyond a mesh size corresponding to 32 elements around the circumference (Mesh 4), and hence this was selected as a suitable size for regions of low local deformation in the member.



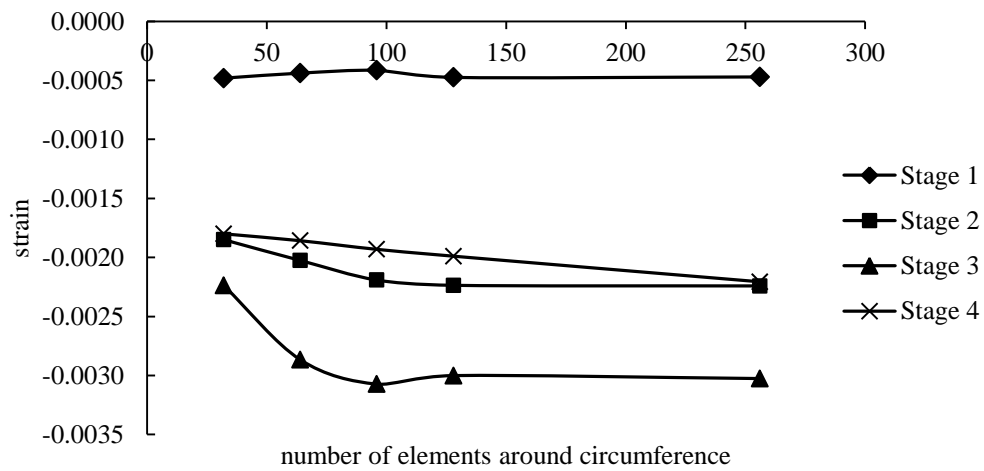
(a)



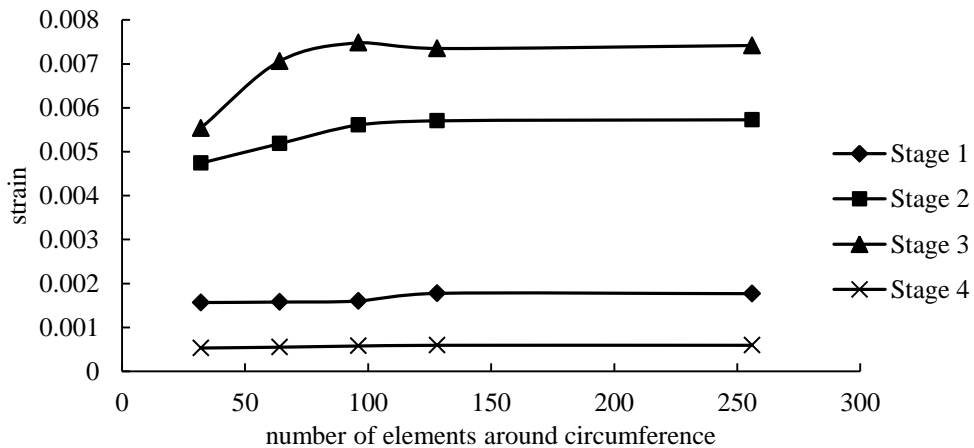
(b)

Figure 4.3 Variation in (a) minimum in-plane strain with mesh size for selected region at quarter-length; (b) maximum strain with mesh size for selected region at quarter-length

Figures 4.4(a) and 4.4(b) show the variation in strain for the portion of tube corresponding to a single element of Mesh 1 near the tube end. For most stages of testing, very little variation was seen beyond a mesh density of 128 elements around the circumference, and hence this was chosen as the mesh density in the FE model. Similar trends are shown for a mid-length element in Figures 4.5(a) and 4.5(b) and hence the same mesh size was selected for the mid-length. Hence Mesh 4 in Table 4.1 was found to be the appropriate mesh size.

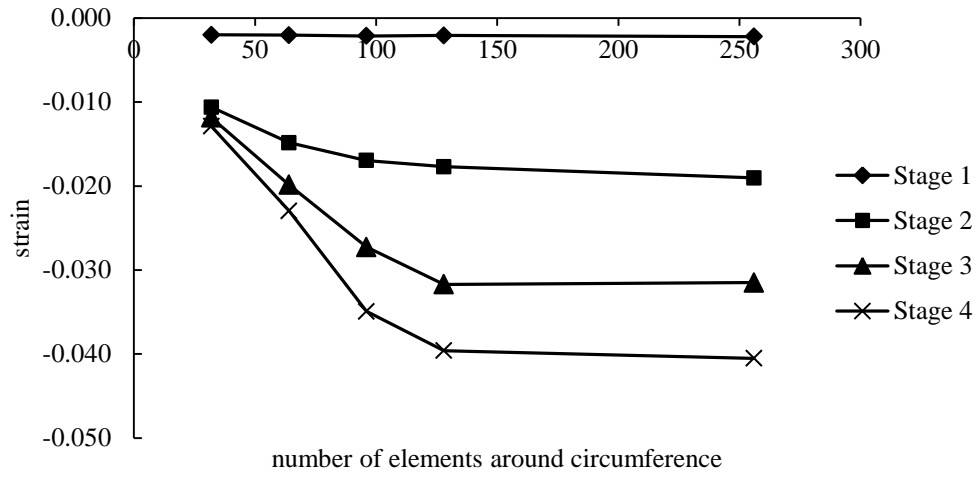


(a)

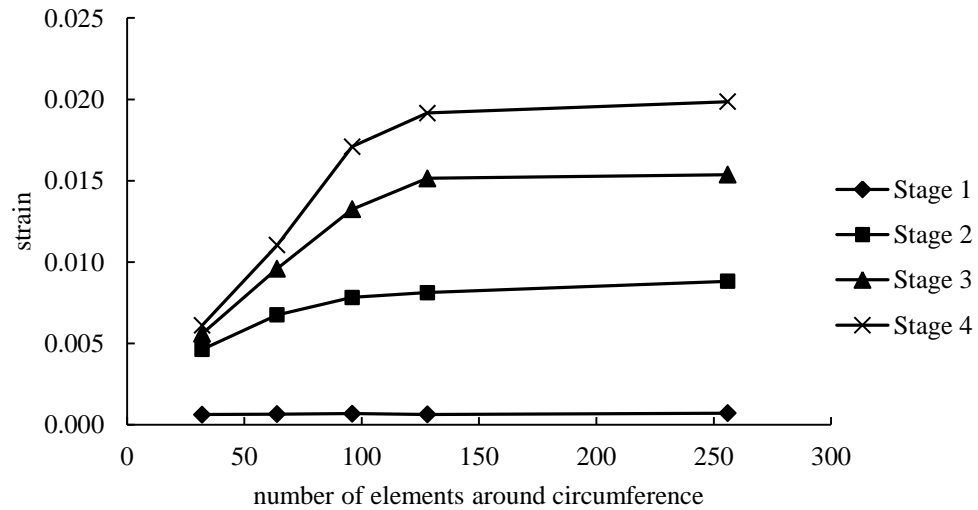


(b)

Figure 4.4 Variation in (a) minimum strain with mesh size for a selected region at specimen end; (b) maximum strain with mesh size for a selected region at specimen end



(a)



(b)

Figure 4.5 Variation in (a) minimum strain with mesh size for a selected region at mid-length; (b) maximum strain with mesh size for a selected region at mid-length

#### 4.2.2 Boundary conditions and loading

As mentioned in Section 4.2.1, half of the brace was modelled owing to symmetry. Fully fixed or pin-ended boundary conditions were employed at the specimen ends where appropriate to simulate the experiments. Cyclic axial loading was applied by means of an axial displacement to one end of the tube. Initially, imperfections in the laboratory boundary conditions were taken into consideration. The test-rig used for the experiments in Chapter 3 had been designed to provide fixed-ended conditions but some small degree of rotation (up to 0.005 radians) was observed and measured

at the specimen ends. The effect of this was assessed by incorporating these rotations into the boundary conditions in conjunction with the displacement protocol. However, when compared with the idealised fixed-ended conditions, the difference in results was found to be negligible and hence this effect was ignored for the remainder of the model calibration.

### 4.2.3 Steel constitutive model

ABAQUS® v. 6.10 provides two inbuilt material models for metals under cyclic loading: a linear kinematic hardening model and a nonlinear combined isotropic/kinematic hardening model. Both models are rate independent plasticity models based on a yield function, a flow rule and a hardening rule. The linear kinematic model is simpler to implement but more approximate, since it assumes a constant hardening modulus. The nonlinear combined model is based on that of Chaboche (1986), which consists of a nonlinear isotropic hardening component and a nonlinear kinematic hardening component, which are illustrated in Figures 4.6(a) and 4.6(b).

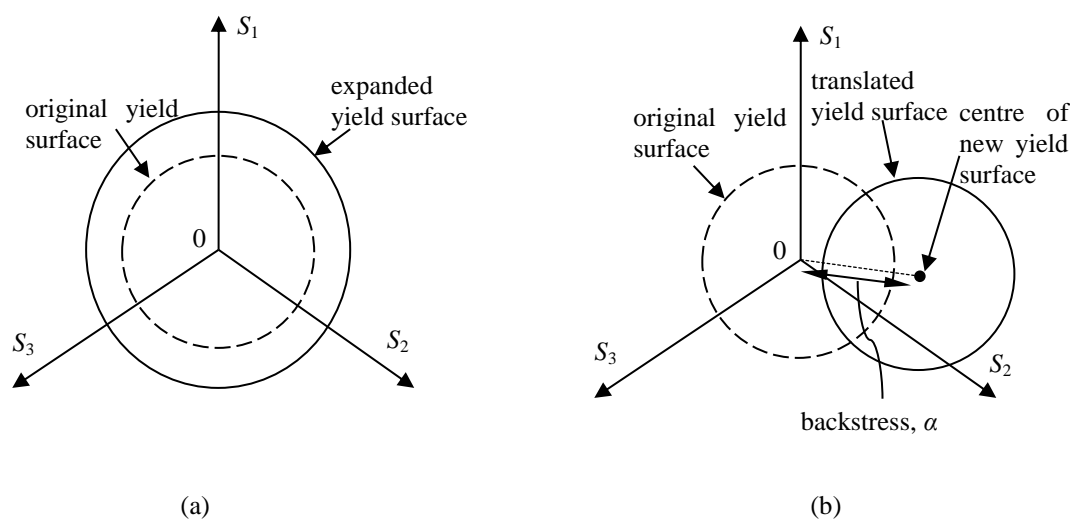


Figure 4.6 Development of yield surface for ABAQUS® nonlinear isotropic/kinematic hardening model: (a) isotropic component; (b) kinematic component

The isotropic part calculates the change in size of the yield surface and the relationship is given by:

$$\sigma^0 = \sigma|_0 + Q_\infty \left(1 - e^{-b\bar{\varepsilon}^{pl}}\right) \quad (4.1)$$

where

$\sigma^0$  is the size of the yield surface

$\sigma|_0$  is the yield stress at zero plastic strain

$Q_\infty$  is the maximum change in size of the yield surface

$b$  is the rate of change of yield surface size with increasing plastic strain

$\bar{\varepsilon}^{pl}$  is the equivalent plastic strain.

The kinematic component is a combination of a purely kinematic term from the linear Ziegler hardening law (Ziegler, 1959) and a relaxation term which introduces the nonlinearity. The kinematic component tracks the movement of the yield surface by means of the backstress,  $\alpha$ , as illustrated in Fig. 4.6(b). The hardening relationship is described by Equation (4.2), taking into account a number of different backstresses, where each backstress covers a different strain range.

$$\dot{\alpha}_k = C_k \frac{1}{\sigma} (\sigma - \alpha) \dot{\bar{\varepsilon}}^{pl} - \gamma_k \alpha_k \dot{\bar{\varepsilon}}^{pl} \quad (4.2)$$

where  $k$  refers to a particular backstress

$\dot{\bar{\varepsilon}}^{pl}$  is the equivalent plastic strain rate

$C_k$  are the initial kinematic hardening moduli

$\gamma_k$  is the rate of decrease of  $C_k$  with increasing plastic deformation

$\alpha$  is the overall backstress given by the summation of the  $\alpha_k$  values.

Although this model is more detailed than the linear model, there are some restrictions. The main issue is that only one set of parameters  $Q_\infty$ ,  $b$ ,  $C_k$  and  $\gamma_k$  can be used for the material behaviour, and these are not updated during the loading process. In reality however, the material parameters alter during increasing cyclic loads, and moreover these will depend not only upon the strains in each cycle but on the loading history prior to this. A number of options are provided in ABAQUS® for defining this model. Arguably the most thorough approach is using data obtained from cyclic material tests. For the isotropic hardening component, data are gathered from a number of loading cycles.

The maximum tensile and compressive stresses and strains per cycle,  $\sigma_n^t$ ,  $\sigma_n^c$ ,  $\varepsilon_t^{pl}$  and  $\varepsilon_c^{pl}$  as depicted in Fig. 4.7, are recorded for each cycle.  $(\sigma^0, \varepsilon^{pl})$  data pairs are determined using the following equations, and then  $Q_\infty$  and  $b$  are obtained by the best fit of Equation (4.1) through the data points.

$$\Delta\varepsilon^{pl} = \varepsilon_t^{pl} - \varepsilon_c^{pl} \quad (4.3)$$

$$\bar{\varepsilon}_i^{pl} = \frac{1}{2}(4i-3)\Delta\varepsilon^{pl} \quad (4.4)$$

where  $i$  is the number of the cycle. The kinematic hardening relationship is determined by establishing the backstress,  $\alpha_i$ , corresponding to each  $(\sigma_i, \bar{\varepsilon}_i^{pl})$  pair in a particular cycle. These parameters are illustrated by Figure 4.8.

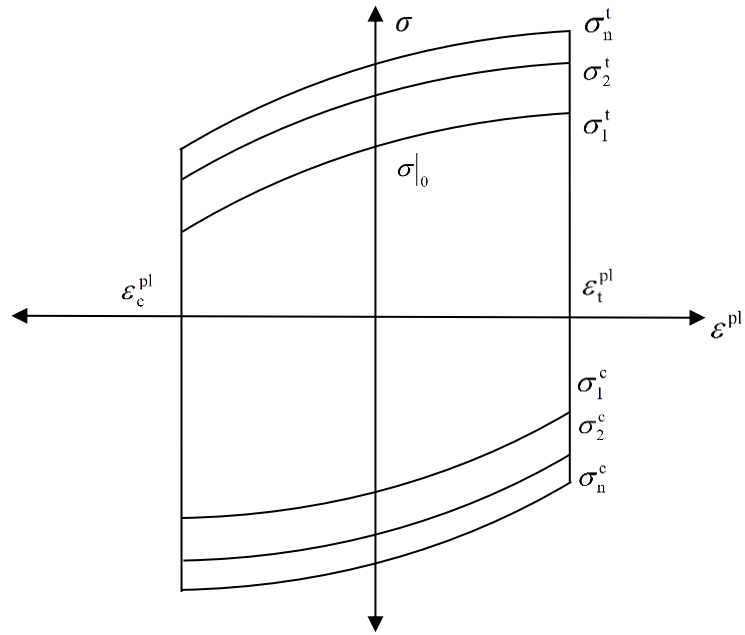


Figure 4.7 Determination of isotropic hardening component for steel material model

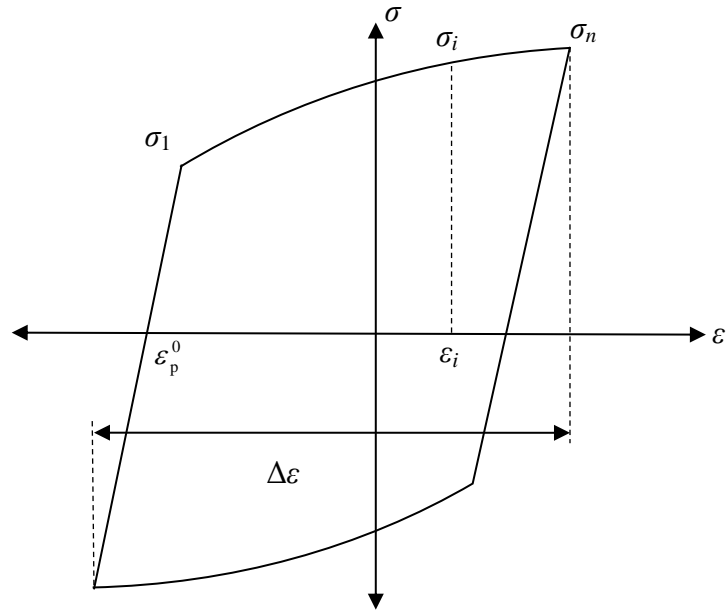


Figure 4.8 Determination of kinematic hardening component for steel material model

$\alpha_i$  is calculated using the following equations:

$$\alpha_i = \sigma_i - \sigma^s \quad (4.5)$$



$$\sigma^s = (\sigma_1 + \sigma_n)/2 \quad (4.6)$$

$C_k$  and  $\gamma_k$  values are established by achieving a best fit of Equation (4.2) through the  $(\sigma_i, \varepsilon_i^{pl})$  points.

ABAQUS® Documentation recommends taking the average values for  $Q_\infty$ ,  $b$ ,  $C_k$  and  $\gamma_k$  from a range of stabilised cycles at different strain amplitudes. This approach was adopted by Nip *et al.* (2010a), where the model was calibrated using results from a number of constant amplitude cyclic material tests, covering a range of strain amplitudes. Reliable predictions were obtained for the cyclic behaviour of hollow, rectangular, steel tubes using the nonlinear isotropic/kinematic hardening model. As it is straightforward to execute and has proven to be highly suitable for hollow steel tubes, this approach was chosen for the material model in this research project. In the absence of cyclic material test data, results from material tests of Nip *et al.* (2010b) were adopted and scaled suitably according to the steel yield stress in this study.

#### 4.2.4 Failure prediction

Three events were of particular interest for the failure prediction of cyclically-loaded braces: global buckling, local buckling and fracture. The occurrence of global buckling was easily detectable from the lateral displacement and axial load-displacement behaviour. Localised deformations predominantly occurred in the mid-length region and hence the initiation of local buckling was defined by observing the strains at two longitudinally adjacent nodes in this region. The point at which the strain values deviated from each other by 10 % was identified as the commencement of local buckling, which became visible in the deformed shape in subsequent cycles. This approach follows the one employed by Kuşyılmaz and Topkaya (2011) for

hollow CHS braces. Local buckling was also observed in the experiments, both by visual inspection and by variations in the recorded strains. It must be understood however that under significant strains, the strain gauges exceeded their recommended working limits ( $\sim 10 - 15 \%$ ) and hence the reliability of strain readings as the test progressed must be called into question.

For predicting fracture of the tube, a model by Coffin (1954) and Manson (1954) was used, in which the number of cycles to failure is given for a specimen under repeated cycles at the same strain as:

$$\frac{\Delta \varepsilon_p}{2} = \varepsilon'_f (2N_f)^c \quad (4.7)$$

where  $\Delta \varepsilon_p/2$  is the plastic strain amplitude,  $2N_f$  is the number of reversals to failure,  $\varepsilon'_f$  is the fatigue ductility coefficient and  $c$  is the fatigue ductility exponent. In the adopted approach, values of  $\varepsilon'_f$  and  $c$  were taken from material tests, previously conducted by Nip *et al.* (2010b). Hence the number of cycles to failure,  $N_f$ , could be determined for a particular plastic strain amplitude,  $\Delta \varepsilon_p/2$ . Since the strain range in the monitoring zone varied significantly throughout the progression of the tests, the total accumulated damage was determined using Miner's rule (Miner, 1945). This consisted of a damage index,  $D$ , given by Equation (4.8).

$$D = \sum_{i=1}^n \frac{n_i}{N_{fi}} \quad (4.8)$$

where  $N_{fi}$  was the number of cycles to failure for a particular strain amplitude and  $n$  was the number of cycles undergone by the test specimen at that strain. According to this damage model, failure occurred when the value of  $D$  reached 1. In theory, this model was applicable for specimens undergoing complete strain reversals in

compression and tension. However, the plastic strain in the monitoring region did not always follow this loading pattern.

A technique known as the “rainflow counting algorithm” was proposed by Matsuishi and Endo (1968) to define strain cycle amplitudes for a specimen undergoing irregular loading patterns. There are several variations to the method of counting, as discussed by Downing and Socie (1982), and in this study the author adopted the ‘one-pass’ algorithm, since knowledge of the entire strain history was not required prior to commencing the count. The method of rainflow counting was applied by plotting the relationship between strain and time, with strain on the horizontal axis, and imagining the peaks and troughs as a ‘pagoda’ roof with rain dripping down from one level to the next, as illustrated in Figure 4.9.

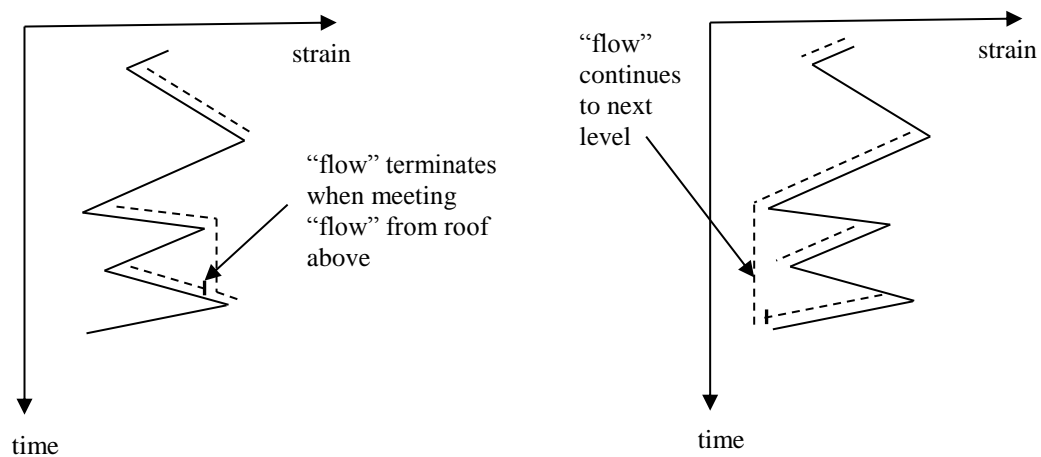


Figure 4.9 Illustration of rainflow analysis technique

Two separate counts were taken for the half-cycles, one for the ‘peaks’ and one for the ‘troughs’. A half-cycle terminated if it arrived opposite a peak/trough of greater magnitude than that from which it originated, or if it encountered ‘flow’ from a previous peak or trough. Otherwise the flow continued to drop from one “level” to the next. The amplitude of a particular half-cycle was equal to the difference

between the maximum and minimum strains for that cycle. Half-cycles of the same amplitude and opposite sense were paired together and there were usually some residual half-cycles.

This approach enabled the determination of the particular plastic strain amplitudes corresponding to individual loading cycles, and using the material test data and damage index described previously, the total number of cycles to fracture was determined for strains on the inside face, outside face and average strain values between the two faces. Using this technique, a particular strain amplitude could be computed by summing the accumulated strains over a number of cycles. As the loading progressed, the damage caused by a particular half cycle was not taken into account until a strain reversal of equal magnitude occurred. This approach did not appear to be entirely suitable, since at certain stages of the analysis, the specimen underwent half-cycles of significant strain amplitudes without undergoing reversals of these amplitudes. In order to account for the residual damage from half cycles, an alternative estimation was conducted, counting individual half-cycles as they occurred during the analysis. Comparisons between these two methods will be discussed in Sections 4.2.5 and 4.2.6.

### **4.2.5 Imperfection amplitudes**

Using the four hollow specimens tested in Chapter 3, 5 global imperfection amplitudes were considered for each brace length:  $L/500$ ,  $L/750$ ,  $L/1000$ ,  $L/1500$  and  $L/2000$ , where  $L$  was the length of the brace. The shape and magnitude of the local imperfection was fixed at a nominal value of  $t/10$  at this stage of the analysis. However, in order to account for any influence from this parameter, a second set of analyses was carried out later with a local imperfection of  $t/100$ . The main criterion used to determine a suitable global imperfection amplitude was the buckling load

observed in the experiments. A summary of buckling loads for each global and local imperfection amplitude is provided in Tables 4.2 and 4.3.

Table 4.2 Buckling load for CF-H-1500 with various global imperfection amplitudes

Global imperfection	$N_{c,max} \text{ (FE)}/N_{c,max} \text{ (experiments)}$	
	Local imperfection = $t/10$	Local imperfection = $t/100$
$L/500$	0.82	0.79
$L/750$	0.91	0.91
$L/1000$	0.98	0.97
$L/1500$	1.04	1.04
$L/2000$	1.08	1.05

Table 4.3 Buckling load for CF-H-3000 with various global imperfection amplitudes

Global imperfection	$N_{c,max} \text{ (FE)}/N_{c,max} \text{ (experiments)}$	
	Local imperfection = $t/10$	Local imperfection = $t/100$
$L/500$	0.88	0.89
$L/750$	0.98	0.98
$L/1000$	1.04	1.04
$L/1500$	1.13	1.13
$L/2000$	1.61	1.16

The amplitude of the local imperfection had little influence on the buckling load. Following from the results, amplitudes of  $L/1000$  and  $L/750$  were selected for the 1500 mm and 3000 mm long specimens respectively, since these provided the closest agreement to the experimental results. It was noted that an imperfection value of  $L/1000$  was used by Beer and Schultz (1970) in deriving the current European design buckling curve and hence the imperfection value for the 1500 mm braces complied with this while the imperfection for the 3000 mm specimens was slightly conservative. The assumed imperfection values were also conservative when compared with the measured global imperfections which tended to be smaller.

The values given in Table 3.6 for this study give measured global imperfection ranges of  $L/6800 - L/2200$  for 1500 mm specimens and  $L/2300 - L/850$  for 3000 mm specimens. Furthermore, previous research on tubular columns by Bjorhovde (1977) reported a mean global imperfection magnitude of  $L/6300$ .

A suitable local imperfection amplitude was selected by means of a sensitivity study using specimen CF-H-1500. Strain-based fatigue-life estimations as described in Section 4.2.4 were employed to achieve this. A variation in strain occurred through the tube wall thickness, since it was under both axial and bending stresses. Strain output from the numerical models was available for both the inside and outside faces of the tube. The maximum strain amplitudes occurred on the outside face but using these alone could underestimate the fracture life of the tube, since most of the section was experiencing a smaller magnitude of strain. Similarly, considering only the inside face could overestimate the number of cycles to fracture. Employing the average value between the outside and inside faces and assuming that this was constant through the section thickness could also overestimate the fracture life of the tube since in reality, fracture would initiate on the outside face, which was experiencing a larger strain amplitude than the average. Hence comparisons were drawn between using strains from both the outside and inside faces, in addition to the average value between the two, to assess if these would provide suitable upper and lower bounds for the predicted number of cycles to failure. The next step was to define an appropriate area of the tube over which to monitor the strains. Figure 4.10 shows the variation in strain in the vicinity of the tube mid-length. Significantly larger strains were observed over a distance equal to  $\frac{1}{4}$  of the tube diameter. For the sensitivity study various portions of the tube length were taken into consideration,

varying from a single row of elements at the mid-length, to the region indicated in Fig. 4.10 corresponding to one quarter of the tube diameter.

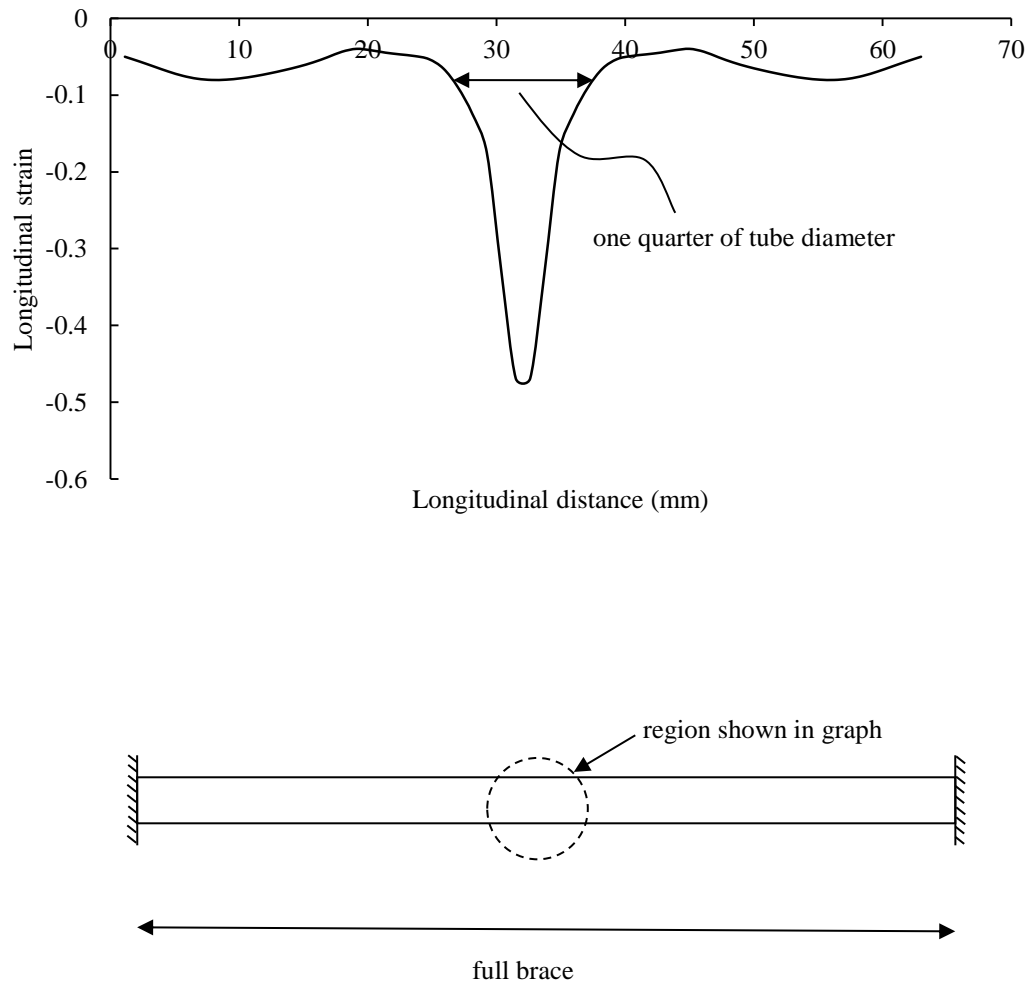


Figure 4.10 Strain variation along brace length for model of CF-H-1500

The longitudinal strain around the circumference at the specimen mid-length is given in Figure 4.11. The tension half of the tube is from 0 to 1.57 radians and from 4.71 radians back to 0. It is seen from the strain distribution that the tube underwent relatively low strains on the tension side, whereas a notable strain variation occurred across the compression face. Peak strain values were seen at the centre of the compression face and the edge. Strains from both the centre and edge regions were

considered for predicting the number of cycles to failure. Owing to the continuity of the circular perimeter the entire compression face was also taken into consideration. The deformed shape and details of the selected regions are illustrated in Figures 4.12 and 4.13.

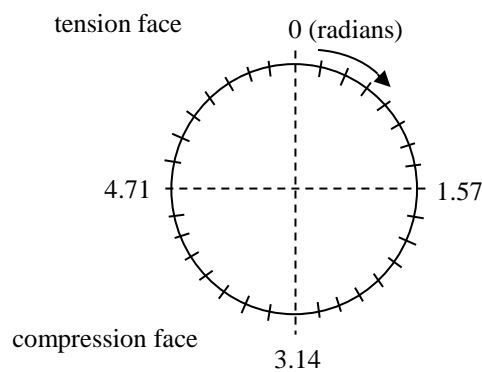
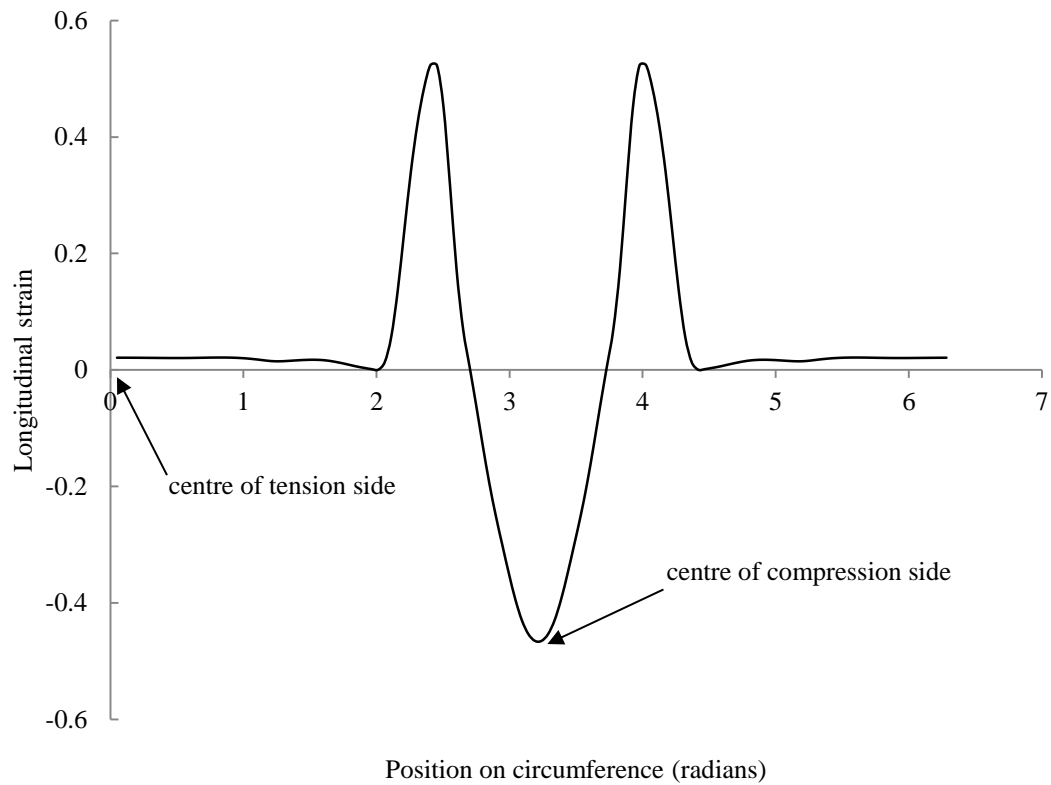


Figure 4.11 Strain variation around circumference for model of CF-H-1500



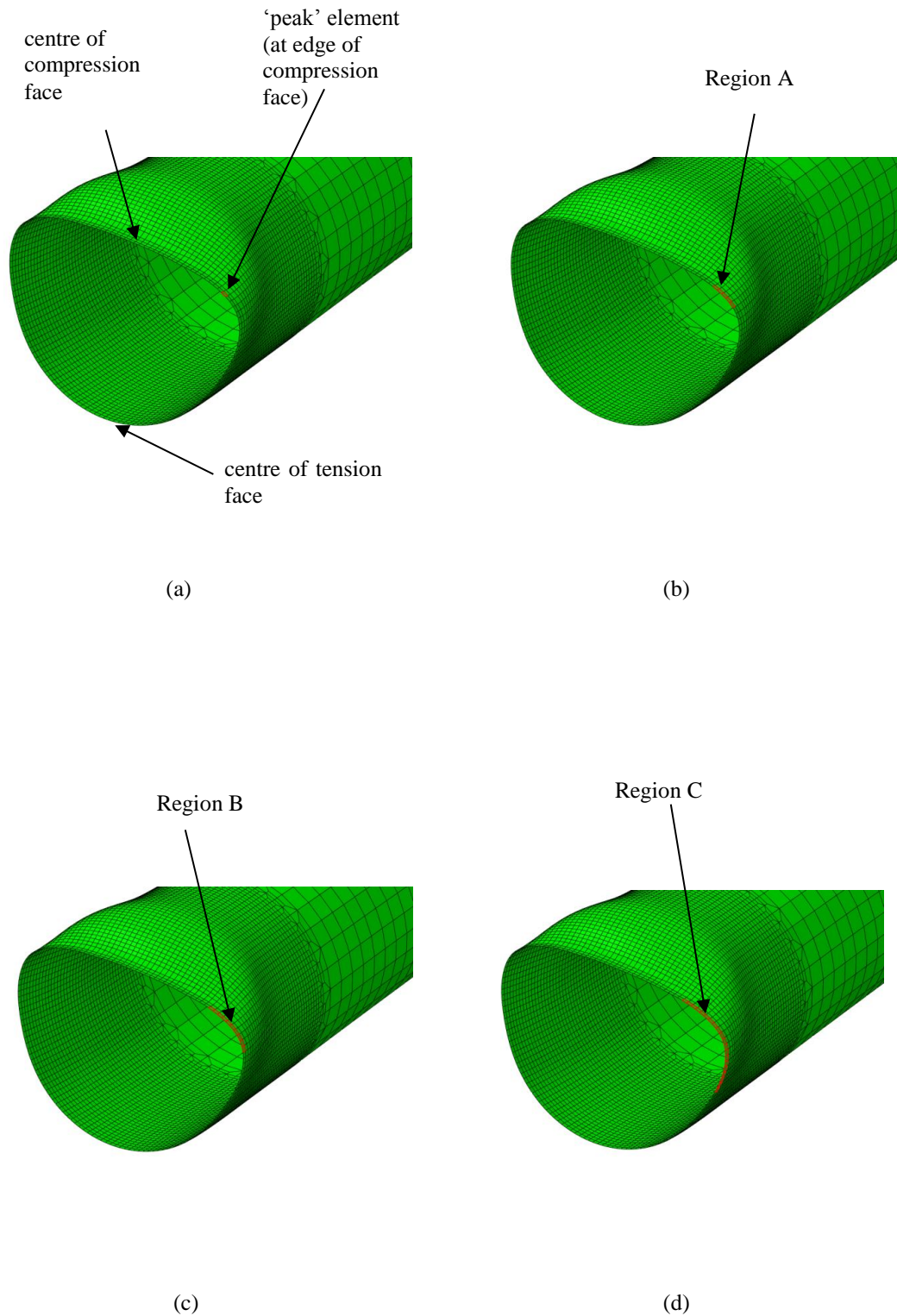


Figure 4.12 Deformed shape at mid-length showing: (a) peak strain at edge of compression face; (b) Region A; (c) Region B; (d) Region C

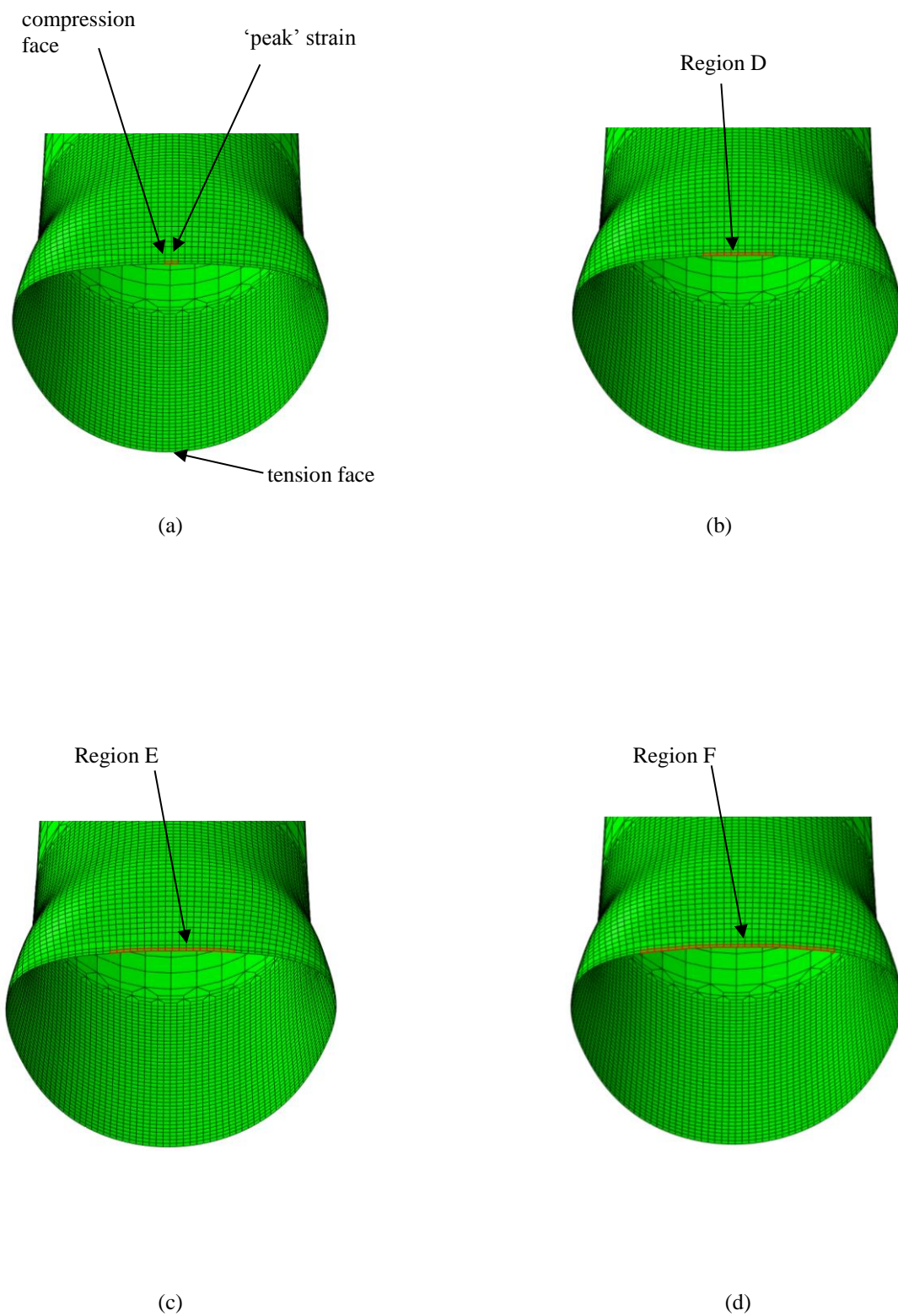


Figure 4.13 Deformed shape at mid-length showing: (a) peak strain at centre of compression face; (b) Region D; (c) Region E; (d) Region F

Five local imperfection amplitudes were considered:  $t/25$ ,  $t/50$ ,  $t/100$ ,  $t/200$  and  $t/500$ , where  $t$  is the thickness of the steel tube. In the absence of cyclic material test data, parameters  $\varepsilon'_f$  and  $c$  from Nip *et al.* (2010b) were used to define the Coffin-Manson relationship for the fracture prediction. In addition to using these original parameters (Nip *et al.*, 2010b), a separate estimation was conducted in which values of  $\varepsilon'_f$  and  $c$  from Nip *et al.* (2010b), were scaled to the steel yield stress value used in the current study. Tables 4.4 and 4.5 summarise the results for a local imperfection of  $t/100$ , using the second approach, obtained with scaled values of  $\varepsilon'_f$  and  $c$ . Each table consists of five main rows, indicating the number of rows of elements taken into account, where the 1<sup>st</sup> row is the circumferential ring of elements at the specimen mid-length, as shown in Figure 4.14. Each of the major horizontal rows in the table is divided into three sub-rows, showing the results for different strain outputs (i.e. inside face, outside face or average value). The columns in the table describe the length of tube around the section circumference over which the strains were included. These regions are illustrated in Figures 4.12 and 4.13.

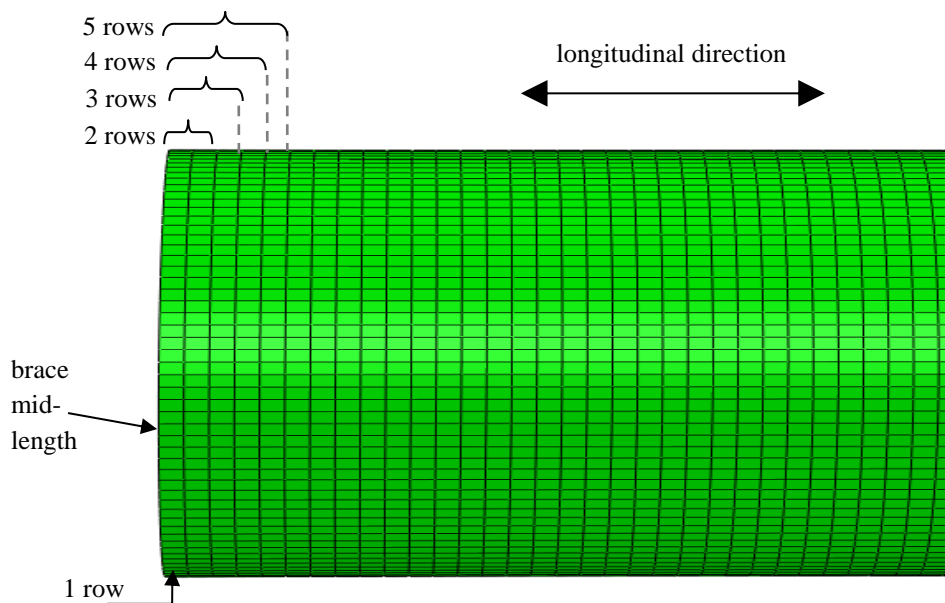


Figure 4.14 Rows of elements used for predicting the number of cycles to fracture

## Chapter 4 Numerical Simulations of Hollow Steel Braces

Table 4.4 No. of cycles to fracture for local imperfection =  $t/100$ , taking centre of compression face; scaled fracture parameters from Nip *et al.* (2010b)

No. of rows (counted in longitudinal direction)	Strain output	No. of cycles to failure									
		rainflow technique					counting individual ramps				
		Region					Region				
		peak	D	E	F	whole	peak	D	E	F	whole
1	Avg	-	-	-	-	-	-	-	-	-	10
	Inside face	-	-	-	-	-	-	-	-	-	10
	Outside face	-	-	-	-	12	-	-	-	-	10
2	Avg	9	9	9	9	10	9	9	9	9	9
	Inside	18	18	18	18	11	9	9	9	9	10
	Outside	9	9	9	9	10	8	8	8	8	9
3	Avg	17	17	16	11	14	9	9	9	9	10
	Inside	-	-	-	-	17	11	11	11	10	11
	Outside	9	9	9	9	11	9	9	9	9	10
4	Avg	-	-	-	-	16	11	11	10	10	11
	Inside	-	-	-	-	17	-	-	19	15	12
	Outside	11	14	11	10	14	9	9	9	9	10
5	Avg	-	-	-	-	17	-	-	19	14	12
	Inside	-	-	-	-	17	-	-	19	15	12
	Outside	-	-	-	-	17	11	11	10	10	11

Table 4.5 No. of cycles to fracture for local imperfection =  $t/100$ , taking edge of compression face; scaled fracture parameters from Nip *et al.* (2010b)

No. of rows (counted in longitudinal direction)	Strain output	No. of cycles to failure									
		rainflow technique					counting individual ramps				
		Region					Region				
		peak	A	B	C	whole	peak	A	B	C	whole
1	Avg	9	9	9	13	-	8	8	9	9	10
	Inside face	9	9	9	13	-	8	8	9	9	10
	Outside face	9	9	10	11	12	8	8	9	9	10
2	Avg	9	9	9	10	10	9	9	9	9	9
	Inside	9	9	9	10	11	9	9	9	9	10
	Outside	9	9	9	10	10	9	9	9	9	9
3	Avg	10	10	10	11	14	9	9	9	10	10
	Inside	10	10	10	11	17	9	9	9	10	11
	Outside	10	10	9	10	11	9	9	9	10	10
4	Avg	10	10	10	11	16	9	9	9	10	11
	Inside	10	10	10	11	17	9	9	10	10	12
	Outside	9	10	10	11	14	9	9	9	10	10
5	Avg	10	10	11	14	17	9	9	10	11	12
	Inside	11	11	11	14	17	10	10	10	11	12
	Outside	10	10	10	13	17	9	9	9	11	11

The location of maximum strain was not always exactly at the mid-length. Although larger strains were generally observed in the mid-length region as displayed in Figure 4.10, depending on the buckled shape, the maximum value could occur in the second or third row instead of the first. Furthermore, the row which exhibited the largest tensile strain value was not necessarily the one with the largest strain reversals (i.e. differences between successive peaks and troughs). Therefore, the number of cycles to failure estimated from 1 row alone did not always exceed that taken from an average of more than one row. In some cases, particularly in Table 4.4, no estimation was obtained, since the strain development over the selected region did not undergo reversals of sufficient magnitude to reach a failure prediction, and exhibited a predominantly monotonic strain increase instead. The complete set of results for each imperfection amplitude is given Appendix A.1. Little variation in results was observed beyond an imperfection amplitude of  $t/100$ . This imperfection amplitude was also close to the measured local imperfection for the equivalent specimen in the experiments, and hence a local imperfection amplitude of  $t/100$  was adopted for the remainder of the study. Although specimen CF-H-1500 in the experiments endured 14 cycles in total, it was evident that the numerical model had failed after 11 cycles, from both the load-displacement hysteresis behaviour and the deformed shape. Taking the strains on the outside face across the entire compression side of the tube, using the row of elements at the mid-face, provided a good estimation of the fracture behaviour, with the approach of counting individual ramps and the ‘rainflow’ method computing suitable lower and upper bounds respectively to the number of cycles to fracture.

#### 4.2.6 Verification of FE model

The proposed FE modelling approach was validated by simulating the four hollow test specimens from Chapter 3 in addition to five additional specimens from Elchalakani *et al.* (2003), Packer *et al.* (2010) and Takeuchi and Matsui (2011). The section identification, section type, local slenderness ratio and global slenderness ratio are presented for each specimen in Table 4.6, where  $D$  is the section outer diameter,  $t$  is the tube wall thickness and  $\varepsilon = \sqrt{235/f_y}$ , where  $f_y$  is the steel yield strength.

Table 4.6. Specimens used for validation of FE model

Reference	Specimen ID	Section type	$D/te^2$	$\bar{\lambda}$
This study	CF-H-1500	cold formed	36	0.90
This study	HF-H-1500	hot-finished	27	0.78
This study	CF-H-3000	cold formed	36	1.98
This study	HF-H-3000	hot-finished	27	1.72
Elchalakani <i>et al.</i> (2003)	S7C	cold formed	64	0.55
Packer <i>et al.</i> (2010)	CHS-C	cold formed	20	1.12
Takeuchi and Matsui (2011)	721	cold formed	33	0.98
Takeuchi and Matsui (2011)	728	cold formed	41	0.95
Takeuchi and Matsui (2011)	732	cold formed	48	0.95

As mentioned in sections 4.2.3 and 4.2.5, the input parameters for the ABAQUS® isotropic/kinematic hardening model and the fracture parameters for the Coffin-Manson relationship were determined by scaling the values obtained for cold formed and hot-finished specimens in Nip (2010b) in proportion to the steel yield stress. The values of  $Q_\infty$ ,  $b$ ,  $C_k$ ,  $\gamma_k$ ,  $\varepsilon'_f$  and  $c$  which were used in the FE model validation are presented in Table 4.7 for each specimen.

## Chapter 4 Numerical Simulations of Hollow Steel Braces

Table 4.7. Material parameters for FE models

Specimen ID	$Q_\infty$	$b$	$C_k$	$\gamma_k$	$\varepsilon'_t$	$c$
CF-H-1500	44	1.41	154085	541	0.51	-0.81
HF-H-1500	49	2.12	21021	124	0.57	-0.59
CF-H-3000	44	1.41	154085	541	0.51	-0.81
HF-H-3000	49	2.12	21021	124	0.57	-0.59
S7C (Elchalakani <i>et al.</i> , 2003)	33	1.05	114260	401	0.39	-0.62
CHS-C (Packer <i>et al.</i> , 2010)	27	0.87	95568	336	0.32	-0.51
721 (Takeuchi and Matsui, 2011)	32	1.01	110371	388	0.37	-0.59
728 (Takeuchi and Matsui, 2011)	30	0.96	105186	370	0.36	-0.57
732 (Takeuchi and Matsui, 2011)	31	0.98	107507	378	0.36	-0.58

Table 4.8 presents the number for cycles to global buckling, local buckling and fracture for each test specimen and the corresponding numerical model. The numbers of cycles to local and global buckling showed close agreement in most cases except for the local buckling of specimen HF-H-1500 and CHS-C (Packer *et al.*, 2010). The number of cycles to fracture was underestimated by the numerical model in all cases except for specimen S7C (Elchalakani *et al.*, 2003). Overall, the models provided conservative predictions of the brace behaviour.

Table 4.8 Comparison between FE and experimental results

Specimen	No. of cycles to					
	global buckling		local buckling		fracture	
	FE	test	FE	Test	FE	test
CF-H-1500	5	5	8	8	11	14
HF-H-1500	6	5	11	15	11	17
CF-H-3000	3	3	8	9	11	17
HF-H-3000	3	4	9	8	17	24
S7C (Elchalakani <i>et al.</i> , 2003)	4	4	9	7	13	13
CHS-C (Packer <i>et al.</i> , 2010)	*	*	22	30	25	31
721 (Takeuchi and Matsui, 2011)	4	5	10	12	10	14
728 (Takeuchi and Matsui, 2011)	4	5	7	9	8	13
732 (Takeuchi and Matsui, 2011)	6	7	9	8	10	11

\* not reported

Figures 4.15 - 4.23 compare the load-displacement hysteresis curves between each of the numerical and experimental specimens. Despite undergoing earlier failures than their experimental counterparts, the numerical models produced similarly-shaped hysteresis curves, indicating a reliable simulation of the behaviour of each specimen. Further details of the model verification are given in Appendix A.2.

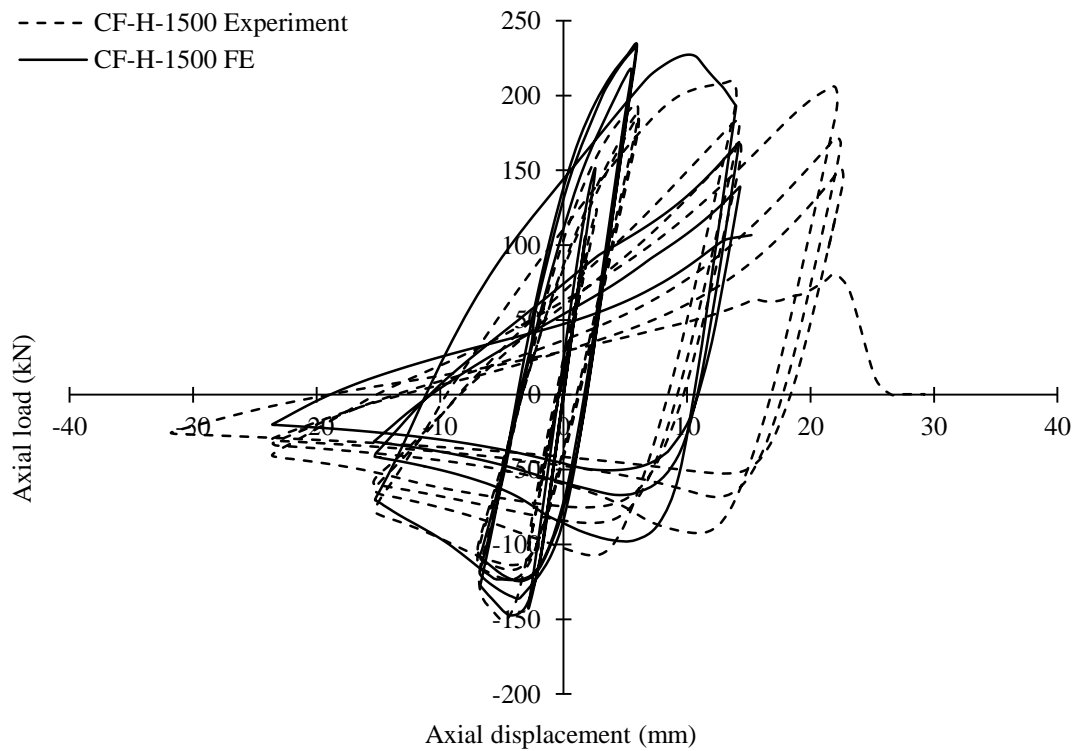


Figure 4.15 Load displacement hysteresis curves for specimen CF-H-1500



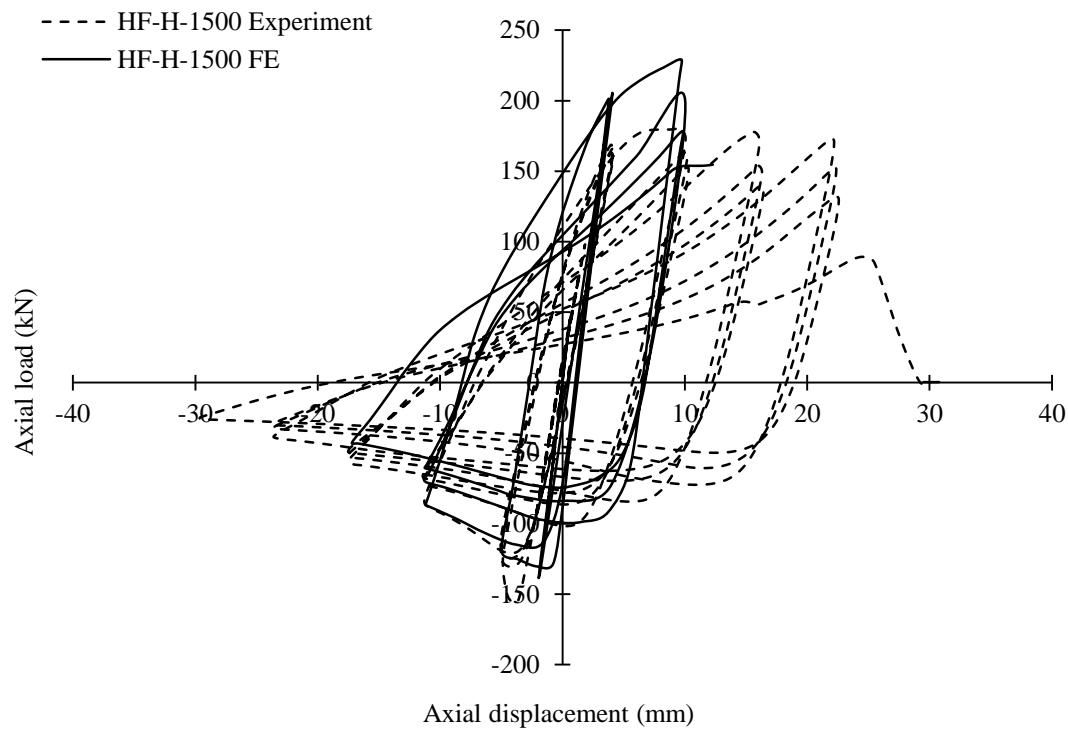


Figure 4.16 Load displacement hysteresis curves for specimen HF-H-1500

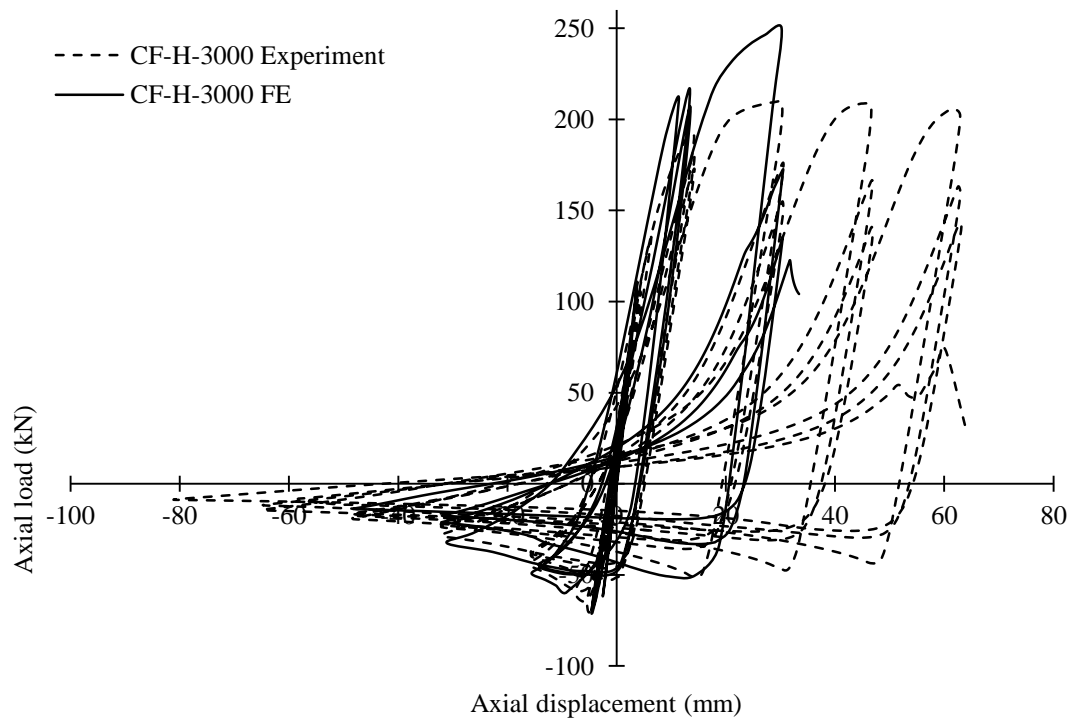


Figure 4.17 Load displacement hysteresis curves for specimen CF-H-3000

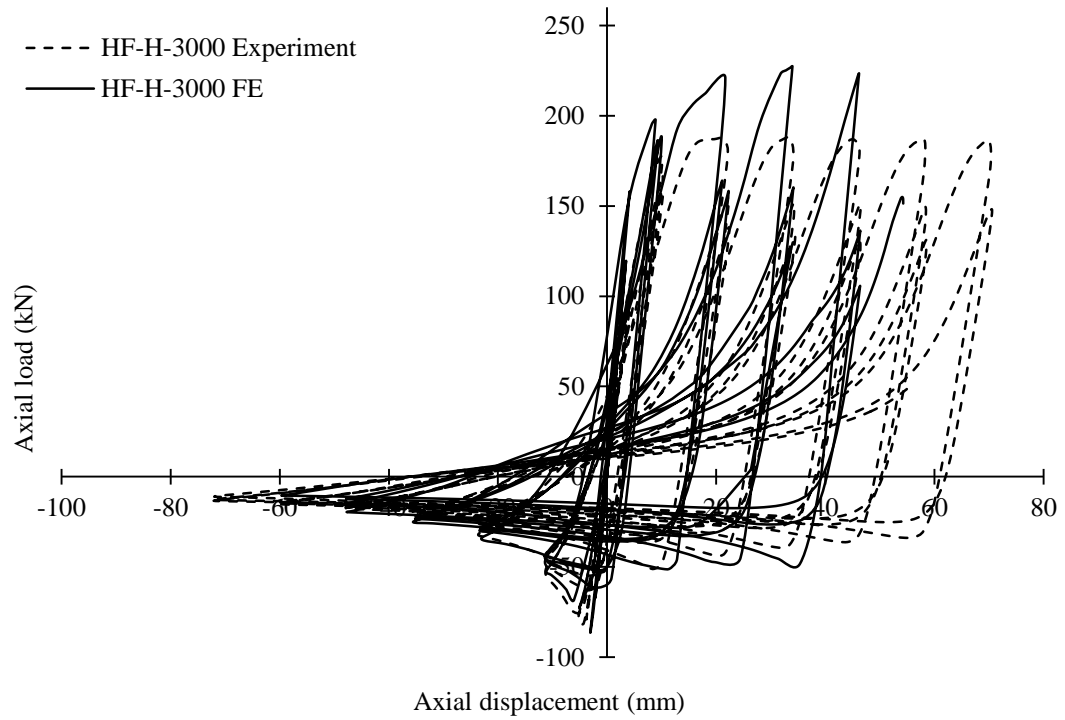


Figure 4.18 Load displacement hysteresis curves for specimen HF-H-3000

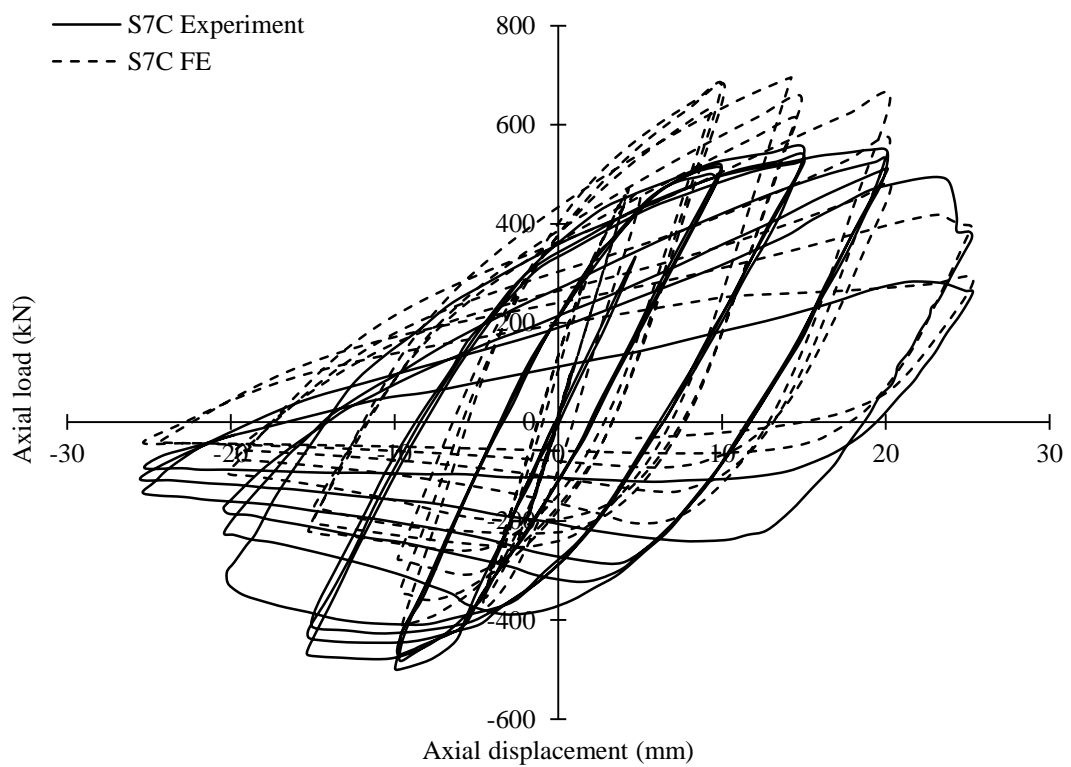


Figure 4.19 Load displacement hysteresis curves for specimen S7C (Elchalakani *et al.*, 2003)

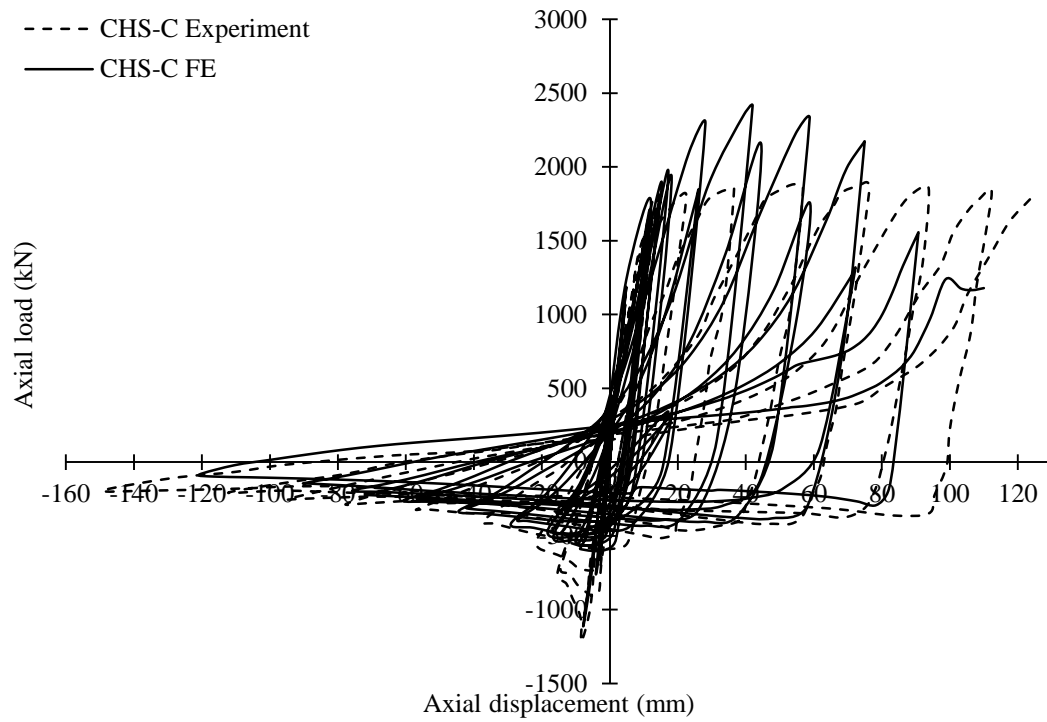


Figure 4.20 Load displacement hysteresis curves for specimen CHS-C (Packer *et al.*, 2010)

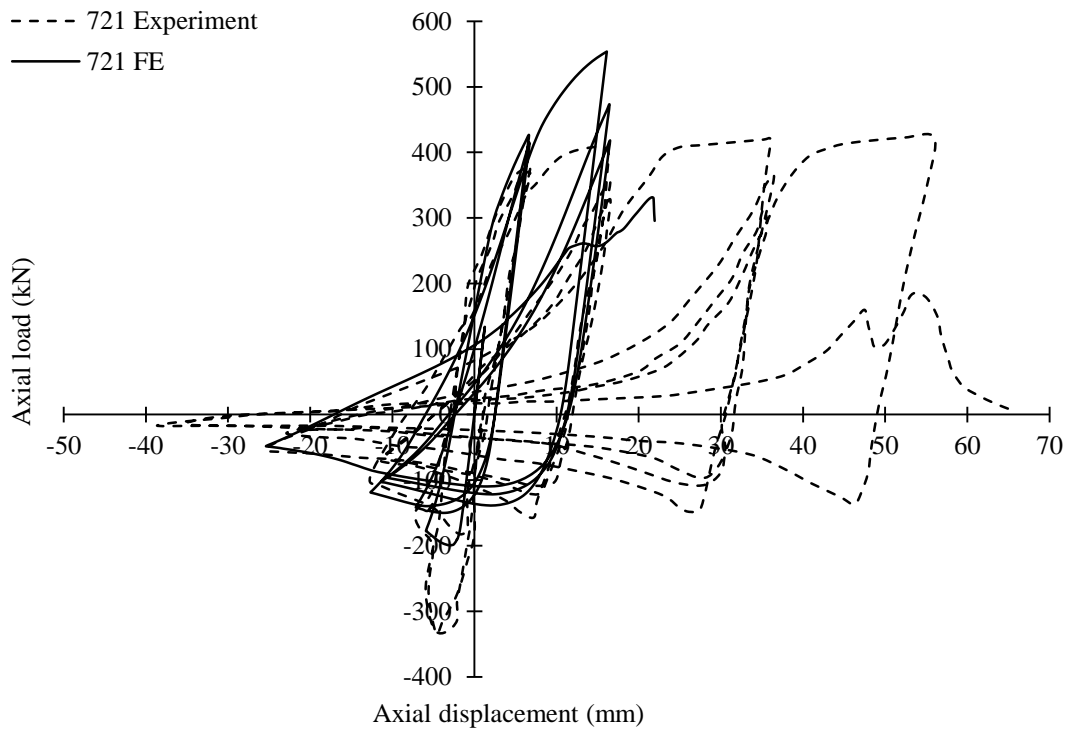


Figure 4.21 Load displacement hysteresis curves for specimen 721 (Takeuchi and Matsui, 2011)

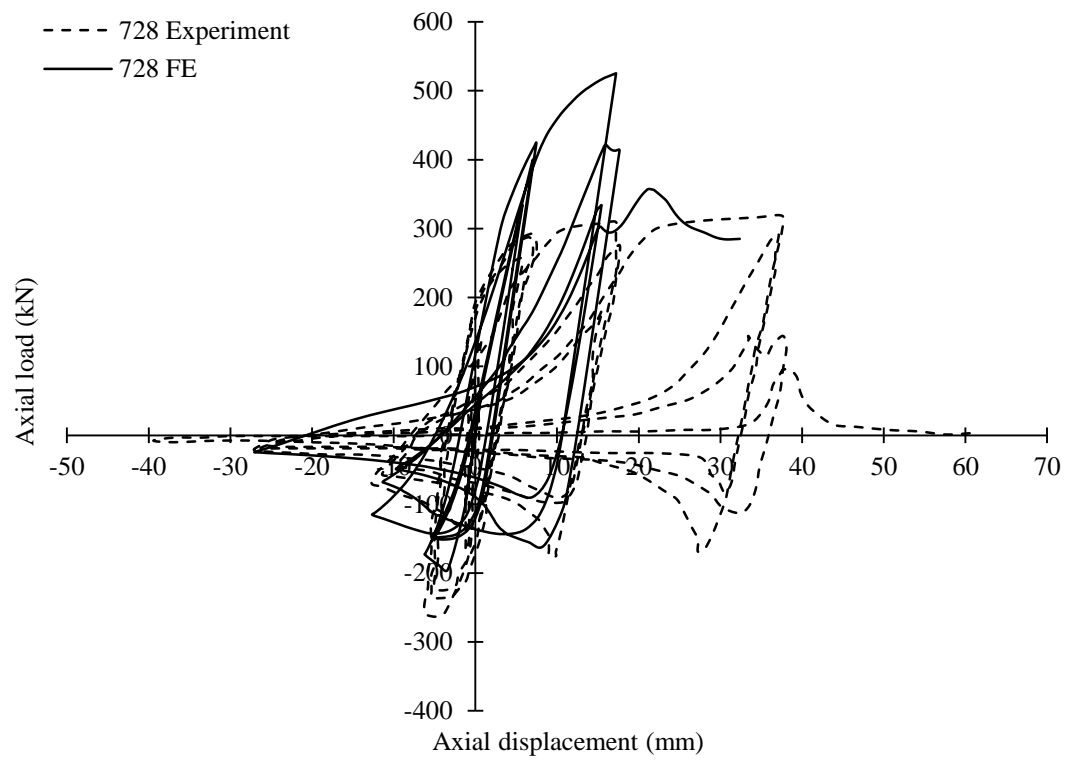


Figure 4.22 Load displacement hysteresis curves for specimen 728 (Takeuchi and Matsui, 2011)

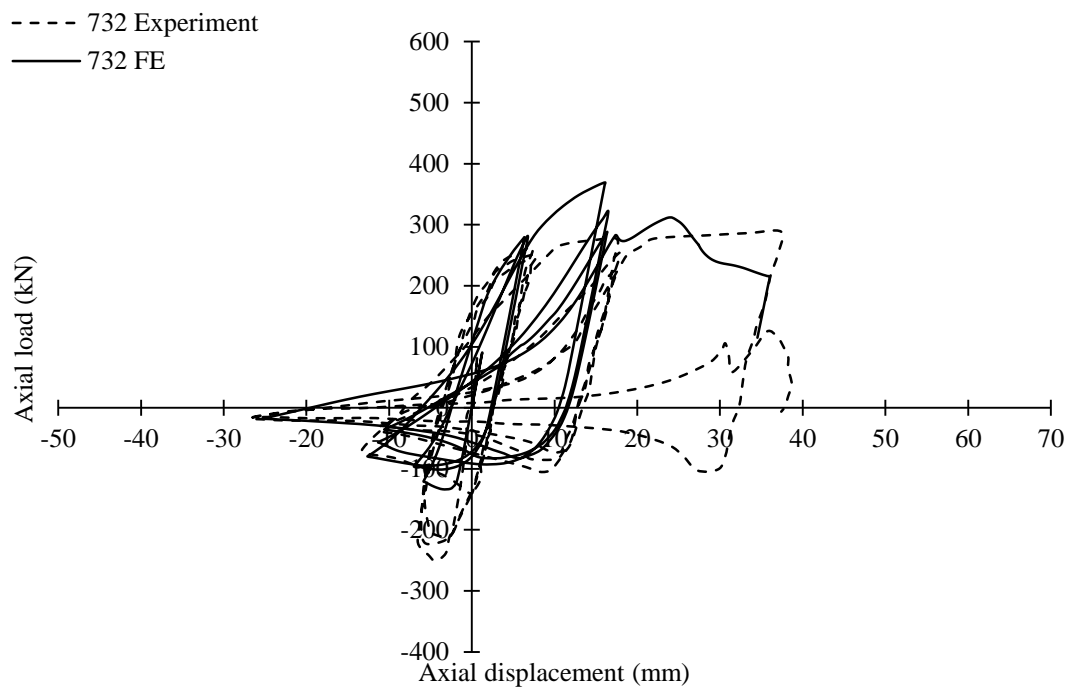


Figure 4.23 Load displacement hysteresis curves for specimen 732 (Takeuchi and Matsui, 2011)

#### 4.2.7 Parametric studies

Parametric studies were conducted once a satisfactory approach to the numerical modelling was established. Four specimen lengths were utilised to give  $\bar{\lambda} = 0.5, 1.0, 1.5$  and  $2.0$  in accordance with BS EN 1993-1-1 (2005). All braces were within the limit of  $\bar{\lambda} \leq 2.0$  given in BS EN 1998-1 (2004). Four different tube wall thicknesses were employed to give cross-sectional classifications of 1, 2, 3, and 4 (BS EN 1993-1-1, 2005). Details are provided for cold formed and hot-finished specimens in Tables 4.9 and 4.10 respectively.

Table 4.9 Specimen details for cold formed steel parametric studies

Specimen	$D$ mm	$t$ mm	$D/t\epsilon^2$	Class	$A_a$ mm <sup>2</sup>	$L$ mm	$\bar{\lambda}$
CF1	48.3	2.84	36.1	1	405.6	700	0.5
CF2	48.3	2.84	36.1	1	405.6	1400	1.0
CF3	48.3	2.84	36.1	1	405.6	2100	1.5
CF4	48.3	2.84	36.1	1	405.6	2800	2.0
CF5	48.3	1.7	60.3	2	248.9	715	0.5
CF6	48.3	1.7	60.3	2	248.9	1430	1.0
CF7	48.3	1.7	60.3	2	248.9	2145	1.5
CF8	48.3	1.7	60.3	2	248.9	2860	2.0
CF9	48.3	1.3	78.9	3	192.0	720	0.5
CF10	48.3	1.3	78.9	3	192.0	1440	1.0
CF11	48.3	1.3	78.9	3	192.0	2160	1.5
CF12	48.3	1.3	78.9	3	192.0	2880	2.0
CF13	48.3	1	102.6	4	148.6	725	0.5
CF14	48.3	1	102.6	4	148.6	1450	1.0
CF15	48.3	1	102.6	4	148.6	2175	1.5
CF16	48.3	1	102.6	4	148.6	2900	2.0

## Chapter 4 Numerical Simulations of Hollow Steel Braces

Table 4.10 Specimen details for hot finished steel parametric studies

Specimen	$D$ mm	$t$ mm	$D/t\epsilon^2$	Class	$A_a$ mm <sup>2</sup>	$L$ mm	$\bar{\lambda}$
HF1	48.3	3.2	26.7	1	453.4	800	0.5
HF2	48.3	3.2	26.7	1	453.4	1600	1.0
HF3	48.3	3.2	26.7	1	453.4	2400	1.5
HF4	48.3	3.2	26.7	1	453.4	3200	2.0
HF5	48.3	1.4	60.9	2	206.3	830	0.5
HF6	48.3	1.4	60.9	2	206.3	1660	1.0
HF7	48.3	1.4	60.9	2	206.3	2490	1.5
HF8	48.3	1.4	60.9	2	206.3	3320	2.0
HF9	48.3	1.1	77.5	3	163.1	835	0.5
HF10	48.3	1.1	77.5	3	163.1	1670	1.0
HF11	48.3	1.1	77.5	3	163.1	2505	1.5
HF12	48.3	1.1	77.5	3	163.1	3340	2.0
HF13	48.3	0.85	100.3	4	126.7	840	0.5
HF14	48.3	0.85	100.3	4	126.7	1680	1.0
HF15	48.3	0.85	100.3	4	126.7	2520	1.5
HF16	48.3	0.85	100.3	4	126.7	3360	2.0

All braces were fixed-ended and subjected to the ECCS (1986) cyclic axial loading protocol used in Chapter 3. In addition to this the same material properties were used as those for simulating the experiments in Chapter 3. The monitoring zone for predicting the number of cycles to fracture was taken circumferentially as the entire compression face and longitudinally as the row of elements which underwent the maximum strain. The majority of numerically tested specimens exhibited similar local buckling behaviour to the experimental braces, and hence the circumferential portion was easy to identify. Braces CF13, HF9 and HF13, each of which had a

large  $D/t$  ratio and  $\bar{\lambda} = 0.5$ , displayed a different buckled shape to the rest of the specimens, as shown in Figure 4.24. Hence the region for these was simply the section of perimeter at the centre of the compression face which underwent the maximum strain.

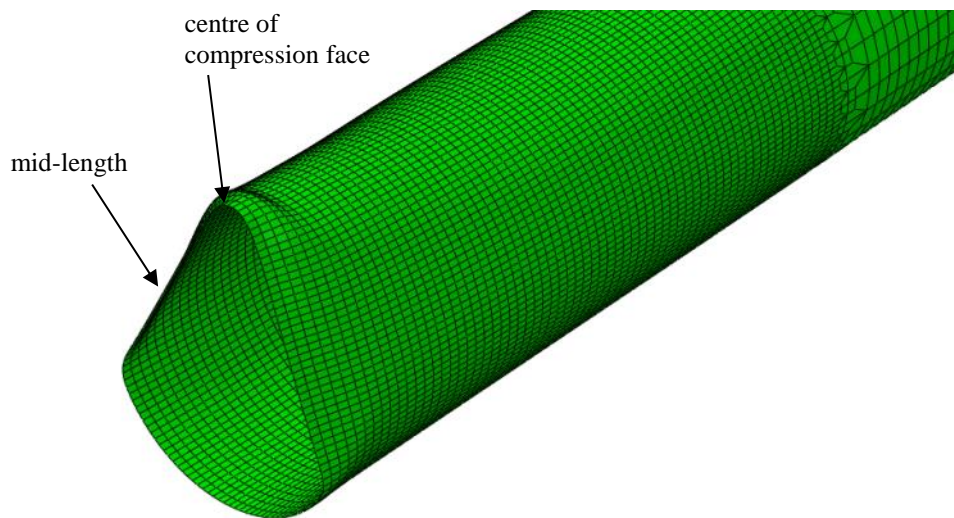


Figure 4.24 Buckled shape at mid-length for specimens CF13, HF9 and HF13

The load-displacement hysteresis curves for the braces defined in Tables 4.7 and 4.8 are presented in Appendix A.3. For the parametric study, predictions obtained from counting the individual strain amplitudes between successive ramps were closer to the results observed in the deformed shape and load-displacement hysteresis curves, than those resulting from the rainflow technique. Since it was also more conservative, the former approach was selected as the preferred method for predicting the number of cycles.

Once the number of cycles to failure was computed for each of the finite element models, the variation of this parameter was examined across different specimen sizes. Figures 4.25(a) to 4.25(d) show the variation in the number of cycles to failure

with  $\bar{\lambda}$  for each cross-section class, with a trendline corresponding to each section type.

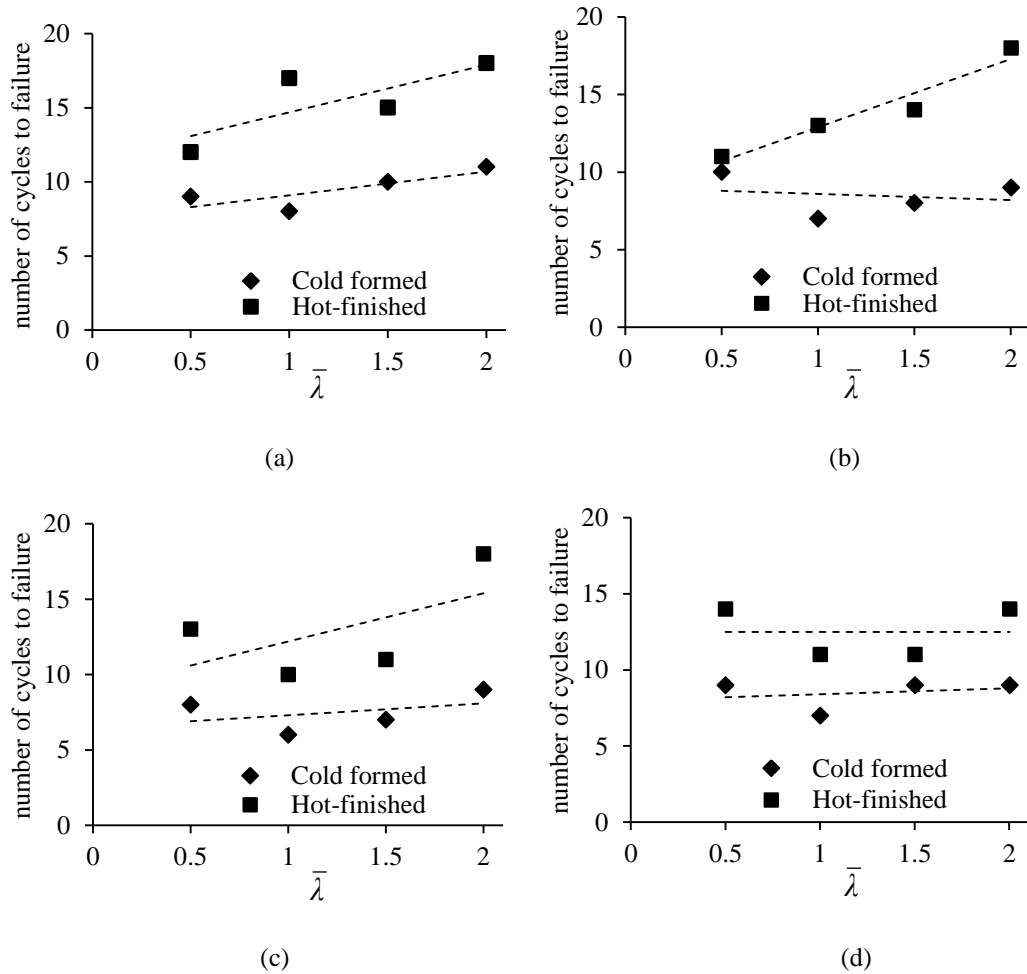


Figure 4.25 Relationship between number of cycles to failure and  $\bar{\lambda}$  for cross-section classifications of (a) Class 1; (b) Class 2; (c) Class 3; (d) Class 4 in accordance with BS EN 1993-1-1 (2005)

Hot-finished specimens endured noticeably larger numbers of cycles than cold formed specimens for all cross-section types and  $\bar{\lambda}$  values. For Class 1 and Class 2 sections, the number of cycles to failure generally increased with global slenderness increase. For Class 3 and 4 cross-sections however, higher numbers of cycles were endured by the shortest members, a result which was not observed for the thicker-walled sections. Overall, it was difficult to detect a trend between the number of cycles to failure and global slenderness that occurred for all cross-section classes.



Figures 4.26(a) to 4.26(d) illustrate the relationship between the number of cycles to failure and local slenderness,  $D/t\epsilon^2$ . Similarly to the findings in Figure 4.25, this relationship did not follow a consistent trend for members of each global slenderness value.

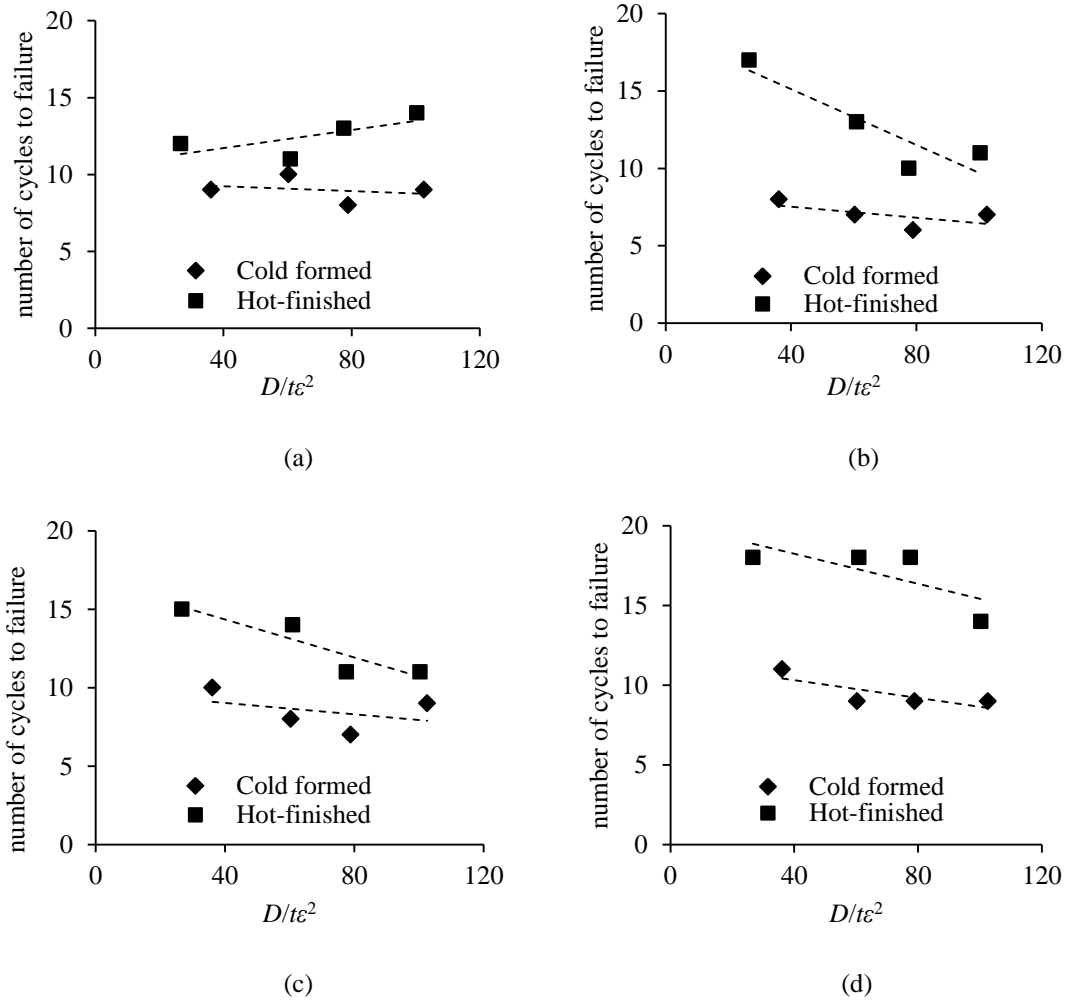


Figure 4.26 Relationship between number of cycles to failure and cross-sectional slenderness for global slenderness values of (a)  $\bar{\lambda} = 0.5$ ; (b)  $\bar{\lambda} = 1.0$ ; (c)  $\bar{\lambda} = 1.5$ ; (d)  $\bar{\lambda} = 2.0$  in accordance with BS EN 1993-1-1 (2005)

Previous relationships have been proposed to predict the number of cycles to failure of RHS braces in terms of local and global slenderness values. The number of cycles has been considered in terms of displacement ductility,  $\mu_{\Delta}$ , which is defined in this study as the maximum axial displacement divided by the yield displacement

parameter,  $\delta_y$ , where  $\delta_y$  is a function of material yield stress and member length. Goggins *et al.* (2006) proposed separate expressions for displacement ductility in terms of local slenderness and global slenderness. Nip *et al.* (2010a) developed expressions to predict the displacement ductility in terms of local and global slenderness combined. From Figures 4.25 and 4.26 it is evident that the displacement ductility would be difficult to predict in relation to local or global slenderness alone. Hence using the parametric studies results, the following relationships were proposed to predict the number of cycles to fracture for CHS braces using local and global slenderness combined.

For hot-finished specimens:

$$\mu_{\Delta} = 6.17 + 3.36\bar{\lambda} - 0.052D/t\epsilon^2 + 0.00045(D/t\epsilon^2)^2 - 0.022\bar{\lambda}D/t\epsilon^2 \quad (4.9)$$

For cold-formed specimens:

$$\mu_{\Delta} = 6.08 + 1.39\bar{\lambda} - 0.1D/t\epsilon^2 + 0.00073(D/t\epsilon^2)^2 - 0.013\bar{\lambda}D/t\epsilon^2 \quad (4.10)$$

Figure 4.27 compares the predicted displacement ductility from Equations (4.9) and (4.10) with the results from the parametric studies. The numerical simulations show a reasonable correlation to the predictions.

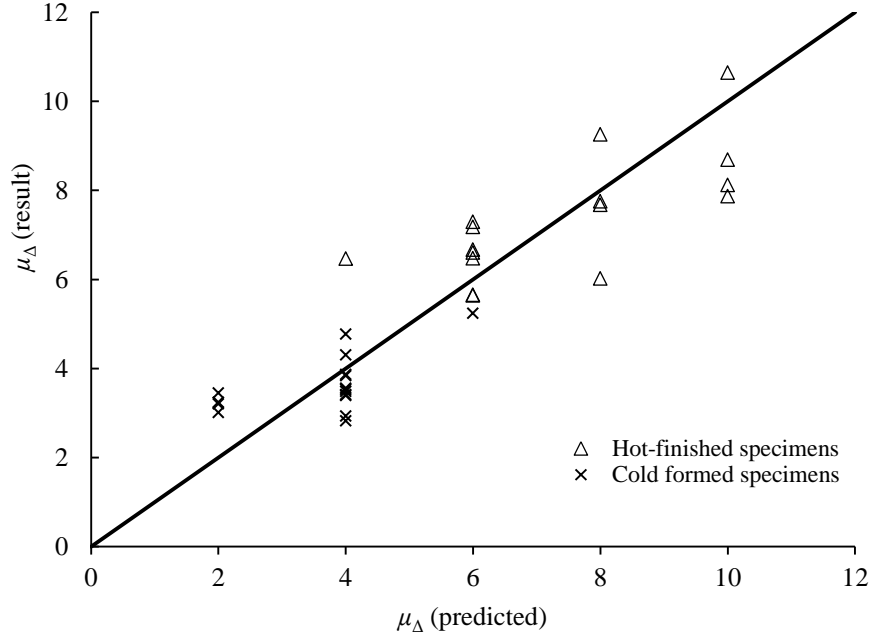


Figure 4.27 Comparison between predicted and actual values of displacement ductility,  $\mu_{\Delta}$

As mentioned previously, a primary function of the diagonal braces is the dissipation of the energy from the applied seismic loading. The dissipated energy was defined in this study as the external work carried out on the specimen, i.e. the area enclosed by the hysteresis curve. In previous research conducted on RHS braces by Goggins *et al.* (2006), the energy dissipated during the 8<sup>th</sup> loading cycle was used to assess the suitability of the specimens for their intended purpose. The energy dissipation during the 8<sup>th</sup> cycle for the CHS braces in this study is presented in relation to global slenderness and local slenderness in Figures 4.28(a) and 4.28(b) respectively for Class 1 cross-sections. The extent of energy dissipation per cycle decreased for increases in  $D/t\epsilon^2$  and  $\bar{\lambda}$  values. Similar trends were observed for cross section Classes 2-4. In these graphs, the energy was normalised with respect to the yield energy,  $W_y = A_a f_y \delta_y$ , where  $A$  was the cross-sectional area,  $f_y$  was the steel yield stress and  $\delta_y$  was the yield displacement. Hot-finished specimens dissipated relatively larger amounts of energy during the 8<sup>th</sup> cycle than cold formed specimens for cross-

sections with low  $D/t$  ratios and stocky members whereas cold-formed braces tended to dissipate higher amounts of energy as the local and global slendernesses were increased.

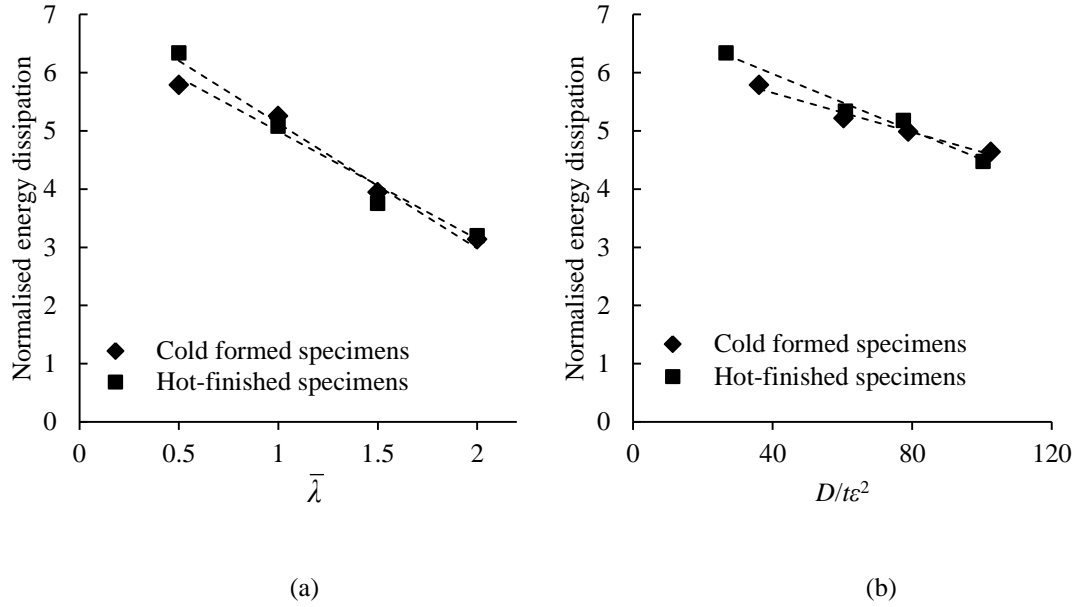


Figure 4.28 Relationship between normalised energy dissipation during 8<sup>th</sup> cycle and (a) global slenderness,  $\bar{\lambda}$ ; (b) local slenderness,  $D/t\epsilon^2$

Predictive expressions were proposed for the normalised energy dissipation during the 8<sup>th</sup> cycle,  $W_8$ , for cold formed and hot-finished tubes by (4.11) and (4.12) respectively.

For cold formed braces:

$$W_8 = 7.98 - 0.029D/t\epsilon^2 - 2.38\bar{\lambda} + 0.011\bar{\lambda} D/t\epsilon^2 + 0.075\bar{\lambda}^2 \quad (4.11)$$

For hot-finished braces:

$$W_8 = 9.2 - 0.036D/t\epsilon^2 - 4.46\bar{\lambda} + 0.016\bar{\lambda} D/t\epsilon^2 + 0.77\bar{\lambda}^2 \quad (4.12)$$

The correlation between the predicted energy dissipation from (4.11) and (4.12) and the actual energy dissipation from the finite element models in the 8<sup>th</sup> cycle is shown

in Figure 4.29. A close agreement was observed between the predicted and actual values, demonstrating that Equations (4.11) and (4.12) could provide reliable indicators of the specimen performance.

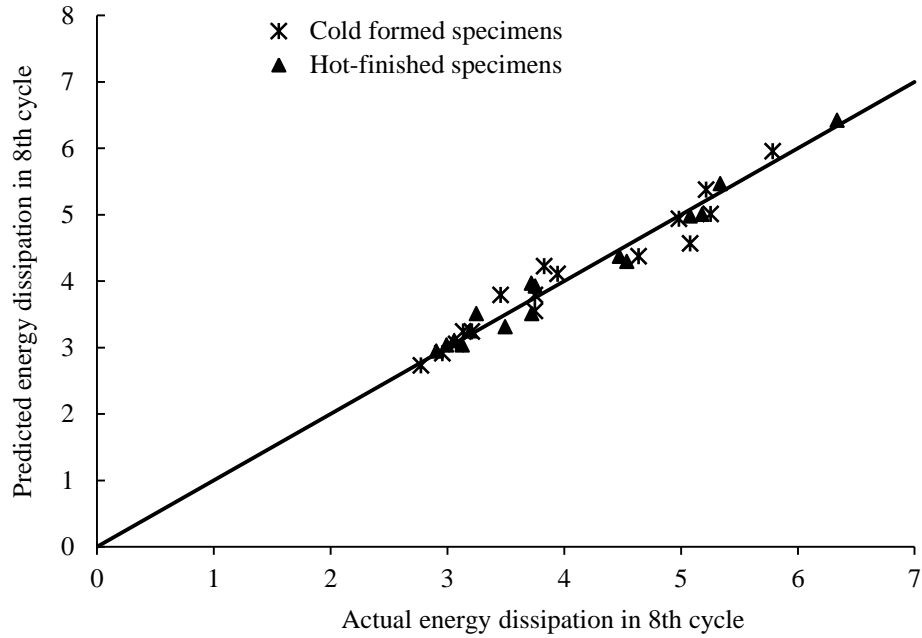


Figure 4.29 Comparison between predicted and actual energy dissipation during 8<sup>th</sup> cycle for cold formed and hot-finished specimens

Following this, the total energy dissipated prior to failure was also investigated for each cross-section type. Figures 4.30(a) and 4.30(b) present the relationship between the total normalised energy and the global and local slendernesses. Hot-finished braces were superior to cold formed braces in terms of total energy dissipation in most cases.

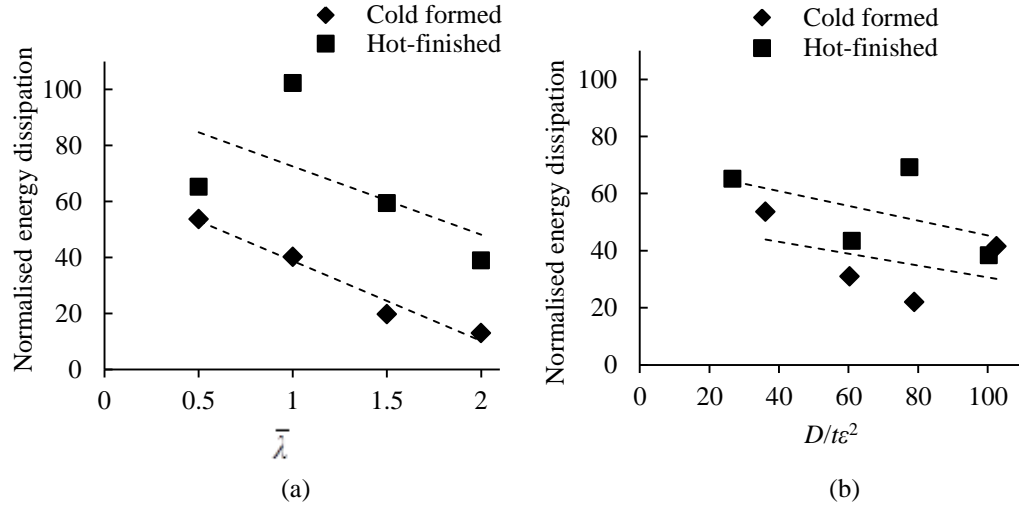


Figure 4.30 Relationship between total normalised energy dissipation prior to specimen failure and (a) global slenderness,  $\bar{\lambda}$ ; (b) local slenderness,  $D/t\epsilon^2$

The relationships between total energy dissipation and local/global slenderness were not as apparent as for the energy dissipated per cycle. Expressions for the total normalised energy dissipation prior to failure,  $W_T$ , were developed for each steel section type and are presented as follows:

For cold formed braces:

$$W_T = 155.5 - 2.75D/t\epsilon^2 - 91.6\bar{\lambda} + 0.0057(D/t\epsilon^2)^2 + 2.26\bar{\lambda} D/t\epsilon^2 + 0.00011(D/t\epsilon^2)^3 - 0.015\bar{\lambda} (D/t\epsilon^2)^2 \quad (4.13)$$

For hot-finished braces:

$$W_T = 66.39 - 5.86D/t\epsilon^2 - 345.3\bar{\lambda} + 0.092(D/t\epsilon^2)^2 + 0.65\bar{\lambda} D/t\epsilon^2 - 278.2\bar{\lambda}^2 - 0.0004(D/t\epsilon^2)^3 - 0.0076\bar{\lambda} (D/t\epsilon^2)^2 + 0.68\bar{\lambda}^2 (D/t\epsilon^2) + 58.62\bar{\lambda}^3 \quad (4.14)$$

Satisfactory predictions were obtained from these expressions. Figure 4.31 illustrates the correlation between the predictions of Equations (4.13) and (4.14). A

reasonable estimate was obtained in some cases, particularly for the cold formed specimens, but larger discrepancies occurred for the hot-finished braces.

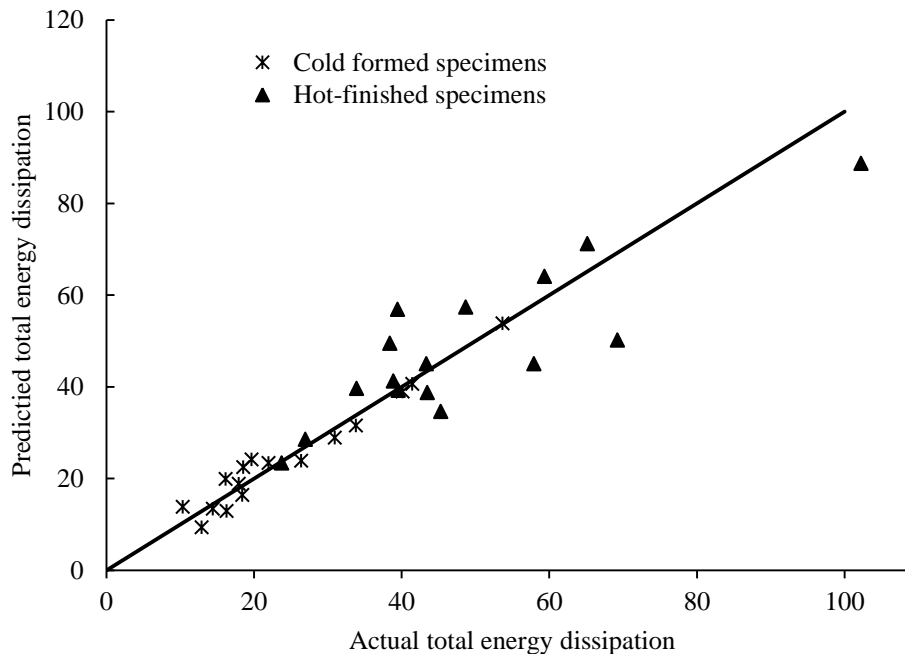


Figure 4.31 Comparison between predicted and actual total energy dissipation prior to specimen failure

### 4.3 Concluding remarks

The behaviour of cold formed and hot-finished CHS braces under cyclic axial loading was successfully simulated using finite element software. The nonlinear isotropic/kinematic hardening material model in ABAQUS® provided reliable computations of the maximum compressive and tensile forces in the members. The model also produced accurate simulations of the energy dissipation behaviour, as illustrated by the close correlation of the load-displacement hysteresis curve shapes with the experimental results. A strain-based approach proved satisfactory for analysing the fatigue behaviour in conjunction with Miner's rule (Miner, 1945) and the Coffin-Manson relationship (Coffin, 1954; Manson, 1954). Different approaches

were compared for calculating the strain amplitudes for each cycle: counting the individual half-cycles as they occurred or using the rainflow algorithm. The former method provided a suitable lower bound, whereas the latter gave an upper bound to the number of cycles to failure. Both local and global slenderness parameters were found to influence the displacement ductility,  $\mu_{\Delta}$ , and energy dissipation capability, and expressions were developed to predict these in terms of  $D/t\epsilon^2$  and  $\bar{\lambda}$ . The displacement ductility,  $\mu_{\Delta}$ , increased with increasing global slenderness,  $\bar{\lambda}$ , and decreased with increasing cross-sectional slenderness,  $D/t\epsilon^2$ . The energy dissipation per cycle decreased with increases in both  $\bar{\lambda}$  and  $D/t\epsilon^2$ . Overall, the finite element models underestimated the numbers of cycles to failure and hence there is scope for further work on this topic in future. However, since the results were slightly conservative, reasonable design recommendations could still be derived.



## **Chapter 5**

### **Numerical Simulations of Concrete-Filled Tubular Braces**

#### **5.1 Introduction**

This chapter describes the simulation of concrete-filled tubular braces under cyclic axial loading. Full three-dimensional models were developed in ABAQUS® following the approach of Chapter 4 but with the inclusion of concrete infill. Particular attention was paid to the definition of the concrete constitutive behaviour in both compression and tension.

#### **5.2 Modelling of concrete-filled steel braces**

##### **5.2.1 Boundary conditions and loading**

The concrete-filled tube models employed similar geometry and boundary conditions to those used for hollow steel tubes in the previous chapter. Models were generated in which the steel tube and concrete core were constructed as separate components. The axial cyclic loading protocol outlined in the ECCS guidelines (1986) was applied to the specimens in order to simulate the experiments described in Chapter 3.

##### **5.2.2 Element type and mesh**

Following from the simulations of hollow steel tubes described in Chapter 4, S4R shell elements were used for the steel shell. C3D8R elements were employed for the concrete core. These are 8-noded solid continuum elements, consisting of three translational degrees of freedom per node. The size of the mesh was determined from a sensitivity analysis in a similar approach to that of the steel tube and the mesh sizes are outlined in Table 5.1.

Table 5.1 Proposed mesh densities for concrete-filled tubes

Mesh	No. of elements around circumference
Mesh 1	6
Mesh 2	8
Mesh 3	12
Mesh 4	18

Monitoring regions were selected at a few locations along the tube length and the average strain values were recorded over each of these areas for each mesh. The relationship between strain and mesh density is depicted in Figure 5.1 at three different stages during the analysis. Stages 1, 2 and 3 correspond to the maximum axial compressive displacement in each of the first three loading cycles. Little change in response was observed for refinement beyond the level of that of Mesh 3 and hence this was selected for the remainder of the modelling.

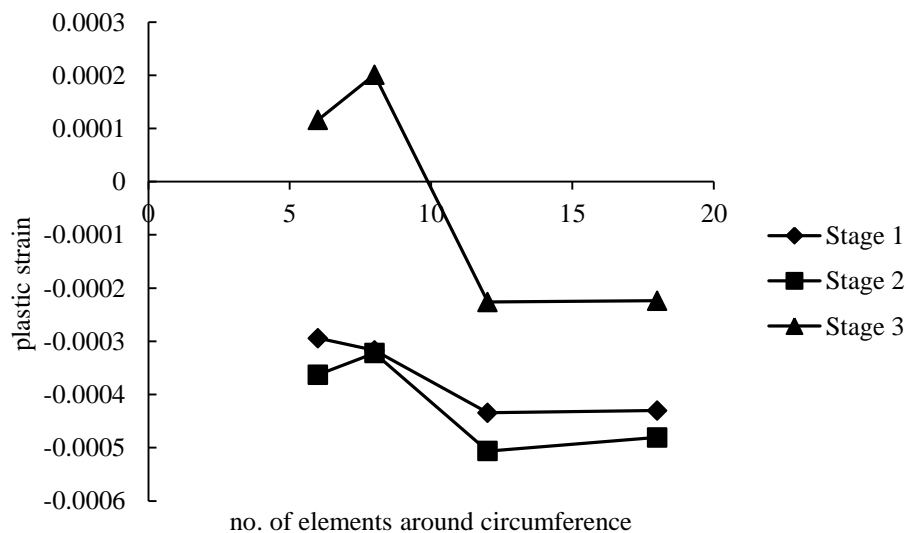


Figure 5.1 Variation in strain over monitoring area with increasing mesh density

### 5.2.3 Contact modelling

When modelling contact between two surfaces in ABAQUS®, one surface is selected as the ‘master’ surface while the other is the ‘slave’, the displacement of

which is monitored with respect to the master surface. Generally, the role of the master surface is more suited to the stronger/stiffer of the two contacting domains. This role is ambiguous in a concrete-filled steel tube, since the steel is a stiffer material, but is susceptible to local buckling and occupies a smaller portion of the cross-sectional area than the concrete. From preliminary analyses, the difference in results obtained from switching these roles was found to be negligible, and so the inner surface of the steel tube was selected for the master surface. This decision was made to better accommodate the inclusion of local geometric imperfections in the steel. The same variations in geometry were employed as those used for the hollow braces in Chapter 4 and the positions of the slave nodes (concrete core) were adjusted with respect to the master surface (steel tube) to remove overclosure between the contacting surfaces and ensure initial contact.

Contact conditions were employed following from previous research towards the modelling of concrete-filled tubes (Dai and Lam, 2010), using a ‘hard’ normal relationship in order to prevent penetration between the components, and a Coulomb friction model tangentially, with a coefficient of friction of 0.25. Due to the high confining pressure, little slip was expected to occur between the steel tube and concrete core under cyclic loading.

### **5.2.4 Concrete constitutive model**

For elastic behaviour, the value of Poisson’s ratio was taken as 0.3, following the approach of Goto *et al.* (2010) and the modulus of elasticity was 21,750 MPa, taking the average of the two values obtained from the material tests for the bracing experiments described in Chapter 3. The damaged plasticity model in ABAQUS® was used to define the concrete plastic behaviour. This employed a model proposed by Lubliner (1989) for frictional materials, which used a plastic damage variable

corresponding to a loss of cohesion in the material. The ABAQUS® model takes into account modifications to the Lubliner (1989) model which were later developed by Lee and Fenves (1998) to include distinct damage parameters for the material in compression and in tension. The yield surface of the model is given by:

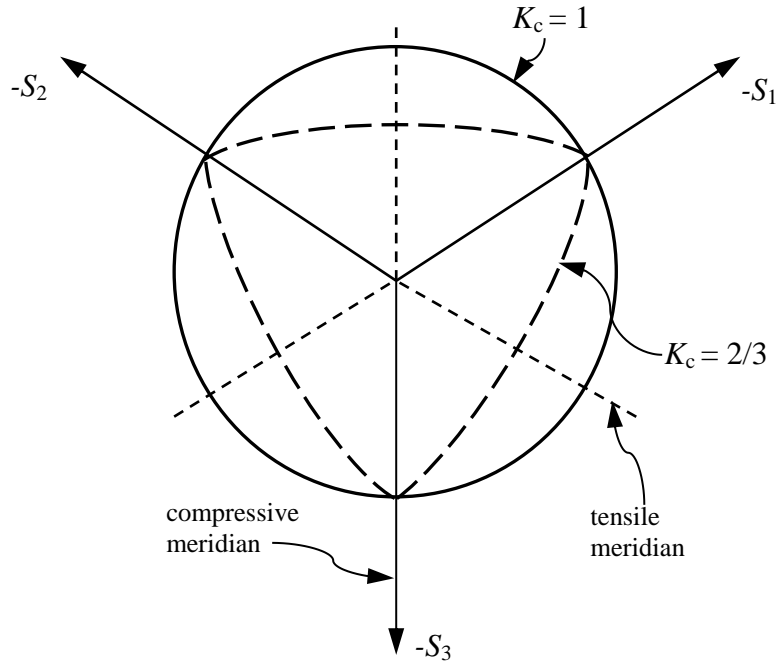
$$F = \frac{1}{1-\alpha} \left( \bar{q} - 3\alpha\bar{p} + \beta \left( \tilde{\varepsilon}^{pl} \right) \left( \hat{\sigma}_{\max} \right) - \gamma \left( -\hat{\sigma}_{\max} \right) \right) - \bar{\sigma}_c \left( \tilde{\varepsilon}_c^{pl} \right) = 0 \quad (5.1)$$

$\hat{\sigma}_{\max}$  is the maximum principal effective stress and the two variables,  $\tilde{\varepsilon}_t^{pl}$  and  $\tilde{\varepsilon}_c^{pl}$ , are used to control the yield surface, and are referred to as the tensile and compressive equivalent plastic strains. Expression of the equation is simplified by implementing the functions  $\alpha$ ,  $\beta$  and  $\gamma$ .  $\alpha$  incorporates the relationship between the initial equibiaxial compressive stress,  $\sigma_{b0}$ , to the initial uniaxial compressive stress,  $\sigma_{c0}$ , into the yield function, while  $\beta$  accounts for the ratio between the effective compressive cohesion stress,  $\bar{\sigma}_c(\tilde{\varepsilon}_c^{pl})$  and the effective tensile cohesion stress,  $\bar{\sigma}_t(\tilde{\varepsilon}_t^{pl})$ .  $\gamma$  only enters the yield function for states of triaxial compression and is expressed in terms of the variable  $K_c$ , which is the ratio of the second stress invariant on the tensile meridian,  $q_{(TM)}$ , to that on the compressive meridian,  $q_{(CM)}$ , at initial yield for any given value of the pressure invariant  $p$  such that the maximum principal stress is negative,  $\hat{\sigma}_{\max} < 0$ , with  $0.5 < K_c \leq 1.0$ . The compressive meridian is defined as the locus of stress states such that  $\hat{\sigma}_{\max} = \hat{\sigma}_1 = \hat{\sigma}_2 > \hat{\sigma}_3$  and the tensile meridian is defined as the locus of stress states such that  $\hat{\sigma}_{\max} = \hat{\sigma}_1 > \hat{\sigma}_2 = \hat{\sigma}_3$ , where  $\hat{\sigma}_1$ ,  $\hat{\sigma}_2$  and  $\hat{\sigma}_3$  are the eigenvalues of the effective stress tensor.  $\alpha$ ,  $\beta$  and  $\gamma$  are expressed mathematically by the following equations and the effect of the value of  $K_c$  on the yield surface in deviatoric space is depicted in Figure 5.2.

$$\alpha = \frac{(\sigma_{b0}/\sigma_{c0})-1}{2(\sigma_{b0}/\sigma_{c0})-1} \quad \text{with } 0 \leq \alpha \leq 0.5 \quad (5.2)$$

$$\beta = \frac{\bar{\sigma}_c(\tilde{\epsilon}_c^{pl})}{\bar{\sigma}_t(\tilde{\epsilon}_t^{pl})}(1-\alpha)-(1+\alpha) \quad (5.3)$$

$$\gamma = \frac{3(1-K_c)}{2K_c-1} \quad (5.4)$$


 Figure 5.2 Effect of  $K_c$  on yield surface in deviatoric space

Definitions of the variables in Equations (5.2) to (5.4) can be found in the Notation list at the beginning of the thesis. The damaged plasticity model uses a non-associated flow rule, which means that the relationship between stress and plastic strain after yielding is independent of the yield function. The flow rule used in the concrete damaged plasticity model is given by the function:

$$G = \sqrt{(e\sigma_{10} \tan \psi)^2 + \bar{q}^2} - \bar{p} \tan \psi \quad (5.5)$$

$$\text{with } \dot{\epsilon}^{pl} = \dot{\lambda} \frac{\partial G(\bar{\sigma})}{\partial \bar{\sigma}} \quad (5.6)$$

This is used to describe the relationship between stress and strain after yield. In this equation,  $\psi$  is the angle of dilation which describes the plastic volumetric strain during shearing. This is measured in the  $p$ - $q$  plane under high confining pressure and the value is usually in the range of  $36^\circ - 40^\circ$  for the ABAQUS® damage plasticity model.  $e$  is the eccentricity, which defines the rate at which the flow approaches the asymptote. For low values of  $e$ , the flow function is almost a straight line.  $\dot{\lambda}$  in Equation (5.6) is the plastic loading factor.

This plasticity model was described in ABAQUS® using five input parameters:  $\psi$ ,  $\sigma_{b0}/\sigma_{c0}$ ,  $e$ ,  $K_c$  and a viscosity parameter,  $\mu$ . In this thesis, values of 1.16, 0.1 and 0.67 were employed for  $\sigma_{b0}/\sigma_{c0}$ ,  $e$  and  $K_c$  respectively, since these were the recommended values in the ABAQUS® Analysis User Manual. A value of  $38^\circ$  was selected for  $\psi$  following from Goto *et al.* (2010). Use of the viscosity parameter incorporates viscoplastic regularisation into the model, allowing the tangent stiffness of the concrete to become positive for short periods of time during softening. This can be utilised to ease convergence issues in the model. The default value of  $\mu$  was 0, but this led to difficulties in convergence. Hence a separate model was constructed in order to determine an appropriate value for  $\mu$ . This consisted of a short concrete column which was placed under axial tension. The axial capacity of the section was compared with the predicted strength based on the material properties. Using a large value of  $\mu$  (0.1) in relation to the time increment (0.002), resulted in overestimating the concrete strength by a factor of approximately 2. Following this, models were analysed using progressively smaller values of  $\mu$  until the resulting axial loads complied with the input material properties. Eventually a value of 0.0001 was

selected for  $\mu$ , since this eased convergence issues but was sufficiently small to maintain reliable predictions of the material response.

The constitutive relationships for uniaxial tension and compression were defined separately in addition to the compressive and tensile damage. The response under uniaxial compression was defined using the model developed by Hu *et al.* (2003) for concrete-filled tubes. In this model, the strength of confined concrete,  $f'_{cc}$ , and the corresponding strain,  $\epsilon'_{cc}$ , were calculated using the relationship proposed by Mander *et al.* (1988), given as:

$$f'_{cc} = f'_c + k_1 f_l \quad (5.7)$$

$$\epsilon'_{cc} = \epsilon'_c \left( 1 + \frac{k_2 f_l}{f'_c} \right) \quad (5.8)$$

where  $f'_c$  was the compressive strength of unconfined concrete,  $\epsilon'_c$  was the corresponding strain taken as 0.003 and  $f_l$  was the lateral pressure of the concrete. Values of 4.1 and 20.5 were taken for constants  $k_1$  and  $k_2$  respectively from Richart *et al.* (1928), and the following expressions were proposed by Hu *et al.* (2003) for  $f_l$

$$\text{For } 21.7 \leq D/t \leq 47, f_l/f_y = 0.044 - 0.00083 (D/t) \quad (5.9)$$

$$\text{For } 47 \leq D/t \leq 150, f_l/f_y = 0.0062 - 0.000036(D/t) \quad (5.10)$$

The nonlinear concrete stress-strain relationship up to  $f'_{cc}$  was given by Saenz (1964):

$$f_c = \frac{E_c \epsilon_c}{1 + (R + R_E - 2) \left( \frac{\epsilon_c}{\epsilon'_{cc}} \right) - (2R - 1) \left( \frac{\epsilon_c}{\epsilon'_{cc}} \right)^2 + R \left( \frac{\epsilon_c}{\epsilon'_{cc}} \right)^3} \quad (5.11)$$

where  $f_c$  and  $\varepsilon_c$  were the concrete stress and strain;  $R = \frac{R_E(R_\sigma - 1)}{(R_\varepsilon - 1)^2} - \frac{1}{R_\varepsilon}$ ;

$$R_E = \frac{E_c \varepsilon_{cc}'}{f_{cc}'}; R_\sigma = R_\varepsilon = 4$$

The maximum stress was followed by a linear softening region, shown in Figure 5.3, defined from the point  $(\varepsilon_{cc}', f_{cc}')$  to  $(11\varepsilon_{cc}', k_3 f_{cc}')$ , where  $k_3$  was given by Hu *et al.* (2003) as:

$$1 \text{ for } 21.7 \leq D/t \leq 40 \quad (5.12)$$

$$0.000034(D/t)^2 - 0.010(D/t) + 1.35 \text{ for } 40 \leq D/t \leq 150 \quad (5.13)$$

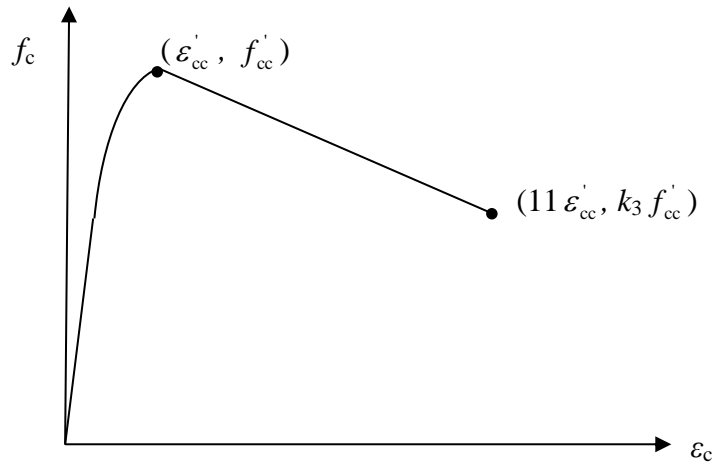


Figure 5.3 Concrete constitutive behaviour in compression from Hu *et al.* (2003)

ABAQUS® provides a number of options for defining the tensile behaviour of concrete. The stress can either be related to the strain in the direction of cracking, ‘displacement’, which refers to the crack width,  $u_{cr}$ , or the fracture energy,  $G_f$ . Once the tensile stress reaches the yield stress value (assumed to be equal to  $0.1 \times$  the compressive yield stress), cracking initiates. As the crack opens, the stress transmitted across this region degrades until it reaches zero. The parameter  $G_f$  describes the amount of energy required to open a crack across a unit area, and



usually has a value in the range of 40 N/m – 120 N/m for concrete with compressive strengths of 20 – 40 MPa. Assuming a linear degradation in stress with increasing crack-width, the fracture energy is calculated as the area under the graph in Figure 5.4.

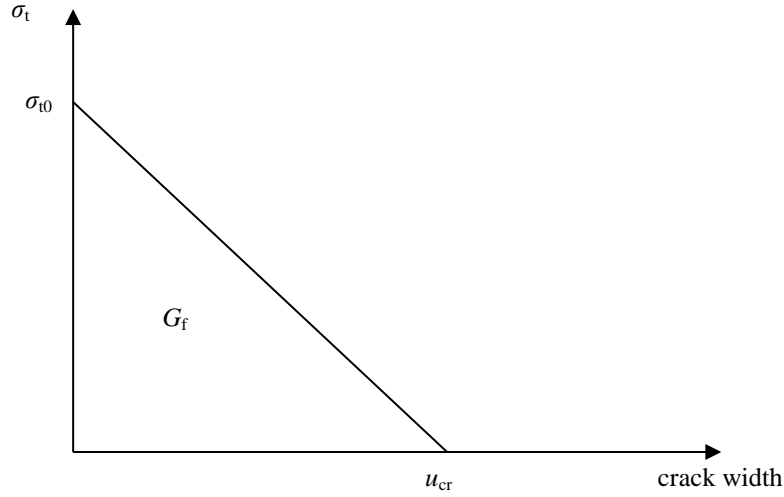


Figure 5.4 Relationship between tensile stress and crack width for concrete

For this model, the ‘displacement’ parameter was used. For C30 concrete, a value of 80 N/m was assumed for  $G_f$ , and the corresponding crack-width was calculated as

$$u_{cr} = 2G_f/\sigma_{t0} \quad (5.14)$$

As described in Chapter 2, the damaged plasticity model employs damage parameters,  $d_c$  and  $d_t$ , to compute the degradation of the elastic modulus during unloading. The compression damage in this thesis was defined using the following relationship by Goto *et al.* (2010).

$$d_c = \frac{k_{ci} \varepsilon_{cp}}{\left(1 + \left(\frac{\varepsilon_{cp}}{\varepsilon_0}\right)^n\right)^n} \quad (5.15)$$

where  $\varepsilon_{cp}$  is the plastic strain,  $\varepsilon_0$  is the strain at yield,  $n = 1.08$  and  $k_{ci} = 155$ .

Following from the linear relationship shown in Figure 5.4, the tension damage parameter,  $d_t$ , was also assumed to increase linearly with increasing crack width for the sake of simplicity. The model also included stiffness recovery factors,  $w_t$  and  $w_c$ , to describe the stiffness during load reversals. These are illustrated in Figure 5.5. The default values in ABAQUS® were chosen for this research, which are  $w_t = 0$  and  $w_c = 1$ . A value of  $w_t = 0$  means that when the loading is reversed from compression into tension, the tensile stiffness is not recovered, owing to the development of micro-cracks in the material from crushing in compression. The assumption of  $w_c = 1$  indicates that as the loading is reversed from tension into compression, the full compressive stiffness is recovered ( $E_0$  in Figure 5.5), since the cracks which occurred during tensile loading are closed.

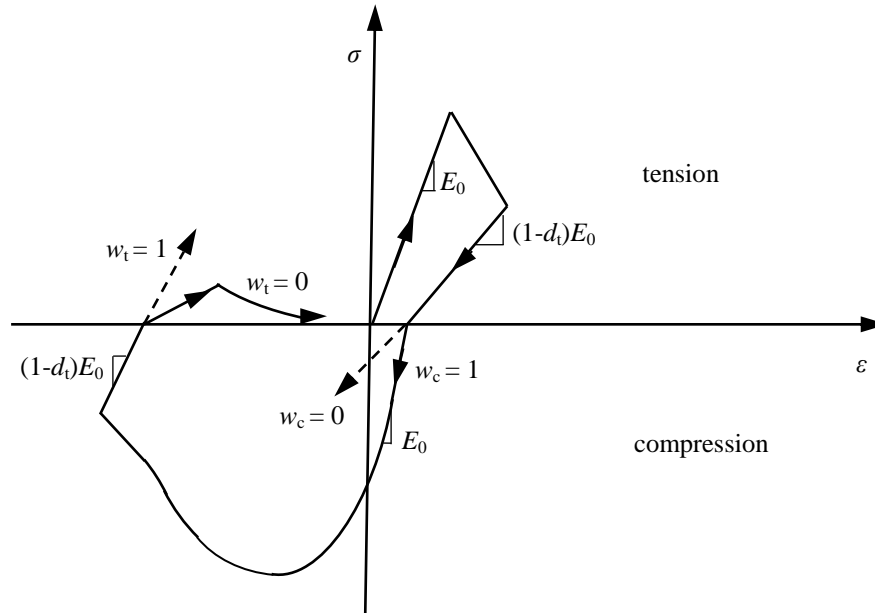


Figure 5.5 Illustration of stiffness recovery factors for concrete in tension and compression

### 5.2.5 Verification of FE model

The results from the finite element models are compared with the laboratory test results in Table 5.2. The specimen identifications are shown in the first column. The numbers of cycles to global buckling are presented for the finite element models and test specimens in the second and third columns respectively. The numbers of cycles to local buckling are compared in the fourth and fifth columns while the numbers of cycles to fracture are in the sixth and seventh columns. In addition to this, the maximum tensile and compressive loads are presented for the numerical simulations and each corresponding laboratory test specimen in the columns further to the right in Table 5.2. The numbers of cycles to global buckling, presented in the second and third columns, were identified from the load displacement hysteresis behaviour and from visual observations in the tests. A reasonable agreement was achieved between the test specimens and FE simulations for the number of cycles to global buckling, with results differing by no more than one cycle.

Table 5.2 Comparison between laboratory test specimen and finite element model results for concrete-filled tubular braces

Specimen	No. of cycles to						Max tension		Max	
	global		local		fracture		force		compression	
	FE	test	FE	test	FE	test	FE	test	FE	test
CF-F1-1500	4	5	8	8	8	15	260	220	201	174
CF-F2-1500	4	5	8	8	8	16	260	216	201	164
HF-F1-1500	4	5	11	8	14	28	247	198	196	174
HF-F2-1500	4	5	11	7	14	19	247	198	196	175
CF-F1-3000	2	3	8	8	10	17	270	223	83	72
CF-F2-3000	2	3	8	8	10	18	270	227	83	71
HF-F1-3000	3	3	12	8	19	25*	225	203	95	83
HF-F2-3000	3	3	12	8	19	25*	225	198	95	88

\* test terminated when actuator stroke limit reached

Although some outward local buckling was visible in the concrete-filled braces during the experiments, this was not as apparent in the numerical simulations, as depicted by the deformed shape at the mid-length in Figure 5.6. Hence the initiation of ‘local buckling’ in the finite element models was defined as the stage at which the plastic strains in two longitudinally adjacent nodes at the mid-length deviated from each other by more than 10%, following from the definition used in the hollow brace simulations in Chapter 4. It was found that once a small divergence such as this occurred, the strain values continued to diverge by increasingly larger amounts as the analysis progressed. From the experimental data, initiation of local buckling was detected using the strain gauge readings. An abrupt increase in strain was simultaneously observed in all four strain gauges around the cross-section perimeter at this stage.

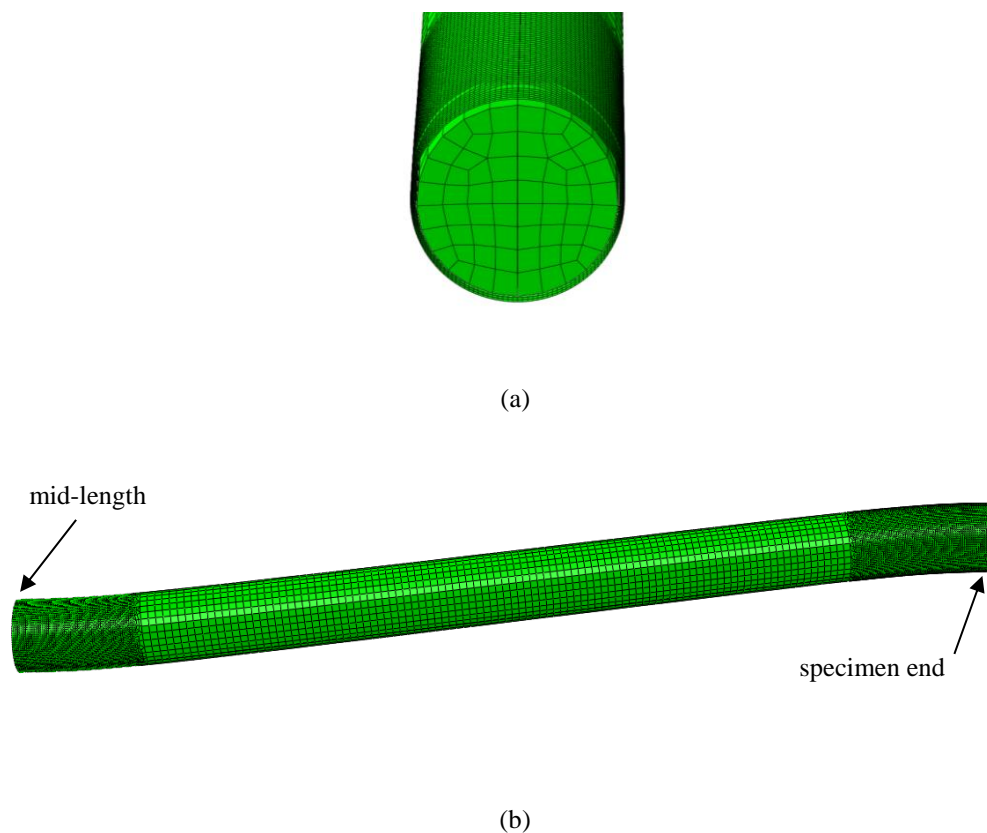


Figure 5.6 Deformed shape of FE specimen CF-F-1500: (a) cross-section view at mid-length; (b) side view of specimen

The numbers of cycles to fracture were identified in the FE specimens following a similar procedure to that for the hollow specimens in Chapter 4, using the Coffin-Manson relationship (Coffin, 1954; Manson, 1954), Miner's Rule (Miner, 1945) and the fatigue ductility parameters obtained by Nip *et al.* (2010b). Considering a particular specimen in Table 5.2, say, HF-F1-1500, it is shown that the finite element model provides a reasonable estimation of the number of cycles to global buckling (4 in FE, 5 in test), but overestimates the number of cycles to local buckling (11 in FE, 8 in test) and underestimates the number of cycles to fracture (14 in FE, 28 in test). The maximum tensile force is noticeably larger in the finite element model (247 kN) than that which occurred in the experiment (198 kN) but there is a better agreement between the maximum compression forces (196 kN in FE, 174 kN in test). In general, the cold formed models CF-F-1500 and CF-F-3000 had the same number of cycles to local buckling as their equivalent test specimens, CF-F1-1500, CF-F2-1500, CF-F1-3000 and CF-F2-3000. It has been established that the hot-finished models HF-F-1500 and HF-F-3000 experienced local buckling at 3 to 4 cycles later than in the laboratory tests. Larger discrepancies occurred in predicting the number of cycles to fracture for both cold formed and hot-finished braces. Greater values for maximum tensile and compressive force were always obtained for the computational work. Differences in tensile and compressive forces are also apparent in the load-displacement hysteresis curves, which are compared for CF-F1-1500 (experiment) and CF-F-1500 (FE model) in Figure 5.7. The same sign convention is adopted in this figure as in Chapters 3 and 4 with the positive sense of the axes conveying tensile forces and displacements and negative direction denoting compressive forces and displacements.

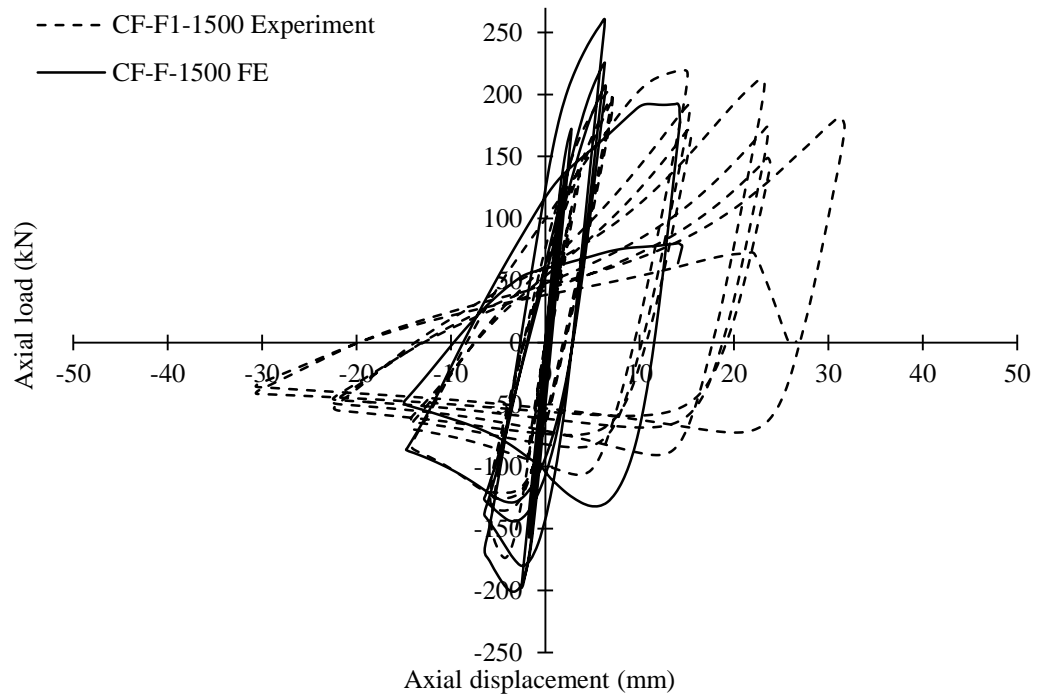


Figure 5.7 Load displacement hysteresis curves for specimen CF-F1-1500

The shapes of the hysteresis curves are similar during the early cycles but greater differences are apparent in the later stages of the tests. Models of the other specimens produced similar results, and the hysteresis curve for each of these is compared with the equivalent laboratory specimen in Figures 5.8 to 5.14. In some cases, the tensile resistance was reduced dramatically during the cycles prior to fracture, and this is particularly noticeable for the hot-finished 3000 mm brace shown in Figures 5.13 and 5.14.

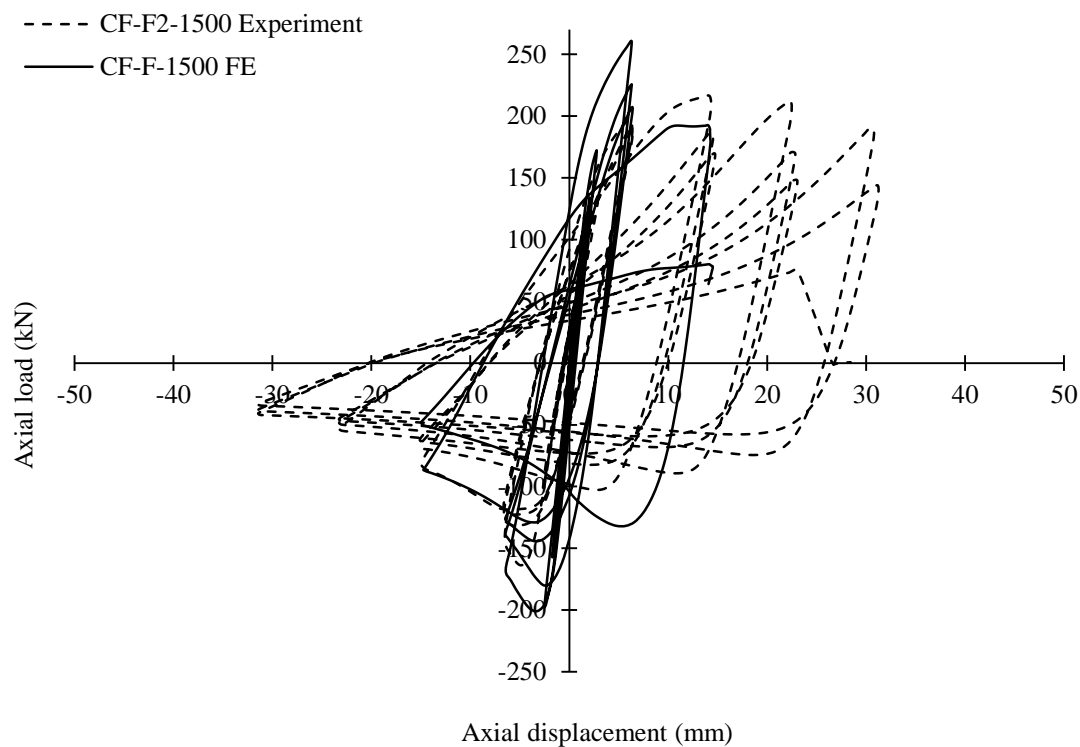


Figure 5.8 Load displacement hysteresis curves for specimen CF-F2-1500

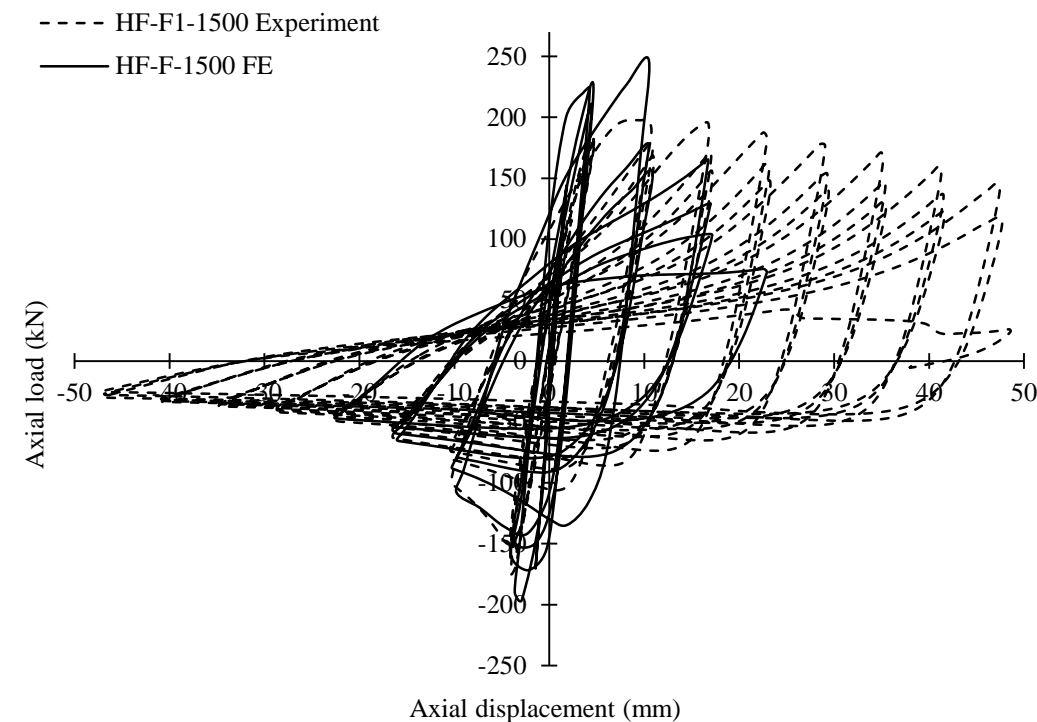


Figure 5.9 Load displacement hysteresis curves for specimen HF-F1-1500

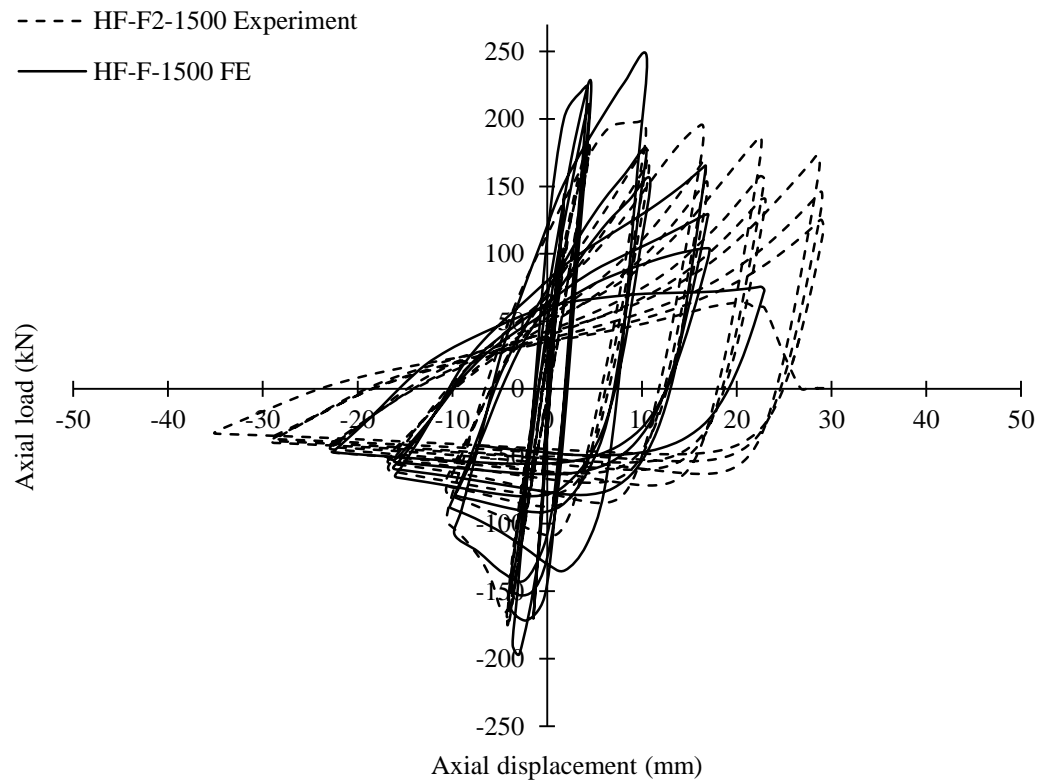


Figure 5.10 Load displacement hysteresis curves for specimen HF-F2-1500

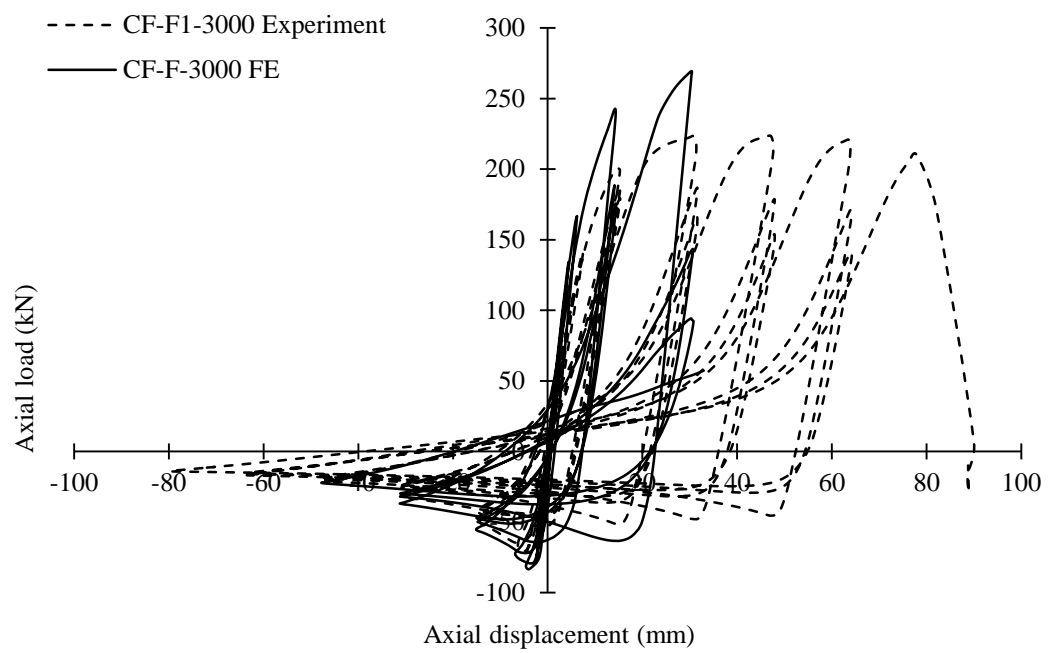


Figure 5.11 Load displacement hysteresis curves for specimen CF-F1-3000



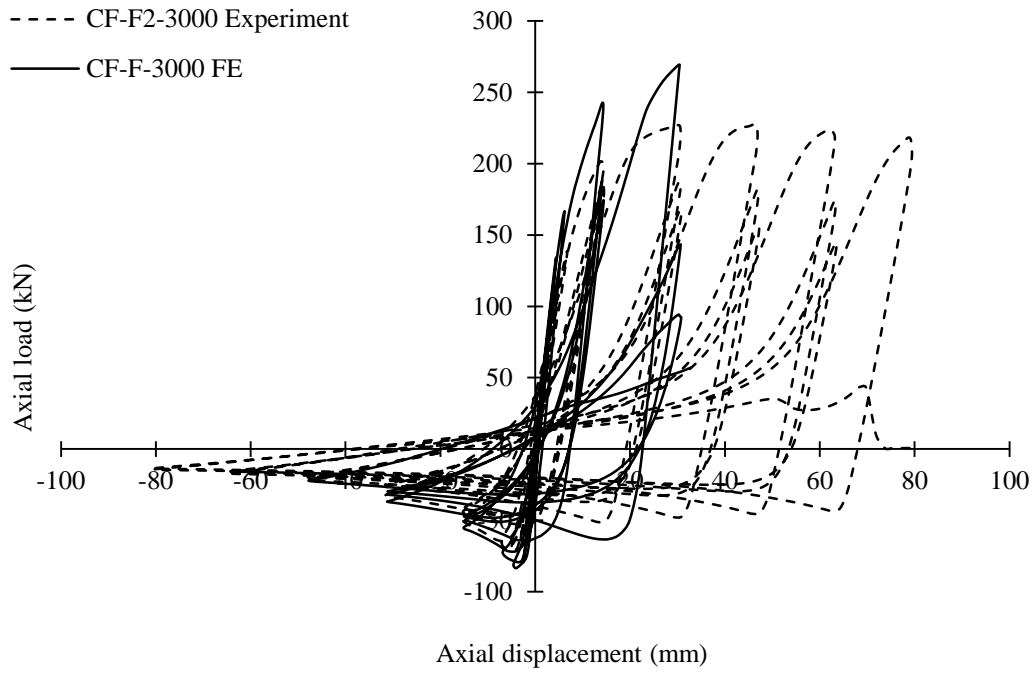


Figure 5.12 Load displacement hysteresis curves for specimen CF-F2-3000

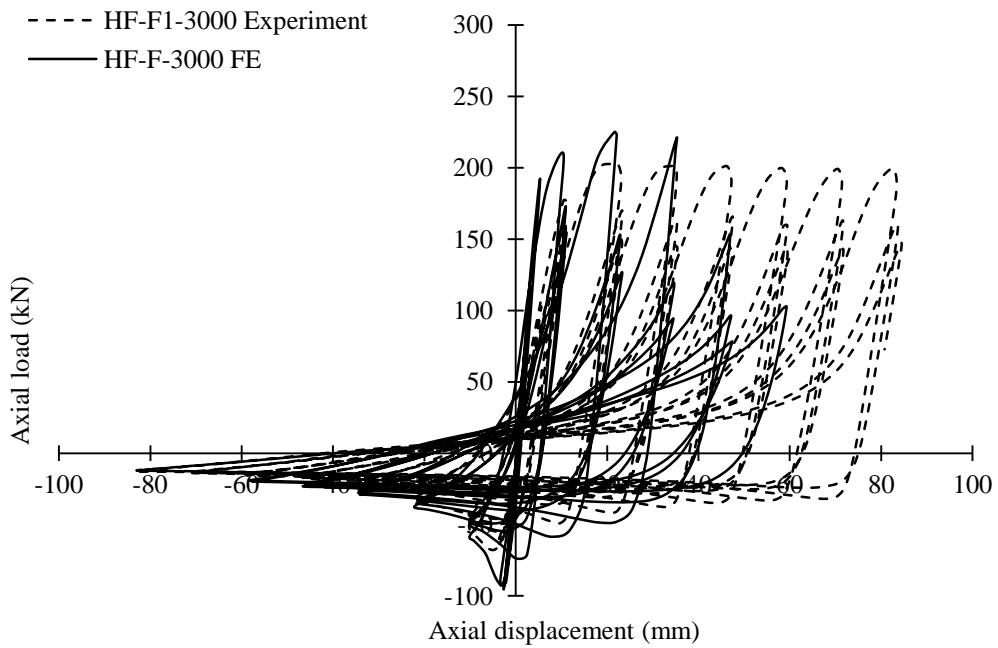


Figure 5.13 Load displacement hysteresis curves for specimen HF-F1-3000

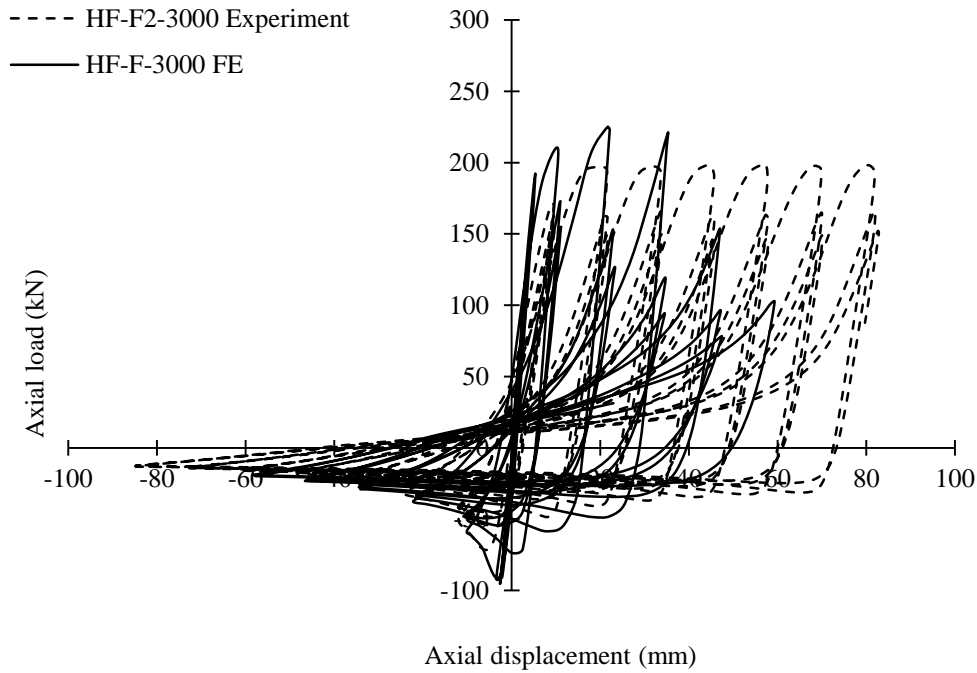


Figure 5.14 Load displacement hysteresis curves for specimen HF-F2-3000

The influence of a number of parameters was investigated with the objective of alleviating this issue. The first source of concern was the coefficient of friction at the steel-concrete interface, which had been assigned a value of 0.25. However, decreasing or increasing this value was found to have a negligible effect on the results. The input parameters for the material models were also explored but most of these were found to have little influence on the outcome. Consideration was also given to altering the amplitude and shape of the local imperfections, but this did not mitigate the premature failure predicted by the numerical models. It was concluded that the adopted modelling approach could not adequately capture the response of composite braces under cyclic loading. One possible solution would be to employ a different steel material model, such as the three-surface plasticity model of Goto *et al.* (2010), implemented by a user subroutine in ABAQUS®. While this would be more complex to implement, it should provide more reliable simulations of the steel material hardening, since the model parameters are updated as the analysis

progresses. Another possible issue is the interface properties which were assumed between the steel tube and concrete core. A more detailed simulation of this interface may improve the accuracy of the simulations. An alternative option would be to simplify the model and to assign equivalent properties to a composite section, instead of constructing separate steel and concrete constituents. Although the material properties may be difficult to determine, this would reduce the computational demand and potentially eliminate concerns regarding the steel-concrete interface.

### **5.3 Concluding remarks**

Initial numerical simulations have been carried out for concrete-filled tubular braces under cyclic axial loading. The response in the early stages of the analysis bore a close resemblance to that observed in the experiments, but deviated from the test specimen behaviour as the loading protocol progressed. Thus, while the finite element models computed reasonable estimations of the maximum tensile and compressive resistances, the number of cycles to fracture was significantly underestimated. Initial sources of inaccuracy were explored but it was concluded that an adequate simulation technique could not be developed within the scope of this thesis. Alternative approaches have been proposed for future work in this area.

## **Chapter 6**

### **Design Recommendations**

#### **6.1 Introduction**

This chapter discusses the results from the experimental and numerical work and the implications of these on existing design guidelines. The discussion covers aspects such as the first cycle buckling load, post-buckling resistance, tensile resistance and displacement ductility with regard to the design philosophy of BS EN 1998-1 (2004).

#### **6.2 First cycle buckling load**

As discussed in Chapter 2, overstrength is an important feature of seismic design. Hence, reliable predictions of compressive resistance are vital in concentrically braced frames. While members must be able to withstand several loading cycles prior to failure, excessive compressive forces may overload other structural components or lead to undesirable failure modes. Results for the first cycle buckling load were presented in Chapter 3. In all cases the maximum test load exceeded the predicted buckling load from BS EN 1993-1-1 (2005)/BS EN 1994-1-1 (2004). For the 1.5 m long specimens ( $\bar{\lambda} = 0.78 - 0.92$ ) the actual buckling load exceeded the predicted by less than 20 % in all cases, except for the cold formed hollow specimen, CF-H-1500. For the 3.0 m specimens ( $\bar{\lambda} = 1.72 - 2.02$ ), the first cycle buckling load was greater than 1.3 times the predicted load, and again, the cold formed hollow tube resistance surpassed the prediction to a greater extent, being 1.66 times the prediction. The experimental evidence suggests that alternative methods to the current buckling curves should be developed in order to predict the maximum compressive force of cyclically loaded braces, particularly for longer tubes with  $\bar{\lambda} >$

1.0 and for cold formed tubes. Similar results were obtained from the finite element analysis for most specimens. The data are presented in Tables 6.1 and 6.2 for cold formed and hot-finished members respectively. The first column of each table presents the specimen identification which was used in Chapters 3 to 5. Both laboratory test specimens from Chapter 3 and their equivalent finite element models are included, followed by the specimens from the parametric finite element study of hollow steel braces covered in Chapter 4. The second and third columns contain for the specimens the cross-section classification and non-dimensional global slenderness value,  $\bar{\lambda}$ , calculated in accordance with BS EN 1993-1-1 (2005)/BS EN 1994-1-1 (2004). The first cycle buckling load,  $N_{c,max}$ , from the tests and numerical analyses are compared with the buckling load,  $N_{b,Rd}$ , from BS EN 1993-1-1 (2005)/BS EN 1994-1-1 (2004) for each member in the 4<sup>th</sup>, 5<sup>th</sup> and 6<sup>th</sup> columns of the tables. Similarly to the laboratory tests, the first cycle buckling loads in the numerical simulations exceeded the predicted buckling loads in all cases except for the braces with  $\bar{\lambda} = 0.5$ . The increase in first cycle buckling load from the theoretical monotonic load case that was observed for the majority of members, can be attributed to cyclic hardening of the steel during the initial cycles. In the case of the cold formed tubes, there may have been additional work hardening present from the forming process. The difference in response of the members with  $\bar{\lambda} = 0.5$  may be explained by the fact that the behaviour was governed more by the cross-section response than the material stiffness, in contrast with the longer members. Furthermore, the end conditions may have had a greater influence on the results of the shortest members. As discussed in Chapter 4, some of these specimens also exhibited a different local buckling shape to the more slender members. Similar

## Chapter 6 Design Recommendations

trends were seen for both cold formed and hot-finished braces with respect to post-buckling resistance.

Table 6.1 Comparison between maximum first cycle buckling loads in tests/FE and predictions from BS EN 1993-1-1 (2005)/BS EN 1994-1-1 (2004) for cold formed members

Specimen	Class	$\bar{\lambda}$	$N_{c,max}$ (test/FE)	$N_{b,Rd}$ (BS EN 1993-1-1, 2005; BS EN 1994-1-1, 2004)	$N_{c,max}/N_{b,Rd}$
CF-H-1500 <sub>test</sub>	1	0.90	151	105	1.43
CF-F1-1500 <sub>test</sub>	1	0.92	174	147	1.18
CF-F2-1500 <sub>test</sub>	1	0.92	164	147	1.11
CF-H-3000 <sub>test</sub>	1	1.98	71	43	1.66
CF-F1-3000 <sub>test</sub>	1	2.02	72	54	1.33
CF-F2-3000 <sub>test</sub>	1	2.02	71	54	1.32
CF-H-1500 <sub>FE</sub>	1	0.90	147	105	1.40
CF-F-1500 <sub>FE</sub>	1	0.92	201	147	1.37
CF-H-3000 <sub>FE</sub>	1	1.98	69	43	1.60
CF-F-3000 <sub>FE</sub>	1	2.02	83	54	1.54
CF1	1	0.50	147	170	0.86
CF2	1	1.00	134	108	1.24
CF3	1	1.50	93	63	1.48
CF4	1	2.00	66	39	1.69
CF5	2	0.50	91	104	0.88
CF6	2	1.00	79	67	1.18
CF7	2	1.50	57	39	1.46
CF8	2	2.00	39	24	1.63
CF9	3	0.50	67	81	0.83
CF10	3	1.00	62	51	1.22
CF11	3	1.50	42	30	1.40
CF12	3	2.00	30	19	1.58
CF13	4	0.50	49	60	0.82
CF14	4	1.00	47	39	1.21
CF15	4	1.50	33	23	1.43
CF16	4	2.00	23	14	1.64

## Chapter 6 Design Recommendations

Table 6.2 Comparison between maximum first cycle buckling loads in tests/FE and predictions from BS EN 1993-1-1 (2005)/BS EN 1994-1-1 (2004) for hot-finished members

Specimen	Class	$\bar{\lambda}$	$N_{c,max}$ (test/FE)	$N_{b,Rd}$ (BS EN 1993-1-1, 2005; BS EN 1994-1-1, 2004)	$N_{c,max}/N_{b,Rd}$
HF-H-1500 <sub>test</sub>	1	0.78	155	133	1.17
HF-F1-1500 <sub>test</sub>	1	0.81	174	152	1.14
HF-F2-1500 <sub>test</sub>	1	0.81	175	152	1.15
HF-H-3000 <sub>test</sub>	1	1.72	81	55	1.47
HF-F1-3000 <sub>test</sub>	1	1.78	83	61	1.36
HF-F2-3000 <sub>test</sub>	1	1.78	88	61	1.44
HF-H-1500 <sub>FE</sub>	1	0.78	130	133	0.98
HF-F-1500 <sub>FE</sub>	1	0.81	196	152	1.29
HF-H-3000 <sub>FE</sub>	1	1.72	86	55	1.56
HF-F-3000 <sub>FE</sub>	1	1.78	95	61	1.56
HF1	1	0.50	126	174	0.72
HF2	1	1.00	127	125	1.02
HF3	1	1.50	93	70	1.33
HF4	1	2.00	66	42	1.57
HF5	2	0.50	57	79	0.72
HF6	2	1.00	58	57	1.02
HF7	2	1.50	42	32	1.31
HF8	2	2.00	29	19	1.53
HF9	3	0.50	45	63	0.71
HF10	3	1.00	46	45	1.02
HF11	3	1.50	34	25	1.36
HF12	3	2.00	23	15	1.53
HF13	4	0.50	36	47	0.77
HF14	4	1.00	36	34	1.06
HF15	4	1.50	26	19	1.37
HF16	4	2.00	18	12	1.50

### 6.3 Post-buckling resistance

Post-buckling resistance is another important function for diagonal bracing members, since excessive deterioration in compressive resistance can lead to an asymmetric response in the frame. As discussed in Chapter 3, the predictions of AISC (2002) and CSA (1994) guidelines tend to underestimate or overestimate this parameter at large axial displacements. BS EN 1998-1 (2004) does not provide a formula to calculate the post-buckling resistance corresponding to a particular axial displacement value. Figures 6.1 to 6.3 show the post-buckling resistance from the finite element models and laboratory test specimens at displacement ductilities,  $\mu_{\Delta}$ , of 2, 3 and 5, which were examined previously in Section 3.4.6. The vertical axis in each figure represents the post-buckling resistance which has been normalised with respect to  $A_g f_{yd}$ , the product of the tube cross-section and the steel yield stress. The horizontal axis represents the non-dimensional global slenderness, calculated in accordance with BS EN 1993-1-1 (2005)/BS EN 1994-1-1 (2004). The experiment and finite element results are compared with the predictions from the AISC (2002) guidelines and from the CSA (1994) guidelines, Tremblay (2002) and Nakashima *et al.* (1992), defined by Equations (3.5), (3.7) and (3.8) in Chapter 3. For members with lower global slenderness values ( $\bar{\lambda} < 1.0$ ), the finite element models tended to underestimate the post-buckling resistance when compared with the laboratory test results. A closer agreement is found for the longer members. Overall a reasonable correlation can be seen for Class 1 hollow sections in the finite element models (filled square data points) and test specimens (hollow square data points) in each Figure. The finite element modelling also provided an opportunity to examine the post-buckling resistance of cross-sections with higher  $D/t$  ratios, as shown in Figures 6.1 to 6.3. The data points for Class 2, 3 and 4 cross-sections generally lie below the



predictions of the CSA guidelines (1994), Tremblay (2002) and Nakashima *et al.* (1992). This is to be expected since the predictive expressions in Chapter 3 have been derived for Class 1 sections, which are usually preferred for seismic design.

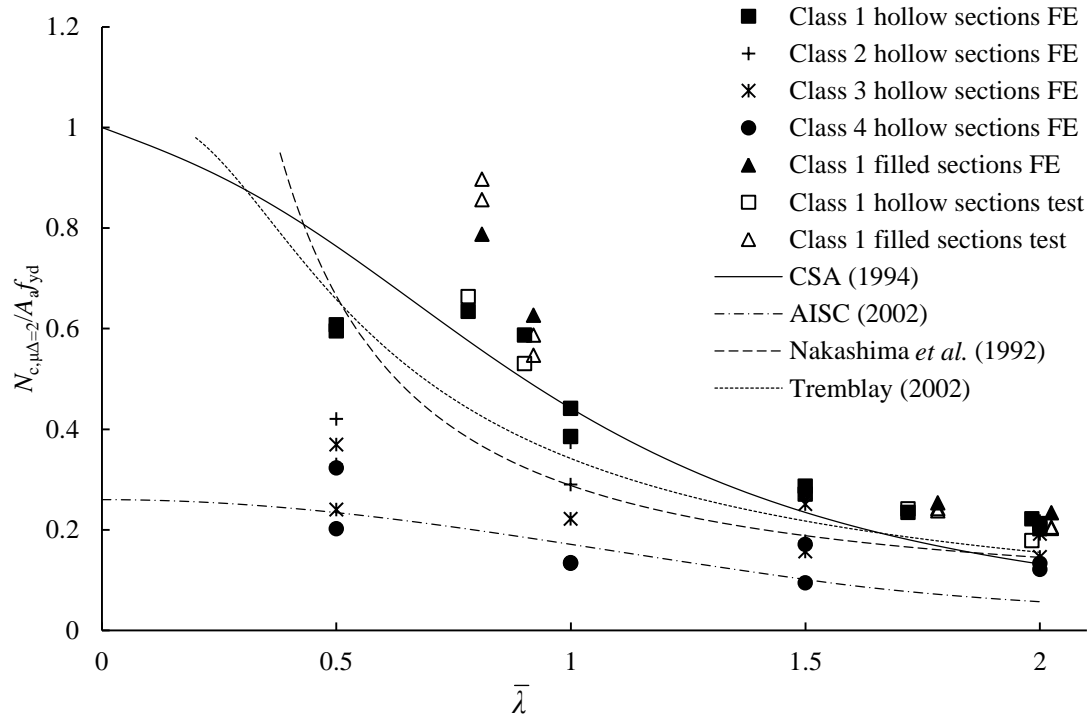


Figure 6.1 Post-buckling resistance of FE and laboratory test specimens at  $\mu_{\Delta} = 2$

Examining Figure 6.1, at a  $\bar{\lambda} = 0.5$ , it is found that the post-buckling resistance of all cross-sections is less than the predicted resistances by the CSA guidelines (1994), Tremblay (2002) and Nakashima *et al.* (1992). The AISC (2002) expression appears to give a reliable estimation of the resistance of Class 3 sections, and is conservative for Class 1 and 2 sections. At  $\bar{\lambda} = 1.0$ , the post-buckling resistance of Class 3 sections exceeds the AISC (2002) predictions while the expression from Nakashima *et al.* (1992) provides a good estimate for Class 2 sections. The relationship derived by Tremblay (2002) computes a higher post-buckling resistance than that of Nakashima *et al.* (1992) and shows a better (slightly conservative) estimate of the

resistance of Class 1 sections at this particular global slenderness value. Similar observations apply at  $\bar{\lambda} = 1.5$ . The predicted post-buckling resistance values appear to converge at  $\bar{\lambda} = 2.0$ , with the expressions of the CSA guidelines (1994), Tremblay (2002) and Nakashima *et al.* (1992) providing safe predictions for Class 1, 2 and 3 cross-sections. For global slenderness values of 0.5, 1.0 and 1.5, the AISC (2002) prediction provides the best fit to the Class 4 cross-section data, while all other predictions exceed it. This is not a major concern since Class 4 cross-sections are not generally employed in earthquake-resisting structures. Similar trends can be seen for the results in Figure 6.2, when the displacement ductility ( $\mu_{\Delta}$ ) is increased from 2 to 3. It is observed that as  $\mu_{\Delta}$  increases, the predictive expressions prove to be less conservative. Considerably less data were available for constructing Figure 6.3, since not all specimens attained a  $\mu_{\Delta}$  of 5 prior to failure. Several of the data points lie below the predictions by Tremblay (2002), Nakashima *et al.* (1992) and the design guidelines, but more data would be required to draw conclusions for the post-buckling resistance at this displacement amplitude.

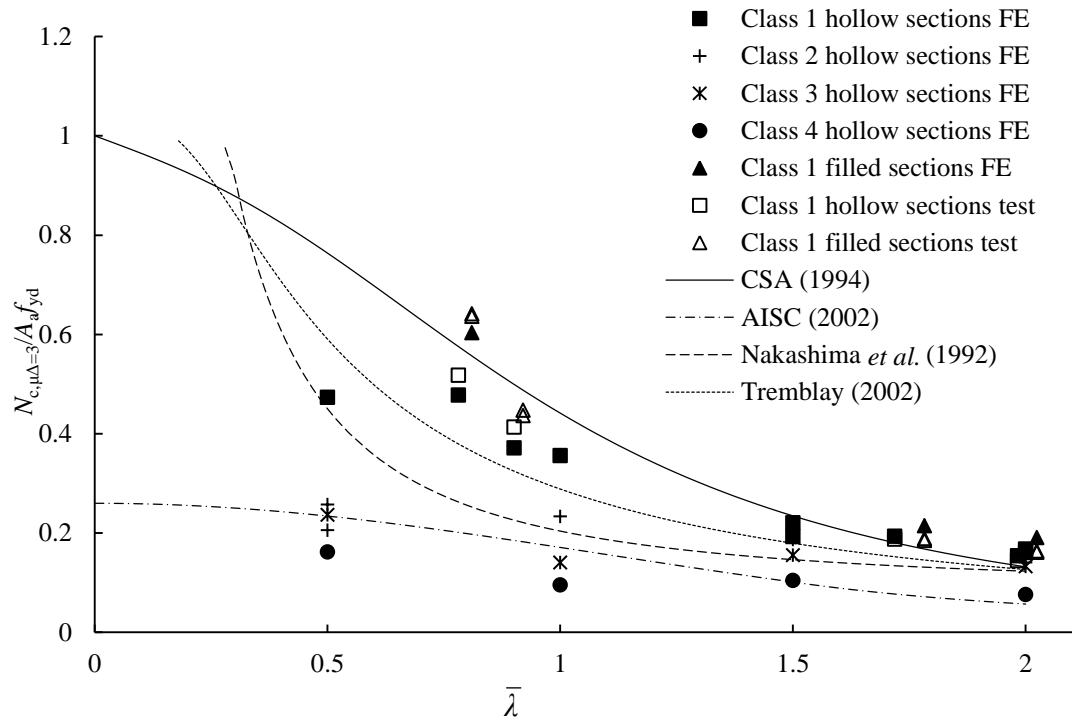


Figure 6.2 Post-buckling resistance of FE and laboratory test specimens at  $\mu_{\Delta} = 3$

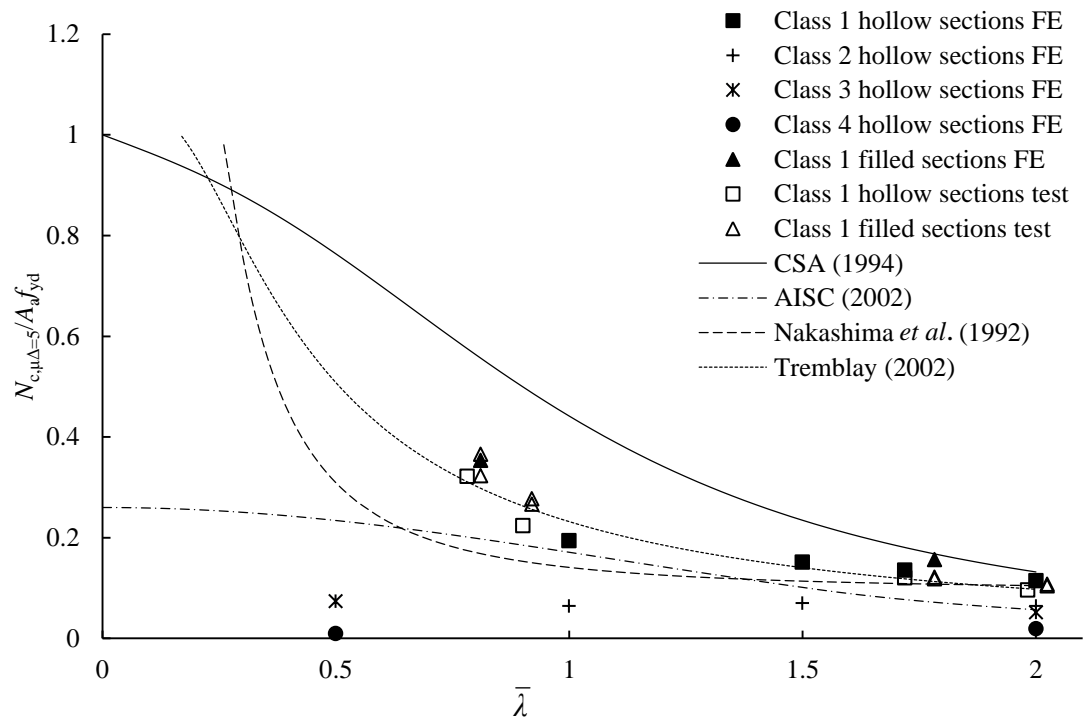


Figure 6.3 Post-buckling resistance of FE and laboratory test specimens at  $\mu_{\Delta} = 5$

In light of the first cycle buckling loads presented in Section 6.2, it is worth noting that the post-buckling resistance predictions of the stockiest members ( $\bar{\lambda} = 0.5$ ) may not be entirely reliable, and hence design recommendations for these members should be subject to further experimental investigations. As proposed in Chapter 3, the expressions derived by Tremblay (2002) or Nakashima *et al.* (1992) could be adopted for Class 1 sections. At  $\bar{\lambda} = 1.0$ , the AISC (2002) expression provides a reasonable estimation for Class 2 and 3 cross-sections overall, whereas the predictions of Nakashima *et al.* (1992) show a superior correlation for  $\bar{\lambda} = 1.5$ . With further work, predictions should be altered to take account of the contribution of the concrete infill, particularly in the case of shorter braces. Comparing the experimental results of hollow and composite members, the enhancement provided by the presence of concrete is generally less than that observed for the cross-sections in the compressive stub column tests and decreases under increasing axial displacement. The concrete contribution also appears to diminish with specimen length. It is expected that concrete infill would have a greater influence on the post-buckling resistance of Class 2, 3 and 4 cross-sections, since it would occupy a larger percentage of the cross-sectional area, but this is yet to be verified. Therefore a comprehensive experimental study would be required to establish the increase in post-buckling resistance with concrete infill and the relationship between this, local slenderness, global slenderness and axial displacement.

### 6.4 Tensile resistance

Similarly to the case of compressive resistance, acceptable predictions of the maximum tensile force can prove to be crucial in providing the correct degree of overstrength. Owing to elongation of the braces in compression, the members predominantly underwent straightening during the cycle reversals in the experiments

and finite element analyses. In reality the axial displacement cycles experienced during an earthquake are random and unlikely to be of equal tensile and compressive amplitudes in each cycle. As discussed in Chapter 3, the concrete-filled members experienced significantly higher tensile forces than the hollow members since the steel tube was subjected to biaxial stresses. Increases ranging from 3.3 % to 10 % were observed across the laboratory test specimens and this phenomenon needs to be taken into consideration in future design recommendations. The extent of increase would be affected by the concrete grade, since high strength concrete undergoes a greater degree of lateral expansion for a given axial displacement than normal strength concrete and hence would exert larger stresses on the steel tube. Since all concrete-filled specimens in this study used the same concrete grade, it was not possible to formulate a prediction that included concrete strength as a variable.

### **6.5 Ductility**

As outlined in Chapter 2, BS EN 1998-1 (2004) employs a behavioural factor,  $q$ , to characterise the ductility level of a seismic building. This is an estimation of the ratio of the forces in the structure if the response was completely elastic with 5% viscous damping to the design forces that would be obtained from a conventional elastic analysis model. Three ductility classes are outlined in BS EN 1998-1 (2004) for earthquake-resisting structures: low ductility, medium ductility and high ductility. Although structures may exhibit different  $q$  factors in each horizontal direction, only one ductility class is assigned to each structure. Table 6.3 presents the upper  $q$ -limits and cross-sectional classifications corresponding to each ductility class.

Table 6.3 Outline of ductility classes in BS EN 1998-1 (2004)

Design concept	Ductility class	Upper limit for behaviour factor, $q$	Cross-section classification
Low dissipative structural behaviour	DCL	1.5 – 2	-
Dissipative structural behaviour (medium)	DCM	4 (diagonal bracing) 2 (V-bracing)	Class 1, 2 or 3
Dissipative structural behaviour (high)	DCH	4 (diagonal bracing) 2.5 (V-bracing)	Class 1

BS EN 1998-1 (2004) also recommends an upper limit of 2.0 for the brace global slenderness, in addition to a lower limit of 1.3 when x-bracing is employed. Figures 6.4 and 6.5 show the relationship between the anticipated displacement ductility,  $\mu_{\Delta}$ , and global slenderness,  $\bar{\lambda}$ , for hot-finished and cold formed hollow sections of each class using Equations (4.9) and (4.10). Cross-sections having four different  $D/t\epsilon^2$  values were considered, using the classification system of BS EN 1993-1-1 (2005):

1. Class 1 cross-sections with  $D/t\epsilon^2 = 30$ : “Class 1”.
2. Sections with  $D/t\epsilon^2 = 50$ , the upper limit for Class 1: “Class 1 limit”.
3. Sections with  $D/t\epsilon^2 = 70$ , the upper limit for Class 2: “Class 2 limit”.
4. Sections with  $D/t\epsilon^2 = 90$ , the upper limit for Class 3: “Class 3 limit”.

The objective was to compare the abilities of various cross-section sizes to achieve a particular displacement ductility. Overall, the hot-finished braces (Figure 6.4) reached higher axial displacement amplitudes than the cold formed braces (Figure 6.5), and hence the hot-finished braces of various local and global slenderness values were compared with respect to a displacement ductility of 8 while the cold formed braces were compared with respect to a displacement ductility value of 4. These values do not translate directly to a particular  $q$ -value reported in Table 6.3, but

merely provide a means of comparison between sections of particular slenderness values. As class number increases, the rate of increase in  $\mu_{\Delta}$  with  $\bar{\lambda}$  decreases. For hot-finished sections, only sections of Class 1 and Class 2 obtain a displacement ductility of 8 for a global slenderness less than 1.8, which supports the finding that these classes are generally more suitable for dissipative behaviour than Class 3 sections. Little difference can be observed between Class 2 and Class 3 sections for  $\bar{\lambda} < 1.0$ , which suggests that little distinction is required between these sections, in terms of the limits outlined in Table 6.3 for structures of each ductility classification.

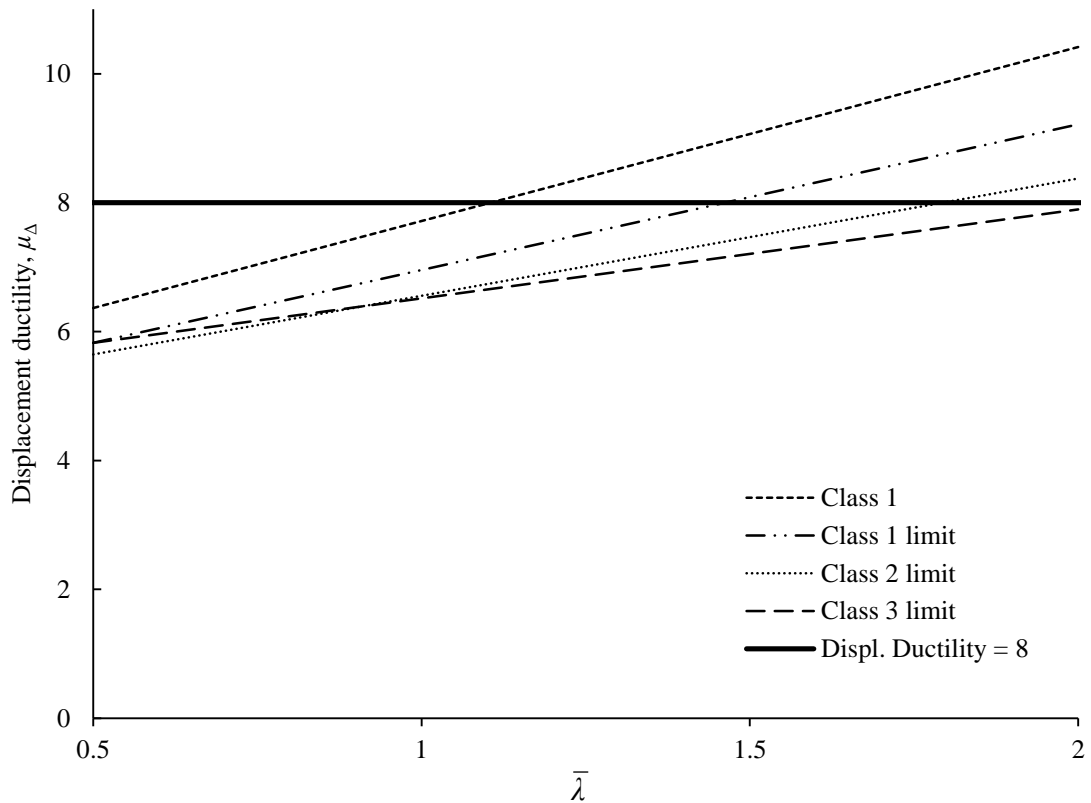


Figure 6.4 Relationship between predicted displacement ductility and global slenderness for hot-finished hollow steel sections

The cold formed sections achieved lower  $\mu_{\Delta}$  values overall, as shown in Figure 6.5.

Class 2 and 3 sections did not obtain displacement ductilities of 4 within the

allowable global slenderness limits. This finding strongly indicates that for cold formed braces, only Class 1 sections should be utilised for dissipative elements.

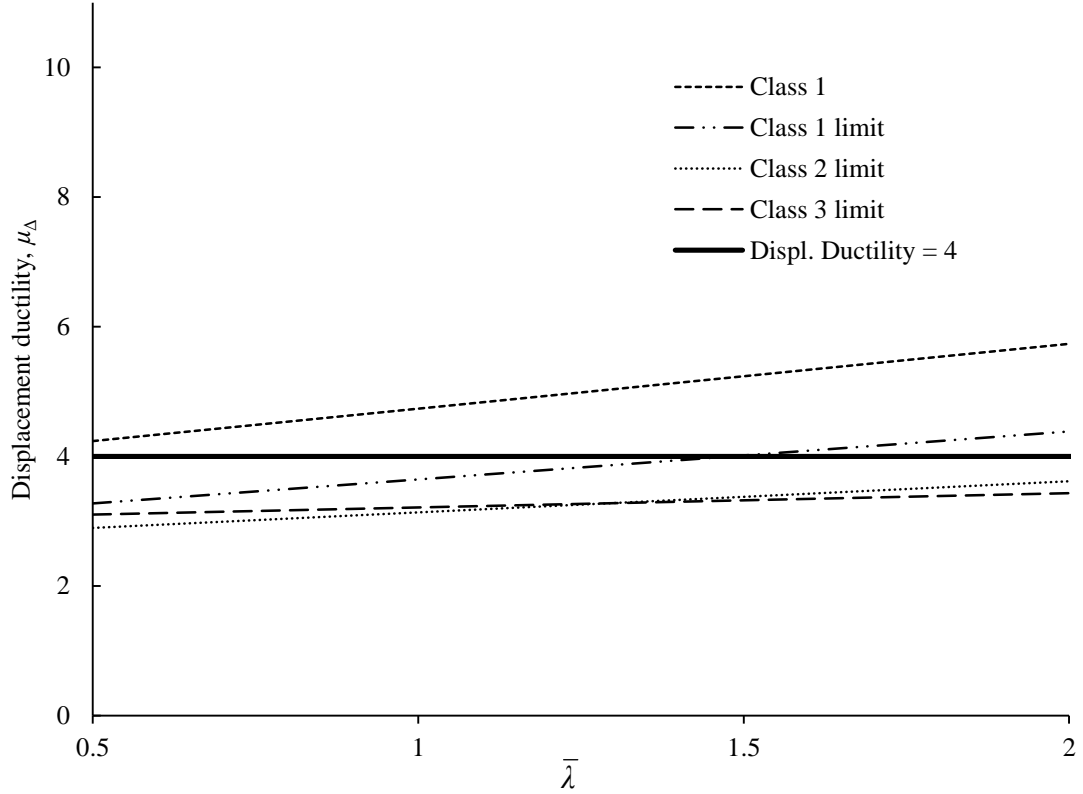


Figure 6.5 Relationship between predicted displacement ductility and global slenderness for cold formed hollow steel sections

Figures 6.6 and 6.7 compare the predicted  $\mu_{\Delta}$  with cross-sectional slenderness for global slenderness values of 0.5, 1.0, 1.5 and 2.0, using the predictions by Equations (4.9) and (4.10) for hot-finished and cold formed sections respectively. Similarly to Figures 6.4 and 6.5, target displacement ductilities of 8 and 4 were chosen for hot-finished and cold formed specimens respectively, for the purposes of comparison. The  $D/t\epsilon^2$  upper limits for Class 1 and Class 2 cross-sections outlined in BS EN 1993-1-1 (2005) are also illustrated in each Figure. For the hot-finished case in Figure 6.6, the stockiest member size does not achieve a displacement ductility of 8 within the given range of  $D/t\epsilon^2$  values whereas members with  $\bar{\lambda} = 1.0$  only obtain



this when  $D/t\epsilon^2$  is  $< 20$ . Members with global slenderness values of 1.5 achieve this for  $D/t\epsilon^2 < 50$  (Class 1) and braces at the upper limit of 2 reach this for all  $D/t\epsilon^2 < 70$ . This implies that a wider range of cross-section sizes is permissible for slender members ( $\bar{\lambda} = 1.5 - 2.0$ ) than for shorter members ( $\bar{\lambda} < 1.5$ ). The superior ductility of longer members is to be expected from an evaluation of the experimental results in Chapter 3, since these members are more flexible, can achieve a greater distribution of plasticity along the length and are less influenced by the end restraints.

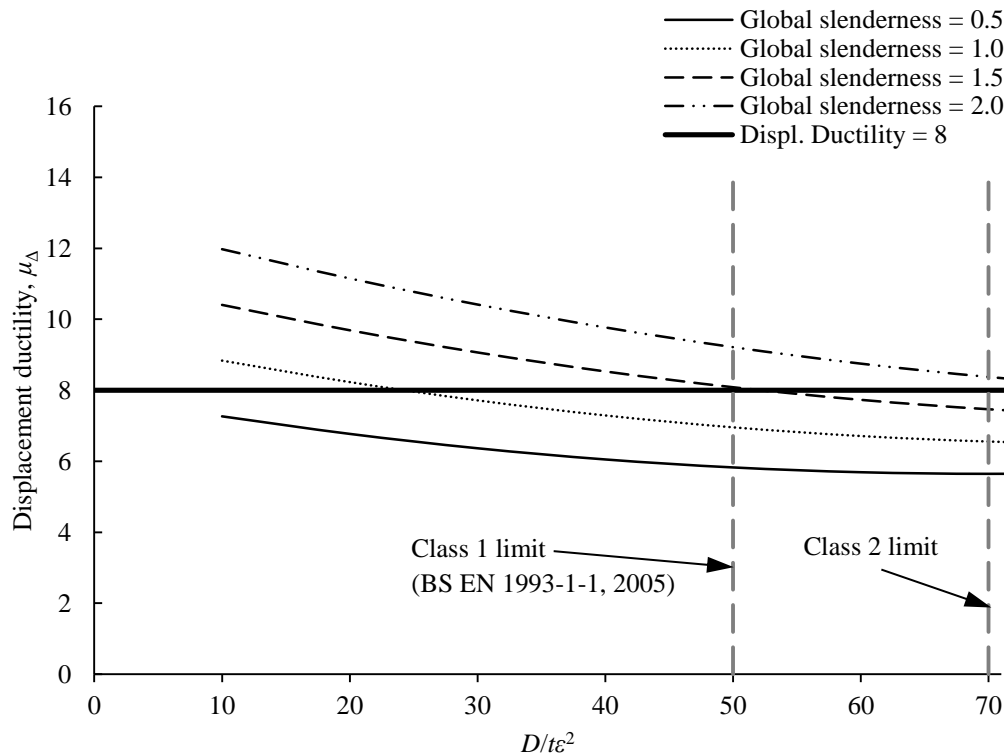


Figure 6.6 Relationship between predicted displacement ductility and local slenderness for hot-finished hollow steel sections

As seen in Figure 6.7, less variation in  $\mu_{\Delta}$  is observed when  $\bar{\lambda}$  varies from 0.5 to 2.0 for cold formed members. Members at the upper global slenderness limit of 2.0 are seen to obtain a displacement ductility of 4 when  $D/t\epsilon^2 < 60$ . It is observed that this

limit is reduced to 35 when  $\bar{\lambda} = 0.5$ . This further reinforces the finding that only Class 1 cross-sections are suitable for cold formed dissipative CHS members.

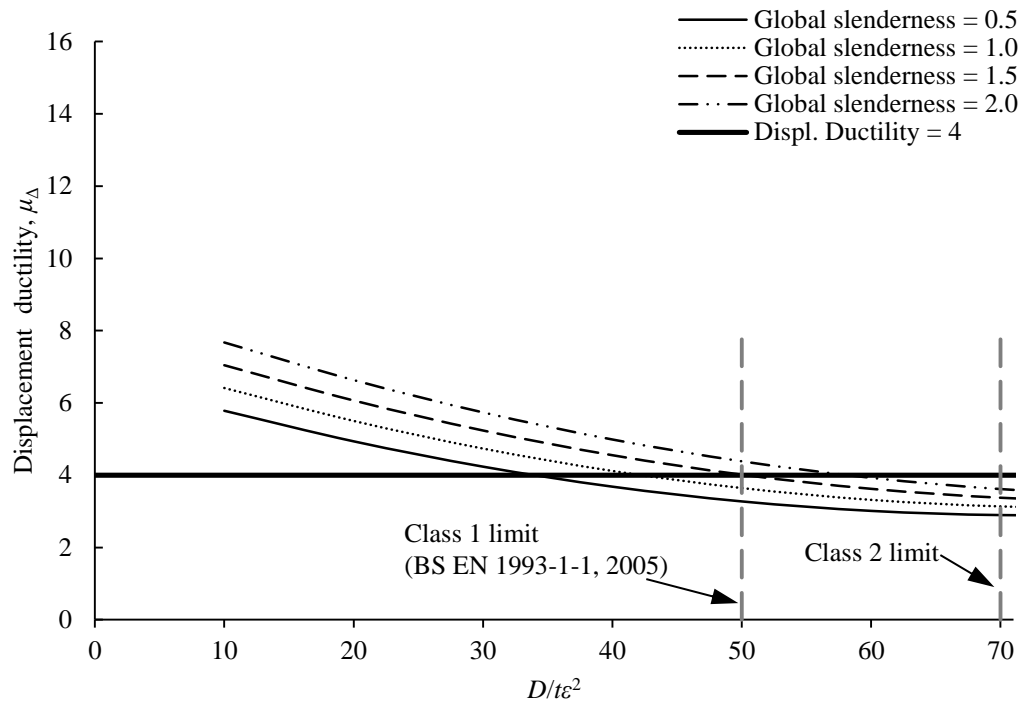


Figure 6.7 Relationship between predicted displacement ductility and local slenderness for cold formed hollow steel sections

## 6.6 Concluding remarks

The findings of the laboratory tests in Chapter 3 and finite element models in Chapter 4 have been examined with respect to the design approach of BS EN 1998-1 (2004). Differences were observed between the responses of cold formed and hot-finished braces and hollow and concrete-filled braces. Particular aspects of design were highlighted in which there is scope to propose distinct rules for each cross-section type, such as the cross-section classification limits corresponding to structures of each ductility class. This chapter has drawn attention to the difference between the buckling resistance under monotonic loading calculated using BS EN 1993-1-1 (2005)/BS EN 1994-1-1 (2004) and the first cycle buckling load of cyclically loaded braces which is influenced by cyclic hardening. Another issue

discussed has been the tensile resistance of composite tubular braces, which noticeably exceeds that of hollow steel braces, and which is not taken into account in current European design recommendations. Post-buckling resistance has also been discussed in this chapter, for which there is currently no provision in BS EN 1998-1 (2004). Post-buckling resistance was found to greatly decrease with increasing cross-sectional slenderness and further work will be required in order to verify if this is also the case for concrete-filled tubes.

Overall, further research will be necessary to confirm the findings of this thesis and to develop the proposed changes to BS EN 1998-1 (2004). It is envisaged that with supplementary experimental evidence there is potential to greatly enhance the design efficiency of CHS braces in concentrically braced, earthquake-resisting frames.

## **Chapter 7**

### **Conclusions and Recommendations for Further Work**

#### **7.1 Summary**

The aim of this research project was to explore the differences between hot-finished and cold formed circular tubular braces under cyclic axial loading, and to investigate the influence of concrete infill on member performance. The ultimate objective was to assess the current design guidelines for steel tubular braces in seismic applications and to suggest any suitable modifications.

Chapter 1 provided a brief introduction to the topics covered in this thesis, presented some examples of tubular structures and concentrically braced frames around the world, discussed the use of concrete-filled tubes and outlined the types of steel section which were used for this research.

Chapter 2 provided a more detailed background to the research topic, delving into the different approaches to seismic design and comparing the concentrically braced frame system, chosen to be explored in this thesis, with other popular structural configurations. The findings of previous laboratory experiments on tubular braces were summarised, highlighting the improvements achieved in RHS brace behaviour by the inclusion of concrete infill, and also the difference in response between cold formed and hot-finished RHS braces. The need for further data on CHS braces was identified, to assess whether or not similar improvements/differences in behaviour would be observed for this shape. Chapter 2 also introduced the second aspect to the research methodology: finite element modelling. Previous modelling approaches

were presented and discussed and a suitable technique was proposed for this particular task.

Chapter 3 described the laboratory experiments in detail. Stub column tests were carried out on cold formed and hot-finished filled and hollow specimens initially to assess the compressive response of each cross-section type. Results were compared with the predictions of BS EN 1993-1-1 (2005) and BS EN 1994-1-1 (2004), and also with those from previous research. Reasonable agreement was found between the test results and predictions. Chapter 3 also covered the testing of CHS braces under cyclic axial loading. Similarly to the stub column tests, hot-finished and cold formed sections, with or without concrete infill were compared. Two bracing lengths were used: 1500 mm braces with values of global slenderness,  $\bar{\lambda} = 0.78 - 0.92$ , and 3000 mm braces with  $\bar{\lambda} = 1.72 - 2.02$ . Both cross-section type and  $\bar{\lambda}$  value were found to influence the response. Comparisons were drawn between the deformed shape, first cycling buckling load, post-buckling resistance, tensile resistance, energy dissipation capability and lateral displacement at the mid-height for each specimen type. Results were also compared with predictions using design recommendations from BS EN 1993-1-1 (2005), BS EN 1994-1-1 (2004), CSA-S16 1-94 (1994) and the AISC (2002) guidelines for seismic structures, and empirically-derived relationships from previous researchers, such as Nakashima *et al.* (1992), Tremblay (2002) and Shaback and Brown (2003).

Chapter 4 covered the numerical simulations of hollow steel CHS braces using the software package ABAQUS®. A sensitivity analysis and comparisons with the experimental results were used to establish a suitable mesh size in addition to appropriate local and global geometric imperfection amplitudes. Test data were also

utilised to verify the modelling of the material behaviour, which was achieved through the nonlinear isotropic/kinematic hardening model in ABAQUS®. This chapter also assessed methods to envisage the number of cycles to fracture of the steel tube, looking at the low cycle fatigue behaviour of the material. Once satisfactory modelling and failure prediction techniques were established, parametric studies were conducted to cover a wider range of cross-sectional and global slenderness values. Predictive expressions were then developed for the displacement ductility and energy dissipation capability in terms of these parameters.

After the analysis of hollow tubular braces, further finite element modelling was carried out for concrete-filled braces, as described in Chapter 5. The main challenge outlined in this chapter was capturing the contrasting responses of concrete in compression and tension without creating excessive convergence difficulties in the model solver. The inbuilt damaged plasticity model in ABAQUS® was utilised for this purpose. Overall, the model was not found to be entirely satisfactory and significantly underestimated the number of cycles to fracture. It was concluded that further work would be required on this topic in future.

Chapter 6 discussed the implications of the findings on current design guidelines, taking into account the compiled results from the experimental and numerical studies. Aspects such as the tensile resistance, first cycle buckling load, post-buckling resistance and displacement ductility were explored and attention was drawn to areas where design provisions were either over-conservative or under-cautious. Differences were emphasised between cold formed and hot-finished specimens in relation to design guidelines, revealing that distinct rules could be developed for these cross-section types in future. The effect of concrete infill was

also highlighted in this chapter, noting that the use of this material could be accounted for in future revisions of the design codes.

This chapter presents a final summary of the thesis and the conclusions that can be drawn from the aforementioned chapters. The findings of the research and some recommendations for future work are discussed in the following sections.

### 7.2 Conclusions

The following conclusions have been derived from this research:

1. The overall response of tubular braces was influenced by both local and global buckling, with local buckling playing a more prominent role for shorter members than for longer members.
2. Hot-finished steel braces displayed a superior performance overall to cold formed braces. They endured a larger number of cycles before failure and hence obtained larger displacement ductility values. They also exhibited higher tensile and compressive resistances and greater levels of energy dissipation relative to the material yield stress than cold formed braces.
3. The inclusion of concrete infill significantly improved cyclic brace performance. Composite braces with  $\bar{\lambda} < 1.0$  had higher first cycle buckling loads and post-buckling resistances than hollow steel braces, and members of all lengths had greater tensile resistances. Concrete-filled specimens also underwent a greater number of cycles before fracture.
4. The number of cycles to failure increased with increasing global slenderness. It tended to decrease with increasing local slenderness but this trend was not as clear as that observed for global slenderness.

5. The energy dissipation per cycle, relative to the material properties and brace length, tended to decrease with increasing global slenderness. This was reflected in the axial load-displacement hysteresis curve shape, which had a less rounded profile for slender members than for stocky members and enclosed a smaller area in the case of the slender members.
6. Expressions to estimate the lateral displacement at the mid-height, derived theoretically from the member geometry, tended to predict larger displacements than those observed in the experiments. Better approximations were derived by using ‘best-fit’ curves through the data points which were obtained from the experiments.
7. The first cycle buckling loads predicted in BS EN 1993-1-1 (2005)/BS EN 1994-1-1 (2004) do not take into account the effects of cyclic hardening of the steel when subjected to seismic loading. Therefore, the first cycle buckling loads which occurred in the experiments significantly exceeded the design code predictions. This could have implications for determining the design overstrength and should be taken into account in order to avoid overloading adjacent structural members, e.g. columns.
8. The tensile resistance of the concrete-filled braces exceeded the anticipated values following from BS EN 1993-1-1 (2005) and BS EN 1994-1-1 (2004), owing to the biaxial tensile stress state of the steel. This should be taken into consideration in the design guidelines in order to mitigate any undesired overstrength.
9. The inbuilt nonlinear isotropic/kinematic hardening model in ABAQUS® produced a reliable simulation of the test results for hollow tubular braces, in terms of the maximum axial loads and hysteresis curve shape. It slightly



underestimated the number of cycles to failure but a reasonable correlation with the experimental results was obtained by employing the Coffin Manson relationship (Coffin, 1954; Manson, 1954), Miner's Rule (Miner, 1945) and the material input parameters of Nip *et al.* (2010b).

10. The number of cycles to fracture was greatly underestimated by the finite element models for concrete-filled tubes in comparison with the laboratory test results. The model response was not found to be very sensitive to the material parameters used for the damaged plasticity model. Possible sources of difficulty were the interaction between components or inadequacies in simulating the steel hardening behaviour.
11. Differences were observed between the displacement ductility values of hot-finished and cold formed sections, both in the laboratory tests and the numerical models. For hot-finished specimens, it is possible to achieve higher displacement ductilities for cross-sections of a particular slenderness value than it is for cold formed specimens of the same cross-section slenderness. Therefore, findings suggest that in order to achieve a particular target displacement ductility, different recommendations could be given in BS EN 1998-1 (2004) for hot-finished and cold formed members, regarding the cross-section classification limit for structures of each ductility class (i.e. DCL, DCM, DCH).
12. The ductility of the braces is influenced by both global and local slenderness values. This was discussed in Chapter 4 for hollow steel braces and predictive expressions were proposed for displacement ductility in terms of the slenderness parameters, following from the numerical modelling results. If members are designed to achieve a target displacement ductility, the

findings suggest that different cross-section classification limits are suitable for members of each global slenderness value. For example, since displacement ductility increases with increasing global slenderness, higher cross-section classes may be allowable for a member with  $\bar{\lambda} = 2.0$ , than for a member with  $\bar{\lambda} = 1.0$ . To optimise the use of material, different cross-section classification limits could be introduced into BS EN 1998-1 (2004) (corresponding to each structural ductility class) for each global slenderness range, e.g. ( $0.5 \leq \bar{\lambda} < 1.0$ ;  $1.0 \leq \bar{\lambda} < 1.5$ ;  $1.5 \leq \bar{\lambda} < 2.0$ ).

### 7.3 Suggestions for future research

The observations of this research project indicate the potential to significantly improve design provisions for concentrically braced earthquake-resisting building frames. BS EN 1993-1 (2005) already provides a separate section for cold formed steel (BS EN 1993-1-3, 2006). However, the behavioural distinctions between hot-finished and cold formed braces under cyclic loading suggest that a supplementary section could also be provided for cold formed steel structures in BS EN 1998-1 (2004) to account for these differences in seismic applications. The benefits of concrete infill have been demonstrated in the laboratory tests. Although BS EN 1998-1 (2004) states that in composite structures, the dissipative zones are in the steel elements only, this research has shown that the concrete contribution could also be taken into account in concrete-filled tubular elements. There is scope to modify the current cross-section classification limits corresponding to the behaviour factor,  $q$ , in BS EN 1998-1 (2004). Detailed guidelines could be developed in future for cross-section limits, taking the section type and member slenderness into consideration.

More test data will be required in order to develop and implement these proposed changes. Further experiments and numerical modelling would supplement the existing data. Numerical modelling would reduce the time and expense of the research but improved accuracy will be desired if it is to be heavily relied upon, since the model employed for this research tended to underestimate the number of cycles to failure. The reliability of the model could potentially be improved by carrying out cyclic material tests on samples of the test material instead of scaling the input parameters from other material tests. Overall, reasonable results were obtained for the hollow steel braces but a sizeable amount of work will be required for developing models of the concrete-filled braces. A simulation technique encompassing reliability, computational efficiency and simplicity of implementation will lead to the derivation of predictive expressions for displacement ductility and energy dissipation to complement those proposed for hollow steel braces in this thesis.

In future, consideration should also be given to higher strength carbon and stainless steel circular hollow section braces. Research by Nip *et al.* (2010a) on carbon and stainless steel braces demonstrated that stainless steel may provide superior strength and ductility to carbon steel. Recent improvements in technology and manufacturing methods have made stainless steels and high strength carbon steels more widely available but few design recommendations are provided for these materials in seismic applications.

## References

ABAQUS® (2012). ABAQUS Analysis User's Manual. Version 6.12. Dassault Systèmes.

AISC (2002). Seismic provisions for structural steel buildings. Chicago, IL: American Institute of Steel Construction.

Beer, H. and Schultz, G. (1970). Bases theoriques des courbes européennes de flambement. *Construction Metallique*, **3**, 37-57.

Bergmann, R., Matsui, C., Meinsma, C. and Dutta, D. (1995). Design Guide 5: For concrete filled hollow section columns under static and seismic loading. CIDECT International committee for development and study of tubular structures, Köln: TÜV Verlag GmbH.

Bjorhovde, R. (1977). Strength and behaviour of cold-formed HSS columns. Structural Engineering Report No. 65. Department of Civil Engineering, University of Alberta, Edmonton, Canada.

Broderick, B. M., Goggins, J. M. and Elghazouli, A. Y. (2005). Cyclic performance of steel and composite bracing members. *Journal of Constructional Steel Research*, **61**(4), 493-514.

BS EN ISO 6892-1 (2009). Metallic materials – Tensile testing – Method of test at room temperature. Milton Keynes: BSI.

BS EN 12390-3 (2002). Testing hardened concrete: Part 3: Compressive strength of test specimens. Milton Keynes: BSI.

## References

BS EN 1992-1-1 (2004). Design of concrete structures, Part 1-1: General rules and rules for buildings. Milton Keynes: BSI.

BS EN 1993-1-1 (2005). Design of steel structures, Part 1-1: General rules and rules for buildings. Milton Keynes: BSI.

BS EN 1994-1-1 (2004). Design of composite steel and concrete structures, Part 1-1: General rules and rules for buildings. Milton Keynes: BSI.

BS EN 1998-1 (2004). Design of structures for earthquake resistance – Part 1: General rules, seismic actions and rules for buildings. Milton Keynes: BSI.

Buyukozturk, O. (1977). Nonlinear analysis of reinforced concrete structures. *Computers and Structures*, **7**(1), 149-156.

Cai, S. H. (1987). Ultimate strength of concrete-filled tube columns, topics in composite construction in steel and concrete II. *Proceedings of an Engineering Foundation Conference*. New York: ASCE, 702-727.

CAN/CSA-S16 1-94 (1994). Limit state design of steel structures. Rexdale, Ont: Canadian Standard Association.

Chaboche, J. L. (1986). Time-independent constitutive theories for cyclic plasticity. *International Journal of Plasticity*, **2**(2), 149-188.

Chan, T. M. and Gardner, L. (2008). Compressive resistance of hot-rolled elliptical hollow sections. *Engineering Structures*, **30**(2), 522-532.

Coffin, L. F. Jr. (1954). A study of the effects of cyclic thermal stresses on a ductile metal. *Transactions of the ASME*, **76**(6), 931-950.

## References

- Dafalias, Y. F. and Popov, E. P. (1976). Plastic internal variables formalism of cyclic plasticity. *Journal of Applied Mechanics*, **43**(4), 645-651.
- Dai, X. and Lam, D. (2010). Numerical modelling of the axial compressive behaviour of short concrete-filled elliptical steel columns. *Journal of Constructional Steel Research*, **66**(7), 931-942.
- Darwin, D. and Pecknold, D. A. (1976). Analysis of RC shear panels under cyclic loading, *Proceedings of the ASCE - Journal of the Structural Division*, **102**(2), 355-369.
- Downing, S. D. and Socie, D. F. (1982). Simple rainflow counting algorithms. *International Journal of Fatigue*, **4**(1), 31-40.
- ECCS (1986). *Recommended Testing Procedure for Assessing the Behaviour of Structural Steel Elements under Cyclic Loads*, Brussels: European Convention for Constructional Steelwork.
- Elchalakani, M., Zhao, X. L. and Grzebieta, R. (2003). Tests of cold formed circular tubular braces under cyclic axial loading. *Journal of Structural Engineering*, **129**(4), 507-514.
- Elremaily, A. and Azizinamini, A. (2002). Behavior and strength of circular concrete-filled tube columns. *Journal of Constructional Steel Research* **58**(12), 1567-1591.
- Fam, A., Qie, F., and Rizkalla, S. (2004). Concrete-filled steel tubes subjected to axial compression and lateral cyclic loads. *Journal of Structural Engineering*, **130**(4), 631-640.

## References

- Ge, H. and Usami, T. (1996). Cyclic tests of concrete-filled steel box columns. *Journal of Structural Engineering*, **122**(10), 1169-1177.
- Goggins, J. M., Broderick, B. M., Elghazouli, A. Y. and Lucas, A. S. (2006). Behaviour of tubular steel members under cyclic axial loading. *Journal of Constructional Steel Research*, **62**(1-2), 121-131.
- Goto, Y., Kumar, G. and Kawanishi, N. (2010). Nonlinear finite-element analysis for hysteretic behavior of thin-walled circular steel columns with in-filled concrete. *Journal of Structural Engineering*, **136**(11), 1413–1422.
- Hajjar, J. F. and Gourley, B. C. (1997). A cyclic nonlinear model for concrete-filled tubes. I: Formulation. *Journal of Structural Engineering*, **123**(6), 736-744.
- Hajjar, J. F., Gourley, B. C. and Olson, M. C. (1997). A cyclic nonlinear model for concrete-filled tubes. II: Verification. *Journal of Structural Engineering*, **123**(6), 745-754.
- Han, L. H., He, S. H. and Liao, F. Y. (2011). Performance and calculations of concrete-filled steel tubes (CFST) under axial tension. *Journal of Constructional Steel Research*, **67**(11), 1699-1709.
- Hillerborg, A., Modeer, M. and Petersson, P. E. (1976). Analysis of crack formation and crack growth in concrete by means of fracture mechanics and finite elements. *Cement and Concrete Research*, **6**(6), 773–781.
- Hu, H. T., Huang, C. S., Wu, M. H. and Wu, Y. M. (2003). Nonlinear analysis of axially loaded concrete-filled tube columns with confinement effect. *Journal of Structural Engineering*, **129**(10), 1322-1329.

## References

- Iwan, W. D. (1967). On a class of model for the yielding behavior of continuous and composite system. *Journal of Applied Mechanics*, **34**(3), 612-617.
- Johansson, M. and Gylltoft, K. (2002). Mechanical behaviour of circular steel-concrete composite stub columns. *Journal of Structural Engineering*, **128**(8), 1073-1081.
- Kuşyılmaz, A. and Topkaya, C. (2011). A numerical study on local buckling and energy dissipation of CHS seismic bracing. *Thin-Walled Structures*, **49**(8), 984-996.
- Lee, C., Grzebieta, R. H. and Zhao, X. L. (2000). The importance of further studies on the capacity evaluation of concrete-filled steel tubes under large deformation cyclic loading. *Structural Failure and Plasticity*. Oxford: Pergamon, 685-690.
- Lee, J. and Fenves, G. L. (1998). Plastic-damage model for cyclic loading of concrete structures, *Journal of Engineering Mechanics*, **124**(8), 892–900.
- Liu, Z. and Goel, S. C. (1988). Cyclic load behavior of concrete-filled tubular braces. *Journal of Structural Engineering*, **114**(7), 1488-1506.
- Lubliner, J., Oliver, J., Oller, S. and Oñate, E. (1989). A plastic-damage model for concrete. *International Journal of Solids and Structures*, **25**(3), 299–326.
- Mamaghani, I. H. P., Usami, T. and Mizuno, E. (1996). Inelastic large deflection analysis of structural steel members under cyclic loading. *Engineering Structures*, **18**(9), 659-668.
- Mander, J. B., Priestley, M. J. N. and Park, R. (1988). Theoretical stress-strain model for confined concrete. *Journal of Structural Engineering*, **114**(8), 1804-1826.



## References

- Manson, S. S. (1954). Behaviour of materials under conditions of thermal stress. National Advisory Commission on Aeronautics: Report 1170. Lewis Flight Propulsion Laboratory, Cleveland, USA.
- Mao, X. Y. and Xiao, Y. (2006). Seismic behaviour of confined square CFT columns. *Engineering Structures*, **28**(10), 1378-1386.
- Matsuishi, M. and Endo, T. (1968). "Fatigue of metals subjected to varying stress", paper presented to Japanese Society of Mechanical Engineers (Jukuoka, Japan).
- Miner, M. A. (1945). Cumulative damage in fatigue. *Journal of Applied Mechanics*, **12**(3), A159-A164.
- Mroz, Z. (1967). On the description of anisotropic work hardening. *Journal of the Mechanics and Physics of Solids*, **15**(3), 163-175.
- Nakashima, M., Nishino, T., Tsuji, B. and Iwasa Y. (1992). Effect of strain hardening on post-buckling resistance of steel braces. *Proceedings of Third Pacific Structural Steel Conference*, Tokyo, Japan, 561-568.
- Nip, K. H., Gardner, L. and Elghazouli, A. Y. (2010a). Cyclic testing and numerical modelling of carbon steel and stainless steel tubular bracing members. *Engineering Structures*, **32**(2), 424-441.
- Nip, K. H., Gardner, L., Davies, C. M. and Elghazouli, A.Y. (2010b). Extremely low cycle fatigue tests on structural carbon steel and stainless steel. *Journal of Constructional Steel Research*, **66**(1), 96-110.
- NZS 4203 (1992). General structural design and design loadings for buildings. Wellington, New Zealand: Standards Association of New Zealand.

## References

- Packer, J. A., Chiew, S. P., Tremblay, R. and Martinez-Saucedo, G. (2010). Effect of material properties on hollow section performance. *Proceedings of the ICE – Structures and Buildings*, **163**(6), 375 – 390.
- Richart, F. E., Brandtzaeg, A. and Brown, R. L. (1928). A study of the failure of concrete under combined compressive stresses. *Bulletin 185*, University of Illinois Engineering Experimental Station, Champaign, III.
- Saenz L. P. (1964). Discussion of ‘Equation for the stress-strain curve of concrete’ by P. Desayi and S. Krishnan. *ACI Journal*, **61**(1), 1229-1235.
- Shaback, B. and Brown, T. (2003). Behaviour of square hollow structural steel braces with end connections under reversed cyclic axial loading. *Canadian Journal of Civil Engineering*, **30**(4), 745-753.
- Sheehan, T., Dai, X. H., Chan, T. M. and Lam, D. (2012). Structural response of concrete-filled elliptical steel hollow sections under eccentric compression. *Engineering Structures*, **45**, 314-323.
- Sheehan, T. and Chan, T. M. (2013). Cyclic response of hollow and concrete-filled CHS braces. *Proceedings of the ICE – Structures and Buildings*, (in press).
- Sheehan, T., Chan, T. M. and Gardner, L. (2013). Numerical investigation of the cyclic response of CHS braces. *Proceedings of the 5th International Conference on Structural Engineering, Mechanics and Computation*. Cape Town, South Africa, 2<sup>nd</sup> – 4<sup>th</sup> September 2013 (submitted).
- Shen C., Mamaghani, I. H. P., Mizuno, E. and Usami, T. (1995). Cyclic behavior of structural steels. II: Theory. *Journal of Engineering Mechanics*, **121**(11), 1165-1172.

## References

- Takeuchi, T. and Matsui, R. (2011). Cumulative cyclic deformation capacity of circular tubular braces under local buckling. *Journal of Structural Engineering*, **137**(11), 1311-1318.
- Thalayan, P., Aly, T., and Patnaikuni, I. (2009). Behaviour of concrete-filled steel tubes under static and variable repeated loading. *Journal of Constructional Steel Research*, **65**(4), 900-908.
- Tremblay, R. (2002). Inelastic seismic response of steel bracing members. *Journal of Constructional Steel Research*, **58**(5-8), 665-701.
- Varma, A. H., Ricles, J. M., Sause, R., and Lu, L. W. (2002). Experimental behavior of high strength square concrete filled steel tube (CFT) columns. *Journal of Structural Engineering*, **128**(3), 309-318.
- Yang, H., Lam, D. and Gardner, L. (2008). Testing and analysis of concrete-filled elliptical hollow sections. *Engineering Structures*, **30**(12), 3771-3781.
- Young, B. and Ellobody, E. (2006). Experimental investigation of concrete-filled cold-formed high strength stainless steel tube columns. *Journal of Constructional Steel Research*, **62**(5), 484-492.
- Ziegler, H. (1959). A modification of Prager's hardening rule. *Quarterly Applied Mathematics*, **17**(1), 55-65.

**APPENDIX A   Supplementary data for modelling of hollow  
steel braces**

**A.1        Local imperfection amplitude determination.**

**No. of cycles to fracture for CF-H-1500**

**A.2        Verification of finite element models**

**A.3        Load-displacement hysteresis curves for  
parametric studies**

### A.1 Local imperfection amplitude determination. No. of cycles to fracture for CF-H-1500

Figures A.1.1 and A.1.2 illustrate the part of the steel circumference in Specimen CF-H-1500 which is included in each of the Regions A to C, used to estimate the number of cycles to fracture for finite element models of cyclically loaded braces. Figure A.1.1 illustrates the regions with respect to the longitudinal strains around the section circumference whereas Figure A.1.2 shows a view through the cross-section at the mid-length and highlights the regions in relation to their positions on the section circumference.

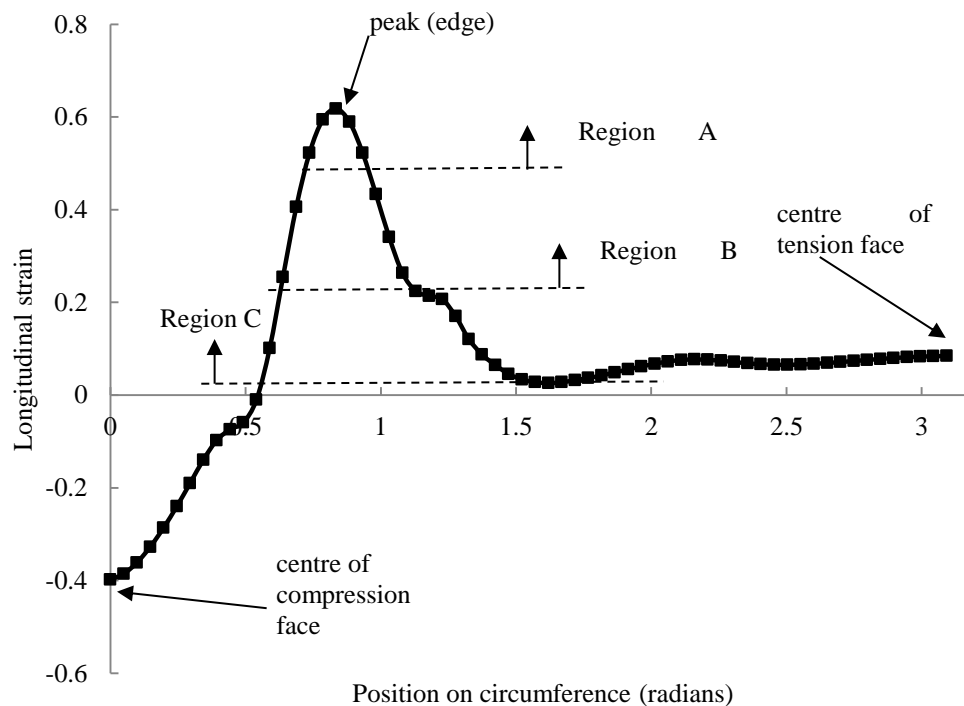


Figure A.1.1 Regions at edge of compression face for monitoring strain progressions

## Appendix A

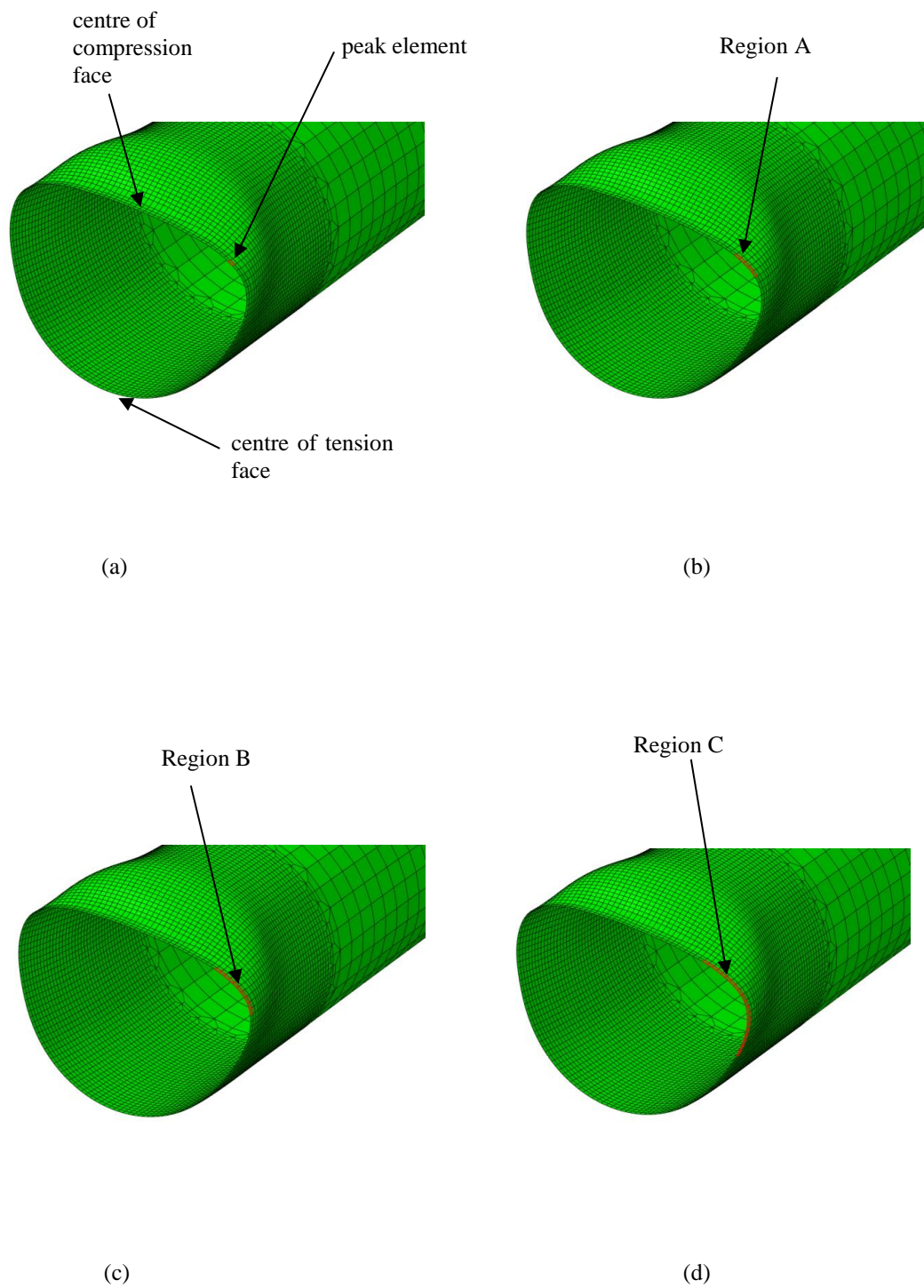


Figure A.1.2 Buckled shape of cold formed CHS at mid-length, showing (a) Element undergoing maximum strains ('peak' element) at compression face edge; (b) Region A for monitoring strains; (c) Region B; (d) Region C

## Appendix A

Tables A.1.1 to A.1.10 present the estimated number of cycles to fracture for the finite element model of specimen CF-H-1500, using the Coffin-Manson relationship (Coffin, 1954; Manson, 1954) given by

$$\frac{\Delta \varepsilon_p}{2} = \varepsilon'_f (2N_f)^c \quad (\text{A.1})$$

where

$\Delta \varepsilon_p$  = plastic strain amplitude

$\varepsilon'_f$  = fatigue ductility coefficient

$N_f$  = number of cycles to fracture

$c$  = fatigue ductility exponent

and Miner's Rule (Miner, 1945) to determine the accumulated damage resulting from undergoing strain cycles of varying magnitudes. The different columns compare results using various portions of the steel circumference as shown in Figure A.1.2 in addition to the 'whole' compression face of the tube. The major rows represent the number of rows in the half-specimen model over which the strain was monitored, starting at the specimen mid-length. Each major row consists of three minor rows to compare the results of using strain values on the inside face of the tube, the outside face and the average between these two values. Two counting techniques are compared in each table for determining  $\Delta \varepsilon_p$ . The first approach (left side of the table) employed the rainflow counting algorithm (Matsuishi and Endo, 1968) and the second (right side) entailed counting the differences in plastic strain between successive peaks and troughs as they occurred during the loading sequence. Local imperfections were incorporated into the model geometry taking the shape of a

## Appendix A

sinusoidal wave along the brace length. Tables A.1.1.to A.1.10 compare the predicted number of cycles to fracture for local imperfection amplitudes of  $t/25$ ,  $t/50$ ,  $t/100$ ,  $t/200$  and  $t/500$ , where  $t$  is the tube wall thickness. Tables A.1.1.to A.1.5 use the parameters  $\epsilon'_f$  and  $c$  obtained from material tests in Nip *et al.* (2010b) for the Coffin-Manson relationship and for Tables A.1.6. to A.1.10 these parameters were scaled to according to the steel yield stress used in the finite element models.

In some cases no estimate was obtained owing to the fact that the strain values in the monitoring region were predominantly monotonic and did not exhibit reversals of sufficient magnitude to compute a prediction for the number of cycles to fracture.

Table A.1.1 No. of cycles to fracture for local imperfection =  $t/25$ , taking edge of compression face; original fracture parameters  $\epsilon'_f$  and  $c$  from Nip *et al.* (2010b)

No. of rows of elements	Strain output	No. of cycles to failure									
		rainflow technique					counting individual ramps				
		Region					Region				
		peak	A	B	C	whole	peak	A	B	C	whole
1	Avg	-	-	-	-	-	-	-	-	-	-
	Inside face	-	-	-	-	-	-	-	-	-	-
	Outside face	-	-	-	-	-	11	11	11	14	-
2	Avg	-	-	-	-	-	-	-	-	-	-
	Inside	-	-	-	-	-	-	-	-	-	-
	Outside	-	-	-	-	-	11	11	11	14	15
3	Avg	-	-	-	-	-	13	13	13	13	-
	Inside	-	-	-	-	-	-	-	-	-	-
	Outside	14	14	14	17	14	11	11	11	12	12
4	Avg	-	-	-	-	-	14	14	14	15	-
	Inside	-	-	-	-	-	-	-	-	-	-
	Outside	16	16	19	17	16	11	11	11	12	13
5	Avg	-	-	-	-	-	18	17	15	17	-
	Inside	-	-	-	-	-	-	-	-	-	-
	Outside	-	19	19	-	-	11	11	12	13	14



## Appendix A

Table A.1.2 No. of cycles to fracture for local imperfection =  $t/50$ , taking edge of compression face; original fracture parameters  $\epsilon'_f$  and  $c$  from Nip *et al.* (2010b)

No. of rows of elements	Strain output	No. of cycles to failure									
		rainflow technique					counting individual ramps				
		Region					Region				
		peak	A	B	C	whole	peak	A	B	C	whole
1	Avg	-	-	-	-	-	8	8	8	8	10
	Inside face	-	-	-	-	-	8	8	8	8	11
	Outside face	15	15	15	16	19	8	8	8	9	9
2	Avg	9	9	9	10	10	8	8	8	8	9
	Inside	9	9	9	10	10	8	8	8	8	9
	Outside	14	9	9	9	9	8	8	8	8	8
3	Avg	10	10	10	10	11	9	9	9	9	9
	Inside	10	10	10	11	11	9	9	9	9	9
	Outside	17	9	9	10	10	8	9	9	9	9
4	Avg	14	17	11	14	14	9	9	9	9	10
	Inside	16	11	11	14	16	9	9	9	10	10
	Outside	17	10	10	11	13	9	9	9	9	9
5	Avg	-	19	18	19	16	10	10	10	11	11
	Inside	-	-	19	19	19	10	10	10	11	11
	Outside	-	-	-	-	17	9	9	10	10	11

Table A.1.3 No. of cycles to fracture for local imperfection =  $t/100$ , taking edge of compression face; original fracture parameters  $\epsilon'_f$  and  $c$  from Nip *et al.* (2010b)

No. of rows of elements	Strain output	No. of cycles to failure									
		rainflow technique					counting individual ramps				
		Region					Region				
		peak	A	B	C	whole	peak	A	B	C	whole
1	Avg	9	9	9	13	-	8	8	8	9	11
	Inside face	9	9	9	9	-	8	8	8	9	11
	Outside face	9	9	9	11	12	8	8	8	9	11
2	Avg	9	9	9	10	10	9	9	9	9	9
	Inside	9	9	9	10	18	9	9	9	9	9
	Outside	9	9	9	10	10	9	9	9	9	9
3	Avg	9	9	9	11	16	9	9	9	10	10
	Inside	10	10	10	11	-	9	9	9	10	11
	Outside	9	9	9	10	11	9	9	9	10	10
4	Avg	10	10	10	14	19	9	9	9	10	12
	Inside	10	10	10	14	-	9	9	9	11	13
	Outside	9	9	10	13	17	9	9	9	10	11
5	Avg	10	10	11	15	-	9	9	10	11	14
	Inside	11	11	11	15	-	10	10	10	11	15
	Outside	10	10	10	14	-	9	9	9	11	13

## Appendix A

Table A.1.4 No. of cycles to fracture for local imperfection =  $t/200$ , taking edge of compression face; original fracture parameters  $\varepsilon'_f$  and  $c$  from Nip *et al.* (2010b)

No. of rows of elements	Strain output	No. of cycles to failure									
		rainflow technique					counting individual ramps				
		Region					Region				
		peak	A	B	C	whole	peak	A	B	C	whole
1	Avg	9	9	9	11	13	8	8	8	9	10
	Inside face	9	9	9	9	-	8	8	8	9	11
	Outside face	9	9	9	12	12	8	8	8	9	10
2	Avg	9	9	9	10	10	9	9	9	9	9
	Inside	9	9	9	10	17	9	9	9	9	9
	Outside	9	9	9	10	9	8	8	8	9	9
3	Avg	9	9	10	11	16	9	9	9	10	10
	Inside	10	10	10	11	-	9	9	9	10	11
	Outside	9	9	9	11	11	9	9	9	9	9
4	Avg	10	10	10	14	19	9	9	9	10	11
	Inside	10	10	11	15	-	9	9	9	10	13
	Outside	9	9	10	13	17	9	9	9	10	11
5	Avg	11	11	11	15	-	9	9	10	11	14
	Inside	11	15	16	15	-	10	10	10	11	15
	Outside	10	10	10	14	-	9	9	9	11	13

Table A.1.5 No. of cycles to fracture for local imperfection =  $t/500$ , taking edge of compression face; original fracture parameters  $\varepsilon'_f$  and  $c$  from Nip *et al.* (2010b)

No. of rows of elements	Strain output	No. of cycles to failure									
		rainflow technique					counting individual ramps				
		Region					Region				
		peak	A	B	C	whole	peak	A	B	C	whole
1	Avg	9	9	9	9	-	8	8	8	9	10
	Inside face	9	9	9	9	-	8	8	8	9	11
	Outside face	9	9	9	9	12	8	8	8	9	10
2	Avg	9	9	9	10	10	8	8	8	9	9
	Inside	9	9	9	10	11	9	9	9	9	9
	Outside	9	9	9	10	9	8	8	8	9	9
3	Avg	9	9	9	11	15	9	9	9	9	10
	Inside	10	10	10	11	-	9	9	9	10	11
	Outside	9	9	9	11	11	9	9	9	9	9
4	Avg	10	10	10	14	-	9	9	9	10	11
	Inside	10	10	11	14	-	9	9	9	10	12
	Outside	9	9	10	13	16	9	9	9	10	10
5	Avg	10	11	11	15	-	9	9	10	11	13
	Inside	11	11	16	15	-	10	10	10	11	14
	Outside	10	10	10	15	-	9	9	9	11	12

## Appendix A

Table A.1.6 No. of cycles to fracture for local imperfection =  $t/25$ , taking edge of compression face; scaled fracture parameters  $\varepsilon'_f$  and  $c$  from Nip *et al.* (2010b)

No. of rows of elements	Strain output	No. of cycles to failure									
		rainflow technique					counting individual ramps				
		Region					Region				
		peak	A	B	C	whole	peak	A	B	C	whole
1	Avg	-	-	-	-	-	-	-	18	16	-
	Inside face	-	-	-	-	-	-	-	-	-	-
	Outside face	-	-	-	-	17	11	11	11	13	15
2	Avg	-	-	-	-	-	-	-	19	16	-
	Inside	-	-	-	-	-	-	-	-	-	-
	Outside	-	-	-	-	19	11	11	11	13	13
3	Avg	-	-	19	19	-	12	12	12	14	16
	Inside	-	-	-	-	-	-	-	-	-	-
	Outside	14	14	14	17	14	11	11	11	12	12
4	Avg	-	-	-	-	-	13	13	13	14	18
	Inside	-	-	-	-	-	-	-	-	-	-
	Outside	16	16	14	17	16	11	11	11	12	13
5	Avg	-	-	-	-	-	14	14	14	15	19
	Inside	-	-	-	-	-	-	-	-	-	-
	Outside	16	19	16	19	-	11	11	11	13	13

Table A.1.7 No. of cycles to fracture for local imperfection =  $t/50$ , taking edge of compression face; scaled fracture parameters  $\varepsilon'_f$  and  $c$  from Nip *et al.* (2010b)

No. of rows of elements	Strain output	No. of cycles to failure									
		rainflow technique					counting individual ramps				
		Region					Region				
		peak	A	B	C	whole	peak	A	B	C	whole
1	Avg	-	-	19	19	-	9	9	9	9	10
	Inside face	-	-	-	-	-	9	9	9	9	11
	Outside face	15	15	15	15	18	9	9	9	9	10
2	Avg	9	9	9	10	10	8	8	8	9	9
	Inside	9	10	10	10	10	8	8	9	9	9
	Outside	14	9	9	10	9	8	8	8	9	9
3	Avg	10	10	10	10	11	9	9	9	9	9
	Inside	10	10	10	11	11	9	9	9	9	10
	Outside	17	11	10	10	10	9	9	9	9	9
4	Avg	14	14	11	11	12	9	9	9	10	10
	Inside	15	11	11	11	15	9	10	10	10	10
	Outside	17	10	10	11	11	9	9	9	9	10
5	Avg	-	18	17	14	14	10	10	10	10	11
	Inside	-	17	17	16	16	10	10	10	11	11
	Outside	19	19	19	19	15	9	9	10	10	10

## Appendix A

Table A.1.8 No. of cycles to fracture for local imperfection =  $t/100$ , taking edge of compression face; scaled fracture parameters  $\varepsilon'_f$  and  $c$  from Nip *et al.* (2010b)

No. of rows of elements	Strain output	No. of cycles to failure									
		rainflow technique					counting individual ramps				
		Region					Region				
		peak	A	B	C	whole	peak	A	B	C	whole
1	Avg	9	9	9	13	-	8	8	9	9	10
	Inside face	9	9	9	13	-	8	8	9	9	10
	Outside face	9	9	10	11	12	8	8	9	9	10
2	Avg	9	9	9	10	10	9	9	9	9	9
	Inside	9	9	9	10	11	9	9	9	9	10
	Outside	9	9	9	10	10	9	9	9	9	9
3	Avg	10	10	10	11	14	9	9	9	10	10
	Inside	10	10	10	11	17	9	9	9	10	11
	Outside	10	10	9	10	11	9	9	9	10	10
4	Avg	10	10	10	11	16	9	9	9	10	11
	Inside	10	10	10	11	17	9	9	10	10	12
	Outside	9	10	10	11	14	9	9	9	10	10
5	Avg	10	10	11	14	17	9	9	10	11	12
	Inside	11	11	11	14	17	10	10	10	11	12
	Outside	10	10	10	13	17	9	9	9	11	11

Table A.1.9 No. of cycles to fracture for local imperfection =  $t/200$ , taking edge of compression face; scaled fracture parameters  $\varepsilon'_f$  and  $c$  from Nip *et al.* (2010b)

No. of rows of elements	Strain output	No. of cycles to failure									
		rainflow technique					counting individual ramps				
		Region					Region				
		peak	A	B	C	whole	peak	A	B	C	whole
1	Avg	9	9	9	11	13	8	8	8	9	10
	Inside face	9	9	9	9	-	8	8	8	9	11
	Outside face	9	9	9	12	12	8	8	8	9	10
2	Avg	9	9	9	10	10	9	9	9	9	9
	Inside	9	9	9	10	17	9	9	9	9	9
	Outside	9	9	9	10	9	8	8	8	9	9
3	Avg	9	9	10	11	16	9	9	9	10	10
	Inside	10	10	10	11	-	9	9	9	10	11
	Outside	9	9	9	11	11	9	9	9	9	9
4	Avg	10	10	10	14	19	9	9	9	10	11
	Inside	10	10	11	15	-	9	9	9	10	13
	Outside	9	9	10	13	17	9	9	9	10	11
5	Avg	11	11	11	15	-	9	9	10	11	14
	Inside	11	15	16	15	-	10	10	10	11	15
	Outside	10	10	10	14	-	9	9	9	11	13

## Appendix A

Table A.1.10 No. of cycles to fracture for local imperfection =  $t/500$ , taking edge of compression face; scaled fracture parameters  $\varepsilon'_f$  and  $c$  from Nip *et al.* (2010b)

No. of rows of elements	Strain output	No. of cycles to failure									
		rainflow technique					counting individual ramps				
		Region					Region				
		peak	A	B	C	whole	peak	A	B	C	whole
1	Avg	9	9	9	13	17	8	8	8	9	10
	Inside face	9	9	9	10	16	8	8	8	9	10
	Outside face	9	9	9	11	11	8	8	8	9	10
2	Avg	9	9	9	10	10	9	9	9	9	9
	Inside	9	9	9	10	11	9	9	9	9	9
	Outside	9	9	9	10	10	9	9	9	9	9
3	Avg	9	9	10	11	11	9	9	9	10	10
	Inside	10	10	10	11	16	9	9	9	10	10
	Outside	9	9	9	10	11	9	9	9	9	9
4	Avg	10	10	10	11	15	9	9	9	10	11
	Inside	10	10	11	11	17	9	9	10	10	11
	Outside	9	10	10	11	14	9	9	9	10	10
5	Avg	10	10	11	14	17	9	9	10	10	12
	Inside	11	11	11	14	-	10	10	10	11	12
	Outside	10	10	10	14	15	9	9	9	10	11

## Appendix A

Figures A.1.3 and A.1.4 illustrate the part of the steel circumference of Specimen CF-H-1500 which is included in each of the Regions D to F, used to estimate the number of cycles to fracture for cyclically loaded braces. Figure A.1.3 shows regions with respect to the longitudinal strains around the section circumference whereas Figure A.1.4 shows a view through the cross-section at the mid-length and highlights the region in relation to their positions on the circumference.

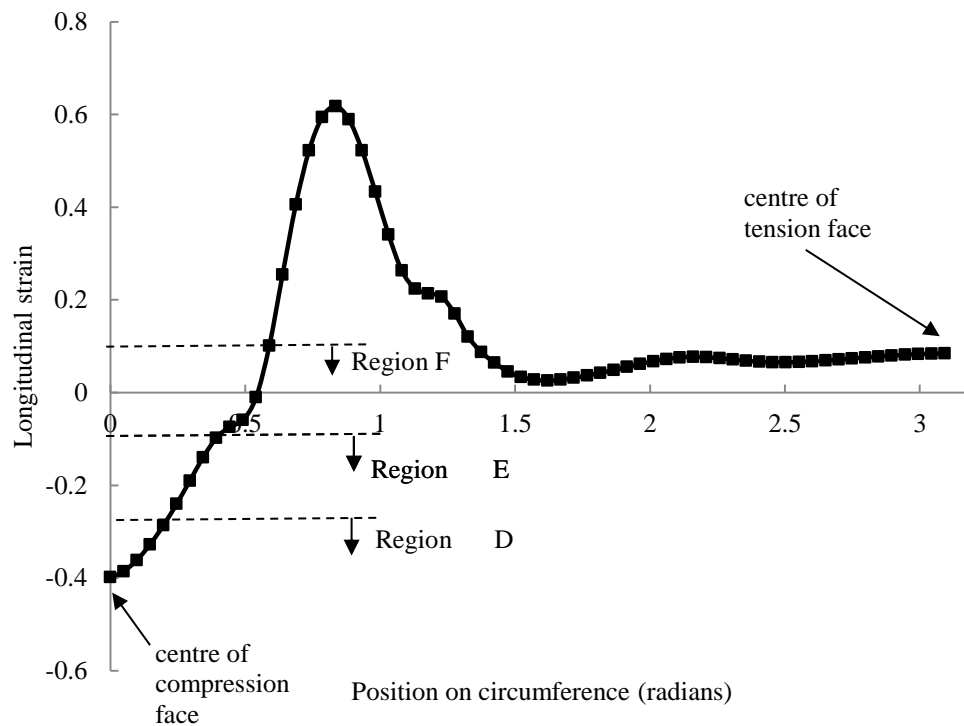
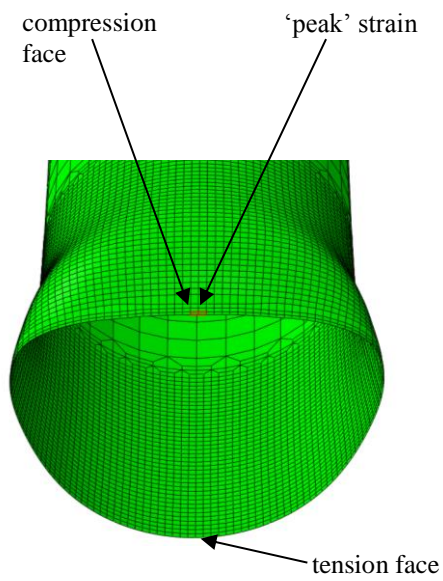
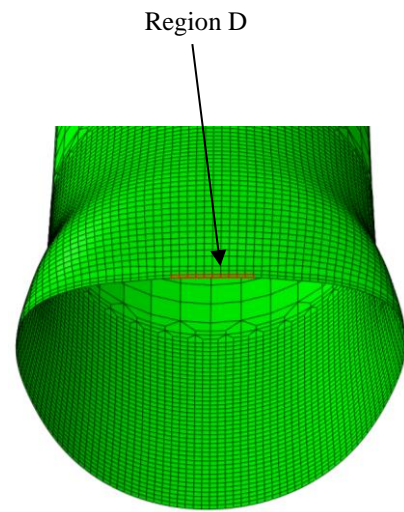


Figure A.1.3 Regions at centre of compression face for monitoring strain progressions

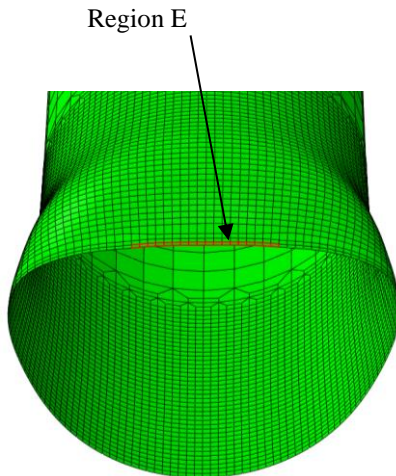
## Appendix A



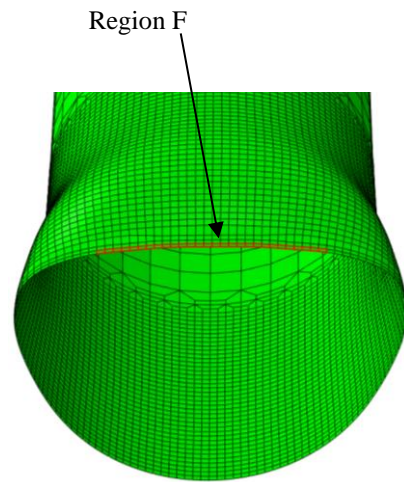
(a)



(b)



(c)



(d)

Figure A.1.4 Buckled shape of cold formed CHS at mid-length, showing (a) Elements undergoing maximum strains ('peak' elements) at centre of compression face; (b) Region D for monitoring strains; (c) Region E; (d) Region F

## Appendix A

Tables A.1.11 to A.1.20 present the estimated number of cycles to fracture for the finite element model of specimen CF-H-1500 using Regions D to F of the steel circumference as shown in Figure A.1.4 in addition to the ‘whole’ compression face of the tube. Similarly to Tables A.1.1 to A.1.10, the results are compared from using strain values on the inside face of the tube, the outside face and the average between these two values, and employing two different counting techniques. Tables A.1.11 to A.1.20 compare the predicted number of cycles to fracture for local imperfection amplitudes of  $t/25$ ,  $t/50$ ,  $t/100$ ,  $t/200$  and  $t/500$ , where  $t$  is the tube wall thickness. Tables A.1.11 to A.1.15 use the parameters  $\varepsilon'_f$  and  $c$  obtained from the material tests in Nip *et al.* (2010b) for the Coffin-Manson relationship and for Tables A.1.16 to A.1.20 these parameters were scaled to according to the steel yield stress used in the finite element models.

Table A.1.11 No. of cycles to fracture for local imperfection =  $t/25$ , taking centre of compression face; original fracture parameters  $\varepsilon'_f$  and  $c$  from Nip *et al.* (2010b)

No. of rows of elements	Strain output	No. of cycles to failure									
		rainflow technique					counting individual ramps				
		Region					Region				
		peak	D	E	F	whole	peak	D	E	F	whole
1	Avg	-	-	-	-	-	-	-	-	-	-
	Inside face	-	-	-	-	-	-	-	-	-	-
	Outside face	-	-	-	-	-	-	-	-	-	-
2	Avg	-	-	-	-	-	-	-	-	-	-
	Inside	14	17	-	-	-	12	13	15	-	-
	Outside	15	15	16	-	-	11	11	11	12	15
3	Avg	-	-	-	-	-	-	-	-	-	-
	Inside	17	17	18	-	-	14	15	15	18	-
	Outside	14	14	14	11	14	12	12	11	11	12
4	Avg	-	-	-	-	-	-	-	-	-	-
	Inside	-	-	-	-	-	18	-	-	-	-
	Outside	-	-	16	15	16	13	13	13	12	13
5	Avg	-	-	-	-	-	-	-	-	-	-
	Inside	-	-	-	-	-	-	-	-	-	-
	Outside	-	-	-	-	-	16	15	14	14	14



## Appendix A

Table A.1.12 No. of cycles to fracture for local imperfection =  $t/50$ , taking centre of compression face; original fracture parameters  $\varepsilon'_f$  and  $c$  from Nip *et al.* (2010b)

No. of rows of elements	Strain output	No. of cycles to failure									
		rainflow technique					counting individual ramps				
		Region					Region				
		peak	D	E	F	whole	peak	D	E	F	whole
1	Avg	-	-	-	-	-	-	-	-	-	10
	Inside face	-	-	-	-	-	-	-	-	-	11
	Outside face	-	-	-	-	19	-	-	-	-	9
2	Avg	9	9	9	9	10	8	8	8	8	9
	Inside	9	9	9	9	10	9	9	9	9	9
	Outside	9	9	9	9	9	8	8	8	8	8
3	Avg	10	10	10	10	11	9	9	9	9	9
	Inside	14	11	11	11	11	9	9	9	9	9
	Outside	9	9	9	9	10	8	8	8	8	9
4	Avg	-	-	-	13	14	9	9	9	9	10
	Inside	15	15	15	14	15	11	11	11	11	10
	Outside	-	-	19	18	13	9	9	9	9	9
5	Avg	19	18	18	18	16	12	12	11	11	11
	Inside	-	-	-	19	18	15	15	14	13	11
	Outside	-	-	-	-	17	9	9	9	9	11

Table A.1.13 No. of cycles to fracture for local imperfection =  $t/100$ , taking centre of compression face; original fracture parameters  $\varepsilon'_f$  and  $c$  from Nip *et al.* (2010b)

No. of rows of elements	Strain output	No. of cycles to failure									
		rainflow technique					counting individual ramps				
		Region					Region				
		peak	D	E	F	whole	peak	D	E	F	whole
1	Avg	-	-	-	-	-	-	-	-	-	11
	Inside face	-	-	-	-	-	-	-	-	-	11
	Outside face	-	-	-	-	13	-	-	-	-	11
2	Avg	9	9	9	9	10	8	8	8	8	9
	Inside	-	-	-	-	18	9	9	9	9	9
	Outside	9	9	9	9	10	8	8	8	8	9
3	Avg	-	-	-	15	16	9	9	9	9	10
	Inside	-	-	-	-	-	16	15	12	10	11
	Outside	9	9	9	9	11	8	8	9	9	10
4	Avg	-	-	-	-	19	18	17	12	10	12
	Inside	-	-	-	-	-	-	-	-	-	13
	Outside	-	-	-	11	17	9	9	9	9	11
5	Avg	-	-	-	-	-	-	-	-	-	14
	Inside	-	-	-	-	-	-	-	-	-	15
	Outside	-	-	-	-	-	-	-	18	10	13

## Appendix A

Table A.1.14 No. of cycles to fracture for local imperfection =  $t/200$ , taking centre of compression face; original fracture parameters  $\varepsilon'_f$  and  $c$  from Nip *et al.* (2010b)

No. of rows of elements	Strain output	No. of cycles to failure									
		rainflow technique					counting individual ramps				
		Region					Region				
		peak	D	E	F	whole	peak	D	E	F	whole
1	Avg	-	-	-	-	13	-	-	-	-	10
	Inside face	-	-	-	-	-	-	-	-	-	11
	Outside face	-	-	-	-	12	-	-	-	-	10
2	Avg	9	9	9	9	10	8	8	8	8	9
	Inside	16	16	16	18	17	9	9	9	9	9
	Outside	10	11	11	11	9	8	8	8	8	8
3	Avg	-	19	18	11	16	9	9	9	9	10
	Inside	-	-	-	-	-	11	11	11	10	11
	Outside	-	-	-	-	11	8	8	8	9	9
4	Avg	-	-	-	-	19	11	11	11	10	11
	Inside	-	-	-	-	-	-	-	-	-	13
	Outside	11	15	16	10	17	9	9	9	9	11
5	Avg	-	-	-	-	-	-	-	-	-	14
	Inside	-	-	-	-	-	-	-	-	-	15
	Outside	-	-	-	-	-	11	11	11	10	13

Table A.1.15 No. of cycles to fracture for local imperfection =  $t/500$ , taking centre of compression face; original fracture parameters  $\varepsilon'_f$  and  $c$  from Nip *et al.* (2010b)

No. of rows of elements	Strain output	No. of cycles to failure									
		rainflow technique					counting individual ramps				
		Region					Region				
		peak	D	E	F	whole	peak	D	E	F	whole
1	Avg	-	-	-	-	-	-	-	-	-	10
	Inside face	-	-	-	-	-	-	-	-	-	11
	Outside face	-	-	-	-	12	-	-	-	-	10
2	Avg	9	9	9	9	10	8	8	8	8	9
	Inside	10	10	10	11	11	9	9	9	9	9
	Outside	10	10	11	11	9	8	8	8	8	9
3	Avg	15	15	15	10	15	9	9	9	9	10
	Inside	-	-	-	-	-	10	10	10	10	11
	Outside	-	-	-	-	11	8	8	8	8	9
4	Avg	-	-	-	-	-	10	10	10	10	11
	Inside	-	-	-	-	-	-	-	-	-	12
	Outside	10	10	10	10	16	9	9	9	9	10
5	Avg	-	-	-	-	-	-	-	-	-	13
	Inside	-	-	-	-	-	-	-	-	-	14
	Outside	-	-	-	-	-	10	10	10	10	12

## Appendix A

Table A.1.16 No. of cycles to fracture for local imperfection =  $t/25$ , taking centre of compression face; scaled fracture parameters  $\varepsilon'_f$  and  $c$  from Nip *et al.* (2010b)

No. of rows of elements	Strain output	No. of cycles to failure									
		rainflow technique					counting individual ramps				
		Region					Region				
		peak	D	E	F	whole	peak	D	E	F	whole
1	Avg	-	-	-	-	-	-	-	-	-	-
	Inside face	-	-	-	-	-	-	-	-	-	-
	Outside face	-	-	-	-	17	-	-	-	-	15
2	Avg	-	-	-	-	-	-	-	-	-	-
	Inside	13	16	18	-	-	12	12	14	17	-
	Outside	14	15	16	18	19	11	11	11	12	13
3	Avg	-	-	-	-	19	-	-	-	-	16
	Inside	15	15	15	17	-	13	14	14	15	-
	Outside	14	14	14	11	14	11	11	11	11	12
4	Avg	-	-	-	-	-	-	-	-	-	18
	Inside	17	17	18	-	-	15	16	16	18	-
	Outside	15	15	15	14	15	12	12	12	12	13
5	Avg	-	-	-	-	-	-	-	-	-	19
	Inside	-	-	-	-	-	17	18	19	-	-
	Outside	-	-	-	-	-	13	13	13	13	13

Table A.1.17 No. of cycles to fracture for local imperfection =  $t/50$ , taking centre of compression face; scaled fracture parameters  $\varepsilon'_f$  and  $c$  from Nip *et al.* (2010b)

No. of rows of elements	Strain output	No. of cycles to failure									
		rainflow technique					counting individual ramps				
		Region					Region				
		peak	D	E	F	whole	peak	D	E	F	whole
1	Avg	-	-	-	-	-	-	-	-	-	10
	Inside face	-	-	-	-	-	-	-	-	-	11
	Outside face	-	-	-	-	19	-	-	-	-	9
2	Avg	9	9	9	9	10	8	8	8	8	9
	Inside	9	9	9	9	10	9	9	9	9	9
	Outside	9	9	9	9	9	8	8	8	8	8
3	Avg	10	10	10	10	11	9	9	9	9	9
	Inside	14	11	11	11	11	9	9	9	9	9
	Outside	9	9	9	9	10	8	8	8	8	9
4	Avg	-	-	-	13	14	9	9	9	9	10
	Inside	15	15	15	14	15	11	11	11	11	10
	Outside	-	-	19	18	13	9	9	9	9	9
5	Avg	19	18	18	18	16	12	12	11	11	11
	Inside	-	-	-	19	18	15	15	14	13	11
	Outside	-	-	-	-	17	9	9	9	9	11

## Appendix A

Table A.1.18 No. of cycles to fracture for local imperfection =  $t/100$ , taking centre of compression face; scaled fracture parameters  $\varepsilon'_f$  and  $c$  from Nip *et al.* (2010b)

No. of rows of elements	Strain output	No. of cycles to failure									
		rainflow technique					counting individual ramps				
		Region					Region				
		peak	D	E	F	whole	peak	D	E	F	whole
1	Avg	-	-	-	-	-	-	-	-	-	10
	Inside face	-	-	-	-	-	-	-	-	-	10
	Outside face	-	-	-	-	12	-	-	-	-	10
2	Avg	9	9	9	9	10	9	9	9	9	9
	Inside	18	18	18	18	11	9	9	9	9	10
	Outside	9	9	9	9	10	8	8	8	8	9
3	Avg	17	17	16	11	14	9	9	9	9	10
	Inside	-	-	-	-	17	11	11	11	10	11
	Outside	9	9	9	9	11	9	9	9	9	10
4	Avg	-	-	-	-	16	11	11	10	10	11
	Inside	-	-	-	-	17	-	-	19	15	12
	Outside	11	14	11	10	14	9	9	9	9	10
5	Avg	-	-	-	-	17	-	-	19	14	12
	Inside	-	-	-	-	17	-	-	19	15	12
	Outside	-	-	-	-	17	11	11	10	10	11

Table A.1.19 No. of cycles to fracture for local imperfection =  $t/200$ , taking centre of compression face; scaled fracture parameters  $\varepsilon'_f$  and  $c$  from Nip *et al.* (2010b)

No. of rows of elements	Strain output	No. of cycles to failure									
		rainflow technique					counting individual ramps				
		Region					Region				
		peak	D	E	F	whole	peak	D	E	F	whole
1	Avg	-	-	-	-	11	-	-	-	-	10
	Inside face	-	-	-	-	16	-	-	-	-	10
	Outside face	-	-	-	-	12	-	-	-	-	10
2	Avg	10	10	10	9	10	9	9	9	9	9
	Inside	11	11	11	15	11	9	9	9	9	9
	Outside	10	10	11	11	10	8	8	8	8	8
3	Avg	11	11	11	10	14	9	9	9	9	10
	Inside	-	-	-	-	17	10	10	10	10	10
	Outside	-	-	-	19	11	9	9	9	9	9
4	Avg	-	-	-	-	15	10	10	10	10	11
	Inside	-	-	-	-	17	19	18	17	14	11
	Outside	10	10	10	10	14	9	9	9	9	10
5	Avg	-	-	-	-	17	18	18	16	12	12
	Inside	-	-	-	-	17	-	-	-	18	12
	Outside	-	-	-	-	16	10	10	10	10	11

## Appendix A

Table A.1.20 No. of cycles to fracture for local imperfection =  $t/500$ , taking centre of compression face; scaled fracture parameters  $\varepsilon'_f$  and  $c$  from Nip *et al.* (2010b)

No. of rows of elements	Strain output	No. of cycles to failure									
		rainflow technique					counting individual ramps				
		Region					Region				
		peak	D	E	F	whole	peak	D	E	F	whole
1	Avg	-	-	-	-	17	-	-	-	-	10
	Inside face	-	-	-	-	16	-	-	-	-	10
	Outside face	-	-	-	-	11	-	-	-	-	10
2	Avg	9	9	9	9	10	8	8	9	9	9
	Inside	10	10	10	11	11	9	9	9	9	9
	Outside	10	10	10	11	10	8	8	8	8	9
3	Avg	10	10	10	10	11	9	9	9	9	10
	Inside	-	-	-	-	16	10	10	10	10	10
	Outside	-	-	-	-	11	9	9	9	9	9
4	Avg	-	-	-	-	15	10	10	10	10	11
	Inside	-	-	-	-	17	-	16	15	12	11
	Outside	10	10	10	10	14	9	9	9	9	10
5	Avg	-	-	-	-	17	16	16	14	11	12
	Inside	-	-	-	-	-	-	-	-	-	12
	Outside	-	-	-	-	15	10	10	10	9	11

## A.2 Verification of finite element models

Appendix A.2 presents the number of cycles to fracture for each of the finite element simulations of laboratory test specimens CF-H-1500, HF-H-1500, CF-H-3000 and HF-H-3000. The number of cycles to failure in the laboratory experiments is presented at the top of each page above the table, in addition to two initial observations from the experiments. The first of these was obtained from inspecting the load-displacement hysteresis curve and identifying the point at which the load suddenly decreased, deviating from the pattern in preceding cycles. The second initial estimation was taken at the stage when all of the strains across tube face (compressive side) exceeded the ultimate strain of the material from the tensile coupon tests. The individual columns and rows of the tables compare the predicted number of cycles to fracture employing the various monitoring regions described in A.1, comparing the two counting algorithms which were described previously. Two tables are presented for each specimen. The first uses the ‘original’ values for the Coffin-Manson relationship (Coffin, 1954; Manson, 1954) and parameters  $\epsilon'_f$  and  $c$  obtained in the material tests of Nip *et al.* (2010b). The second table contains estimations in which these parameters were scaled to match the difference in yield stress between the materials in Nip *et al.* (2010b) and the materials used in this thesis

**CF-H-1500**

Number of cycles to fracture:      Experimental result: 14

Finite element results: Load-displacement hysteresis curve: 11

Strain increase beyond tensile tests: 11

Table A.2.1 No. of cycles to fracture for CF-H-1500 using original fracture parameters  $\varepsilon'_f$  and  $c$  from Nip (2010b)

No. of rows	Strain output	No. of cycles to fracture															
		Rainflow technique								Individual ramps							
		Region (centre)				Region (edge)			Entire face	Region (centre)				Region (edge)			Entire face
		peak	D	E	F	peak	B	C		peak	D	E	F	peak	B	C	
<b>1</b>	Avg	-	-	-	-	9	9	13	-	-	-	-	-	8	8	9	11
	Inside	-	-	-	-	9	9	9	-	-	-	-	-	8	8	9	11
	Outside	-	-	-	-	9	9	11	13	-	-	-	-	8	8	9	11
<b>2</b>	Avg	9	9	9	9	9	9	10	10	8	8	8	8	9	9	9	9
	Inside	-	-	-	-	9	9	10	18	9	9	9	9	9	9	9	9
	Outside	9	9	9	9	9	9	10	10	8	8	8	8	9	9	9	9
<b>3</b>	Avg	-	-	-	15	9	9	11	16	9	9	9	9	9	9	10	10
	Inside	-	-	-	-	10	10	11	-	16	15	12	10	9	9	10	10
	Outside	9	9	9	9	9	9	10	11	8	8	9	9	9	9	10	10
<b>4</b>	Avg	-	-	-	-	10	10	14	19	18	17	12	10	9	9	10	12
	Inside	-	-	-	-	10	10	14	-	-	-	-	-	9	9	11	13
	Outside	-	-	-	11	9	10	13	17	9	9	9	9	9	9	10	11
<b>5</b>	Avg	-	-	-	-	10	11	15	-	-	-	-	-	9	10	11	14
	Inside	-	-	-	-	11	11	15	-	-	-	-	-	10	10	11	15
	Outside	-	-	-	-	10	10	14	-	-	-	18	10	9	9	11	13

Table A.2.2 No. of cycles to fracture for CF-H-1500 using scaled fracture parameters  $\varepsilon'_f$  and  $c$  from Nip (2010b)

No. of rows	Strain output	No. of cycles to fracture															
		Rainflow technique								Individual ramps							
		Region (centre)				Region (edge)			Entire face	Region (centre)				Region (edge)			Entire face
		peak	D	E	F	peak	B	C		peak	D	E	F	peak	B	C	
<b>1</b>	Avg	-	-	-	-	9	9	13	-	-	-	-	-	8	9	9	10
	Inside	-	-	-	-	9	9	13	-	-	-	-	-	8	9	9	10
	Outside	-	-	-	-	9	10	11	12	-	-	-	-	8	9	9	10
<b>2</b>	Avg	9	9	9	9	9	9	10	10	9	9	9	9	9	9	9	9
	Inside	18	18	18	18	9	9	10	11	9	9	9	9	9	9	9	10
	Outside	9	9	9	9	9	9	10	10	8	8	8	8	9	9	9	9
<b>3</b>	Avg	17	17	16	11	10	10	11	14	9	9	9	9	9	9	10	10
	Inside	-	-	-	-	10	10	11	17	11	11	11	10	9	9	10	11
	Outside	9	9	9	9	10	9	10	11	9	9	9	9	9	9	10	10
<b>4</b>	Avg	-	-	-	-	10	10	11	16	11	11	10	10	9	9	10	11
	Inside	-	-	-	-	10	10	11	17	-	-	19	15	9	10	10	12
	Outside	11	14	11	10	9	10	11	14	9	9	9	9	9	9	10	10
<b>5</b>	Avg	-	-	-	-	10	11	14	17	-	-	19	14	9	10	11	12
	Inside	-	-	-	-	11	11	14	17	-	-	19	15	10	10	11	12
	Outside	-	-	-	-	10	10	13	17	11	11	10	10	9	9	11	11



**HF-H-1500**

Number of cycles to fracture:      Experimental result: 17

Finite element results: Load-displacement hysteresis curve: 11

Strain increase beyond tensile tests: 11

Table A.2.3 No. of cycles to fracture for HF-H-1500 using original fracture parameters  $\varepsilon'_f$  and  $c$  from Nip (2010b)

No. of rows	Strain output	No. of cycles to fracture															
		Rainflow technique								Individual ramps							
		Region (centre)				Region (edge)			Entire face	Region (centre)				Region (edge)			Entire face
		peak	D	E	F	peak	B	C		peak	D	E	F	peak	B	C	
<b>1</b>	Avg	12	12	12	12	12	12	12	12	11	11	11	11	11	11	11	11
	Inside	12	12	12	12	13	13	13	12	11	11	11	12	12	12	12	12
	Outside	12	12	12	14	15	15	15	12	11	11	11	11	11	11	11	11
<b>2</b>	Avg	14	14	14	14	13	13	13	13	12	12	12	12	12	12	12	12
	Inside	13	13	14	15	16	16	16	14	12	13	12	13	14	14	14	13
	Outside	14	14	14	16	18	18	18	12	12	12	12	12	11	11	11	12
<b>3</b>	Avg	15	16	16	16	18	18	16	18	13	13	14	13	14	13	13	13
	Inside	15	15	16	18	20	20	20	18	14	14	15	15	18	18	17	15
	Outside	15	15	15	19	21	21	21	20	13	13	13	12	12	12	12	12
<b>4</b>	Avg	19	20	22	21	21	21	21	22	15	15	15	15	18	18	17	16
	Inside	18	19	21	22	24	24	24	22	15	16	18	19	21	21	21	19
	Outside	16	18	20	24	27	27	27	27	14	14	14	13	13	13	13	14
<b>5</b>	Avg	24	-	-	-	-	-	-	-	16	18	20	19	21	21	21	20
	Inside	24	-	-	-	-	-	-	-	19	21	23	23	25	25	25	23
	Outside	21	22	-	-	-	-	-	-	15	16	17	15	15	15	15	16

Table A.2.4 No. of cycles to fracture for HF-H-1500 using scaled fracture parameters  $\varepsilon'_f$  and  $c$  from Nip (2010b)

No. of rows	Strain output	No. of cycles to fracture															
		Rainflow technique								Individual ramps							
		Region (centre)				Region (edge)			Entire face	Region (centre)				Region (edge)			Entire face
		peak	D	E	F	peak	B	C		peak	D	E	F	peak	B	C	
<b>1</b>	Avg	12	12	12	12	12	12	12	12	11	11	11	11	11	11	11	11
	Inside	12	12	12	12	13	13	13	12	11	11	11	11	11	11	11	11
	Outside	12	12	12	14	15	15	15	12	11	11	11	11	11	11	11	11
<b>2</b>	Avg	14	14	14	14	13	13	13	13	12	12	12	12	12	12	12	12
	Inside	13	13	14	15	16	16	16	14	12	12	13	13	14	14	14	13
	Outside	14	14	14	16	18	18	18	12	12	12	12	11	11	11	11	12
<b>3</b>	Avg	15	16	18	18	19	18	18	18	13	13	14	13	14	14	13	14
	Inside	15	15	18	19	21	21	21	19	14	14	15	16	19	19	18	15
	Outside	15	15	15	20	22	22	21	21	13	13	13	12	12	12	12	12
<b>4</b>	Avg	20	22	27	22	24	24	22	24	15	15	16	16	19	19	19	16
	Inside	19	21	26	24	-	-	-	27	16	17	19	20	23	23	22	21
	Outside	17	19	21	-	-	-	-	-	14	14	15	13	13	13	13	14
<b>5</b>	Avg	-	-	-	-	-	-	-	-	19	20	23	21	24	24	23	23
	Inside	-	-	-	-	-	-	-	-	22	24	27	26	-	-	-	27
	Outside	26	-	-	-	-	-	-	-	16	17	19	15	17	16	16	18

**CF-H-3000**

Number of cycles to fracture:      Experimental result: 17

Finite element results: Load-displacement hysteresis curve: 11

Strain increase beyond tensile tests: 11

Table A.2.5 No. of cycles to fracture for CF-H-3000 using original fracture parameters  $\varepsilon'_f$  and  $c$  from Nip (2010b)

No. of rows	Strain output	No. of cycles to fracture															
		Rainflow technique								Individual ramps							
		Region (centre)				Region (edge)			Entire face	Region (centre)				Region (edge)			Entire face
		peak	D	E	F	peak	B	C		peak	D	E	F	peak	B	C	
<b>1</b>	Avg	-	-	-	-	-	-	-	-	11	11	11	11	9	9	13	11
	Inside	-	-	-	-	-	-	-	-	11	11	13	13	10	13	14	11
	Outside	-	-	-	-	-	-	-	-	10	11	11	10	9	9	9	10
<b>2</b>	Avg	10	10	10	10	12	12	12	11	10	10	10	9	9	9	9	10
	Inside	10	11	12	12	13	13	13	11	10	10	10	10	11	11	11	10
	Outside	10	10	10	10	10	10	10	10	9	9	9	9	9	9	9	9
<b>3</b>	Avg	11	11	11	11	-	14	13	12	10	10	10	10	10	10	10	10
	Inside	11	12	13	13	-	13	-	13	10	11	11	11	-	12	12	11
	Outside	10	10	11	11	13	12	12	11	10	10	9	9	9	9	9	10
<b>4</b>	Avg	11	11	13	13	-	-	-	13	10	10	11	11	11	11	11	11
	Inside	11	12	-	-	-	-	-	-	10	11	11	11	14	13	13	11
	Outside	11	11	12	12	-	-	-	12	10	10	10	10	9	9	9	10
<b>5</b>	Avg	11	13	-	-	-	-	-	-	10	11	11	11	13	13	13	11
	Inside	11	13	-	-	-	-	-	-	11	11	11	11	18	14	14	11
	Outside	11	12	15	15	-	-	-	18	10	10	10	10	10	10	10	11

Table A.2.6 No. of cycles to fracture for CF-H-3000 using scaled fracture parameters  $\varepsilon'_f$  and  $c$  from Nip (2010b)

No. of rows	Strain output	No. of cycles to fracture															
		Rainflow technique								Individual ramps							
		Region (centre)				Region (edge)			Entire face	Region (centre)				Region (edge)			Entire face
		peak	D	E	F	peak	B	C		peak	D	E	F	peak	B	C	
<b>1</b>	Avg	-	-	-	-	-	-	-	-	11	11	11	11	9	10	13	11
	Inside	-	-	-	-	-	-	-	-	11	11	13	13	10	13	14	11
	Outside	-	-	-	14	-	-	-	-	10	11	11	10	9	9	9	10
<b>2</b>	Avg	10	10	10	11	12	12	12	11	10	10	10	10	9	9	9	10
	Inside	11	11	12	11	13	13	13	11	10	10	10	10	11	11	11	10
	Outside	10	10	10	10	11	10	10	10	9	9	9	9	9	9	9	9
<b>3</b>	Avg	11	11	11	11	13	13	13	11	10	10	10	10	10	10	10	10
	Inside	11	12	12	12	-	12	-	12	10	11	11	11	-	12	12	11
	Outside	10	10	11	11	12	12	12	11	10	10	10	10	9	9	9	10
<b>4</b>	Avg	11	11	12	12	-	-	21	12	10	10	11	11	11	11	11	11
	Inside	11	12	13	13	-	-	-	13	10	11	11	11	13	13	13	11
	Outside	11	11	12	12	14	13	13	12	10	10	10	10	9	9	10	10
<b>5</b>	Avg	11	12	13	13	-	-	-	13	10	11	11	11	12	12	12	11
	Inside	11	12	22	-	-	-	-	21	11	11	11	11	14	14	13	11
	Outside	11	12	13	13	-	-	-	13	10	10	10	10	10	10	10	11

**HF-H-3000**

Number of cycles to fracture:      Experimental result: 24

Finite element results: Load-displacement hysteresis curve: 17

Strain increase beyond tensile tests: 20

Table A.2.7 No. of cycles to fracture for HF-H-3000 using original fracture parameters  $\varepsilon'_f$  and  $c$  from Nip (2010b)

No. of rows	Strain output	No. of cycles to fracture															
		Rainflow technique								Individual ramps							
		Region (centre)				Region (edge)			Entire face	Region (centre)				Region (edge)			Entire face
		peak	D	E	F	peak	B	C		peak	D	E	F	peak	B	C	
<b>1</b>	Avg	-	-	-	-	-	-	-	-	20	20	21	22	15	15	23	20
	Inside	-	-	-	-	-	-	-	-	20	20	23	24	21	23	24	23
	Outside	-	-	-	-	16	15	15	22	17	20	20	21	15	15	15	20
<b>2</b>	Avg	17	17	17	18	-	-	24	18	16	16	16	16	17	17	17	17
	Inside	17	17	20	-	-	-	-	-	16	17	17	17	18	20	20	17
	Outside	16	16	16	16	23	19	19	17	16	16	16	15	15	15	15	16
<b>3</b>	Avg	17	17	21	23	-	-	-	22	17	17	17	17	20	20	20	17
	Inside	17	20	-	-	-	-	-	-	17	17	19	20	-	-	-	20
	Outside	17	17	19	20	-	23	23	21	16	16	16	16	16	16	16	17
<b>4</b>	Avg	17	21	-	-	-	-	-	-	17	17	20	20	-	-	-	20
	Inside	21	-	-	-	-	-	-	-	17	18	21	-	-	-	-	24
	Outside	17	19	23	24	-	-	-	-	17	17	17	17	20	18	19	18
<b>5</b>	Avg	20	-	-	-	-	-	-	-	17	19	23	-	-	-	-	-
	Inside	-	-	-	-	-	-	-	-	18	20	-	-	-	-	-	-
	Outside	18	23	-	-	-	-	-	-	17	17	20	21	-	23	23	22

Table A.2.8 No. of cycles to fracture for HF-H-3000 using scaled fracture parameters  $\varepsilon'_f$  and  $c$  from Nip (2010b)

No. of rows	Strain output	No. of cycles to fracture															
		Rainflow technique								Individual ramps							
		Region (centre)				Region (edge)			Entire face	Region (centre)				Region (edge)			Entire face
		peak	D	E	F	peak	B	C		peak	D	E	F	peak	B	C	
<b>1</b>	Avg	-	-	-	-	-	-	-	-	20	20	21	23	15	15	23	20
	Inside	-	-	-	-	-	-	-	-	20	20	23	23	21	23	24	22
	Outside	24	-	-	23	16	16	16	21	17	20	20	17	15	15	15	20
<b>2</b>	Avg	17	17	17	18	-	-	-	18	16	16	16	16	17	17	17	17
	Inside	17	17	20	-	-	-	-	24	16	17	17	17	18	19	20	17
	Outside	17	16	16	16	20	19	18	17	16	16	16	16	15	15	15	16
<b>3</b>	Avg	17	17	21	23	-	-	-	24	17	17	17	17	19	19	19	17
	Inside	17	19	-	-	-	-	-	-	17	17	19	20	-	-	-	19
	Outside	17	17	19	19	24	22	22	21	16	16	16	16	16	16	16	17
<b>4</b>	Avg	17	20	-	-	-	-	-	-	17	17	19	20	24	23	23	20
	Inside	20	23	-	-	-	-	-	-	17	18	20	23	-	-	-	22
	Outside	17	18	22	22	-	-	-	23	17	17	17	17	18	17	18	18
<b>5</b>	Avg	19	24	-	-	-	-	-	-	17	18	20	22	-	-	-	23
	Inside	-	-	-	-	-	-	-	-	18	20	24	-	-	-	-	-
	Outside	18	20	-	-	-	-	-	-	17	17	20	20	23	22	21	20

### A.3 Load-displacement hysteresis curves for parametric studies

Figures A.3.1 to A.3.32 display the axial load-displacement hysteresis curves for each of the finite element models used in the hollow steel parametric studies of this thesis, with Figures A.3.1 to A.3.16 presenting the results from the cold formed steel models and Figures A.3.17 to A.3.32 covering the results of the hot-finished specimens. A sudden drop in axial load was observed at the point of failure in each model and the hence each of the figures is terminated at this point.

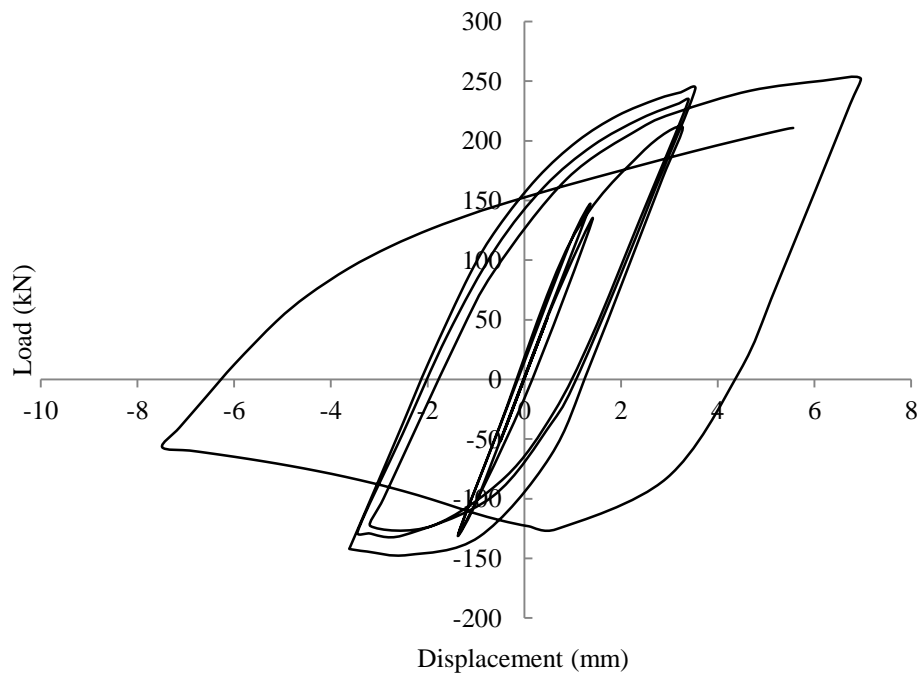


Figure A.3.1 Load-displacement relationship for CF1

## Appendix A

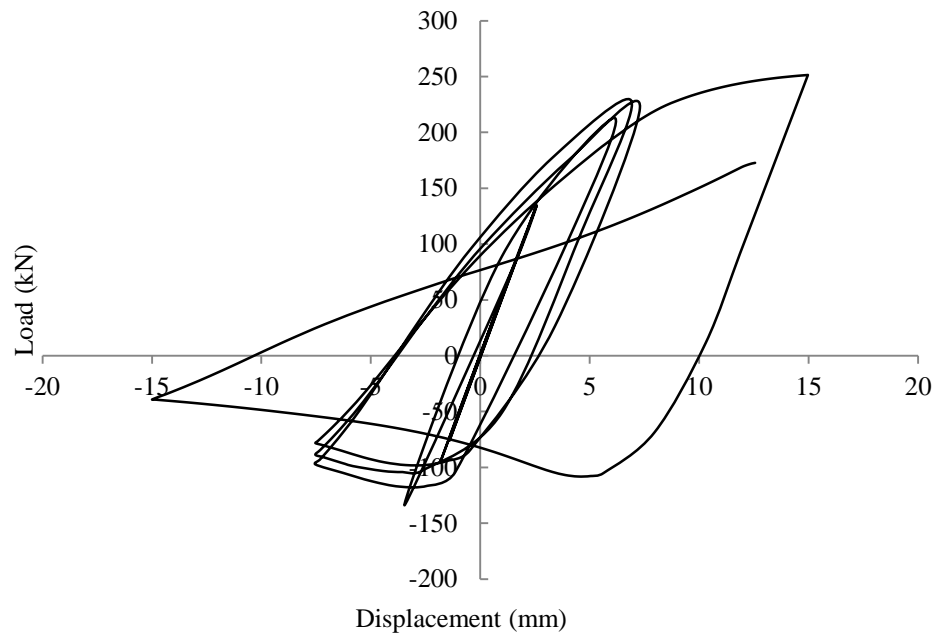


Figure A.3.2 Load-displacement relationship for CF2

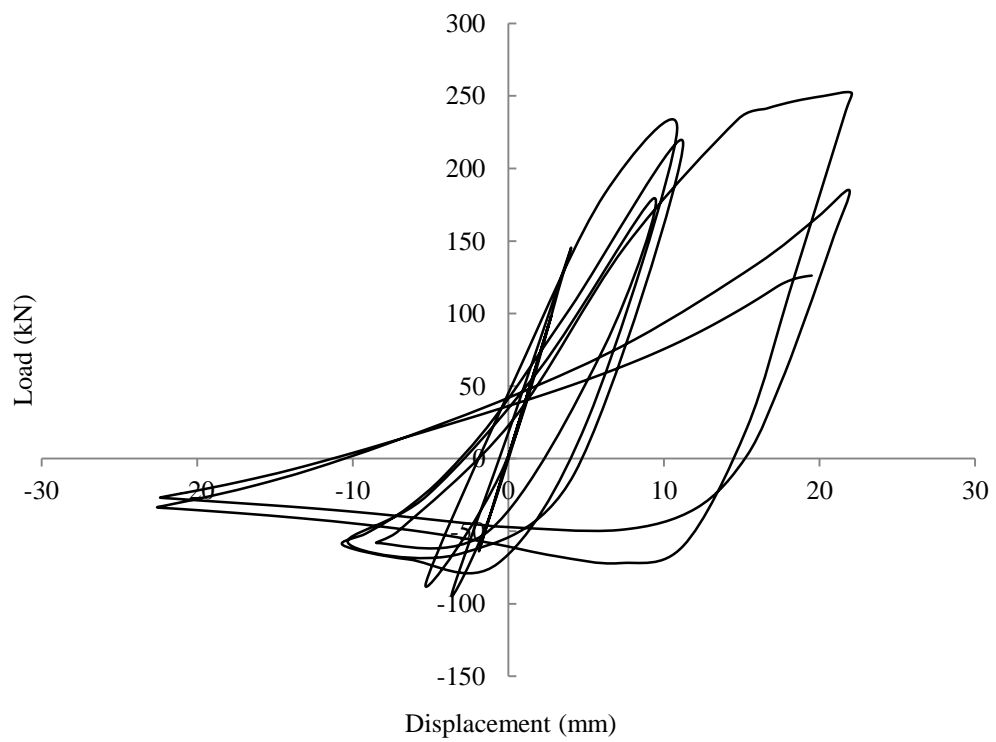


Figure A.3.3 Load-displacement relationship for CF3



## Appendix A

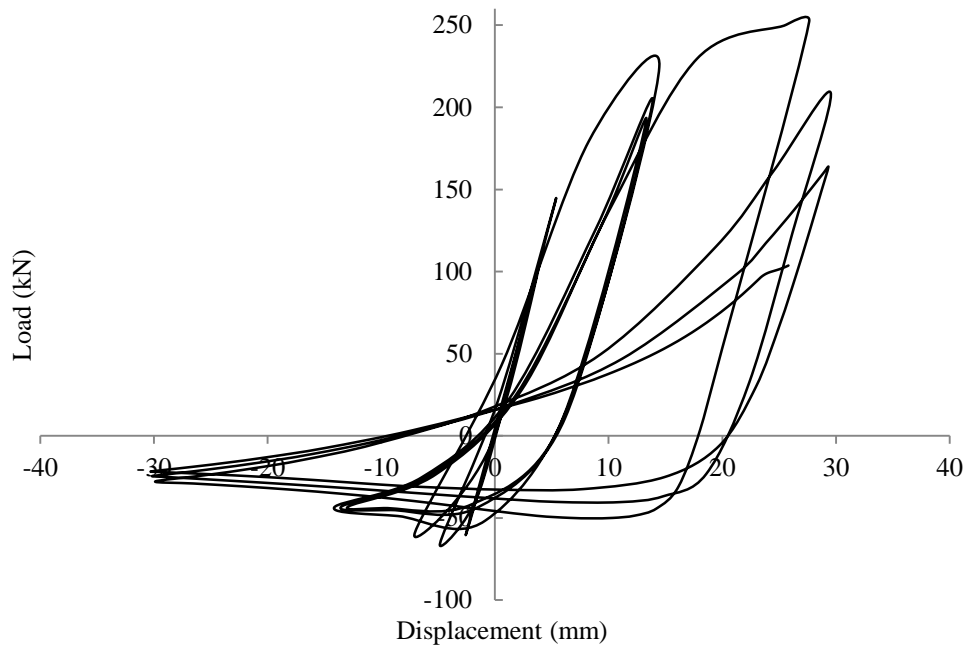


Figure A.3.4 Load-displacement relationship for CF4

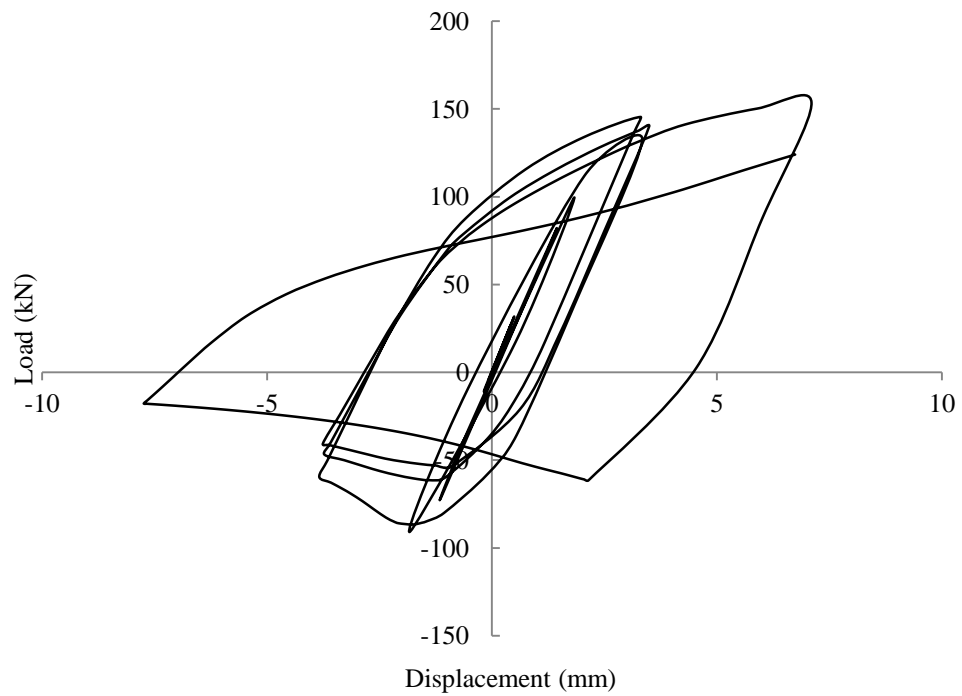


Figure A.3.5 Load-displacement relationship for CF5

## Appendix A

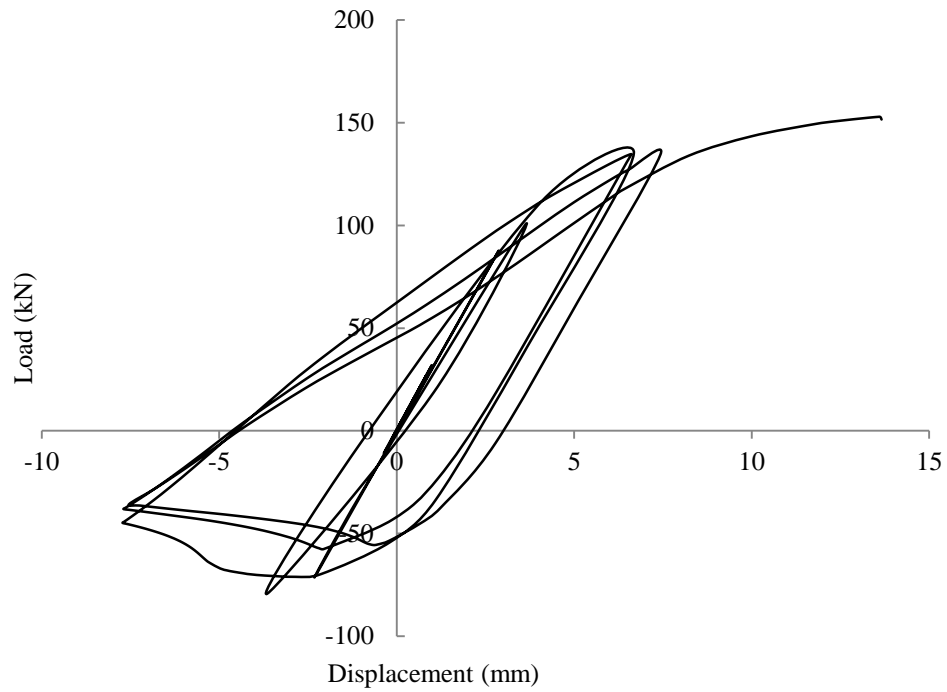


Figure A.3.6 Load-displacement relationship for CF6

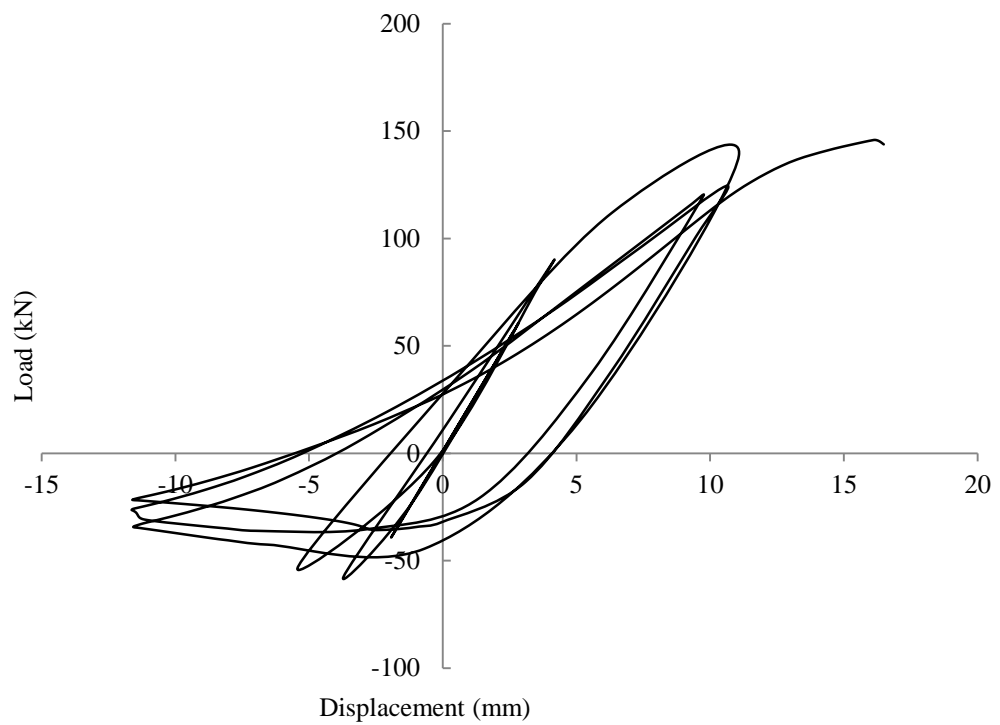


Figure A.3.7 Load-displacement relationship for CF7

## Appendix A

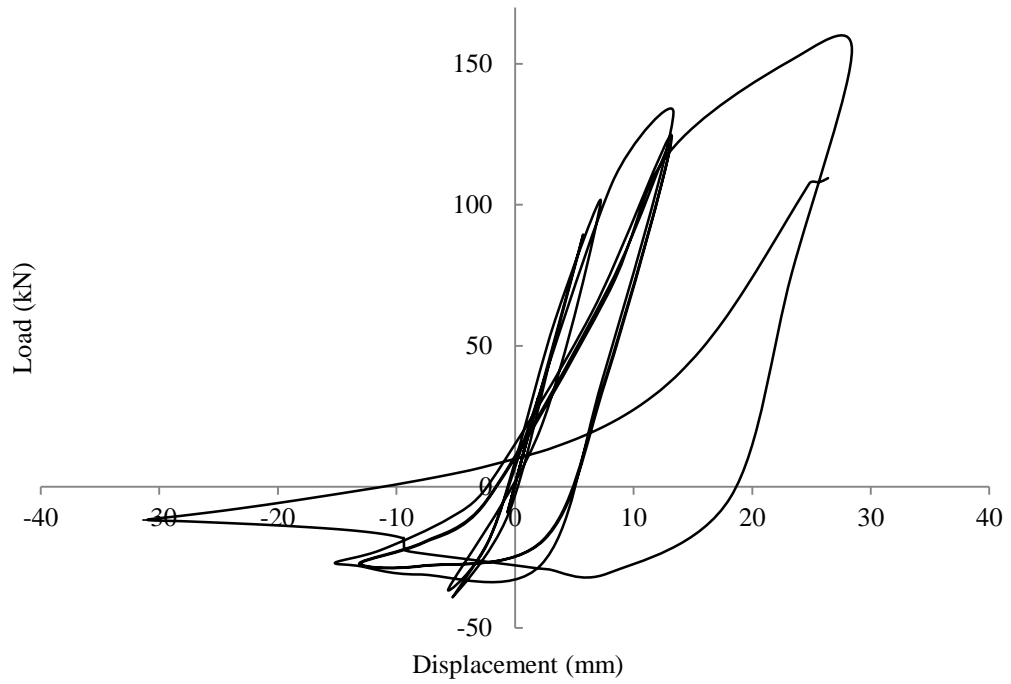


Figure A.3.8 Load-displacement relationship for CF8

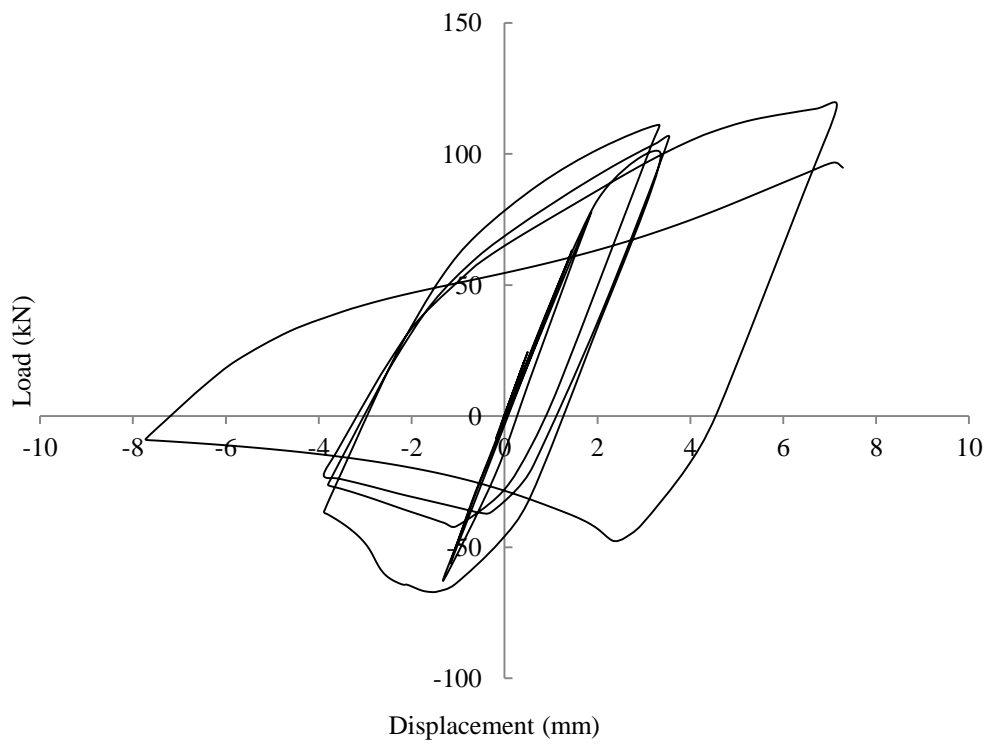


Figure A.3.9 Load-displacement relationship for CF9

## Appendix A

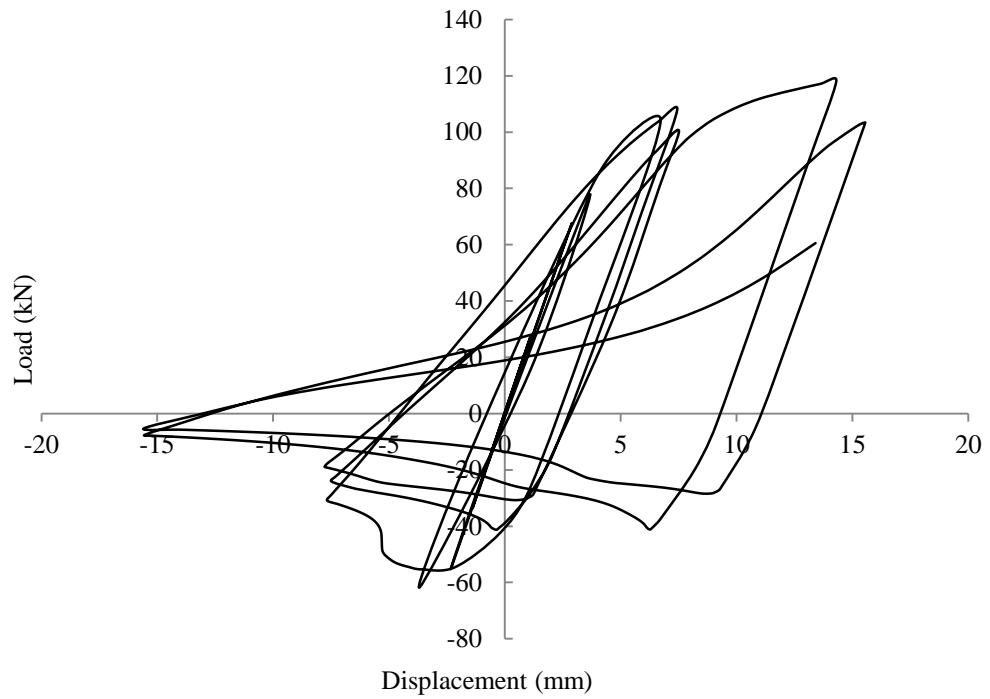


Figure A.3.10 Load-displacement relationship for CF10

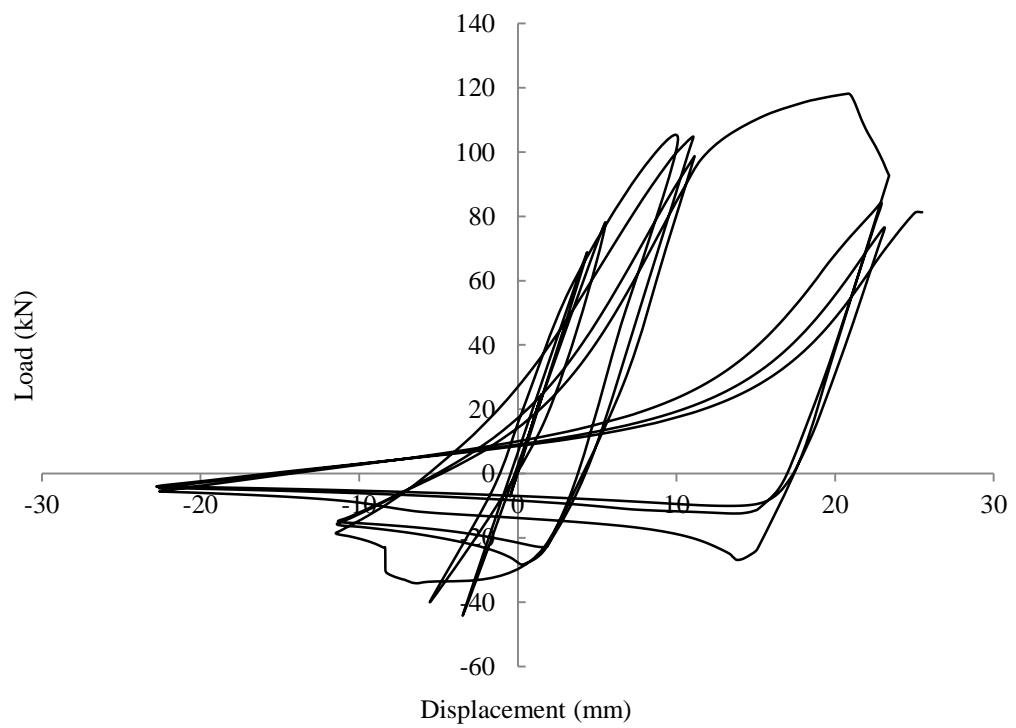


Figure A.3.11 Load-displacement relationship for CF11

## Appendix A

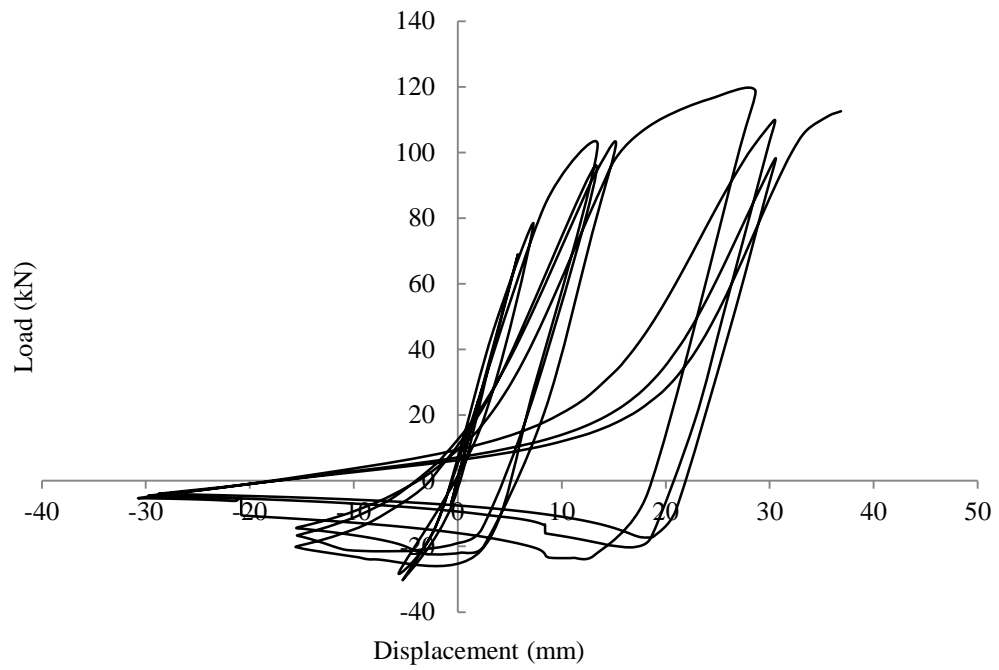


Figure A.3.12 Load-displacement relationship for CF12

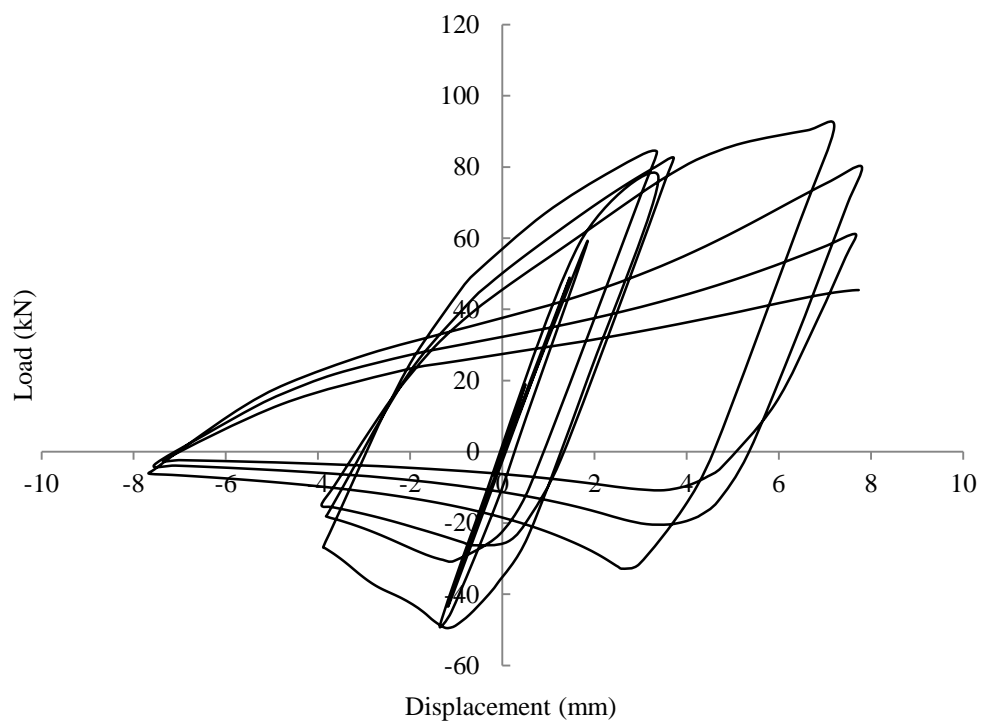


Figure A.3.13 Load-displacement relationship for CF13

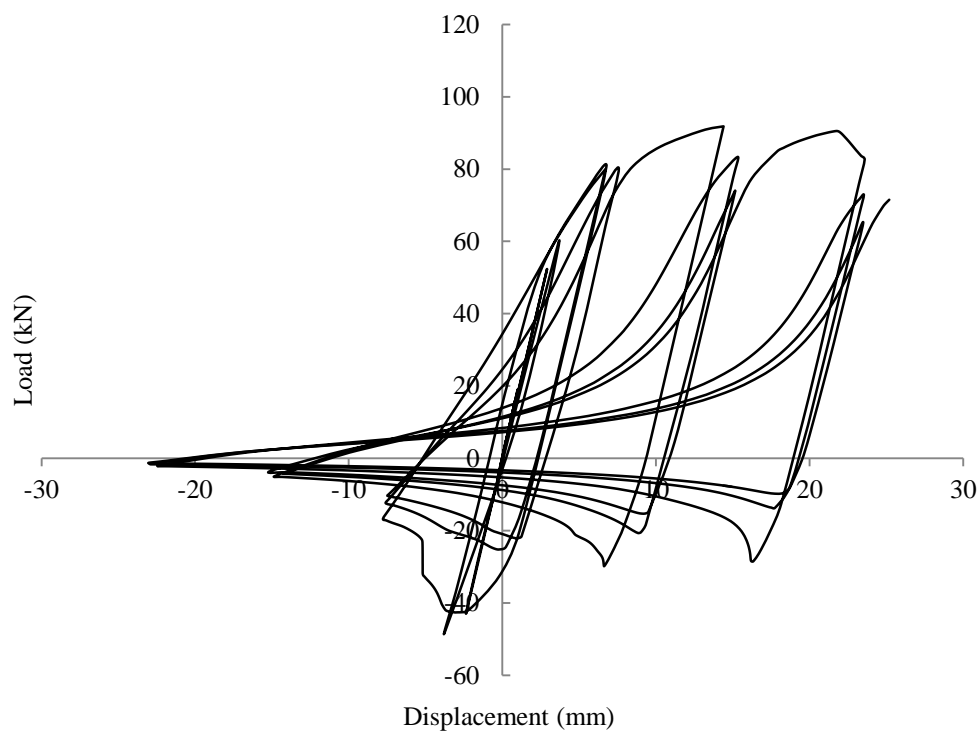


Figure A.3.14 Load-displacement relationship for CF14

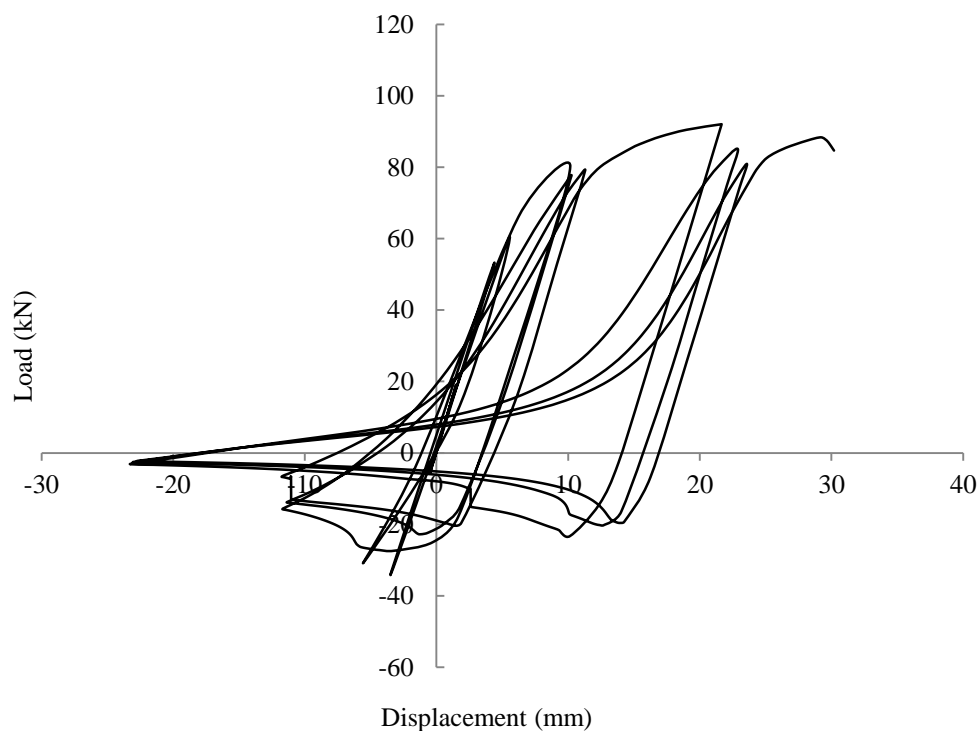


Figure A.3.15 Load-displacement relationship for CF15

## Appendix A

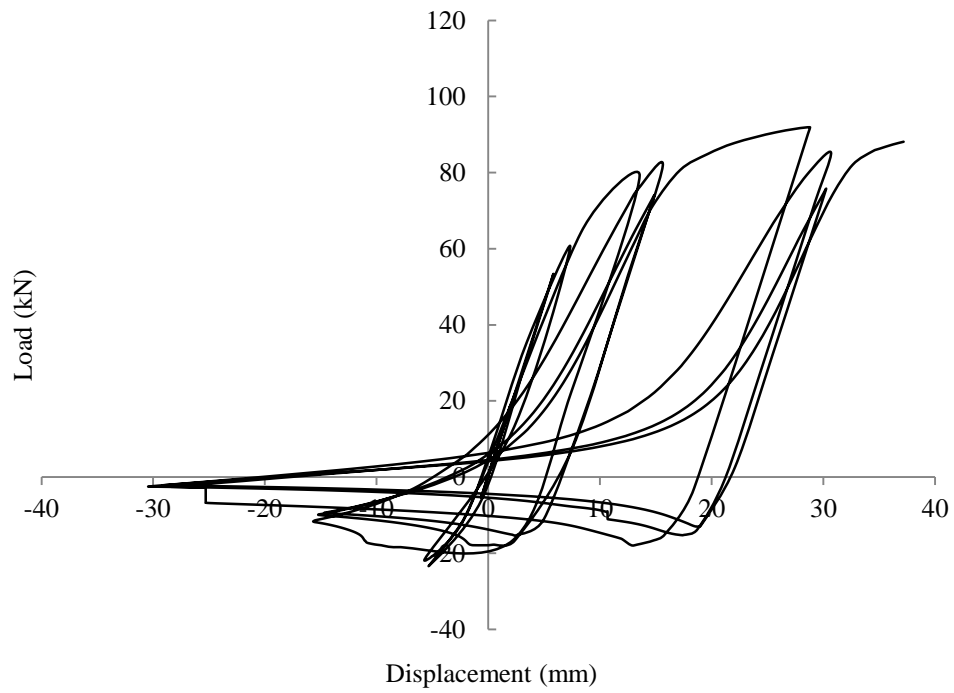


Figure A.3.16 Load-displacement relationship for CF16

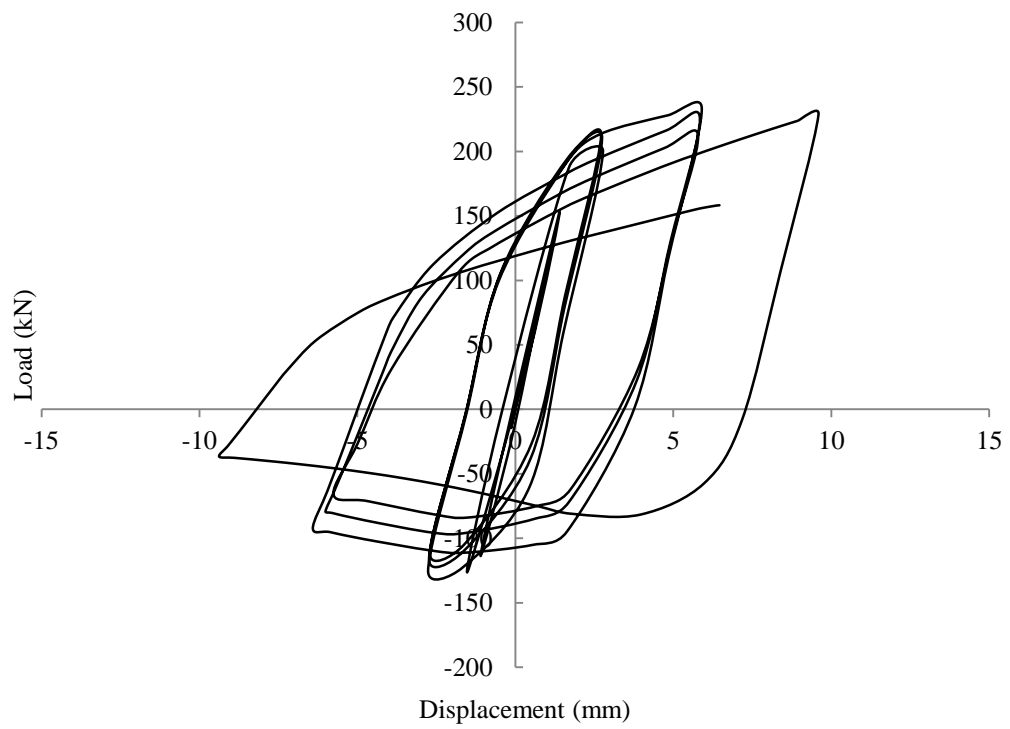


Figure A.3.17 Load-displacement relationship for HF1

## Appendix A

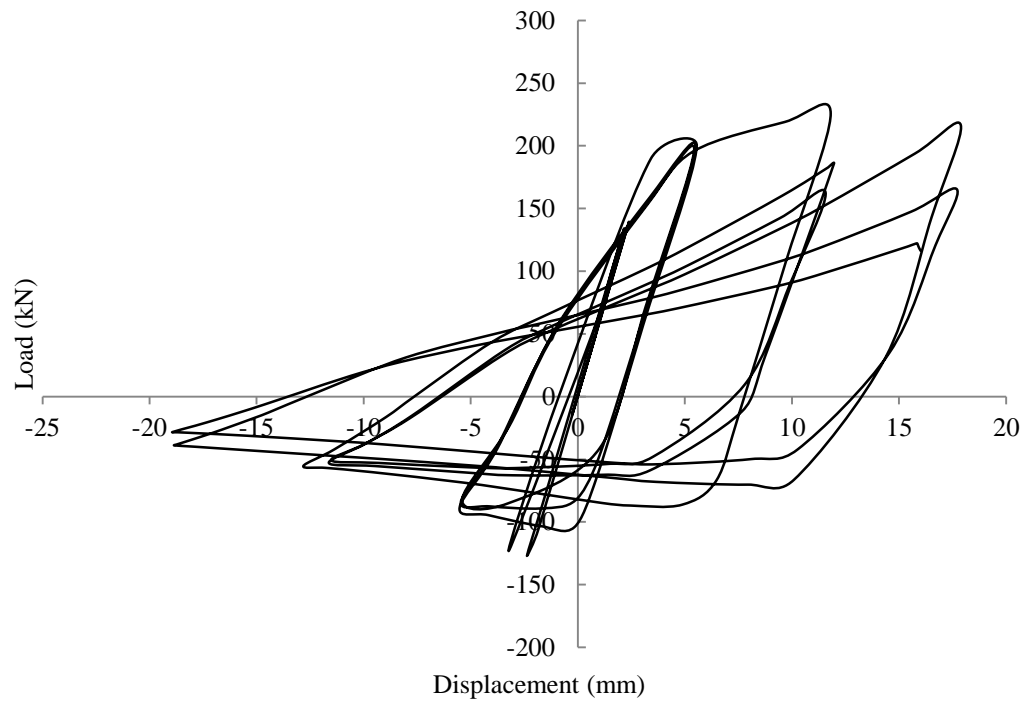


Figure A.3.18 Load-displacement relationship for HF2

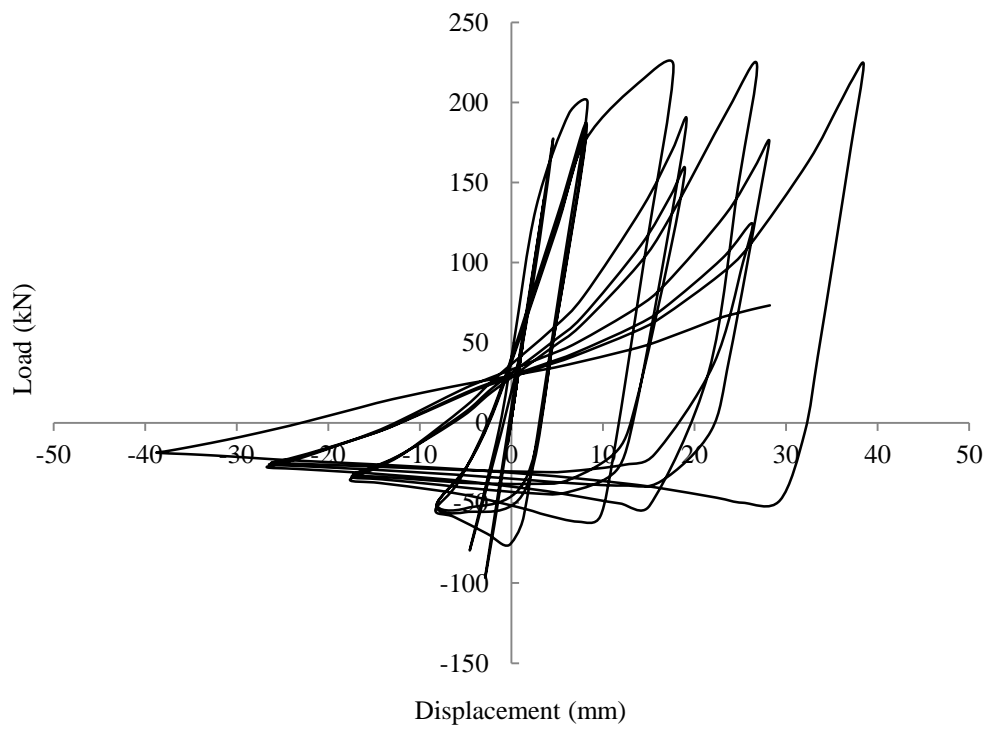


Figure A.3.19 Load-displacement relationship for HF3



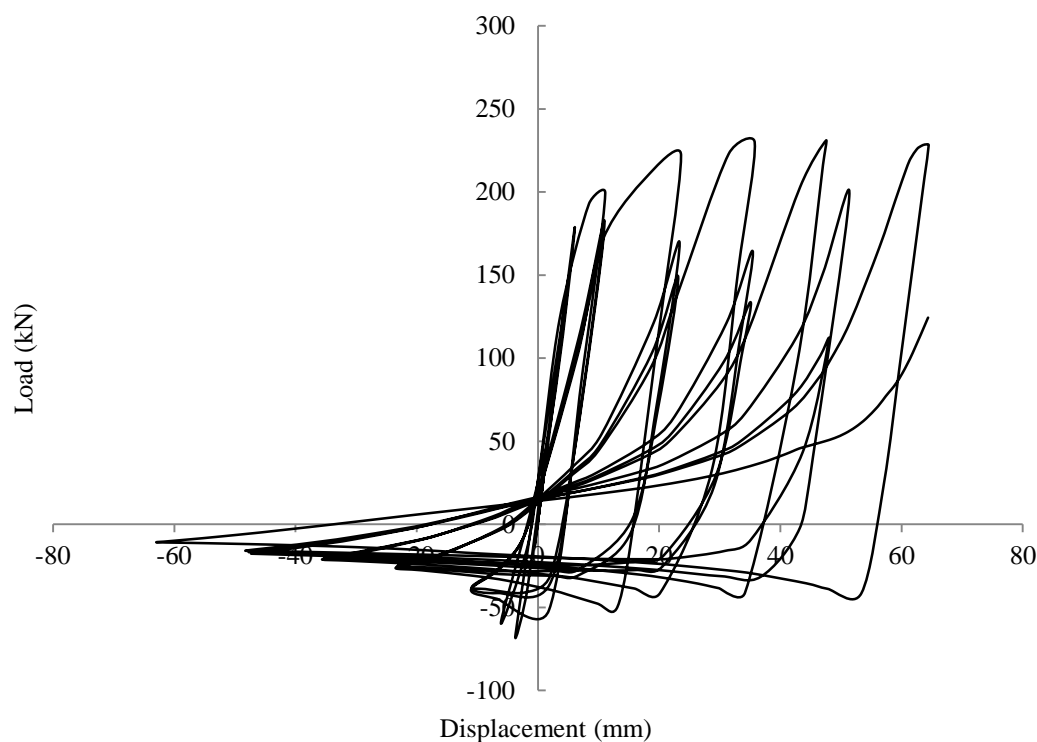


Figure A.3.20 Load-displacement relationship for HF4

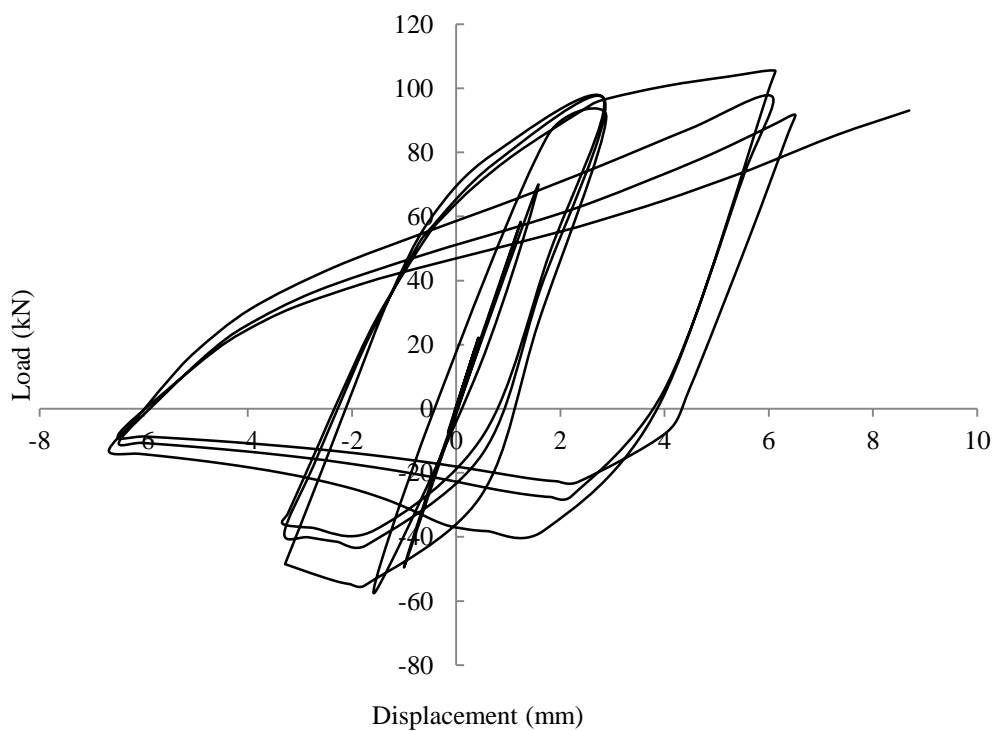


Figure A.3.21 Load-displacement relationship for HF5

## Appendix A

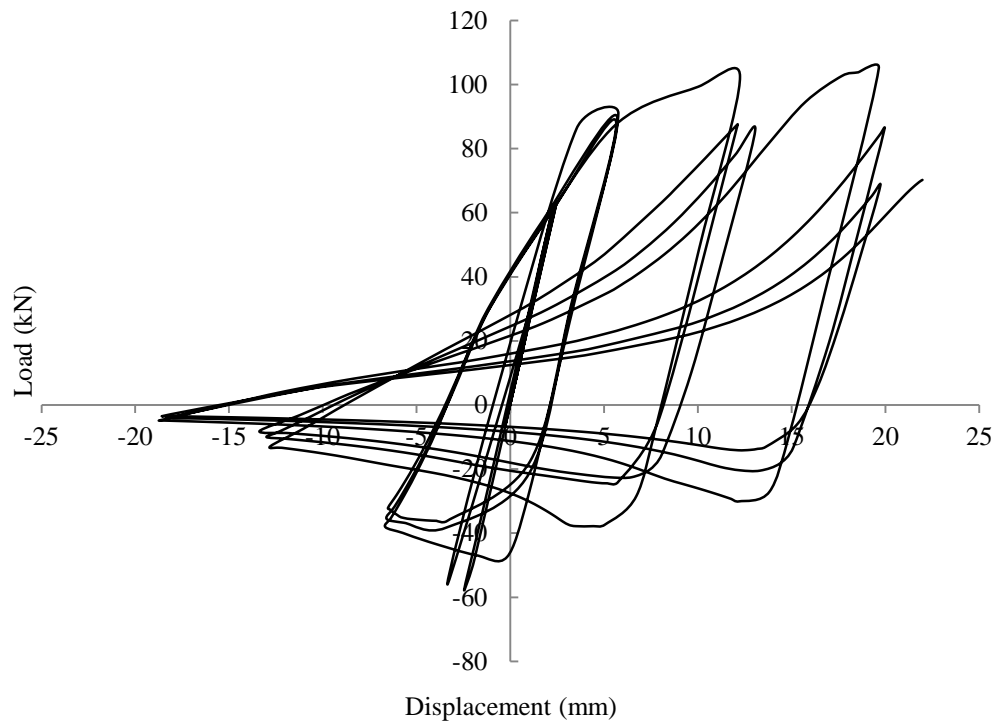


Figure A.3.22 Load-displacement relationship for HF6

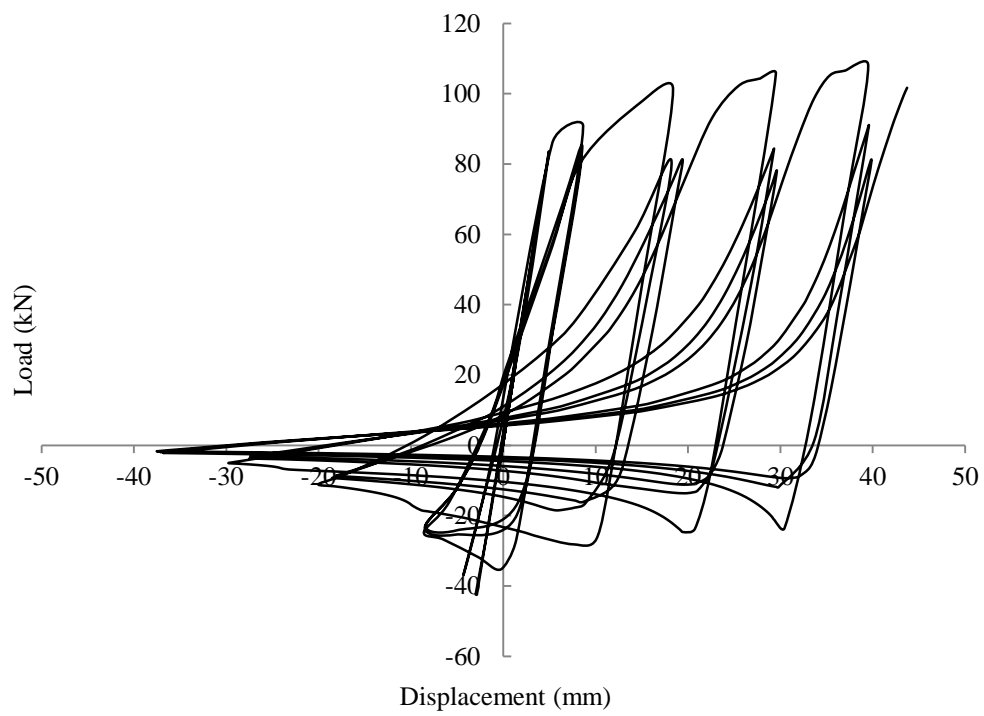


Figure A.3.23 Load-displacement relationship for HF7

## Appendix A

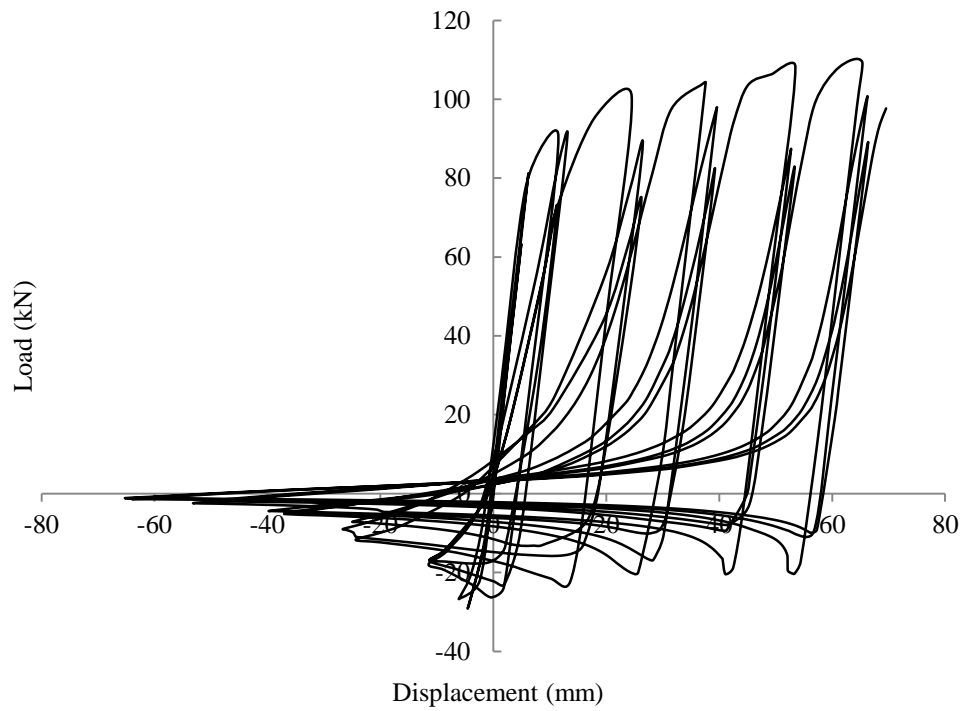


Figure A.3.24 Load-displacement relationship for HF8

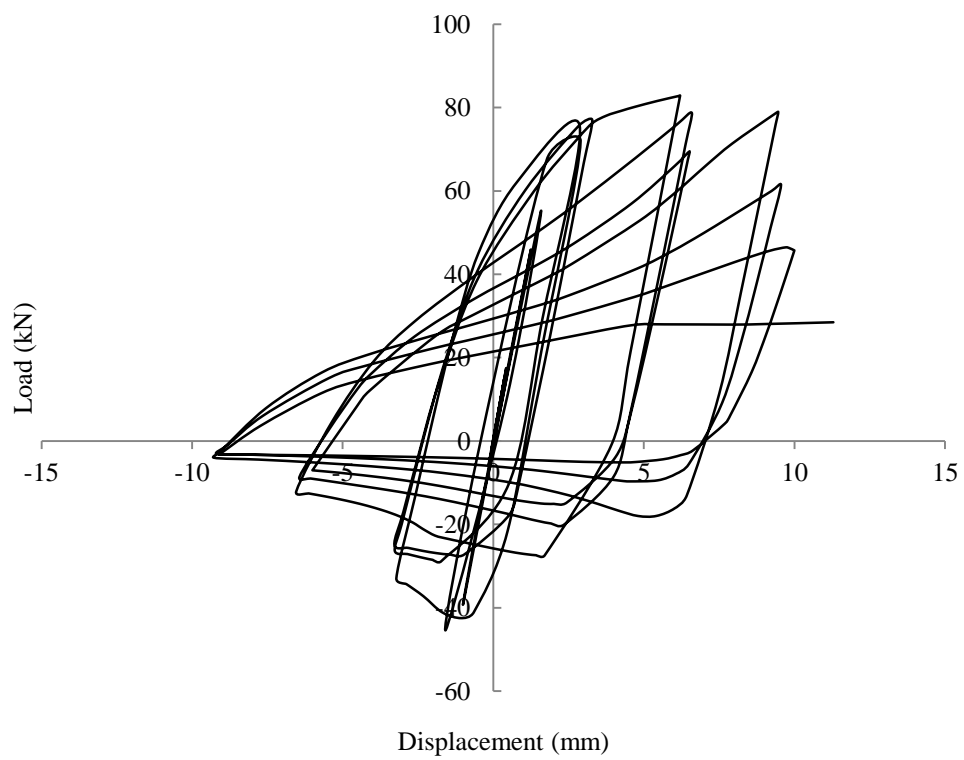


Figure A.3.25 Load-displacement relationship for HF9

## Appendix A

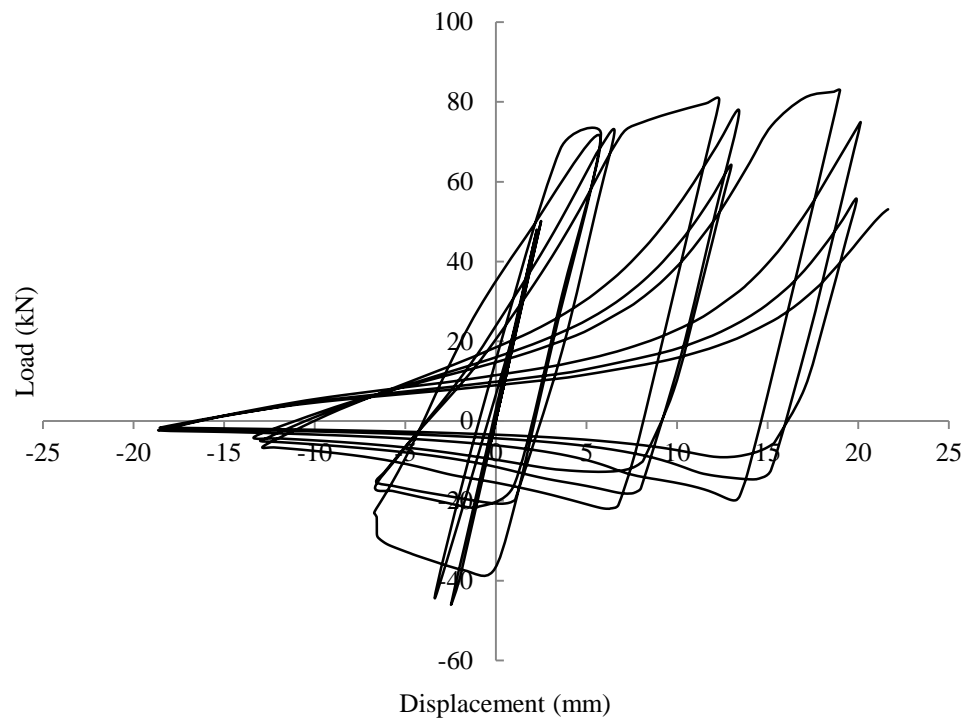


Figure A.3.26 Load-displacement relationship for HF10

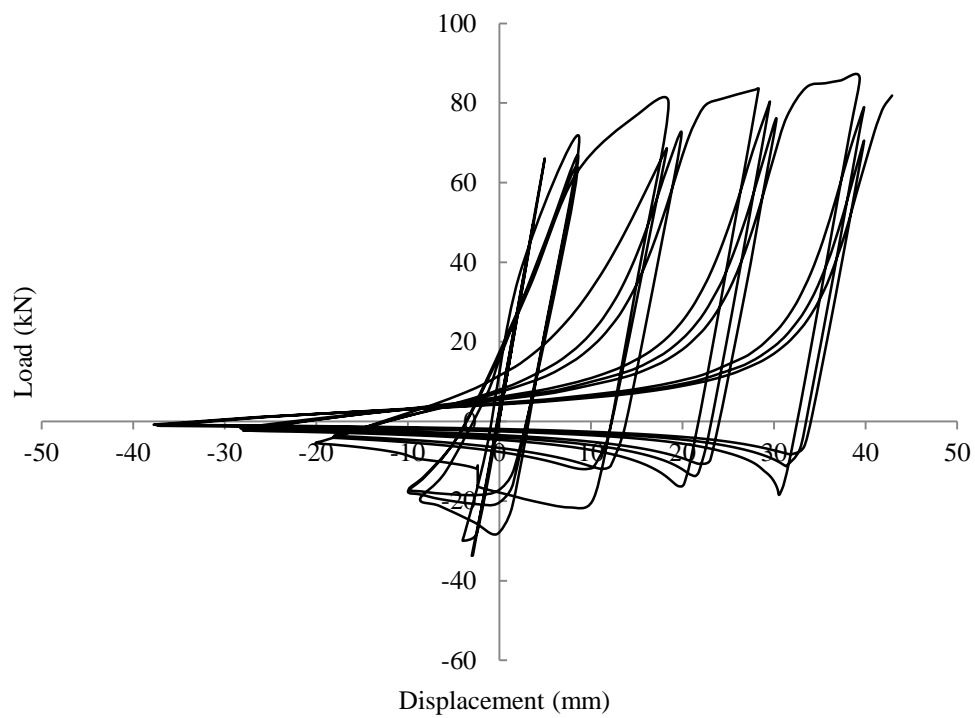


Figure A.3.27 Load-displacement relationship for HF11

## Appendix A

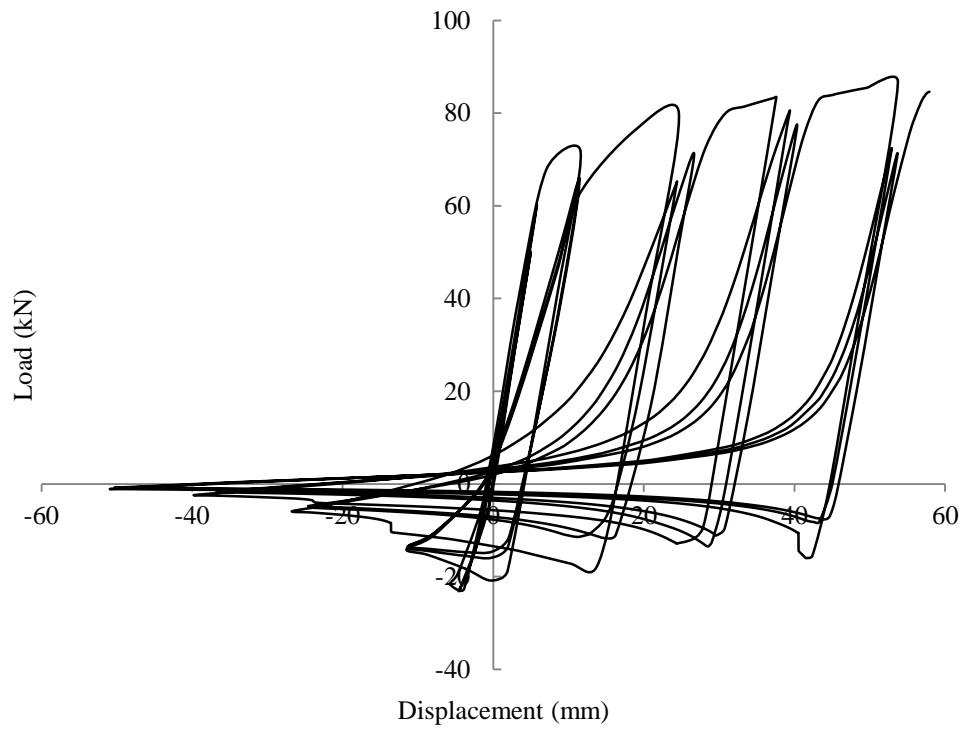


Figure A.3.28 Load-displacement relationship for HF12

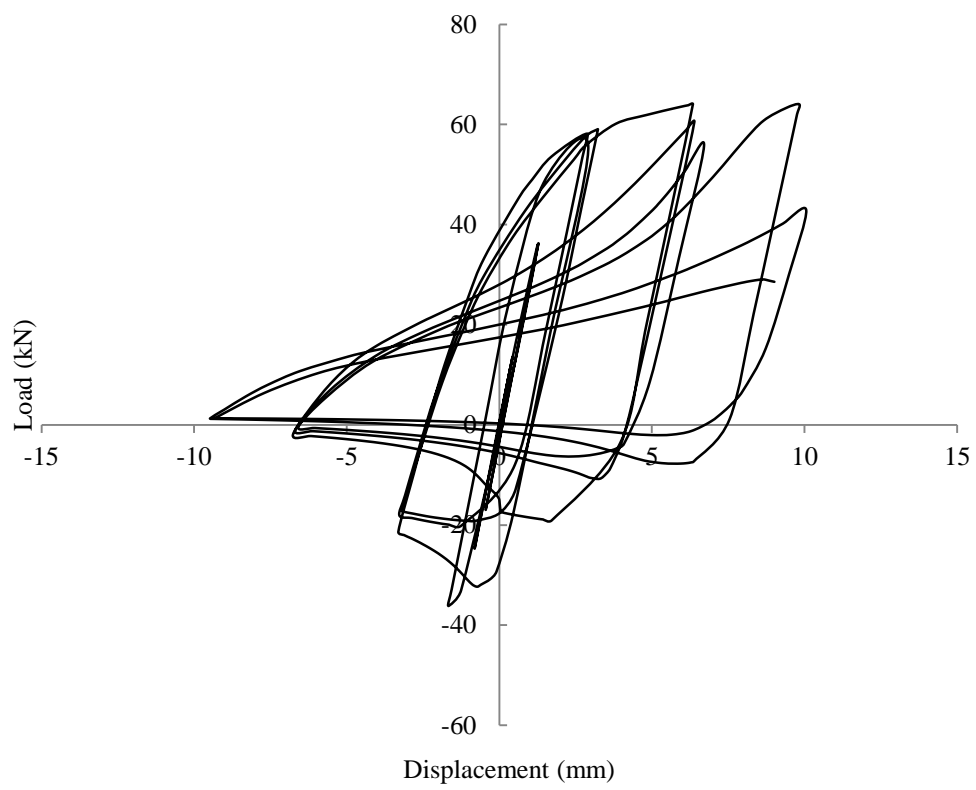


Figure A.3.29 Load-displacement relationship for HF13

## Appendix A

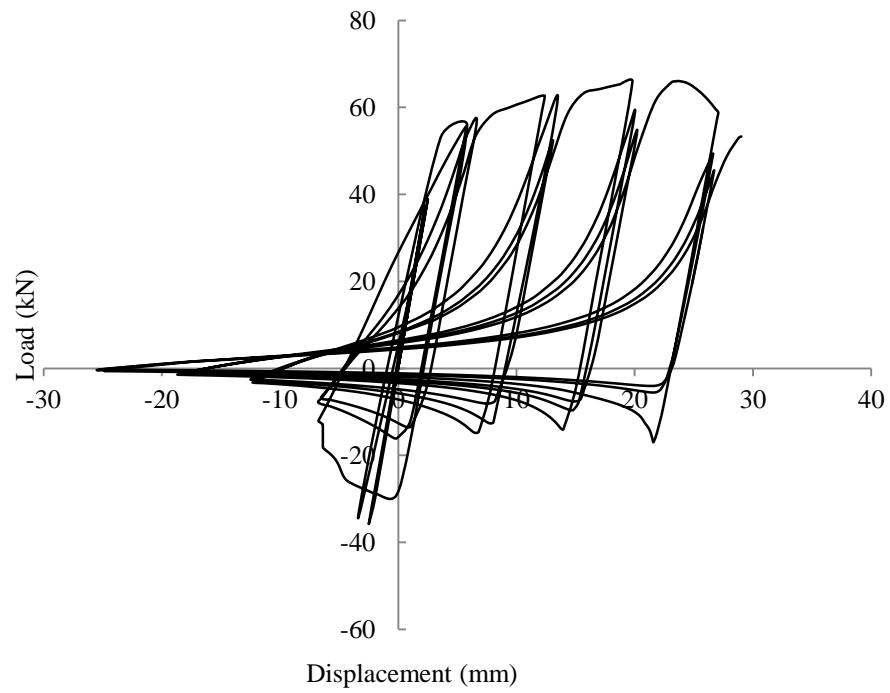


Figure A.3.30 Load-displacement relationship for HF14

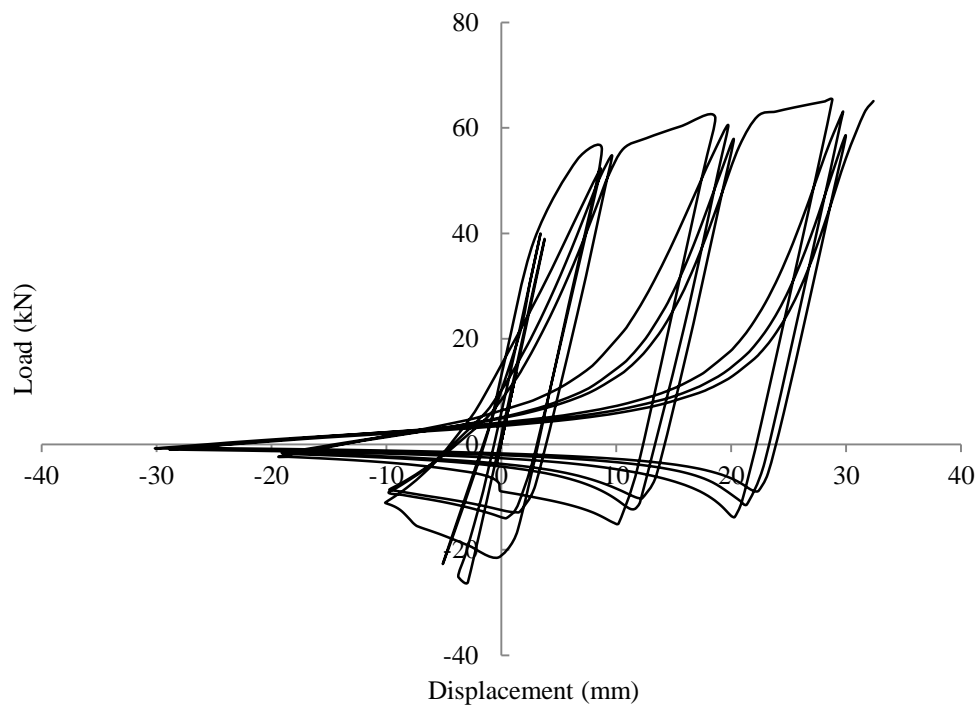


Figure A.3.31 Load-displacement relationship for HF15

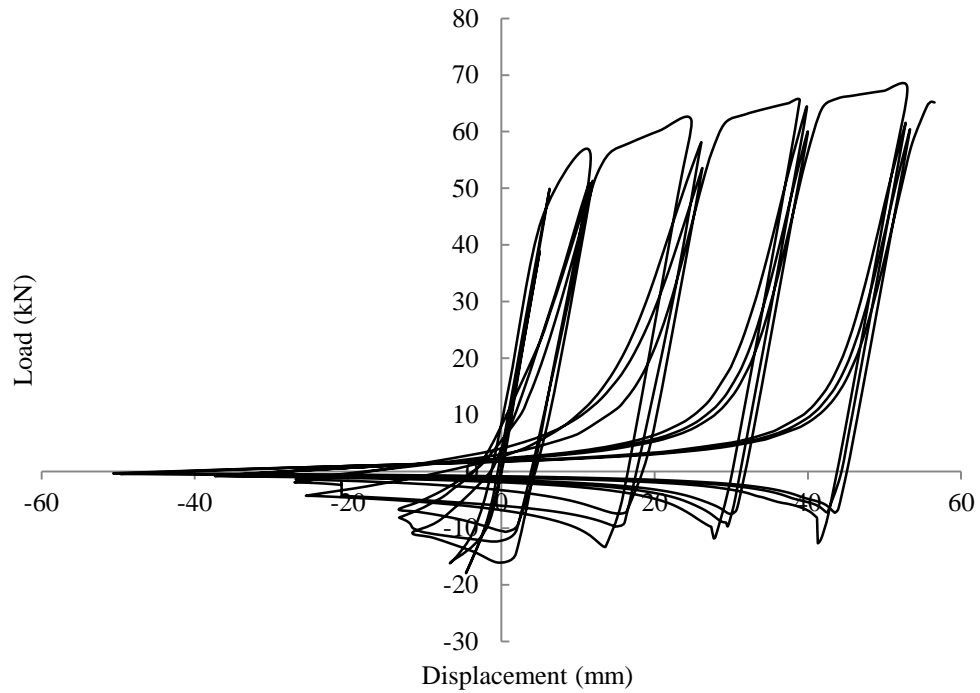


Figure A.3.32 Load-displacement relationship for HF16

Table A.3.1 compares the estimated number of cycles to fracture for each of the hollow brace parametric study specimens. The number of cycles to failure observed in the load-displacement hysteresis relationship is compared with the estimations calculated from the observed strains, using the rainflow counting algorithm (Matsuishi and Endo, 1968) and counting individual ramps in the strain cycles.

## Appendix A

Table A.3.1 Estimated number of cycles to fracture for parametric studies

<b>Specimen</b>	<b>No of cycles to failure (observed)</b>	<b>No of cycles to failure (rainflow)</b>	<b>No of cycles to failure (peak-trough)</b>
CF1	8	17	9
CF2	8	10	8
CF3	9	10	10
CF4	10	11	11
CF5	8	10	10
CF6	7	7	7
CF7	7	8	8
CF8	8	9	9
CF9	8	9	8
CF10	9	7	6
CF11	10	7	7
CF12	10	10	9
CF13	10	10	9
CF14	13	8	7
CF15	10	9	9
CF16	10	10	9
HF1	11	-	12
HF2	12	19	17
HF3	14	15	15
HF4	17	-	18
HF5	10	14	11
HF6	13	-	13
HF7	16	-	14
HF8	19	18	18
HF9	13	-	13
HF10	13	17	10
HF11	16	13	11
HF12	16	22	18
HF13	12	-	14
HF14	16	13	11
HF15	13	-	11
HF16	16	15	14